

Modelling Dynamic Spatial Patterning in Neural Development

A thesis submitted to the University of Manchester for the degree of
Doctor of Philosophy
in the Faculty of Biology, Medicine and Health

2023

Joshua J Hawley

Division of Developmental Biology and Medicine, School of Medical Sciences

Contents

Contents	2
List of figures	5
List of tables	7
List of publications	8
Terms and abbreviations	9
Abstract	11
Declaration of originality	12
Copyright statement	13
Acknowledgements	14
Thesis layout guidance and rationale	16
1 Introduction	18
1.1 The dynamic Waddington landscape	18
1.2 Neurogenesis in the developing neural tube	20
1.2.1 Embryo level: Formation of the neural tube	20
1.2.2 Tissue level: Morphogen gradients set up domains of distinct neural progenitors	22
1.2.3 Single-cell level: Hes genes control differentiation by maintaining a progenitor state	23
1.2.4 Communication between cells: Notch-Hes5 interactions	26
1.2.5 The emergent pattern: A dynamic multicellular spatial pattern of HES5	29
1.3 Existing mathematical models and biological systems with dynamic or spatially periodic patterns	31
1.3.1 A definition of coupling strength	31
1.3.2 Stationary ‘salt and pepper’ patterns	32

1.3.3 Hes5 oscillations and synchronisation	35
1.4 Aims of the thesis	41
2 Manuscript 1: A dynamic, spatially periodic, micro-pattern of HES5 underlies neurogenesis in the mouse spinal cord	42
2.1 Guide to the manuscript and supplementary files	43
2.2 Author contributions	43
2.2 Manuscript	45
2.3 Expanded view figures	72
2.4 Modelling Appendix	81
2.4.1 Stochastic model of auto-repression coupled between cells	81
2.4.2 Numerical implementation of neighbouring cells	84
2.4.3 Parameter space explorations and parameter selection	85
2.4.4 Rate of differentiation from synthetic data	86
3 A travelling wave model of dynamic periodic expression	88
3.1 Introduction	88
3.1.1 The multicellular lateral inhibition HES5 model	91
3.2 Results	93
3.2.1 Perturbations do not result in travelling waves in the base lateral inhibition model	93
3.2.2 A spatial gradient in any model parameter results in travelling waves	95
3.2.3 Steeper gradients result in slower travelling waves and shorter spatial periods	98
3.2.4 Noise in the parameter gradient does not bring the model output closer to the travelling wave behaviour of the neural tube	100
3.2.5 HES5 oscillations are not nested within the longer period, larger amplitude oscillations	102
3.3 Discussion	102
3.4 Methods	105
3.4.1 Measuring temporal periods of single cells	105
3.4.2 Extracting spatial signals from the model	105
3.4.3 Detecting statistically significant spatial periods	106
3.4.4 Coherence	108
4 Manuscript 2: Dynamic switching of lateral inhibition spatial patterns	110
4.1 Guide to the manuscript and supplementary files	111
4.2 Author contributions	111

4.2	Manuscript	112
4.3	Supplementary figures	129
4.4	Supplementary movies	132
5	Characterising protrusions and their role in patterning	133
5.1	Results	135
5.1.1	Sox2CreERT2 mTmG embryos enable visualisation of protrusions in neural progenitors	135
5.1.2	Protrusions exhibit a wide range of possible lengths and angles of extension	139
5.1.3	Protrusions can extend contact distance beyond immediate neigh- bours	141
5.1.4	Expression of Dll1 can be found within protrusions	144
5.2	Discussion	146
5.3	Methods	149
5.3.1	Mosaic membrane marking of progenitor cells using Sox2CreERT2 mTmG system	149
5.3.2	Cryosection preparation and immunostaining	149
5.3.3	Measurment of cell widths and protrusion lengths	150
5.3.4	Measuring protrusion length	150
6	General discussion	151
6.1	Introduction	151
6.2	How are clusters formed?	151
6.2.1	Summary of findings	151
6.2.2	Interpretation and future work	152
6.3	What generates the long-term switching dynamic?	153
6.3.1	Summary of findings	153
6.3.2	Interpretation and future work	154
6.4	What is the function of the dynamic spatial pattern?	155
6.4.1	Interpretation and future work	156
6.5	Overall conclusion	157
	References	159

Word Count: 80,065

List of figures

1.1	The Waddington epigenetic landscape as depicted in (Waddington, 2014) and an example of how cell-to-cell communication would look within the landscape analogy.	19
1.2	The morphology of neural tube development.	21
1.3	How domains of transcription factors in the neural tube correspond to distinct progenitor populations.	23
1.4	The interactions of HES proteins in the regulation of gene transcription and differentiation.	25
1.5	An overview of the Notch-Delta interactions with Hes5.	27
1.6	The emergent HES5 pattern.	30
1.7	Ways of defining coupling in the Notch-Delta pathway	32
1.8	Summary of the Collier et al. mathematical model along with <i>in-silico</i> and <i>in-vivo</i> examples of 2D salt and pepper patterning.	33
1.9	Mathematical models that produce stationary and dynamic spatial patterns with their typical output summarised in kymograph form. . .	36
1.10	How time delay affects in-phase and anti-phase synchronisation dynamics in coupled autonomous oscillators.	40
3.1	How travelling waves progress during somitogenesis and examples of travelling wave behaviour in neural tube HES5 expression.	90
3.2	Schematic of the model and indices used in Chapter 3.	92
3.3	<i>In-silico</i> clamping experiment shows that travelling waves do not naturally occur in a grid of cells coupled by lateral inhibition.	94
3.4	Applying a spatial gradient to any parameter results in travelling waves.	97
3.5	Steeper parameter gradients result in slower travelling waves and shorter spatial periods.	99
3.6	The effect of stationary noise and dynamic noise on travelling waves. . .	101
3.7	Autonomous HES5 oscillations are not nested within the coupling-induced globally synchronised oscillations.	103
M3.1	Outline of the process used for detecting the presence of significant periodic spatial patterns.	107
M3.2	How coherence is calculated from power spectra.	109

S4.1	Exploration of different distal cell geometries.	129
S4.2	Effect of lateral inhibition time delay, T_{LI} , and differentiation time, T_{pert} , on the region of dynamic patterning (red) in 1D simulations. . .	130
S4.3	Effect of lateral inhibition time delay, T_{LI} , and differentiation time, T_{pert} , on the region of dynamic patterning (red) in 2D simulations . . .	131
5.1	Protrusion mediated Notch signalling and the effects of distal and proximal coupling strengths on the resulting pattern	134
5.2	Summary of the Sox2CreERT2 mTmG system used to mosaically label the membranes of neural progenitor cells in the neural tube. . . .	136
5.3	Visualising and tracing of protrusions using confocal imaging of E10.5 Sox2CreERT2 ^{+/-} mTmG ^{+/-} mouse neural tube cryosections.	138
5.4	Quantitative characterisation of protrusion length and orientation, and RG cell width.	140
5.5	Idealised arrangement of RG cells scaled by measured cell widths, and example images of protrusions touching other mG fluorescent cells. . .	142
5.6	Dll1 immunostaining in E10.5 Sox2CreERT2 ^{+/-} mTmG ^{+/-} cryosections.	145

List of tables

2.1	Specific figure contributions from Joshua Hawley in Manuscript 1. . . .	43
3.1	Model parameters used in Figure 3.3.	94
3.2	Nominal model parameters used in Figure 3.4, 3.5, 3.6, 3.7.	96
4.1	Specific figure contributions from Joshua Hawley in Manuscript 2. . . .	111

List of publications

- Biga, V., Hawley, J., Soto, X., Johns, E., Han, D., Bennett, H., Adamson, A. D., Kursawe, J., Glendinning, P., Manning, C. S., et al. (2021). A dynamic, spatially periodic, micro-pattern of *hes5* underlies neurogenesis in the mouse spinal cord. *Molecular systems biology*, *17*(5), e9902 (cit. on pp. 16, 29, 30, 90, 91, 106, 134).
- Doostdar, P., Hawley, J., Marinopoulou, E., Lea, R., Biga, V., Papalopulu, N., & Soto, X. (2022). Cell coupling compensates for changes in single-cell *her6* dynamics and provides phenotypic robustness. *bioRxiv*, 2022–12 (cit. on p. 17).
- Hawley, J., Manning, C., Biga, V., Glendinning, P., & Papalopulu, N. (2022). Dynamic switching of lateral inhibition spatial patterns. *Journal of the Royal Society Interface*, *19*(193), 20220339 (cit. on pp. 17, 91, 105, 106).

Terms and abbreviations

RG	Radial glial
Hes	Hairy and enhancer of split 5 (gene)
HES	Hairy and enhancer of split 5 (protein)
AB	Apical-basal
DV	Dorsal-ventral
Dll	Delta-like
Jag	Jagged
Ngn	Neurogenin
NICD	Notch intracellular domain
bHLH	Basic helix-loop-helix
Mib	Mindbomb
MAML	Mastermind-like
RBPJ	Recombination signal sequence binding protein J
ADAM	A disintegrin and metalloproteinase
Lfng	Lunatic fringe

Abstract

In the developing spinal cord, the transcription factor Hairy and Enhancer of Split 5 (Hes5) exhibits ultradian oscillations (3-5 hrs) in its expression, which maintain cells in a progenitor state, while Hes5 is switched off when cells differentiate. Lateral inhibition via the Notch-Delta signalling pathway facilitates communication of HES5 dynamics between cells and enables appropriate ratios of progenitor and differentiated cell populations to be maintained. Work by others in the lab has found that Notch coupling enables HES5 to organise into small clusters (microclusters) of 3-7 cells which exhibit similar expression levels and synchronised ultradian oscillations in the embryonic mammalian spinal cord. These clusters are periodically repeated along the DV axis with a 3-4 cell spatial period. Furthermore, the pattern is temporally dynamic, with clusters switching between high and low expression on average every 8 hours. Ultradian HES5 oscillations are found to be nested within this longer-term switching. However, how this complex HES5 pattern emerges and what its significance is for neural development was neither intuitive nor understood.

In this thesis, I constructed mathematical models of HES5 dynamics coupled via Notch-mediated lateral inhibition to understand what underlies the generation of this spatiotemporal dynamic HES5 pattern and its potential function in spinal cord neurogenesis. Overall, I found that while features of the spinal cord data such as local synchronisation of ultradian oscillations could arise from simply coupling HES5 dynamics with time-delayed Notch interactions, other aspects of the data required additional mechanisms to be incorporated into the models.

To produce a 3-4 cell spatial period, it was necessary to extend cell-to-cell signalling distance beyond the nearest neighbours with protrusions as the motivating mechanism. Specifically, clusters of HES5 emerged when more signalling occurred at protrusions than at the cell body. The presence and extent of protrusions in the developing neural tube were experimentally characterised, suggesting they may extend the reach of Notch-Delta signalling as assumed in the modelling. Dynamic switching of the pattern in the model was achieved by introducing regular perturbations to HES5 dynamics in the form of altered Notch signalling coming from differentiating cells. Further, ultradian oscillations were found to be nested within the switching dynamics, as observed in the data.

Finally, two main functional roles of this pattern were suggested based on the modelling when the reasonable assumption was made that low HES5 cells have an increased probability of differentiation. Firstly, the rate of differentiation was found to vary with coupling strength due to changes in the cell-cell differences, and this was consistent with experimentally observed differences in differentiation rates observed in the motorneuron versus interneuron spinal cord domains. Secondly, the dynamic spatial pattern was found to spread out differentiating cells in space along the D-V axis over time.

In conclusion, mathematical modelling, in conjunction with experimental data, uncovered a hitherto unknown level of complexity in the spatiotemporal organisation of neurogenesis which arises when single-cell oscillations are synthesised at the tissue level. In addition, mathematical modelling led to specific testable hypotheses on the function and advantages of this emergent tissue-level organisation.

Declaration of originality

I hereby confirm that no portion of the work referred to in the thesis has been submitted in support of an application for another degree or qualification of this or any other university or other institute of learning.

Copyright statement

- i The author of this thesis (including any appendices and/or schedules to this thesis) owns certain copyright or related rights in it (the “Copyright”) and s/he has given The University of Manchester certain rights to use such Copyright, including for administrative purposes.
- ii Copies of this thesis, either in full or in extracts and whether in hard or electronic copy, may be made *only* in accordance with the Copyright, Designs and Patents Act 1988 (as amended) and regulations issued under it or, where appropriate, in accordance with licensing agreements which the University has from time to time. This page must form part of any such copies made.
- iii The ownership of certain Copyright, patents, designs, trademarks and other intellectual property (the “Intellectual Property”) and any reproductions of copyright works in the thesis, for example graphs and tables (“Reproductions”), which may be described in this thesis, may not be owned by the author and may be owned by third parties. Such Intellectual Property and Reproductions cannot and must not be made available for use without the prior written permission of the owner(s) of the relevant Intellectual Property and/or Reproductions.
- iv Further information on the conditions under which disclosure, publication and commercialisation of this thesis, the Copyright and any Intellectual Property and/or Reproductions described in it may take place is available in the University IP Policy (see <http://documents.manchester.ac.uk/DocuInfo.aspx?DocID=24420>), in any relevant Thesis restriction declarations deposited in the University Library, The University Library’s regulations (see <http://www.library.manchester.ac.uk/about/regulations/>) and in The University’s policy on Presentation of Theses.

Acknowledgements

The Paplopulu lab A fabulous team of highly supportive individuals with an incredible range of expertise. Working with such a fun team really makes a difference and they have made my time in the lab an absolute delight.

Nancy Throughout my PhD, Nancy has been a fantastic supervisor, providing support and guidance in the project while allowing me plenty of freedom to explore my own ideas. Her ability to navigate the details of the data and see the big picture is something I admire, but above all, I would like to thank her for creating an environment where I could explore what it means to be a scientist.

Paul As my main maths supervisor, Paul has been instrumental in the development of the models in this thesis. As a very busy man, Paul has always made time to meet me, whether in person or on one of our many zoom calls during the COVID pandemic. I have enjoyed every single one of our discussions and the invaluable ideas that came from them.

Cerys As my wet lab co-supervisor, Cerys has taught me probably most of the wet lab skills I have acquired, as well as the ins and out of experimental design. Cerys is very knowledgeable, highly supportive, and has been a joy to work with. Thanks for all the support and laughs, I hope you don't miss my never-ending questions too much!

Veronica I couldn't have asked for a better maths co-supervisor than Veronica! With a shared background in physics/engineering and a passion for answering biological questions from this viewpoint, I have relished every chat, presentation, and conference with Veronica. Veronica has looked out for me throughout my PhD, suggested amazing conferences for me to go to, and always went above and beyond when it came to collaboration. I really do appreciate everything you have done for me.

Anzy I think most of my TC training was with Anzy and when it came to experimental design, Anzy always made it feel like a team effort, always asking great questions and providing a wide range of expertise. I am especially grateful for the support Anzy gave me through the differentiation experiment that worked the first time, but then never again, leading to 5 months of fruitless troubleshooting. Fun times!

Elli I do believe Elli knows where everything is in the lab, and in my fumbling around in TC or the bench, I could always rely on Elli to point me to the correct fridge, help with experimental design, or to be a generally lovely and funny individual.

Rob Another person who knows where everything in the lab is, Rob is the guy to ask for help. Chatting with Rob usually resulted in a lot of laughing and he taught me the most important lesson of my PhD — the importance of not skipping the ‘washy washy’ step.

Richard Such a caring and intelligent friend and my TC confidant. I have enjoyed every second of his company and sharing in the woes of TC.

Josh & Jenny Scholars, board game players, fellow gig-goers, silly photo-sharers, and my PhD buddies. I am very fortunate to have become friends with these two during my PhD.

Jacob My housemate for most of my PhD, the nicest guy I know, and fellow Rocket League pro.

Neil, Connor, and Tom AKA ‘The boys’.

Jane, Justin & Ben A solid family, can’t fault the service provided, would absolutely recommend to a friend – 5 stars.

Bagel (the kitten) For accompanying me in my final weeks of thesis writing and doubling up as a hot water bottle on the colder days.

Parnian My best scientific discovery while working in the Papalopulu lab. Parnian is a source of laughter, is a fellow nerd, and shares an appreciation for how beautiful the world is when you just stop and look at it. Parnian has certainly made my PhD years more colourful, made my life tastier, introduced me to drinking tea (which I believe now qualifies me as an adult) and provided me with many supportive words and tasty meals during the moderately stressful last weeks of my thesis writing. Thank you very much for existing.

Other people I would like to acknowledge for making my time in the lab such a great experience include: Ximena, Jochen, Ollie, Andy, Tom, Nitin, Flo, Karel, Raf, Sean, and of course the rest of the QBB cohort.

Thesis layout guidance and rationale

This thesis is structured as a hybrid of journal format and traditional format, consisting of two published and peer-reviewed manuscripts (Chapters 2 & 4), and two traditional results chapters (Chapters 3 & 5). The papers were included so as to not require unnecessary rewriting of already published and formatted work, and the traditional chapters were included in between these manuscripts to give a fuller picture of the ideas and models tested that remained unpublished or preliminary. The chapters are ordered chronologically so that the thesis has a more logical flow and so that each chapter develops on the unanswered questions of the previous chapter.

Each manuscript is included as formatted by the journal and so references are self-contained within those. At the end of each published manuscript, the relevant supplementary material is included for ease of access. The bibliography at the end of the thesis contains all other references in the traditional chapters.

Chapter 1 - Introduction

A traditional thesis format introduction that details the necessary background to understand the role of HES5 and Notch signalling in the developing mouse neural tube, and the dynamic HES5 spatial pattern that is the main observation underlying this thesis. This is followed by a section covering the relevant mathematical modelling literature.

Chapter 2 - Manuscript 1

A research article published in *Molecular Systems Biology*, of which I am a co-first author (Biga et al., 2021). This paper characterises the dynamic spatial pattern of HES5 in the developing neural tube, and my main contribution to the paper was the mathematical modelling that explores how the dynamic pattern is generated and the effects of different coupling strengths on the differentiation rate in a multicellular

model of HES5 dynamics.

Chapter 3 - A travelling wave model of dynamic periodic expression

A traditional format chapter which through mathematical modelling explores a travelling wave mechanism as a potential mechanism in generating dynamic spatial patterns. Ultimately this work was never published as it is a negative result but provides important insight into the hypotheses tested and gives context to the second manuscript in the following chapter.

Chapter 4 - Manuscript 2

A research article published in Royal Society Interface, of which I am the first author (Hawley et al., 2022). A computational model study which explores the role of extended signalling distance and altered Notch signalling strength in differentiating cells in generating a dynamic pattern with a spatial period and clustering closely resembling the biological expression of HES5.

Chapter 5 - Characterising protrusions and their role in patterning

A traditional format chapter that begins experimental testing of the idea that protrusions may enable the extended signalling distance put forward in the mathematical modelling of Chapter 4. This Chapter contains preliminary and future work sections as this represents the most recent work carried out during the PhD.

Supplementary manuscript

An additional preprint manuscript was also produced during my PhD (Doostdar et al., 2022), and this includes a modelling contribution to understanding the role of cell-to-cell coupling in rescuing normal development when Her6 dynamics are perturbed in the developing Zebrafish forebrain. It is not included here as it diverges from the main narrative of the thesis and instead is recommended as supplementary material that can be read [here](#).

Chapter 1

Introduction

1.1 The dynamic Waddington landscape

Embryonic development is not only the process by which one cell becomes many but is also the process by which cells differentiate and specialise into the multitude of cell types and tissues in an adult organism. In a cascade of regulation, individual cells act as autonomous decision-makers capable of integrating a multitude of external signals to shape the differentiation process and produce the correct cells at the correct time and in the correct place. In his epigenetic landscape analogy, Waddington compared the differentiation process to a marble, representing a cell, rolling down a hill where variations in the surface guide the marble on a particular path towards its final differentiated fate (Figure 1.1A) (Waddington, 2014).

A cell's genome determines the shape of this epigenetic landscape, which is further illustrated in Figure 1.1B as a series of interconnected ropes pulling on the underside of the landscape. Anchoring the ropes to the surface below are many pegs which represent individual accessible genes and as a cell differentiates, the set of silenced and accessible genes will change not only in response to cascades of internal gene regulation but also to external regulation which is largely influenced by cell-to-cell communication. Therefore the epigenetic landscape is less of a static predetermined shape and more of a continuously morphing structure that is not only shaped by its own history but also by the cells it will interact with as development goes on.

The Notch-Delta pathway is a key signalling network that actively shapes the decisions of individual cells based on the state of neighbouring cells. Notch signalling acts as a lateral inhibition circuit between two contacting cells, forcing one cell to adopt high gene expression and the other low. This subsequently drives two neighbouring cells into two distinct fates and in neurogenesis, this is often a choice between remaining as a progenitor or continuing the differentiation process. In the epigenetic landscape, two neural progenitors would have a similar past trajectory and the current progenitor state would be represented as a local dip where cells remain

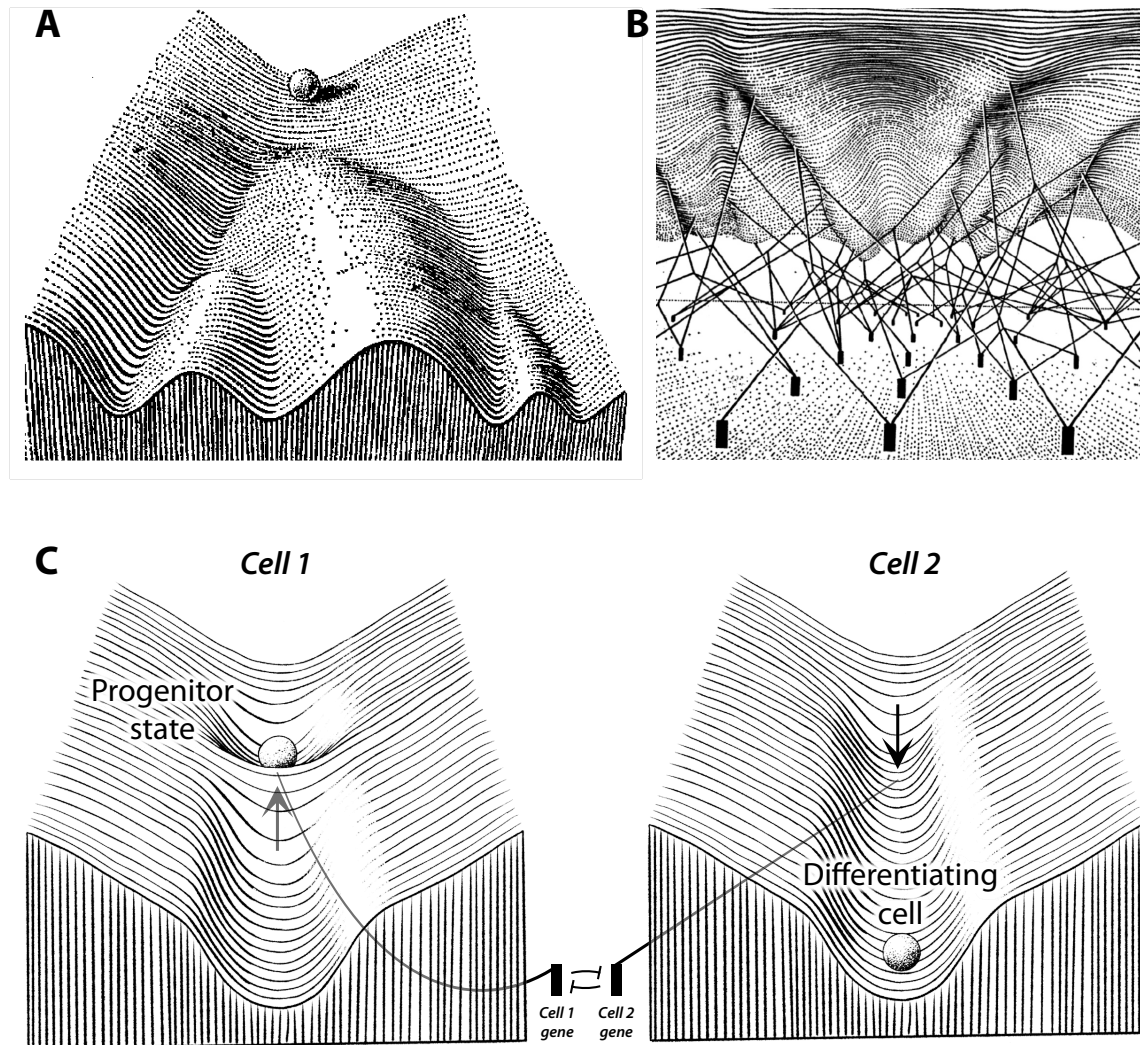


Figure 1.1: The Waddington epigenetic landscape as depicted in (Waddington, 2014) and an example of how cell-to-cell communication would look within the landscape analogy. **A** The view from above the landscape, where a marble representing a cell rolls down a hill with variations in its surface that guide the cell to a particular fate. **B** The underside view of the landscape where ropes and pegs represent the active genes (pegs) and their effect on the landscape. **C** Illustration of how lateral inhibition would look within the epigenetic landscape analogy. The same gene in each cell (represented by the two pegs) controls the process of differentiation. In Cell 1, the local dip in the landscape prevents the cell from progressing further down the landscape and the cell remains stuck in a progenitor state. The gene expression in Cell 2 is able to pull tight on the barrier that prevents the cell from rolling down the landscape, enabling the cell to differentiate. Because these two cells interact via lateral inhibition, the two cells must adopt opposite fates, and so Cell 2 inhibits Cell 1 from also collapsing the barrier.

stuck as illustrated in Figure 1.1C (left). Lateral inhibition between these two cells would then work to ensure that one cell's landscape maintains this local progenitor dip, while in the other cell, the dip would morph into a slope, causing that cell to move towards a more differentiated state (Figure 1.1C (right))(Sáez et al., 2022). Actively sensing the cellular environment rather than following a set path along a predetermined epigenetic landscape gives cells the ability to adapt their differentia-

tion pathway in an inherently noisy internal and external environment, leading to a more robust developmental process where reproducible proportions of cells and tight boundaries can form (Monk, 1997).

In this thesis, the role of lateral inhibition in the developing neural tube is examined from the perspective of how it mechanistically forms dynamic and spatially patterned gene expression as well as its functional role in development. The introduction will cover the morphology of how the brain and spinal cord form, followed by a description of the subsequent process of neurogenesis at the tissue level where morphogen gradients specify neuronal fate. This is followed by a detailed look at how single-cell level dynamics of the transcription factor Hes5 control the differentiation process. Then, building back up from the single-cell level, the role of Notch signalling in cell-to-cell communication of HES5 levels will be discussed. Finally, the dynamic spatial pattern of HES5 will be outlined, followed by the relevant biological and mathematical background required for a contextual understanding of the results presented in the remaining chapters.

1.2 Neurogenesis in the developing neural tube

1.2.1 Embryo level: Formation of the neural tube

The formation of the neural tube begins with the appearance of the neural groove at around embryonic day 7.5 (E7.5) in mice (Figure 1.2A) and ultimately gives rise to the spinal cord, brain, and retina (Chen et al., 2017). The tubular shape is formed when the neural plate – an outer layer of an embryo consisting of a single layer of epithelial cells – invaginates to form a hollow structure that sits just below the surface of the embryo (Figure 1.2B), which completes a closed tube beginning around E8.0 (Figure 1.2C).

The ventricle is at the innermost region of the neural tube which is the cavity that eventually becomes filled with cerebrospinal fluid. The initial population of cells that surround the ventricle are called neuroepithelial cells which undergo exclusively symmetric divisions and thicken the neural tube wall as the population grows (Figure 1.2D) (Ulrich, 2010). As development progresses and neuroepithelial cells elongate into radial glial (RG) cells, asymmetric division becomes more prevalent whereby one cell will continue in an RG state, and the other will go on to differentiate into a neuronal cell (Bansod et al., 2017). Differentiation is accompanied by detachment from the apical surface (at the ventricle) and migration towards the basal side of the tissue, and this process goes on to form the majority of neurons in the central nervous

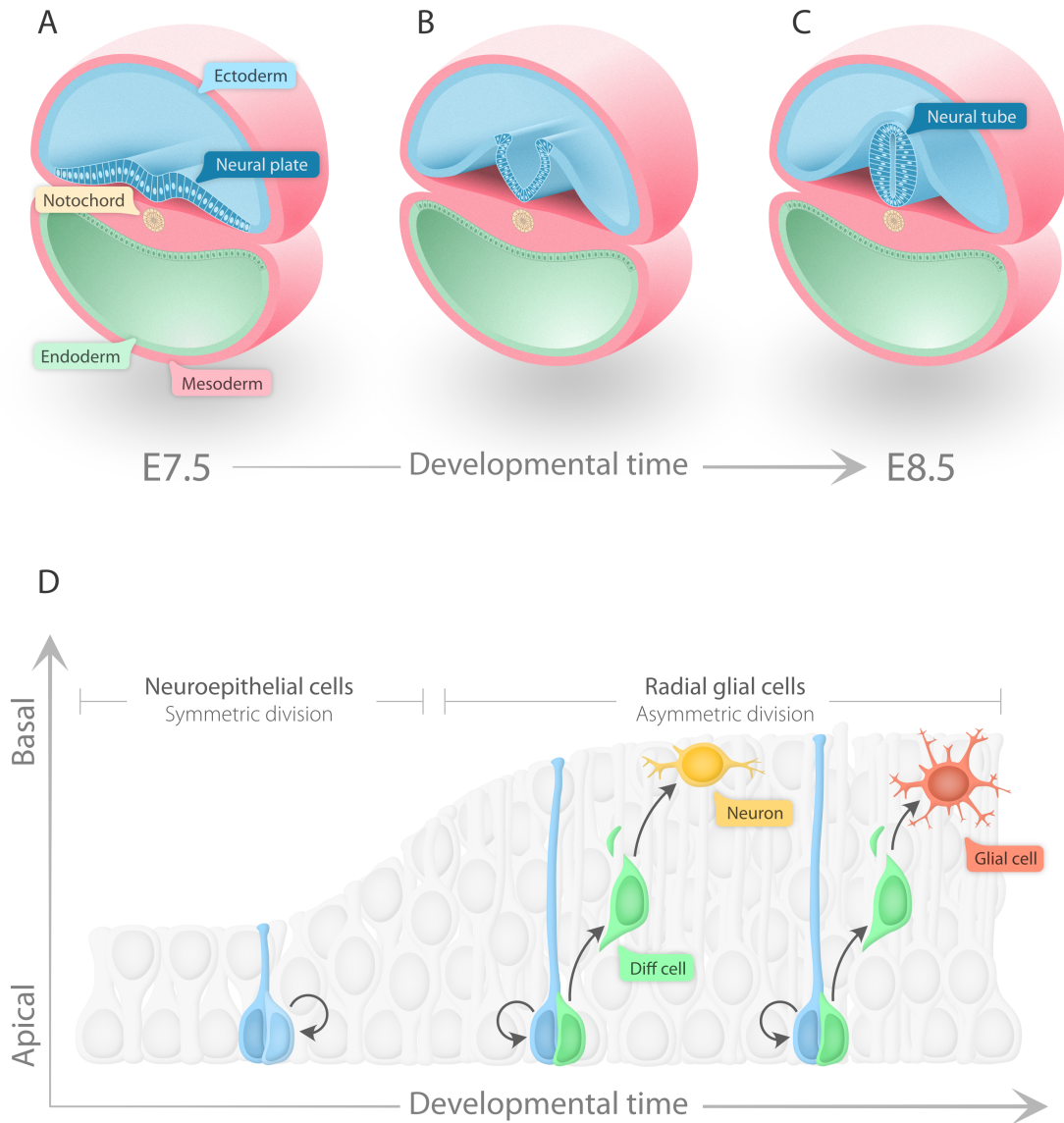


Figure 1.2: The morphology of neural tube development. **A** By embryonic day 7.5 (E7.5), the embryo has three distinct cell layers: The endoderm, mesoderm, and ectoderm. At this stage, part of the ectoderm called the neural plate begins to fold and form a groove along its surface. **B** The folding on the neural plate continues to bring the surface together. **C** By E8.5, the neural plate pinches off to form the separate neural tube structure, composed initially of neuroepithelial cells. **D** The early stages of neuroepithelial division that occur in the neural tube. Starting from the left, neuroepithelial cells undergo symmetric divisions, generating more neuroepithelial cells. Once in the radial glial stage, asymmetric divisions become more prevalent, enabling differentiation into neural and later glial cells (Ogawa et al., 2005).

system (Götz & Huttner, 2005). Neurogenesis in the spinal cord starts as early as E8.0 and reaches its highest rate at around E10.5, followed by gliogenesis where glia are formed instead of neurons (Figure 1.2D) (Götz & Huttner, 2005; Ogawa et al., 2005).

Due to the high density of cells in the neuroepithelium, nuclei cannot all sit at the

same level and instead they spread out in the AB direction and can be found anywhere along the length of an RG cell. This spreading out of nuclei gives the appearance that the neural tube has many layers of cells making up the tissue despite being a single layer, which this arrangement is called pseudostratification. Within this densely packed tissue, RG cells undergo interkinetic nuclear migration, which is where the nuclei migrate within the cell membrane, which is fixed at the apical and basal sides of the tissue (Miyata et al., 2001; Noctor et al., 2001). Around 90% of the time, this nuclear movement is stochastic and undirected (Norden et al., 2009). However, during the G2 phase of the cell cycle, nuclei undergo highly directed movement towards the apical side of the tissue and subsequently undergo mitosis at the apical surface, and then cells begin to migrate back in the basal direction (Spear & Erickson, 2012).

1.2.2 Tissue level: Morphogen gradients set up domains of distinct neural progenitors

Once the structure of the neural tube is established, different regions along the dorsoventral axis are specified for the production of different types of neurons (Zagorski et al., 2017). Domain specification is achieved through opposing diffusion gradients of Sonic Hedgehog (Shh) and Bone morphogenetic protein (Bmp). Shh is initially produced by the notochord which sits just ventral to the neural tube, and later the notochord induces the floorplate which occupies the ventral end of the neural tube to also secrete Shh as shown in Figure 1.3A (Dessaud et al., 2007; Ribes et al., 2010). At the dorsal end of the neural tube, Bmp is produced, and these opposing gradients then induce different transcription factor expression across the dorsal-ventral axis as shown in Figure 1.3B.

The general view of how these morphogen gradients are interpreted by receiving cells has changed somewhat in recent years. In earlier literature, the general hypothesis was that morphogen gradients are read in a concentration-dependent manner as first formalised by Wolpert in 1969 with the French flag model of morphogen patterning (Wolpert, 1969). More recent literature demonstrates that cells in the neural tube interpret not only the concentration but also the duration of exposure to morphogens, implying that these cells are dynamically interpreting signals (Dessaud et al., 2007). It is increasingly clear that various signalling networks (that are sufficiently complex), often are capable of encoding information and carrying out different functions based on their signalling dynamics, rather than just simply their absolute levels at any given time (Adler & Alon, 2018; Dessaud et al., 2007; Goentoro et al., 2009; Iso-

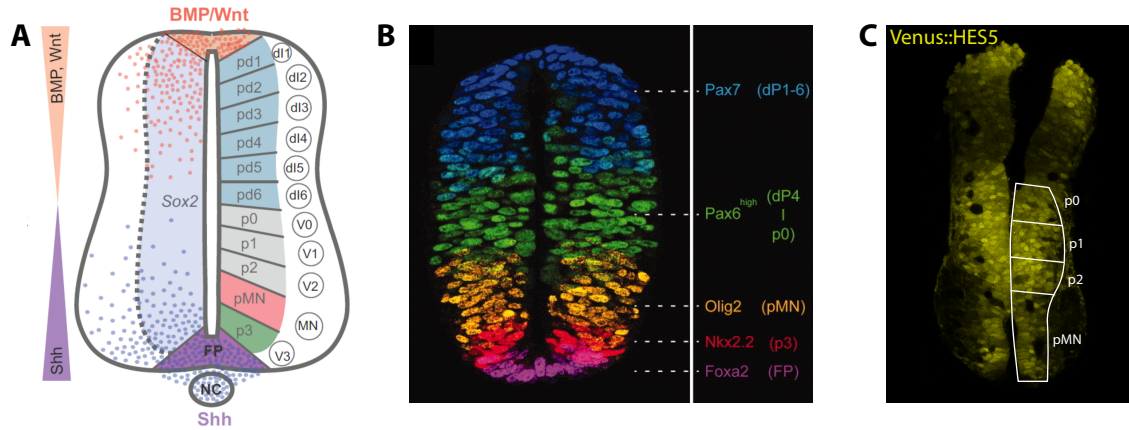


Figure 1.3: How domains of transcription factors in the neural tube correspond to distinct progenitor populations. **A** Schematic of how opposing gradients of Bmp and Shh form distinct neural progenitor domains (reused with permission from (Briscoe & Small, 2015)). **B** Example immunostaining in a neural tube slice for various transcription factors that are induced by the morphogen gradients in **A** (reused with permission from (Le Dréau & Martí, 2012)). **C** Neural tube slice showing Venus::HES5 fluorescence with an overlay showing how the HES5 expression occurs in the p0-p2 and pMN domains of the tissue.

mura & Kageyama, 2014; Nandagopal et al., 2018; Sonnen & Aulehla, 2014).

The initial size of progenitor domains is set early on by the opposing morphogen gradients in the dorsoventral direction and cells have a peak sensitivity to Shh at around E8.5-E9.0 (Balaskas et al., 2012). Due to varying rates of differentiation in each domain, the fraction of the dorsoventral space that each domain takes up changes over development but the number of morphogen-induced domains remains constant, suggesting that the morphogen gradients do not actively control differentiation once the domains are established (Kicheva et al., 2014). Indeed by E10.5, cells lose their sensitivity to Shh signalling (Balaskas et al., 2012), however cell-fate decisions continue to be made and a balance of differentiated vs progenitor cells is maintained. The process through which differentiation continues to be regulated is discussed in the next few sections in relation to transcription factors as well as cell-to-cell signalling.

1.2.3 Single-cell level: Hes genes control differentiation by maintaining a progenitor state

The Hairy and Enhancer of Split (Hes) family of genes encode basic helix-loop-helix (bHLH) transcription factors in mammals. The homologues of Hes genes were first discovered in *Drosophila* flies, where Hairy genes were first discovered as a mutant that showed increased numbers of sensory bristle hairs (Bridges & Morgan, 1923). Enhancer of split genes were found to be involved in similar processes as Hairy, such as somitogenesis, neurogenesis, and myogenesis and share similar conserved struc-

tures with Hairy such as the basic, HLH, orange, and WRPW domains (Dawson et al., 1995). Mammalian Hairy and Enhancer of Split (Hes) genes thus get their name from the fact that they repress similar downstream targets and share structural elements of both of the *Drosophila* homologues (Sasai et al., 1992).

The basic sequence of Hes genes enables the protein to bind to N-box promoter DNA sequences and directly inhibit transcription of target genes, and therefore they are known as *repressor-type* bHLH transcription factors (Ulrich, 2010) (Figure 1.4A). Hes can achieve repression through two distinct mechanisms. Firstly, through dimerisation with another repressor-type transcription factor and Groucho which binds to DNA and actively represses transcription (Figure 1.4C). And secondly, through forming nonfunctional heterodimers with *activator-type* bHLH transcription factors, which passively prevents the activator transcription factor from binding E-box DNA sequences (Figure 1.4D) (Sasai et al., 1992). Three main repressor-type bHLH proteins include Hes1, Hes3, and Hes5. In the developing neural tube, HES1 and HES5 are highly expressed, with HES5 being localised to the progenitor domains p0-p2, pMN, and also at the dorsal end of the tissue (Figure 1.3C).

The general function of HES protein in the neural tube is to maintain radial glial cells in a progenitor state and prevent excessive differentiation, as evidenced by loss of function experiments for Hes1 and Hes5, where a decrease in neural progenitors is observed due to accelerated differentiation (Hatakeyama et al., 2004; Ohtsuka et al., 2001). HES maintains rates of differentiation by inhibiting expression of proneural genes which are activator-type bHLH transcription factors and function by forming heterodimers with the bHLH factor E47 (Figure 1.4B). Proneural genes shown to be targets of Hes5 include Ngn2, Mash1, and Math1 (Holmberg et al., 2008; Imayoshi et al., 2008; Lanford et al., 2000; Mussmann et al., 2014).

Experimental work indicating the similar roles of Hes5 and Hes3 to Hes1 concerns looking at how different regions of Hes expression arise in the neural tube. Hes1 and Hes5 domains are fairly distinct from one another with not much overlap which is the result of Hes genes being able to suppress one another (Hatakeyama et al., 2004; Riesenberg et al., 2018). Furthermore, Hes genes appear to be able to compensate to varying degrees for the function of other Hes genes when one is knocked out. One study found that single knockouts, either Hes1-null or Hes5-null, had weak or no defects present morphologically (Hatakeyama et al., 2004). Areas that originally expressed high Hes1 in wild-type were found in Hes1-null mice to show increased expression of Hes5 in that area (and vice versa), strongly suggesting that the reason for no morphological defects in single knockouts was due to the complementary Hes overtaking the function. In double knockouts of Hes1 and Hes5, embryos did not sur-

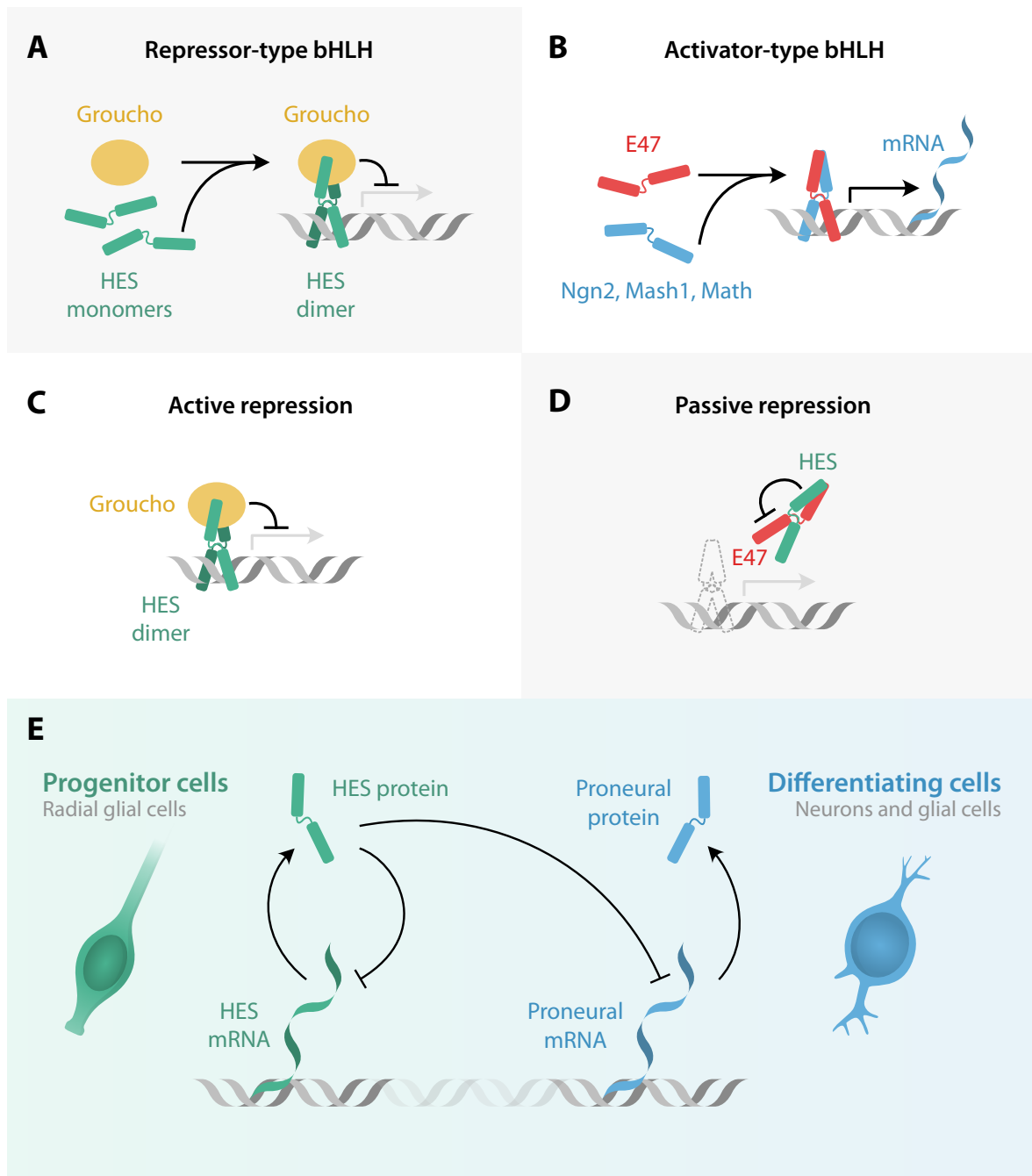


Figure 1.4: The interactions of HES proteins in the regulation of gene transcription and differentiation. **A** Repressor-type bHLH transcription factors dimerise and bind with Groucho to block transcription. **B** Activator-type bHLH transcription factors dimerise and promote gene expression. **C** HES proteins can act through active repression where it dimerises with itself, or can act through **D** passive repression where it binds with proneural bHLH transcription factors and prevents them from binding DNA and promoting gene expression. **E** HES represses downstream proneural gene expression as well as its own expression. High HES expression keeps cells in a progenitor state while low HES and high proneural gene expression leads to differentiation into neurons and glial cells in the developing neural tube.

vive past E10.5, furthering the evidence of compensatory effects between Hes genes.

Hes genes are also capable of inhibiting their own expression through a direct nega-

tive feedback loop (Hirata et al., 2002) (Figure 1.4E). Combined with a time delay, negative feedback loops give rise to the possibility of oscillations, which have been observed in both Hes1 and Hes5 expressing cells in the developing neural tube (Manning et al., 2019; Shimojo et al., 2008, 2011). Whereas HES1 seems to be quite a robust oscillator (Marinopoulou et al., 2021; Ochi et al., 2020), HES5 displays a variety of possible expression dynamics at the single-cell level including oscillatory, aperiodic, decreasing and various combinations of the preceding (Manning et al., 2019). Individual HES5-expressing cells are capable of switching between these different dynamics, though what causes switching to be induced is not known.

Recent work on HES5 expression in the neural tube found that cells in a particular region of the neural tube that generates interneurons had a higher percentage of oscillatory HES5 signals when compared to the motorneuron generating region of the neural tube (Manning et al., 2019). This suggests that different types of HES5 signals may be distinguishable by the downstream gene networks and in turn, may be able to influence cell fate.

1.2.4 Communication between cells: Notch-Hes5 interactions

It is well-established that Hes genes are modulated by Notch signalling (Manning et al., 2019; Ohtsuka et al., 1999; Ohtsuka et al., 2001; Sagner et al., 2018; Shimojo et al., 2011). Notch signalling occurs at the membranes of two contacting cells, where both the ligand (Delta or Jagged) and receptor (Notch) are transmembrane proteins and the integration of Hes5 into this pathway means that levels of HES5 in one cell can influence the levels in a neighbouring cell.

Following the illustration in Figure 1.5 from the top left, the following describes the known interactions between Notch signalling and Hes5. Upon reception of a Delta ligand on a neighbouring cell, Notch undergoes proteolytic cleavage by a disintegrin and metalloproteinase (ADAM) and γ -secretase, resulting in the release of a cytoplasmic peptide called Notch intracellular domain (NICD). NICD translocates to the nucleus where it binds with RBPJ and MAML to enable transcription of many genes including the Hes5 gene (Miele, 2011). HES5 protein can then inhibit proneural transcription factor transcription as well as its own production. Proneural transcription factors enable transcription of the Notch ligand Delta. Therefore if a cell has an increase in NICD, a subsequent decrease in Delta expression is expected due to the inhibitory effect of HES5 on proneural transcription factor production.

Notch signalling can lead to two possible outcomes: the first, as just described, is *lateral inhibition* whereby one cell expressing high amounts of Notch/HES5 will re-

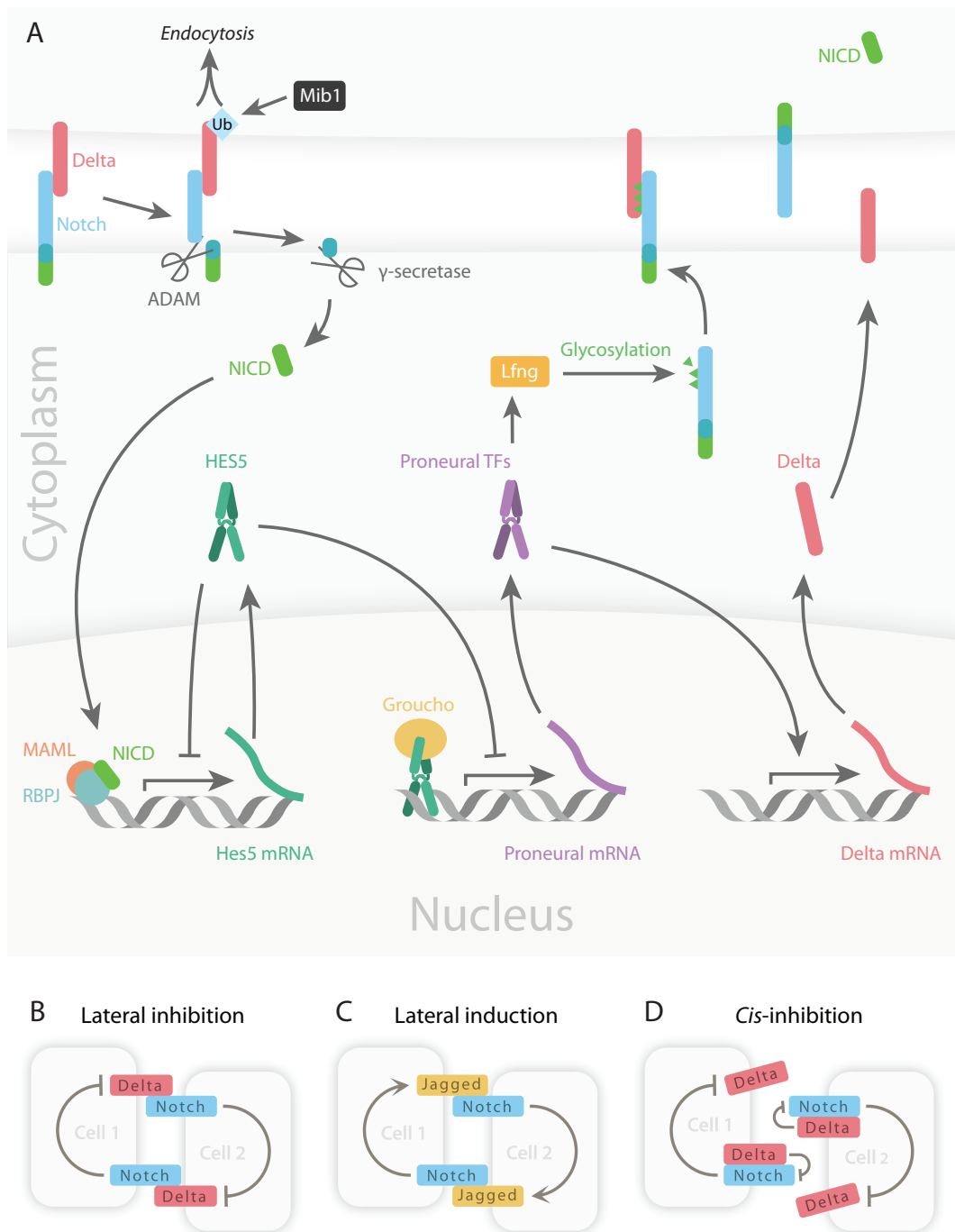


Figure 1.5: An overview of the Notch-Delta interactions with Hes5. **A** In order for Delta to activate a Notch receptor in neighbouring cells, Delta must first be ubiquitinated (Ub) by Mindbomb1 (Mib1). This ubiquitination leads to Delta being endocytosed which pulls on the bound Notch receptor, exposing an extracellular cleavage site. Upon cleavage by the α -secretase ADAM, γ -secretase then cleaves the Notch intracellular domain (NICD), which translocates to the nucleus to bind with MAML and RBPJ and promotes various genes including Hes5. HES5 protein inhibits proneural gene expression which themselves promote Delta and Lunatic fringe (Lfng) ((Nikolaou et al., 2009)). Glycosylation of the Notch receptor by Lfng increases the binding affinity of Notch to Delta. **B** Simplified circuit of lateral inhibition via Notch-Delta. **C** Simplified lateral induction circuit via Notch-Jagged. **D** Simplified circuit of *cis*-inhibition.

press Notch/HES5 expression in the neighbouring cell. The second outcome is *lateral induction* where Notch activation leads to mutual increases in expression between neighbouring cells. Whether lateral inhibition or induction takes place depends on the ligand that the population of Notch signalling cells is expressing. Cells that express the ligand Delta1 (Dll1) or Dll4 lead to lateral inhibition, as increases of NICD result in decreased Delta production within the same cell (Fig 1.5B), whereas cells that express the ligand Jagged1 (Jag1) or Jag2 lead to lateral induction, as increases of NICD result in increased Jagged production within the same cell (Fig 1.5C).

For the case of Notch-Delta interactions, not only do *trans*-activation events occur where Delta on one cell induces activation of Notch on the neighbouring cell, but Delta can also interact with Notch on the surface of the same cell. Rather than being activating, this interaction prevents Notch on the surface of the same cell from being *trans*-activated by a neighbouring cell and is termed *cis*-inhibition (Figure 1.5D). This additional *cis*-inhibition interaction forms a bistable switch between Notch and Delta within the same cell (Figure 1.5D), which results in a sharper (more switch-like) transition between the high and low gene expression, and may be crucial in the pattern-forming ability of this pathway (Sprinzak et al., 2010). The degree to which *cis*-inhibition occurs depends on ligand concentration as well as variants of ligand and receptor. For example, Notch1 interactions with high levels of Dll1 and Dll4 leads to *cis*-inhibition, whereas if the receptor is Notch2, there is less of a *cis*-inhibition effect (Andersson et al., 2011; Nandagopal et al., 2019; Preuße et al., 2015). Dll3 is an example of a dedicated *cis*-inhibitor, incapable of *trans*-activation (Ladi et al., 2005).

The signalling efficiency of Notch can also be modulated by various other proteins. Fringe for example increases the binding affinity of Notch to Delta by glycosylating the external domain of the Notch receptor (Hicks et al., 2000; Kato et al., 2010). Expression of Mindbomb1 (Mib1) also acts to increase Delta *trans*-activation by ubiquitination of the intracellular domain of Delta which marks it for endocytosis. This endocytosis then provides a pulling force on any bound Notch receptor, exposing the ADAM cleavage site and enabling the subsequent activation of Notch in that cell (Baek et al., 2018; Koo et al., 2005; Meloty-Kapella et al., 2012; Yoon et al., 2008). Dll3 lacks this internal ubiquitination site, explaining why it is incapable of *trans*-activation. Although the core Notch-Delta circuitry is relatively simple, the degree to which the pathway can be modulated results in a highly adaptable and tunable signalling network which accounts for why it is found across such a diverse range of developmental processes (Andersson et al., 2011).

1.2.5 The emergent pattern: A dynamic multicellular spatial pattern of HES5

A system with many identical autonomous components can exhibit emergent properties and dynamics when they are able to interact with one another. For example, as described in a model of bird flight – the BOIDS algorithm – simulated agents representing individual birds adjust their flight by aligning with neighbouring birds, matching their velocities, and maintaining a certain distance between themselves (Reynolds, 1987). This simple set of rules reproduces the murmurations observed in real flocks of birds, where swooping, diving, and sudden coordinated changes of direction can be seen in large flocks of birds in the evening sky. Examples of other systems with emergent behaviour include the synchronisation of fireflies flashing, the defensive shimmering of bees protecting their nest, Mexican waves in crowds at sports matches, the organised behaviour of ants, and the complex spatiotemporal arrangement of cells during development.

In a group of cells that interact via Notch lateral inhibition, the alternating high-low gene expression is an emergent behaviour. In the neural tube, Notch is crucial in controlling the rate of differentiation during neurogenesis, with Notch inhibition accelerating differentiation (Imayoshi et al., 2010; Marklund et al., 2010). However, the emergent pattern that arises from Notch interaction had not been characterised in the developing neural tube until recently.

The paper by Manning et al. looked in detail at how different HES5 dynamics at the single-cell level correlated with fate decisions. This was carried out in the mouse spinal cord, focusing on the p0-p2 domains which consist of interneuron progenitors, and the pMN domain which consists of motorneuron progenitors (Manning et al., 2019) (Figure 1.6A). They found that progenitor cells express a mix of noisy and oscillatory dynamics, with the average temporal period of oscillation being 3.3h, which are referred to as ultradian oscillations (Figure 1.6B). Two interesting correlations were found regarding fate; differentiating cells are more likely to be oscillatory and oscillatory cells were more likely to correspond with an interneuron fate rather than a motorneuron fate.

The paper by Biga et al. looked at the same domains of HES5 expression but at the multicellular level (Biga et al., 2021). Within these domains, HES5 expression is clustered into groups of higher and lower expressing cells, with an average of 3-7 cells making up each high or low cluster (Figure 1.6A). The clustered expression was also found to be spatially periodic, repeating on average every 3-4 cells when measured along the dorsoventral axis (Figure 1.6C). In a Notch-Delta system, a spatial pattern is not surprising, however, the period of this pattern is slightly unusual as it is

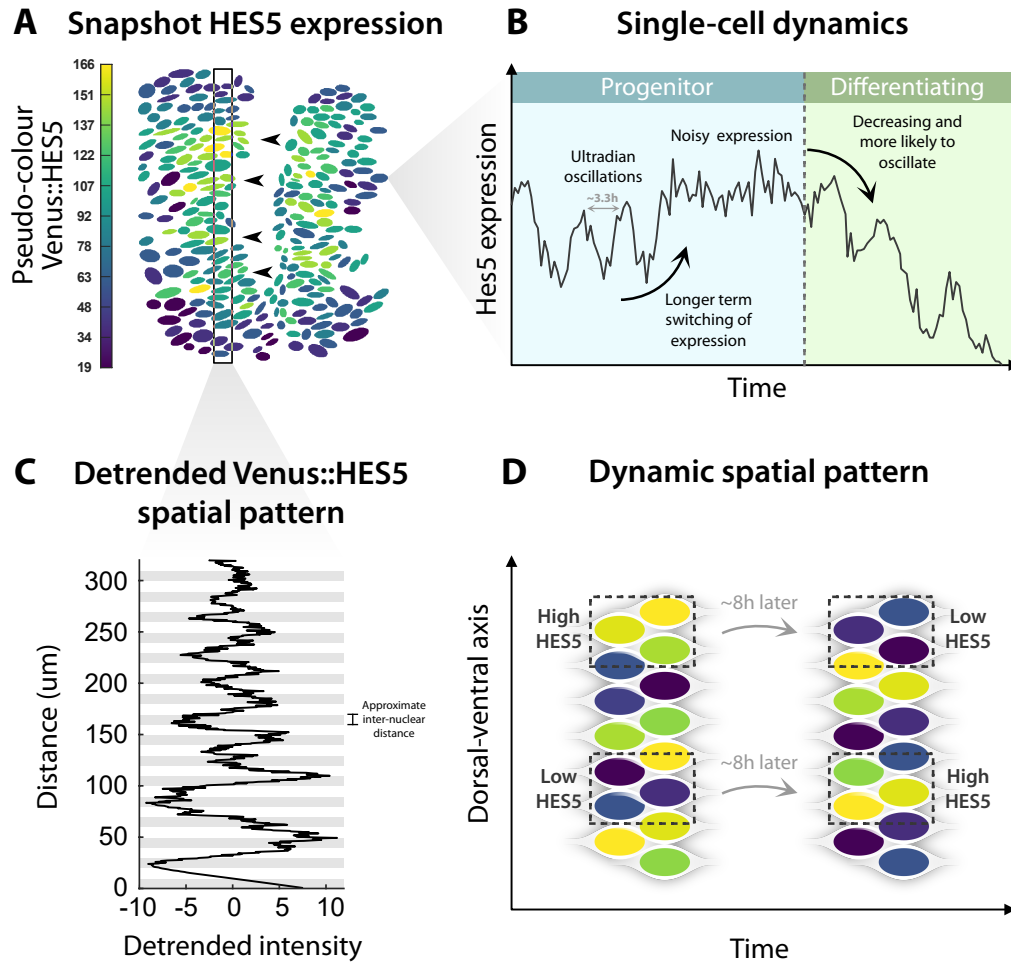


Figure 1.6: The emergent HES5 pattern. **A** Example snapshot of Venus::HES5 expression in the neural tube taken from (Biga et al., 2021) where the vertical axis is the dorsal-ventral (DV) axis. Nuclear HES5 has been masked and false colour representing the fluorescence intensity is shown, and the black arrows indicate clusters of cells expressing similar higher levels of HES5. **B** Summary of the findings in the paper (Manning et al., 2019). Progenitor cells exhibit both noisy (aperiodic) and oscillatory temporal dynamics at the single-cell level (blue box), with the average ultradian oscillation period being 3.3h. Larger amplitude switching behaviour that acts over a longer time scale than ultradian oscillations is also shown as a change in the mean expression in the blue progenitor box in **B**, which is an observation described in (Biga et al., 2021). **C** A detrended spatial signal is constructed by plotting the average expression within the box in **A**, which shows how the signal is periodic over space. Grey and white horizontal bars indicate the approximate internuclear distance in the AB direction to give an indication of how many cells are within each peak and trough of the spatial signal. **D** Summary of the dynamic spatial pattern, exaggerated and simplified for illustration purposes. The example here shows a section of the neural tube with a perfect 4-cell periodicity (whereas there is variation in the actual cluster sizes). Two time points are plotted, and the second shows how the pattern would be expected to change on average 8h later.

longer than the 2-cell periodicity expected from a nearest neighbour signalling model (Collier et al., 1996). The pattern becomes even more interesting when considered over time, where it is found that the location of the high and low expressing clusters changes on average every 8h, while still maintaining the same spatial pattern (Figure 1.6D) (Biga et al., 2021). This longer-term 8h switching also has an amplitude of ap-

proximately twice that of the 3.3h ultradian oscillations (Manning et al., 2019), and so ultradian oscillations and noisy expression are found to be nested with this longer period, larger amplitude switching of HES5 levels within these clusters.

1.3 Existing mathematical models and biological systems with dynamic or spatially periodic patterns

To understand how the dynamic spatial pattern described in §1.2.5 fits into the existing Notch/Hes patterning literature, this section highlights biological systems and mathematical models where similar types of stationary or dynamic patterning have been observed.

1.3.1 A definition of coupling strength

As the idea of coupling strength is used throughout this thesis, this section is included to clarify what exactly is being referred to when talking about coupling strength. In the context of Notch signalling, coupling strength refers to the relationship between the concentration of a protein in a sending cell (referred to here as *input*) and the resulting concentration of another protein in the signal-receiving cell (referred to here as *output*) and the ratio of output to input determines coupling strength. For example, if the concentration of Delta is chosen as the input and NICD as the output (Figure 1.7A), then the amount of NICD produced per Delta molecule would be a measure of coupling strength. Whether a coupling strength is weak or strong is somewhat arbitrary, and can only really be defined relative to another coupling strength. For example, 100 Delta molecules resulting in 1 NICD molecule being produced in a given time frame could be considered a weak coupling strength when compared to a scenario where 100 Delta molecules result in 90 NICD molecules in the neighbouring cell.

Looking at Figure 1.7 it can be seen that Delta and NICD as the input and output is not the only choice that can be made; the input/output can be any two proteins in the signalling network. Figure 1.7B shows the input as being HES5 in the sending cell and the output as HES5 in the receiving cell, which contains more intermediate interactions than in Figure 1.7A. This will obviously result in a different coupling strength because the proteins of interest have changed and highlights that coupling strength is dependent upon the intermediate interactions that are taking place between the chosen input and output. Furthermore, the repressive interaction of HES5

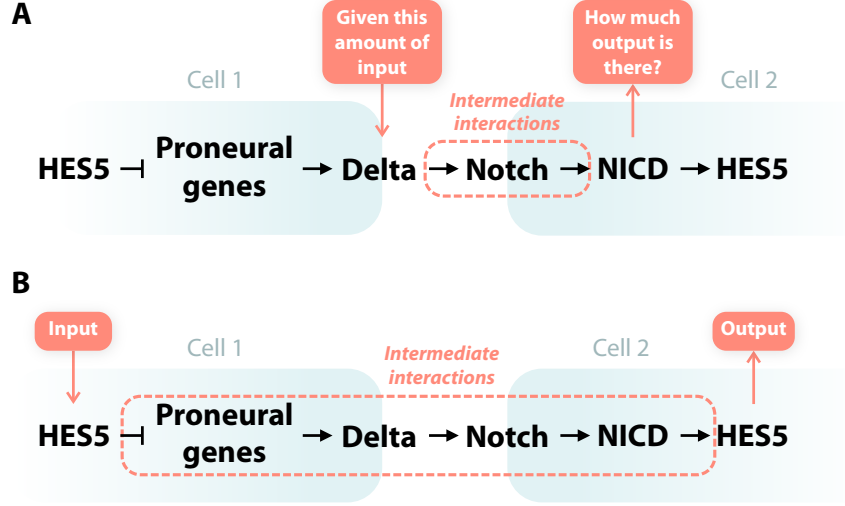


Figure 1.7: Ways of defining coupling in the Notch-Delta pathway. **A** Shows a shorter series of interactions that could be modelled as a coupling function between the two cells where Delta in Cell 1 is the input and NICD in Cell 2 is the output. **B** Shows an equally valid way of defining a coupling function which has more intermediate steps involved but flips the relationship between input and output from positive to inhibitory.

on downstream proneural targets inverts the coupling from being a positive interaction like in Figure 1.7A to an inhibitory coupling with high HES5 input resulting in a low HES5 production in the neighbouring cell.

1.3.2 Stationary ‘salt and pepper’ patterns

The first mathematical study of Notch-Delta patterning was produced by Collier et al. which focussed on explicitly modelling only Notch and Delta concentrations, leaving out intermediate species such as downstream transcription factors or cleaving of the Notch receptor upon activation (Collier et al., 1996). Rewriting the Collier et al. model in a similar notation to that used throughout the rest of this thesis, the model can be written as

$$\frac{dN_i}{dt} = \alpha_N F(\bar{D}_i) - \mu_N N_i, \quad (1.1)$$

$$\frac{dD_i}{dt} = \alpha_D G(N_i) - \mu_D D_i, \quad (1.2)$$

where N_i and D_i are the Notch and Delta concentrations respectively in cell i in either a 1D or 2D (hexagonal lattice) grid. α_N and α_D are the maximal production rates of Notch and Delta protein respectively and μ_N and μ_D are the degradation

rates. \bar{D}_i is the average Delta expression averaged over the neighbouring cells given by

$$\bar{D}_i = \frac{1}{|\mathcal{N}(i)|} \sum_{i \in \mathcal{N}(i)} D_i, \quad (1.3)$$

where $\mathcal{N}(i)$ is the set of neighbours a cell is in signalling contact with and $|\mathcal{N}(i)|$ is the total number of neighbours in the set. In the Collier et al. model, only adjacent neighbours signal to each other.

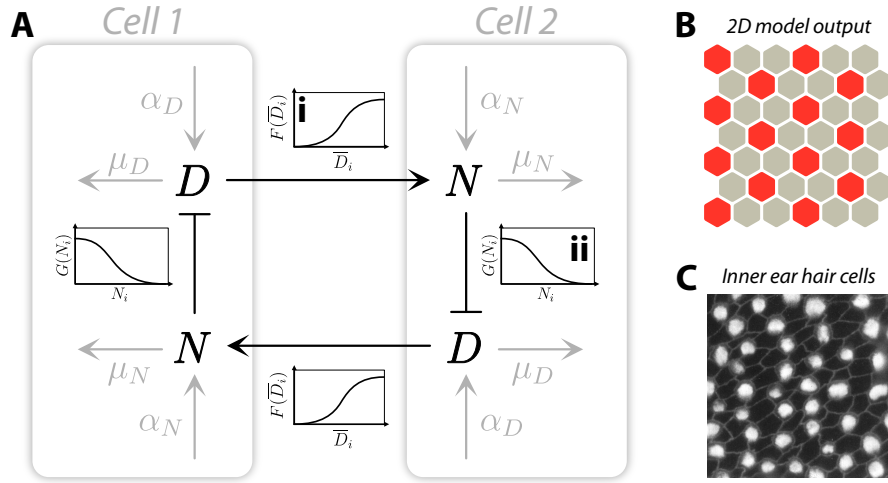


Figure 1.8: Summary of the Collier et al. mathematical model along with *in-silico* and *in-vivo* examples of 2D salt and pepper patterning. A 2-cell model is shown, but 1D lines of cells and 2D hexagonal lattices were also explored in the study. **A** Schematic of the 2-cell model in (Collier et al., 1996) where symbols are defined in §1.3.2. **Ai** Shows the increasing Hill function used to model Delta activating Notch in a neighbouring cell. **Aii** Shows the decreasing Hill function used to model Notch inhibiting Delta production within the same cell. **B** A typical output of a 2D hexagonal grid simulation of nearest neighbour interactions using Collier et al. model. Red cells indicate high Delta cells. **C** Shows inner basilar papilla Notch-Delta patterning where nearest neighbour cells signal to each other (taken from (Goodyear & Richardson, 1997)).

The functions F and G represent a commonly used function throughout this thesis which is the Hill function and these are sigmoidal curves that run between 0 and 1 and can either be increasing or decreasing. Because Notch is activated by Delta, $F(\bar{D}_i)$ is an increasing function defined by

$$F(\bar{D}_i) = \frac{1}{1 + \left(\frac{D_0}{\bar{D}_i}\right)^k} \quad (1.4)$$

where D_0 is the repression threshold which is the concentration of Delta at which the

value of $F(\bar{D}_i) = 0.5$, and in the context of equation (1.1), is the concentration of Delta in neighbouring cells which will result in Notch being produced at half its maximal rate. The other parameter that defines the shape of the Hill function is the Hill coefficient, k , which defines how steep the slope of the Hill function is around the repression threshold (Figure 1.8Ai shows the general shape of the increasing Hill function). Delta on the other hand is repressed by active Notch and so a decreasing Hill function is used

$$G(N_i) = \frac{1}{1 + \left(\frac{N_i}{N_0}\right)^n}, \quad (1.5)$$

where N_0 is the repression threshold for Notch acting on Delta and n is the Hill coefficient (Figure 1.8Aii shows the shape of the decreasing Hill function).

Originally the Hill function was used to model the oxygen binding curve of haemoglobin (Hill, 1910). Haemoglobin has 4 binding sites for oxygen, and each time an oxygen molecule binds, it increases the affinity of haemoglobin for oxygen, which is known as cooperative binding and results in a nonlinear binding curve (saturation of haemoglobin versus concentration of oxygen). The Hill coefficient is interpreted as a measure of how strong this cooperativity is, where $n = 1$ indicates no cooperativity (equivalent to Michaelis-Menten kinetics) and $n > 1$ indicates increasing cooperativity of the reaction and the Hill function becomes more like a step-function as $n \rightarrow \infty$.

In cases where cooperativity is very strong, i.e. the binding affinity changes greatly between each bound molecule, then the Hill coefficient reflects the number of binding sites (Weiss, 1997). Haemoglobin however does not have strong enough cooperativity to have a Hill coefficient of 4 (the number of binding sites), instead, it is estimated to be between 1.7-3.2. In most cases, the Hill coefficient should be taken as an interaction coefficient rather than the number of binding sites, and the number of binding sites or possible affinity changes should be treated as an upper limit in the case of extreme cooperativity.

In cases where cooperative binding is not present, the Hill function can still be used as a transfer function to approximate how signalling pathways behave. In these cases, the Hill coefficient is interpreted depending on the application but is generally a measure of how non-linear an interaction is. The model described in this section by Collier et al. used a Hill coefficient of 2 in their numerical simulations to represent Notch-Delta interactions and the non-linearity introduced by $n > 1$ can be attributed to interactions such as the bistable switch-type interaction produced by *cis*-inhibition (as

discussed in §1.2.4), or the fact that downstream transcription factors such as Hes need to dimerise before functionally binding to DNA.

In this type of model, the Hill functions act as coupling functions, and so it is the Hill function parameters that define coupling strength. The coupling strength will be largely determined by the repression threshold because this determines how much Delta or Notch will be required to activate or inhibit. How sharp or switch-like this response will be is determined by the Hill coefficient, and so this also influences the coupling strength to some extent. In the Collier et al. model, two possible input and output scenarios are valid: either the coupling can be defined as the relationship between Delta in cell 1 and Notch in cell 2 (Figure 1.8A) which is determined by $F(\overline{D}_i)$, or alternatively the coupling can be defined as the relationship between Delta in cell 1 and Delta in cell 2, which would be determined by the combination of both Hill functions $F(\overline{D}_i)$ and $G(N_i)$.

Through a combination of numerical and analytical methods, Collier et al. found that with sufficient coupling strength, steady-state patterns of fine-grained alternating high-low expression emerged, typically with a spatial period of 2-cells which is the classic ‘salt and pepper’ or ‘checkerboard’ patterning. In the 2D hexagonal grid, this type of patterning appears as single high Delta cells surrounded by a ring of high Notch expressing cells as shown in Figure 1.8B, and this matches closest with the Notch pattern observed in the inner ear basilar papilla patterning shown in Figure 1.8C (Goodyear & Richardson, 1997). In kymograph form, the stationary patterns formed by this model produce the horizontal stripes of high and low expression that remain in the same location over time, as shown in Figure 1.9E.

1.3.3 Hes5 oscillations and synchronisation

In 1965, Goodwin detailed the first mathematical formulation describing the possibility of oscillating biological circuits where a negative feedback model of protein inhibiting its own mRNA production was explored using an analogue computer model (Goodwin, 1965). This work found that oscillatory gene expression could be driven autonomously by the presence of an intermediate process between the initiation of mRNA synthesis and mature protein and that the delay induced by this process was the essential component that made sustained oscillations possible. The intuitive explanation for why this is the case is that if there is no delay, any increase in mRNA would lead to an instantaneous increase in protein, which through negative feedback would immediately inhibit any further mRNA being produced. The introduction of a time lag enables a pool of protein to be synthesised followed by a delayed inhibition

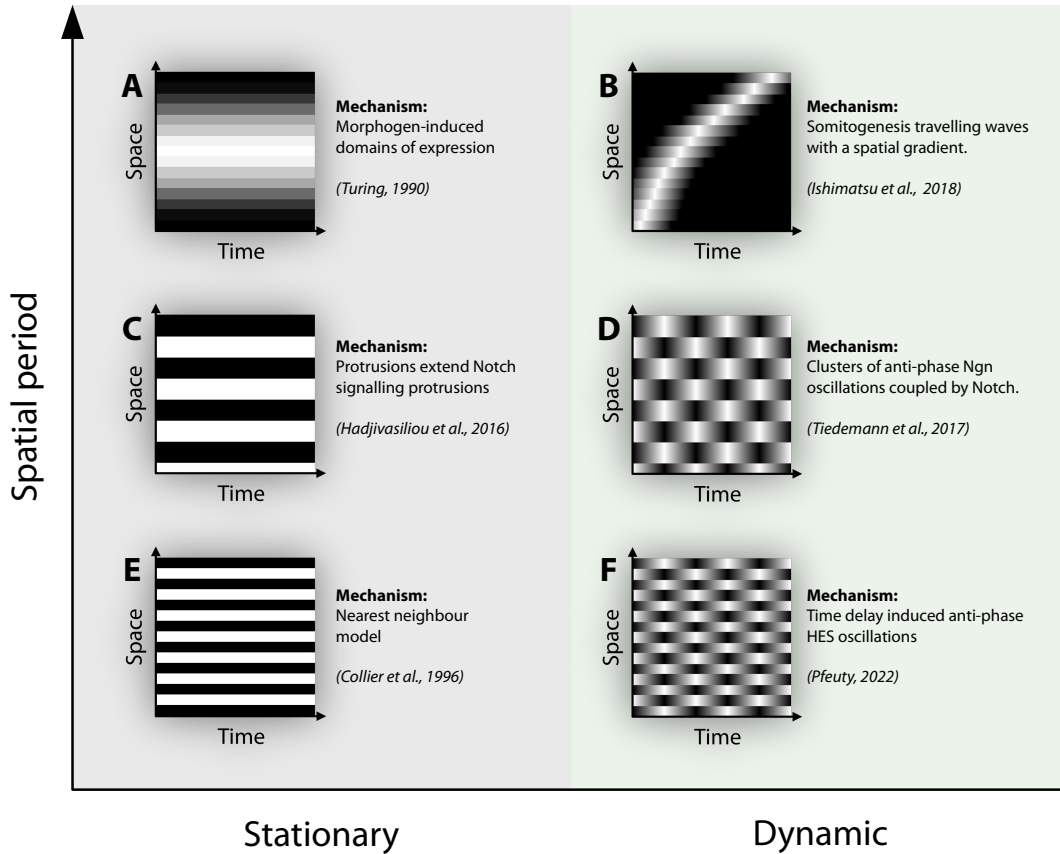


Figure 1.9: Mathematical models that produce stationary and dynamic spatial patterns with their typical output summarised in kymograph form. They are ordered by increasing spatial period on the y -axis and stationary/dynamic patterning on the x -axis. Brief descriptions of the mechanism are given in each panel, and references are given here: **A** (Turing, 1990). **B** (Ishimatsu et al., 2018). **C** (Hadjivasiliou et al., 2016). **D** (Tiedemann et al., 2017). **E** (Collier et al., 1996). **F** (Pfeuty, 2022).

of mRNA production; the protein subsequently degrades, and the process repeats.

The first mathematical model specific to Hes oscillations was formulated by Monk, and again centred around time-delayed negative transcriptional feedback as the basis for oscillation based on experimental observations (Monk, 2003). Instead of modelling an intermediate process between the initiation of mRNA synthesis and mature protein, Monk instead implemented an explicit time-delay term. This time delay was then set to between 10-20 minutes to reflect the average maturation time due to transcript elongation, splicing, processing, and export is around.

The model explicitly includes mRNA and protein as

$$\frac{dm(t)}{dt} = \alpha_m G(p(t - \tau)) - \mu_m m(t), \quad (1.6)$$

$$\frac{dp(t)}{dt} = \alpha_p m(t) - \mu_p p(t), \quad (1.7)$$

where $m(t)$ and $p(t)$ are mRNA and protein levels respectively over time. α_m is the maximal transcription rate and α_p is the translation rate. μ_m and μ_p are the degradation rates of mRNA and protein respectively and τ is the time delay. $G(p(t - \tau))$ is a decreasing Hill function, representative of the repressive action of Hes protein on its own mRNA production. The Hill function here has the form

$$G(p(t - \tau)) = \frac{1}{1 + \left(\frac{p(t - \tau)}{p_0}\right)^n}, \quad (1.8)$$

where p_0 is the repression threshold – the abundance of Hes in the cell that will result in 50% repression of mRNA production, and $p(t - \tau)$ is the protein abundance at τ units of time in the past. n is the Hill coefficient which is estimated by Monk to be $2 \leq n \leq 10$ due to the fact that contributions to cooperativity could be coming from multiple sources such as Hes being a dimer, the fact that the Hes1 promoter has three binding sites, or that Hes is actively imported into the nucleus.

Using reasonable parameter values either measured directly or inferred from the literature, ultradian periods of around 2 hours are produced from these equations which match the observed Hes1 period. A more recent model by Manning et al. re-parameterised the same model as in (1.6) and (1.7) using a Bayesian inference approach and live imaging data to estimate parameter values specific to Hes5 in the neural tube, which has a longer period of around 3.3h (Manning et al., 2019).

The fact that oscillations are driven by the nature of the internal feedback and not by an external oscillator or oscillating energy source means that Hes oscillators can be classed as autonomous oscillators (self-sustaining oscillators). A macro-scale example of an autonomous oscillator is a pendulum in a clock which has a natural frequency determined by the length of the pendulum and the strength of gravity, and which is sustained by potential energy stored in a weight or spring.

An interesting emergent property of autonomous oscillators is that when they are allowed to interact, they can undergo synchronisation. Synchronisation occurs when two or more autonomous oscillators with initially different frequencies evolve to a common frequency and become phase-locked, whereby the difference in phase no longer changes over time. For example, synchronisation can occur when two analogue metronomes are placed on a loose platform with each metronome set to a slightly different natu-

ral frequency. Via momentum transfer through the loose platform, the phase of each metronome can influence the other. With sufficient coupling (coupling here is a measure of how much each metronome can move the platform) the two metronomes will influence the swinging of each other's pendulum and eventually settle to a new frequency somewhere between their two original natural frequencies, becoming synchronised.

Synchronisation can also take place between cells expressing oscillatory Hes as observed during the developmental process of somitogenesis, where blocks of tissue called somites are produced in the pre-somitic mesoderm that eventually form vertebrae, ribs and skeletal muscle (Baron & Galla, 2019; Kageyama et al., 2012; Lewis, 2003; Özbudak & Lewis, 2008; Shimojo et al., 2016). During somitogenesis, a population of cells exist at the tail end of the pre-somitic mesoderm that exhibits a synchronised oscillatory expression of various genes, including Hes, and this wave of synchronisation travels towards the anterior end where a new somite is formed on each cycle of the oscillation (Maroto et al., 2012).

It was known for some time that Notch is involved in somitogenesis (Conlon et al., 1995; Holley et al., 2000), but the exact mechanism of control Notch had over the formation of somite boundaries was unclear. A combination of experimental work and modelling by Özbudak and Lewis neatly narrowed down the role of Notch signalling by observing how long the effects of inhibiting or overactivating the pathway took to appear as somite deformations (Özbudak & Lewis, 2008). They determined that the role of Notch was in maintaining synchronisation of the autonomously oscillating genes such as Hes, by coupling the oscillatory dynamics of the cells. However, given that Notch signalling typically forces gene expression into alternating high and low expression between cells, how do Notch-coupled cells achieve in-phase oscillations during somitogenesis?

The key to in-phase dynamics in a laterally-inhibiting system of cells lies in the relationship between the period of the oscillations (T) and the time delay between cells (τ). If there is no time delay between two laterally inhibiting cells ($\tau = 0$), anti-phase oscillations arise due to the fact that when one cell is high, it will repress the other cell (Figure 1.10C). If the time delay is half a period ($\tau = \frac{T}{2}$), then the maximally repressive signal from the blue cell shown in Figure 1.10D arrives $T/2$ time units later at the red cell, which leads to the red and blue cells being in-phase. This behaviour alternates between anti-phase and in-phase as the time delay continues to increase, depending on if it is an integer value or half value of the oscillation period T .

Therefore in somitogenesis, there must be a sufficient time delay within restricted

ranges in the Notch circuit in order to produce the synchronisation observed. Important to note that while the $T/2$ time delay relationship with phase flipping between in-phase and anti-phase dynamics described here is true for some systems such as (Baron & Galla, 2019; Momiji & Monk, 2009), this relationship between time-delay and phase is more complex in other systems (Prasad et al., 2008).

While somitogenesis is an example of in-phase Notch/Hes oscillations, neurogenesis may represent a scenario where anti-phase oscillations occur. One study of telencephalic neural progenitor cells in mouse found that HES1 is expressed in a salt and pepper type expression in snapshot images, but also that HES1 in individual cells is oscillatory, leading to the indirect conclusion that HES1 expressing progenitors are probably oscillating in antiphase, like in Figure 1.10E (Shimojo et al., 2008). More recently, direct observation of anti-phase oscillations of Dll1 was observed in the developing neural tube where two neighbouring cells alternated expression multiple times before one cell remained high and the other low (Shimojo et al., 2016). The mathematical modelling in this paper looked at the effects of changing these time delays in a Notch-Hes model. This resulted in the discussed transition between in-phase and anti-phase and additionally found that oscillations become damped during the transitions which is also observed experimentally (Shimojo et al., 2016).

Extending anti-phase oscillations to a line of cells, the coupled phase-oscillator model by Pfeuty demonstrates the possibility of a dynamic spatial pattern where a spatial period of 2 forms from the anti-phase oscillations as shown in Figure 1.9F (Pfeuty, 2022). This captures two aspects of the HES5 pattern in that a spatial pattern is formed, and that it is dynamic over time. Coming closer to the dynamic HES5 pattern in the neural tube, Tiedemann et al. modelled Hes1 dynamics in pancreatic development and neurogenesis (Tiedemann et al., 2017). When exploring Hes1 autoinhibition oscillations, they were able to produce clusters of cells that have in-phase dynamics, but where the clusters are in anti-phase with neighbouring clusters. Thus this is a spatial pattern with > 2 -cell periodicity, as well as being dynamic over time. This would result in a kymograph similar to Figure 1.9D.

Out of all models in the literature, the Tiedemann et al. model comes closest to the phenotype that is the focus of this thesis. However, that work did not characterise the pattern in detail and is specific to Hes1 oscillations, and also lacks Hes oscillations being nested within a longer-term, larger-amplitude switching behaviour. In Chapter 2, this idea of clusters of local synchronisation is explored thoroughly in a Hes5-specific model to see what aspects of the data it can reproduce.

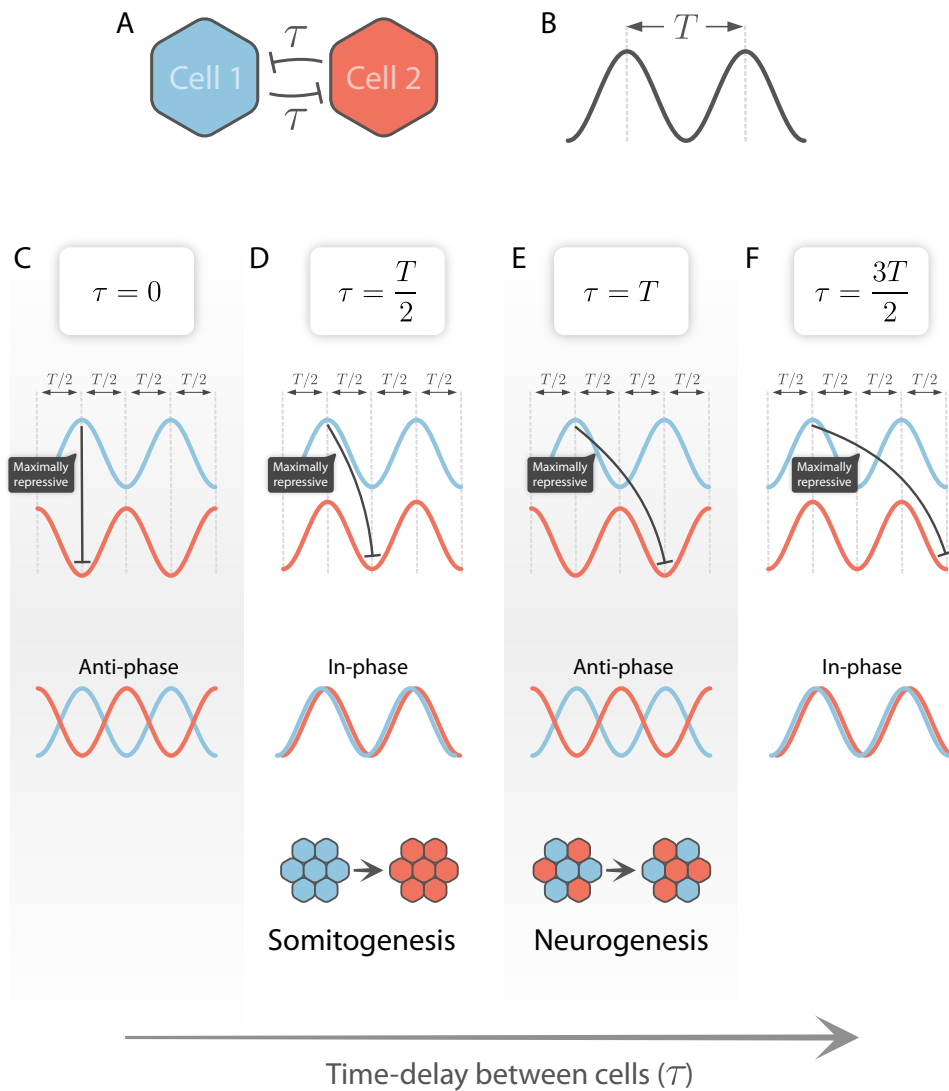


Figure 1.10: How time delay affects in-phase and anti-phase synchronisation dynamics in coupled autonomous oscillators. **A** A simple model of two oscillators coupled with a bidirectional repressive interaction (lateral inhibition) which also has a time-delay τ in the transmission of the oscillator phase/expression level information from one cell to the other. **B** The period T is the amount of time it takes for an oscillator to complete one cycle. **C** When $\tau = 0$, the lateral inhibition can be expected to produce antiphase oscillations. **D** When there is a sufficient time delay (this simplified example uses half the period of oscillation as the delay, $\tau = \frac{T}{2}$), the repressive interaction from one cell is delayed such that the other cell experiences maximal repression when the sending cell is in its trough, thus producing in-phase dynamics. This has been proposed as a possible regime in which somitogenesis operates to achieve synchronisation of Hes/Her genes through Notch coupling (Lewis et al., 2009). **E** When τ is increased further, the maximal repression from each cell again forces the system into anti-phase dynamics. This type of anti-phase dynamics is proposed to operate during neurogenesis. **F** The cycle of in-phase and anti-phase is expected to repeat in a simple two-cell model of coupled oscillators as the time delay is further increased.

1.4 Aims of the thesis

This thesis aims to elucidate the underlying mechanism and understand the developmental function of the dynamic spatial pattern of HES5 described in §1.2.5 by utilising mathematical modelling to explore the various biologically-based mechanisms of patterning as well as use experimental techniques to test the modelling assumptions.

Each results chapter addresses the following aims:

- **Chapter 2** Characterisation of the multicellular pattern and assessment of the emergent patterning behaviours of a mathematical model of multicellular Notch-Hes5 interactions. Additionally, how differentiation rates vary across the different patterning behaviours identified in the model is explored.
- **Chapter 3** Assessment of a travelling wave model in producing dynamic spatial patterns generated by imposing spatial parameter gradients across the simulated tissue.
- **Chapter 4** Assessment of the potential role of protrusions and altered Notch signalling as an underlying mechanism for dynamic spatial patterning. Additionally, the functional role of the pattern is analysed by exploring how differentiation events are spatially distributed when the model exhibits dynamic spatial patterning.
- **Chapter 5** Testing of the modelling assumptions in Chapter 4 is carried out by experimentally characterising the extent of protrusions and Dll1 signalling in the neural tube.

As a hybrid of journal and traditional format, Chapters 2 & 4 are presented in their published manuscript forms, and Chapters 3 & 5 are presented in traditional thesis format.

Chapter 2

Manuscript 1: A dynamic, spatially periodic, micro-pattern of HES5 underlies neurogenesis in the mouse spinal cord

2.1 Guide to the manuscript and supplementary files

Here the manuscript in its published format is included. Alongside the main figures, the manuscript also includes a set of *expanded view* figures that include more data related to some of the main figures, and these are included after the manuscript on page 72.

My contribution to this paper was in the mathematical modelling (see below for specific contributions), and the full details of the model are found in the appendix of the paper. Here, the modelling appendix has been extracted and additional details of the model implementation have been integrated into it, and this can be found on page 81.

[Link to the web version of the manuscript \(easier to view expanded view figures\).](#)

[Link to the full appendix.](#)

2.2 Author contributions

Joshua Hawley: Design and implementation of stochastic coupled HES5 model, parameterisation, analysis and model interpretation, smiFISH and imaging, analysis of cell movement, data interpretation, and manuscript writing. Contributions to specific figures are given below in Table 2.1.

Table 2.1: Specific figure contributions from Joshua Hawley in Manuscript 1.

Figure	Contribution
5 A-C	Design and implementation of the multicellular model.
5 D-F	Analysis and parameterisation of the model through exploration of parameter space.
5 G-J	Visualisation of kymographs and single cell time-traces. Veronica Biga helped with visualising outputs from the code.
6 A-C	Design and implementation of the differentiation algorithm.
EV5 B&C	Performed the cryosection smiFISH experiments. Ximena Soto assisted with image processing.
S5 & S6	Carried out comprehensive parameter space exploration looking at spatial periodicity, temporal periodicity, and cluster size. Veronica Biga developed the cluster size detection algorithm.
S7	Exploration of how many cells differentiate within identified clusters within the model.

Cerys Manning: Study conception and experiment design, wet lab experiments, supervision, data analysis, data interpretation and manuscript writing, data interpretation, and manuscript writing.

Veronica Biga: Supervision and development of method to analyse spatial micro-patterns of HES5 expression both in data and from the model, method for Hilbert phase persistence analysis, data analysis, data interpretation and manuscript writing, data interpretation, and manuscript writing.

Nancy Papalopulu: Study conception and experiment design, data interpretation, and manuscript writing.

Jochen Kursawe: Supervision and assistance in design, analysis and interpretation of the mathematical model, data interpretation, and manuscript writing.

Daniel Han: data interpretation, and manuscript writing.

Paul Glendinning: Supervision and assistance in analysis and interpretation of the mathematical model, data interpretation, and manuscript writing.

Emma Johns: Data collection and development of method to analyse correlations of HES5 nuclear intensity.










Daniel Han: Method to analyse periodic spatial micro-patterns of HES5 expression.

Ximena Soto: smiFISH and imaging.

Antony D Adamson: Design and generation of Neurog2::mScarlet-I knock-in mouse.

Hayley Bennet: Design and generation of Neurog2::mScarlet-I knock- in mouse.

A dynamic, spatially periodic, micro-pattern of HES5 underlies neurogenesis in the mouse spinal cord

Veronica Biga^{1,†} , Joshua Hawley^{1,†} , Ximena Soto¹ , Emma Johns¹ , Daniel Han² , Hayley Bennett¹, Antony D Adamson¹ , Jochen Kursawe³ , Paul Glendinning², Cerys S Manning^{1,*;†;‡}  & Nancy Papalopulu^{1,**;†;‡} 

Abstract

Ultradian oscillations of HES Transcription Factors (TFs) at the single-cell level enable cell state transitions. However, the tissue-level organisation of HES5 dynamics in neurogenesis is unknown. Here, we analyse the expression of HES5 *ex vivo* in the developing mouse ventral spinal cord and identify microclusters of 4–6 cells with positively correlated HES5 level and ultradian dynamics. These microclusters are spatially periodic along the dorsoventral axis and temporally dynamic, alternating between high and low expression with a supra-ultradian persistence time. We show that Notch signalling is required for temporal dynamics but not the spatial periodicity of HES5. Few Neurogenin 2 cells are observed per cluster, irrespective of high or low state, suggesting that the microcluster organisation of HES5 enables the stable selection of differentiating cells. Computational modelling predicts that different cell coupling strengths underlie the HES5 spatial patterns and rate of differentiation, which is consistent with comparison between the motoneuron and interneuron progenitor domains. Our work shows a previously unrecognised spatiotemporal organisation of neurogenesis, emergent at the tissue level from the synthesis of single-cell dynamics.

Keywords Hes5; neurogenesis; notch; oscillations; patterning

Subject Categories Development; Neuroscience

DOI 10.15252/msb.20209902 | Received 3 August 2020 | Revised 30 March 2021 | Accepted 6 April 2021

Mol Syst Biol. (2021) 17: e9902

Introduction

Neurogenesis is the developmental process which generates the variety of neuronal cell types that mediate the function of the

nervous system. Neurogenesis takes place over a period of days during mouse embryogenesis; thus, the transition from progenitor maintenance to differentiation needs to be balanced for development to occur normally. Neurogenesis relies on the integration of positional information with the transcriptional programme of neuronal differentiation. In the spinal cord, notable progress has been made in understanding the role and regulation of the dorsoventral (D-V) positional system, that relies on secreted morphogens and transcriptional networks to generate the stereotyped array of different types of neurons along this axis (Briscoe & Small, 2015; Sagner & Briscoe, 2019). The transcriptional programme that mediates neurogenesis is also well understood in the spinal cord, particularly with the application of single-cell sequencing (Paridaen & Huttner, 2014; Delile *et al.*, 2019; Sagner & Briscoe, 2019).

Recent live imaging studies of cell fate decisions during neurogenesis have added a new dimension to this knowledge (Vilas-Boas *et al.*, 2011; Das & Storey, 2012, 2014; Manning *et al.*, 2019; Nelson *et al.*, 2020; Soto *et al.*, 2020). They have shown the importance of understanding transcription factor (TF) expression dynamics in real time, including the key transcriptional basic helix–loop–helix repressors Hairy and enhancer of split (HES)1 and 5 (Ohtsuka *et al.*, 1999; Imayoshi & Kageyama, 2014; Bansod *et al.*, 2017), in regulating state transitions. We have previously shown that in spinal cord tissue, HES5 exhibits ultradian periodicity of 3–4 h in about half of the progenitor population with the remaining progenitors showing aperiodic fluctuations (Manning *et al.*, 2019). The percentage of cells that show oscillations rises in cells that enter the differentiation pathway; such cells show a transient phase of more coherent oscillations before the level of HES5 is downregulated in differentiated cells (Manning *et al.*, 2019). Furthermore, our studies of a zebrafish paralogue Her6 showed that the transition from aperiodic to oscillatory expression is needed for neuronal differentiation, suggesting that oscillatory expression has an enabling role for cell state

¹ Faculty of Biology Medicine and Health, The University of Manchester, Manchester, UK

² Department of Mathematics, School of Natural Sciences, Faculty of Science and Engineering, The University of Manchester, Manchester, UK

³ School of Mathematics and Statistics, University of St Andrews, St Andrews, UK

*Corresponding author. Tel: +44 161 2757221; E-mail: cerys.manning@manchester.ac.uk

**Corresponding author. Tel: +44 161 3068907; E-mail: Nancy.Papalopulu@manchester.ac.uk

[†]These authors contributed equally to this work

[‡]These authors contributed equally to this work as co-corresponding authors

transitions (Soto *et al*, 2020) as we have previously predicted computationally (Bonev *et al*, 2012; Goodfellow *et al*, 2014; Phillips *et al*, 2016).

Although these studies revealed an unappreciated dynamic behaviour at the level of HES TF protein expression, these live imaging studies are based on recording dynamics from sparsely distributed single cells in the tissue context. Therefore, little is known about how single-cell dynamics are synthesised to tissue-level dynamics. Do cells interact with their neighbours in order to coordinate their cell state transitions and if so, how and what is the mechanism?

Notch is of particular interest in this context because it is a highly conserved cell-to-cell signalling pathway that is well known for generating complex spatial patterns of cell fates in tissue development (Cohen *et al*, 2010; Shaya & Sprinzak, 2011; Hunter *et al*, 2016; Corson *et al*, 2017; Henrique & Schweisguth, 2019). Activation of Notch receptors by Notch ligands, including DLL1 and JAG1, results in downstream expression of HES1 and HES5. HES TFs can influence Notch activity on neighbouring cells by repressing Notch ligand expression either directly (Kobayashi *et al*, 2009; preprint: de Lichtenberg *et al*, 2018) or indirectly through the repression of proneural TFs such as Neurogenin1/2 (NGN1/2) (Ma *et al*, 1998). We argue that in order to understand how the balance of HES progenitor factors can be tipped in favour of proneural factors giving rise to a decision point in neural progenitor cells, we need to address tissue-level patterns of HES expression and use computational models that can integrate the complexity of interactions at multiple scales.

The effects of Notch–Delta signalling combined with HES oscillations have been investigated during somitogenesis. Live imaging of dissociated PSM cells *in vitro* has shown that single-cell oscillators can self-organise through Notch-dependent synchronisation to generate waves in gene expression similar to those observed *in vivo* (Tsiarris & Aulehla, 2016). A model of mRNA and protein production and self-repression with transcriptional delay explains the emergence of autonomous oscillations of Her1 and Her7 as well as synchronisation by Notch activity observed during the formation of somites (Lewis, 2003; Özbudak & Lewis, 2008; Webb *et al*, 2016). A more abstract Kuramoto-style model with time delays explains how a population of initially asynchronous and autonomous oscillators can evolve to adopt the same frequency and phase in order to periodically form somites (Morelli *et al*, 2009; Oates, 2020). The period of the oscillations determines the size of the somite and Notch abundance controls dynamic parameters such as the time to synchronisation (Herrgen *et al*, 2010). Apart from a limited number of studies suggesting an anti-phase relationship of DLL1 oscillations in neighbouring neural cells (Shimojo *et al*, 2016), whether and how neural progenitor cells coordinate fate decisions and dynamic HES activity with their neighbours remains unknown.

In this study, we observe spatially periodic HES5 micro-patterns which are generated through positive correlations in the levels of HES5 between neighbouring cells and by local synchronisation of low coherence single-cell oscillators present in spinal cord tissue. These patterns are maintained in a dynamic way through Notch mediated cell–cell interactions. A computational model predicts that coupling strength changes spatial patterns of expression and, in turn, the probability of progenitor differentiation. We confirm that between adjacent progenitor domains in the spinal cord, the rate of differentiation correlates with spatial patterns of HES5 and cell–cell coupling strength. Thus, organisation of neural progenitors in HES5

phase-synchronised and level-matched progenitors is an exquisite spatiotemporal mechanism conferring tissue-level regulation of the transition of single cells from neural progenitor to neuron.

Results

Positive correlations in Venus::HES5 intensity are indicative of microclusters in spinal cord tissue

Within the peak of spinal cord neurogenesis (E9.5–E11.5), HES5 is expressed in two broad domains in the dorsal and ventral embryonic mouse spinal cord (Sagner *et al*, 2018; Manning *et al*, 2019). Previously, we have characterised the single-cell dynamic behaviour of the more ventral HES5 expression domain that covers the ventral interneuron (p0–p2) and motorneuron progenitors (pMN) (Manning *et al*, 2019). Thus, to understand how the single-cell expression dynamics contributes to tissue-level behaviour we have focussed here on the same ventral area of HES5 expression (Figs 1 and EV1a). In this area, all progenitor cells (marked by SOX2) show HES5 expression (Fig EV1B). To characterise the spatial pattern of HES5 protein expression in this progenitor domain, we made *ex vivo* slices of E9.5–E11.5 Venus::HES5 knock-in mouse embryo spinal cord (Imayoshi *et al*, 2013). In snapshot images of this domain, we noticed multiple local clusters of neural progenitor cells with similar levels of nuclear HES5 (Fig 1A) which we refer to as “microclusters”. These are notable after manual segmentation using a Draq5 live nuclear stain and averaging HES5 intensity across the nucleus (Fig 1A–C). The differences in Venus::HES5 intensity between nuclei did not correlate with the Draq5 nuclear staining indicating this was not related to global effects or effects of imaging through tissue (Fig EV1C). By measuring the number of nuclei in microclusters with high Venus::HES5 levels (see Materials and Methods “Microcluster quantification”), we found that they consisted of 3–4 cells wide in the apical-basal (A-B) and 2–4 cells wide in the dorsoventral (D-V) direction (3–7 cells in total, Fig EV1D) and were similar in size between E9.5 and E11.5 (Fig 1D). Randomisation controls of the nuclear intensities showed that microclusters were significantly larger than is expected by chance (Fig EV1D and Materials and Methods). Consistent with the presence of microclusters of cells with similar levels, nuclei showed a positive correlation in Venus::HES5 between close neighbours that drops with increasing neighbour number (Fig 1E). We took a more quantitative approach and correlated mean nuclear HES5 levels between all pairs of nuclei and found that nuclei close to each other were highly positively correlated and this correlation dropped with increasing distance, becoming negative at distances over 50 μm (Fig 1F). This relationship was similar across E9.5–E11.5 (Fig EV1E) and substantially different to the correlation coefficients calculated from randomisations of the nuclei intensities but keeping the same nuclear spatial arrangement (Fig 1F) which indicates the presence of a pattern in HES5 levels.

The longer-range negative correlations may arise from gradients in HES5 expression in A-B and D-V direction. Indeed, the images indicate the presence of a radial gradient emanating from an area of highly expressing cells (Fig 1G and H, Fig EV1F and Appendix Fig S1A). Such a radial gradient could be due to the downregulation of HES5 as cells differentiate and move basally from the progenitor

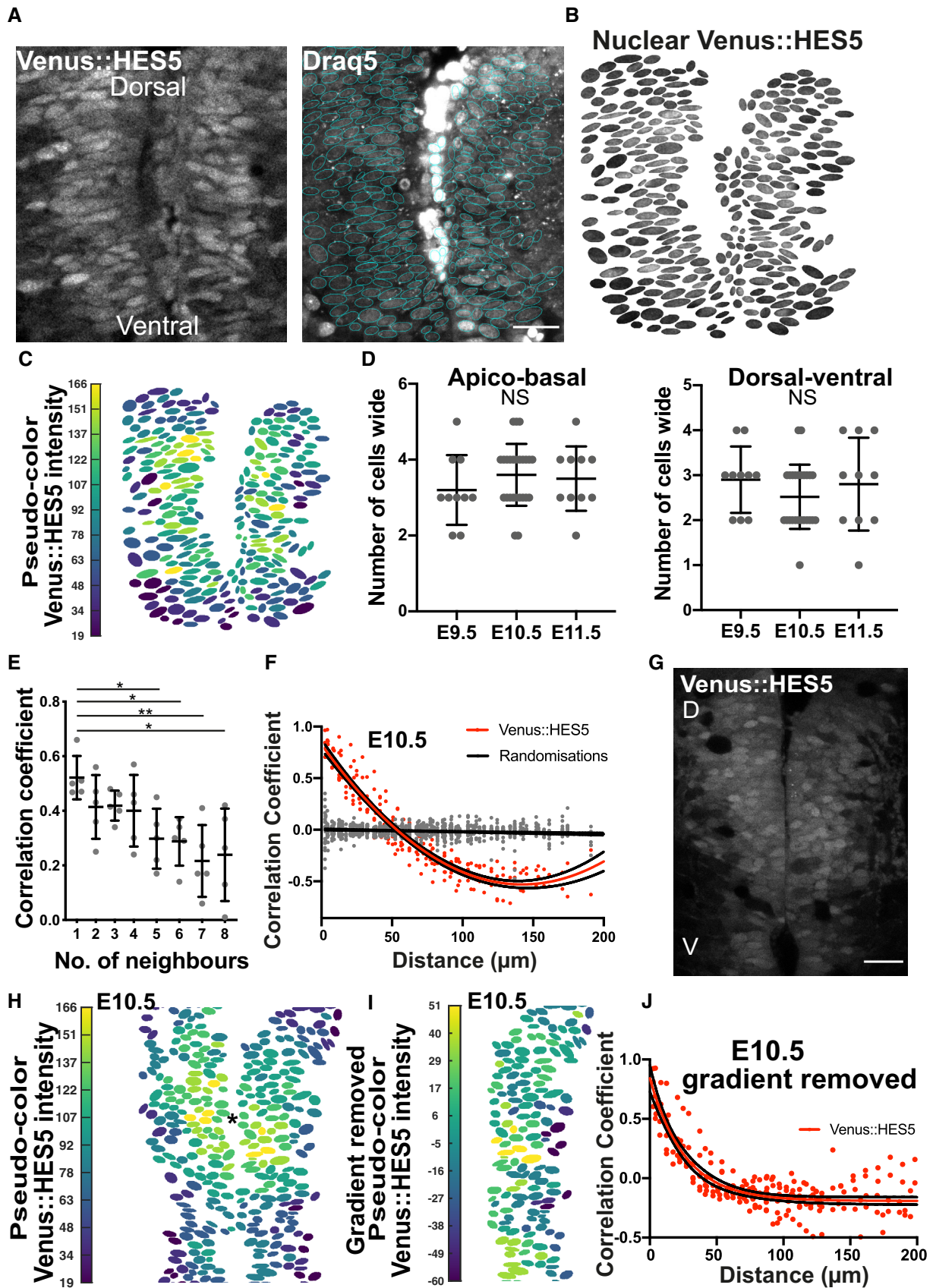


Figure 1.

Figure 1. Microclusters of spinal cord neural progenitor cells have positively correlated HES5 levels.

- A Transverse slice of live E10.5 Venus::HES5 homozygous knock-in mouse showing the ventral HES5 domain in spinal cord *ex vivo* (left panel); Draq5 live nuclear stain with nuclear segmentation overlay (right panel); scale bar 30 μm .
- B Venus::HES5 nuclear signal corresponding to tissue in (A) obtained by applying nuclear segmentation onto Venus channel.
- C Pseudo-color look-up table applied to mean nuclear Venus::HES5 intensity (Materials and Methods) corresponding to segmented image in (B).
- D Dimensions of microclusters in cell numbers with high and similar levels of HES5 in apical–basal axis (left panel) and dorsoventral axis (right panel) at E9.5 (10 microclusters, 3 slices, 3 exps), E10.5 (10 microclusters, 9 slices, 3 exps) and E11.5 (10 microclusters, 3 slices, 3 exps). NS—no significant difference in one-way ANOVA $P = 0.46$ (A–B), $P = 0.38$ (D–V). Bars show mean \pm SD.
- E Pearson correlation coefficient observed in segmented E10.5 homozygous Venus::HES5 spinal cord *ex vivo* slices showing correlation between mean nuclear Venus::HES5 intensity in any cell compared with up to eight nearest neighbours (see Materials and Methods); dots indicate average per slice; bars indicate mean and standard deviation of five slices from three experiments (data set is different from (D)).
- F Pearson correlation coefficient of mean nuclear Venus::HES5 intensity in relationship to distance; red dots indicate average Venus::HES5 correlation per slice of 12 slices from three experiments with corresponding red line indicating polynomial fit (order 2); grey dots with black line indicate correlations and polynomial fit from five randomisations of intensities analysed in the same way (see Materials and Methods).
- G Transverse slice of live E10.5 Venus::HES5 homozygous knock-in mouse showing the ventral HES5 domain in spinal cord *ex vivo*. Scale bar 30 μm , D—dorsal, V—ventral.
- H Pseudo-color look-up table applied to mean nuclear Venus::HES5 intensity of (G); centre of intensity shown with *.
- I Pseudo-color look-up table applied to mean nuclear Venus::HES5 intensity in (H) (only one side of ventricle) after radial gradient removal (see Materials and Methods).
- J Pearson's correlation coefficient of mean nuclear Venus::HES5 intensity with distance after subtraction of radial gradient in Venus::HES5 intensity; red dots represent average in each of 12 slices from three experiments.

Source data are available online for this figure.

domain as well as to D–V differences in the level of expression (see below) and is not further investigated here. To ask whether the local positive correlations in HES5 levels are an artefact of this larger-scale domain expression pattern, we measured and subsequently removed a radial gradient across the tissue from the segmented single-cell images (see Materials and Methods). However even after removing a radial gradient, mean nuclear HES5 levels at E9.5–E11.5 remained highly positively correlated at distances less than 40–50 μm (Figs 1I and J, and EV1G and H). Therefore, a global tissue gradient of HES5 cannot fully explain the detailed spatial pattern and further factors, such as microclusters of cells with similar HES5 levels, must contribute to the formation of the HES5 spatial pattern.

HES5 microclusters are spatially periodic along dorsoventral axis of spinal cord

The high-resolution analysis of single-cell snapshots showed the presence of multiple microclusters in HES5 expression in the ventral domain. Next, we asked whether these microclusters have a regular spatial arrangement. To do this, we drew line profiles 15 μm wide, parallel to the ventricle, in the ventral to dorsal direction (Figs 2A and EV2A and B) and plotted the Venus::HES5 intensity along this line (Fig 2B) from lower resolution 20 \times images of *ex vivo* slice cultures. Throughout the paper, the 0 distance is the ventral-most point of the HES5 domain, and distance extends dorsally (Materials and Methods). Detrending the signal removed a bell-shaped curve

Figure 2. HES5 microclusters are spatially periodic along the dorsal–ventral axis of spinal cord.

- A 20 \times snapshot of an *ex vivo* slice culture of E10.5 spinal cord from Venus::HES5 heterozygous knock-in mouse, transverse section; delineated region (blue) correspond to data shown in (B, C). D—dorsal, V—ventral.
- B Spatial profile of Venus::HES5 intensity averaged over 2.5 h with 0 distance representing the ventral end of kymograph; black line represents the trend in Venus::HES5 data across the domain produced using an polynomial order 6 (see Materials and Methods).
- C Detrended spatial profile of Venus::HES5 corresponding to data shown in (B).
- D Lomb–Scargle Periodogram analysis of detrended Venus::HES5 data in (C); horizontal line indicates Lomb–Scargle significance level $P = 0.0001$; red arrowhead indicate significant peaks.
- E Auto-correlation analysis of detrended Venus::HES5 spatial profile in (C) with multiple peaks indicating spatial periodicity; significant peaks (red arrowhead) lie outside grey area indicating 95% significance based on bootstrap approach (see Materials and Methods) and non-significant peaks (black arrowhead).
- F Peak to peak distance in auto-correlation from detrended Venus::HES5 signal collected in apical regions of spinal cord between E9.5–E11.5; bars indicate mean and SD of individual slices from three independent experiments; Kruskal–Wallis test not significant, $P = 0.44$.
- G Representative example of auto-correlation from detrended Draq5 nuclear signal with peak to peak distances indicative of inter-nuclear distance in live tissue; grey area denotes 95% confidence area for Draq5.
- H Peak to peak distance in auto-correlation of detrended Draq5 spatial profile in apical regions of spinal cord between E9.5–E11.5; bars indicate mean and SD of individual slices from three independent experiments; Kruskal–Wallis test not significant, $P = 0.3$.
- I Schematic of multiple non-overlapping regions of interest identified as Apical, Intermediate and Basal in the spinal cord tissue; width of regions in the apical-to-basal direction was 15 μm .
- J Peak to peak distance in auto-correlation of detrended Venus::HES5 spatial profile corresponding to apical, intermediate and basal regions of spinal cord at E10.5; dataset is different from (H); markers indicate average distance per experiment with a minimum of three z-stacks per experiment and two repeats (left and right of ventricle) analysed per z-stack; bars indicate mean and SD of six independent experiments; Kruskal–Wallis test not significant, $P = 0.115$; distances correspond to 4–5 cells considering the inter-nuclear distance in DV quantified in (H).

Source data are available online for this figure.

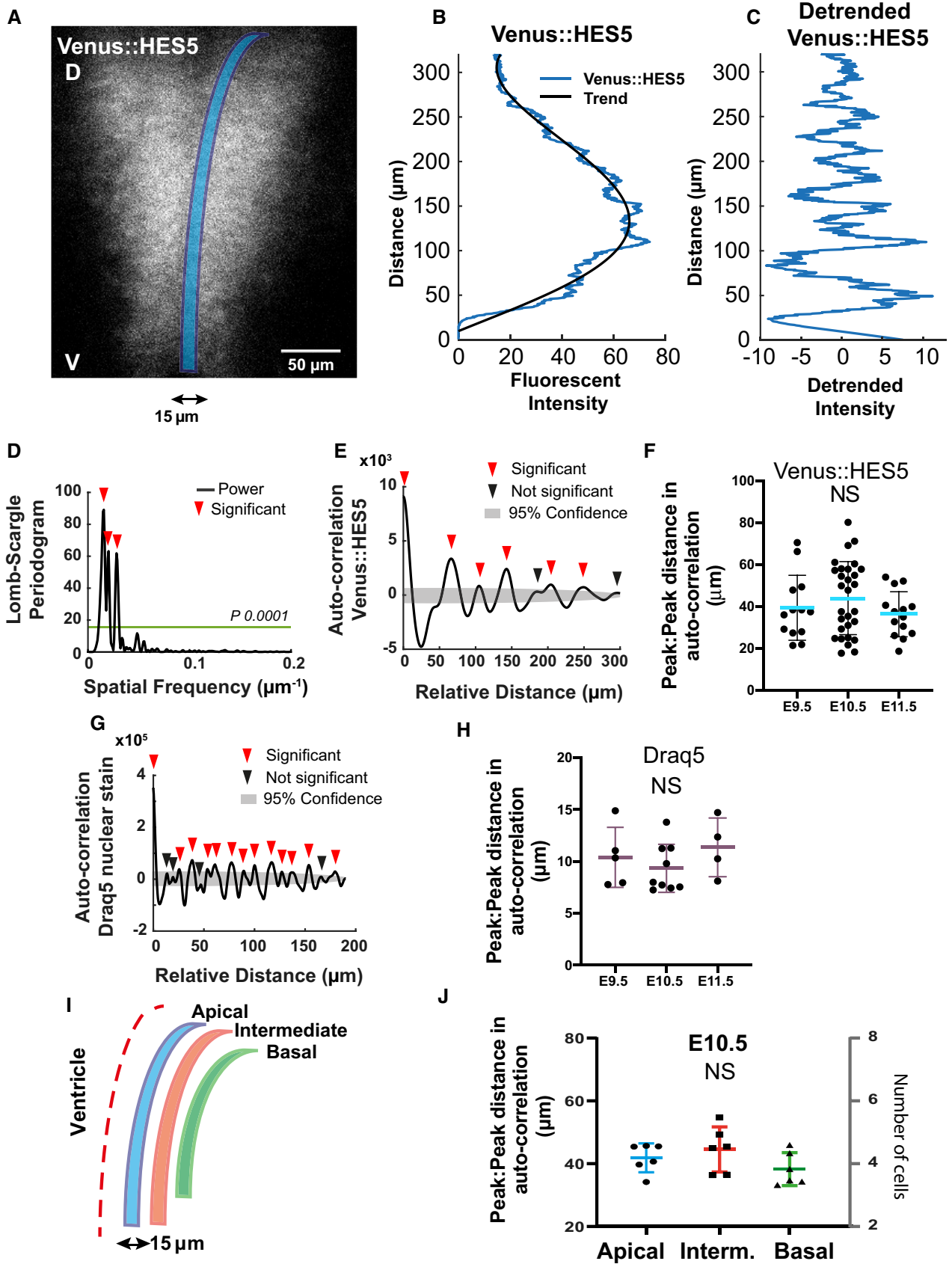


Figure 2.

of expression that is a result of different HES5 levels along the D-V axis and is not further investigated here (Figs 2B and EV2C). The microclusters could be detected as intensity peaks in the detrended Venus::HES5 intensity profile (direct comparison in Fig EV2A–C) and we observed multiple intensity peaks across the D-V axis (Fig 2C). Periodicity analysis of the detrended spatial Venus::HES5 expression profile revealed the presence of dominant frequency peaks in the power spectrum (Fig 2D) and multiple significant peaks in the auto-correlation function in all tissues analysed (Fig 2E, Appendix Fig S1B and Appendix Table S1). A significant peak in the auto-correlation function shows that the signal has similarity to itself at the relative distance (or lag) indicated in the x-axis. Multiple significant peaks in an auto-correlation function are indicative of a periodic signal with the peak to peak distance in the auto-correlation corresponding to the period of the signal. The spatial period in Venus::HES5 expression was 30–60 μm with a median period of 40 μm and no significant difference between E9.5 to E11.5. Periodicity measurements from auto-correlation functions and the power spectrum corresponded well (Fig 2F and Appendix Fig S1C).

To understand how our observed spatial periodicity relates to nuclear count in the tissue, we analysed the spatial profile for the Draq5 nuclear stain from snapshot images of Venus::HES5 *ex vivo* slices. We observed peaks in Draq5 in regions of low Venus::HES5 indicating that the lower Venus::HES5 regions did not correspond to a lack of nuclei at this position of the tissue (Fig EV2D). As expected, the Draq5 signal observed along the D-V axis also showed multiple significant peaks in the auto-correlation that corresponded to a spatial period of 10 μm , a single-cell width and was consistent over developmental time (Fig 2G and H, and Fig EV2E and Appendix Fig S1D). Using this value, we estimate that the periodic occurrence of microclusters of cells with correlated levels of Venus::HES5 has a median period of four cells. This corresponded well to the distance between microclusters in the high-resolution analysis of single-cell snapshots (Fig EV2F).

Since the apical region of spinal cord contains proliferative neural progenitors with high levels of HES5 that become downregulated when progenitors begin to migrate towards basal regions, we interrogated if the spatial periodicity persisted in the A-B axis. Venus::HES5 expression profiles collected from apical, intermediate and basal regions (Fig 2I) within the HES5 expression domain at E10.5 all showed spatial periodicity (both power spectrum, Fig EV2G and auto-correlation, Fig 2J) with the period varying from approximately four cells in the apical side to three cells in the basal region (Fig 2J, Appendix Fig S1E). These results suggest that proliferative progenitors (localised apically) as well as differentiating progenitors (localised more basally) show local spatial correlation in Venus::HES5 levels between neighbouring cells where 3–7 neighbouring cells can be in a high or low state in synchrony with each other and that these clusters are repeated periodically in the D-V axis.

To test whether clusters extended in the anterior–posterior (A-P) axis, we took longitudinal cryosections of the spinal cord and performed auto-correlations of the Venus::HES5 spatial profile along the A-P axis (Fig EV2H–J). Peaks in the auto-correlation show spatial periodicity in A-P axis of around 30 μm (Fig EV2J). Thus, the scale of cluster size in A-P is comparable to that observed in D-V. We confirmed this in our existing kymograph data by correlating the expression of HES5 at subsequent z-positions extending in the A-P axis in the same slice (Materials and Methods). Indeed,

correlations in A-P persisted at less than 30 μm but were lost further away (Fig EV2K).

The microclusters could be set up earlier on in development with fewer or single cells and then clonally expand through cell division. However, the similar microcluster size and Venus::HES5 spatial periodicity between E9.5, E10.5, and E11.5 argues against a clonal expansion mechanism. Coordinated cell behaviours such as nuclear motility may also contribute. We found weak positive correlation in the movement of nuclei in apico-basal axis between cell pairs less than 30 μm apart, but there was a large variation in correlations, and the correlation dropped between cells further apart (Appendix Fig S1F). This weak correlation in apical–basal nuclear movement may contribute weakly to maintaining the microcluster pattern.

The HES5 spatial pattern is dynamic over time

Given that single-cell Venus::HES5 expression dynamically fluctuates (Manning *et al*, 2019), we next investigated whether the spatially periodic pattern in Venus::HES5 is dynamic over a time scale of hours. To do this, we generated kymographs, single images that represent spatial intensity profiles in the same region of tissue over time, from 15 μm wide ventral–dorsal lines in movies of E10.5 Venus::HES5 spinal cord *ex vivo* slices (Fig 3A and B, Appendix Fig S2A and B, and Movie EV1). We noticed stripes in the kymograph, corresponding to the spatially periodic Venus::HES5 pattern (Fig 3B). To investigate how long high HES5 and low HES5 microclusters persist over time we split the kymograph into adjacent 20 μm regions (half of the 40 μm spatial periodicity, chosen to capture the size of a microcluster) along the D-V axis and followed their levels over time (Materials and Methods). Hierarchical clustering of the dynamic behaviour of the kymograph regions revealed changes from low to high Venus::HES5, high to low, or re-occurring high–low–high, showing that clusters of cells can interconvert between low and high HES5 states (Fig 3C and additional examples Appendix Fig S2C). To exclude the possibility of sample drift in the DV axis being responsible for these dynamics, we used single-cell tracking from the same videos as the kymographs to determine that global DV drift is minimal (<20 μm per 12 h, Appendix Table S2) and only one in 10 tissues was excluded from temporal analysis. Thus, we could proceed to analyse the persistence of a microcluster in the high or low state and we found that it was on average 6–8 h with no difference between persistence of high or low states in the same region (Fig 3D and Appendix Fig S2D). We confirmed these results using a second method that detected high/low regions in the first 2 h of kymograph and fixing ROIs around these regions whereby we continued to observe changes in intensity over time with similar persistence (Appendix Fig S2E). This shows that the microstripes of HES5 expression are not stable but are dynamic over time.

Since the HES5 expression is periodic along the D-V axis, it can be represented as a spatial oscillator. Therefore, we used its phase characteristics denoting the position in the spatial cycle, to analyse how the HES5 signal changes from high to low in the same region over time. We transformed the detrended spatial Venus::HES5 intensity (Fig EV2L, Appendix Fig S3A) along the D-V axis to phase of the spatial oscillator of Venus::HES5 using the Hilbert transform (Materials and Methods). All experiments showed a dynamic pattern with changes in phase in any area of the tissue over the 12–24 h movies

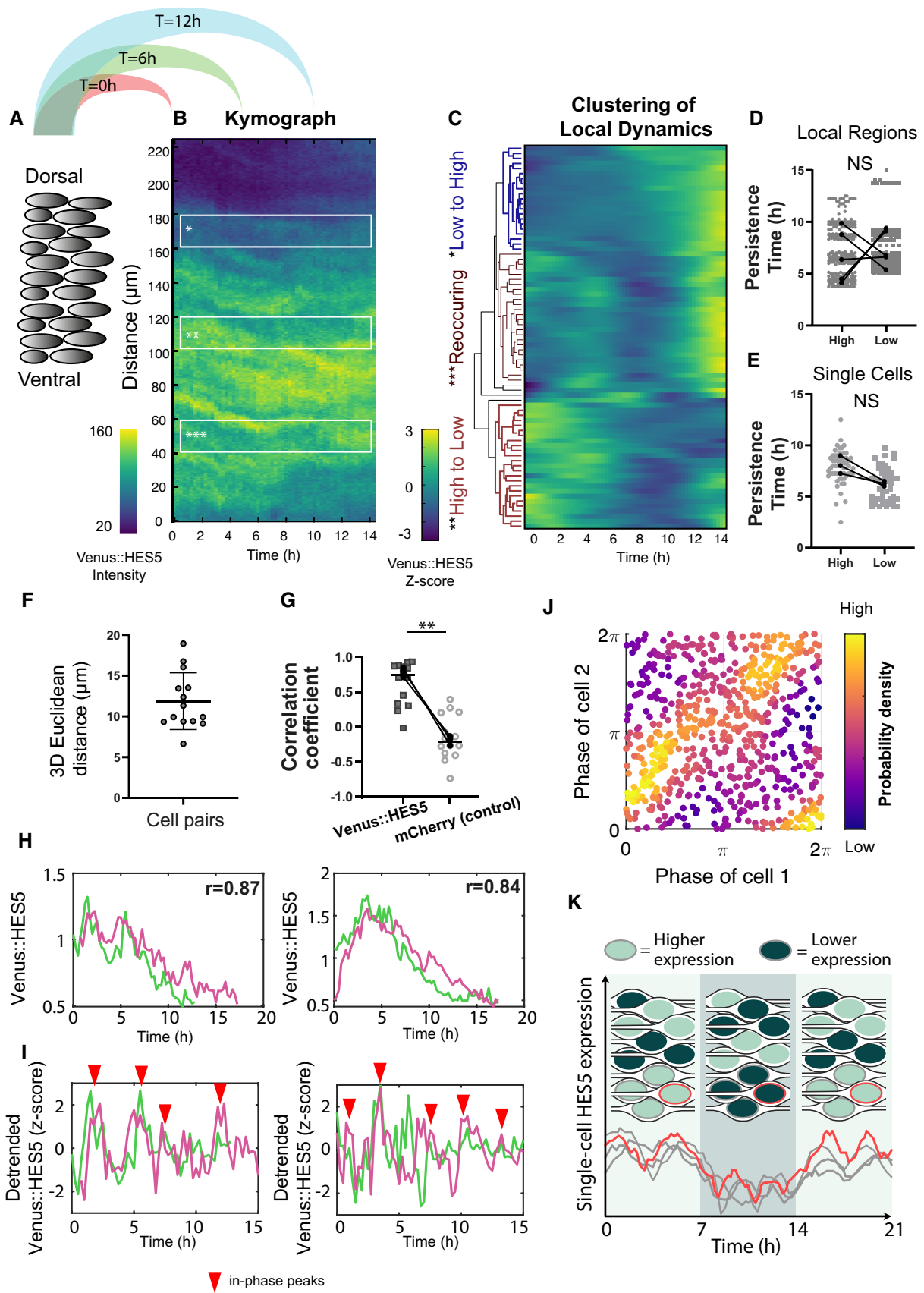


Figure 3.

Figure 3. HES5 protein is expressed in a dynamical spatial periodic pattern modulated by Notch.

- A Schematic of extracting kymograph information from tissue data by averaging Venus::HES5 intensities observed in E10.5 heterozygous spinal cord slices to generate one intensity profile in the dorsal–ventral axis per timepoint (see Materials and Methods).
- B Representative kymograph data showing spatiotemporal Venus::HES5 expression profile along ventral–dorsal direction in a 15 μm wide apical region and observed over 14 h; local bands of 20 μm width in D-V; region of interest markers indicate: *low to high, **high to low and ***re-occurring high/low activity in the same area.
- C Hierarchical clustering of apical Venus::HES5 expression from one representative experiment showing behaviour in the same area over time; columns represent fluctuations in Venus::HES5 intensity in small local areas (bands) obtained by dividing the spatial signal into non-overlapping 20 μm regions and normalising to the mean and standard deviation of each region over time (z-scoring); data have been subject to a Gaussian blur pre-processing step (see Appendix Fig S2B and Materials and Methods).
- D Persistence of Venus::HES5 in 20 μm regions expressed as continuous time intervals when signal in the band is high or low compared with its mean (see Materials and Methods); individual datapoints (grey) indicate quantification of high and low persistence time obtained from over 300 thin bands collected from multiple tissues with 2 z-stacks per tissue and two repeats (left and right of ventricle) per z-stack; dots indicate paired medians of five independent experiments; statistical test is paired t-test of median per experiment with two-tail significance and $P = 0.7171$.
- E Persistence of Venus::HES5 levels in high and low states taken from 60 tracked single cells collected from three independent experiments; paired t-test not significant $P = 0.0533$.
- F Relative distance between cell pairs computed from relative 3D Euclidean distance between nuclei over 12–15 h; dots indicate median distance over tracking period; horizontal lines show mean and SD of 14 cell pairs from three experiments.
- G Spearman correlation coefficients computed in the same cell pairs from Venus::HES5 and H2B::mCherry (control) nuclear intensity timeseries; markers in each condition indicate pairs; black dots indicate median correlation coefficients per experiment (four pairs, three pairs and seven pairs); lines show median of 14 pairs from three experiments; paired t-test with significance $P = 0.0058$.
- H Representative example timeseries of Venus::HES5 in cells pairs identified as remaining in close proximity; r -values indicate Spearman correlation coefficients between time traces over all co-existing timepoints.
- I Detrended Venus::HES5 fluorescent intensity timeseries (after z-scoring) corresponding to examples in (H); red arrows indicate in-phase peaks.
- J Density phase plots from instantaneous Hilbert phase reconstruction at multiple timepoints over a 12–14 h period; dots indicate the phase angle in Cell 1 and Cell 2 from 14 pairs collected from three experiments; colormap indicates probability density showing accumulation of phase values predominantly along the (0,0) and (2π , 2π) diagonal; light colours indicate most frequent.
- K Graphic representation of a neuroepithelial tissue with nuclei colour-coded to indicate clusters of high or low HES5 expression. The tissue is illustrated at three different time points to depict how clusters of cells can dynamically switch from high to low or low to high while the periodic spatial pattern is maintained. In the example time traces (corresponding to the three grey and one red highlighted nuclei), synchronised ultradian oscillations are shown as being overlaid on the slow-varying higher-amplitude switching dynamics.

Source data are available online for this figure.

(Appendix Fig S3B). Regions could be identified that maintained a similar phase over several hours followed by a change, indicating a switch in state of the Venus::HES5 pattern (Fig EV2L). Phase waves could be observed in some movies, indicated by the diagonal lines of similar colours in the spatial phase map (Appendix Fig S3B); however, these were variable across the data and did not have a consistent direction in the D-V axis between experiments. In summary, we find microclusters of cells with correlated Venus::HES5 levels that are a maximum of 2–3 cells wide in D-V and 3–4 in A-B axes and are arranged in a spatially periodic pattern. The pattern is also temporally dynamic with a persistence in a high or low level expression of 6–8 h but no consistent phase wave travel in D-V.

Single cells in a microcluster coordinate HES5 expression at two different timescales

We next addressed how the dynamic tissue pattern may be synthesised from single-cell Venus::HES5 expression. We have previously tracked Venus::HES5 in single nuclei of E10.5 spinal cord *ex vivo* slices and reported that about 40% of the progenitors show oscillations of 3–4 h periodicity (Manning *et al.*, 2019). However, we also observed changes in the mean expression level of apical progenitors that varied at a time scale longer than 3–4 h (Manning *et al.*, 2019). This slowly varying signal in progenitors was not investigated further at the time (Manning *et al.*, 2019). Indeed, when we re-analysed single-cell Venus::HES5 expression data of apical progenitors we found that the slowly varying fluctuations have similar “persistence” time as the microclusters (Fig 3E vs D and Appendix Fig S2E). The distinction between the dynamics at shorter timescale (ultradian oscillations) and

the longer timescale fluctuations in mean HES5 levels is that slow-varying dynamics have larger amplitude compared with the ultradian (Appendix Fig S4A and examples in Manning *et al.*, 2019; Appendix Fig S7). As such, both slow-varying and ultradian changes in HES5 could contribute to the formation and dynamic nature of microclusters with the slower varying fluctuations in HES5 mean levels specifically modulating the microcluster persistence time.

To investigate the single-cell expression inside a microcluster, we identified cell pairs that were in close proximity over 12 h (median Euclidean distance $< 20 \mu\text{m}$) (Fig 3F and Appendix Fig S4B). We found that 10/14 cell pairs showed a high positive correlation in their mean Venus::HES5 levels (Fig 3G: median 0.74 and examples Fig 3H) and this was reproducibly higher than the experimental control of nuclear H2B::mCherry in the same experiment (Fig 3G, median -0.2). Thus, single cells in a microcluster coordinate their HES5 levels over time. We then turned our attention to the ultradian HES5 activity in cell pairs by utilising detrending and subsequent phase reconstruction (Materials and Methods). The instantaneous phase of Venus::HES5 expression in cell pairs persistently showed in-phase peaks (examples Fig 3I red arrowhead). Phase-phase visualisation maps of all pairs at all recorded timepoints exhibited a large accumulation of Venus::HES5 instantaneous phases along the diagonal between (0, 2π) and (2π , 2π) indicating prevalence of in-phase behaviour at single-cell level in the same pair (Fig 3J). We also noted imperfections with some phase activity around (0, 2π) and the presence of anti-phase peaks (Fig 3I and J); however, this was transient and not characteristic of any particular pair (Appendix Fig 4C–E and Materials and Methods). Moreover, we performed a cross-pairing control which showed that while in-phase

activity is reproducibly observed in neighbouring cell pairs, this effect is lost when pairing cells located further away in the same tissue (Appendix Fig S4F and G and Materials and Methods). These findings demonstrate that ultradian activity between neighbouring cells in a microcluster is predominantly in-phase; however, it does not translate to global synchrony across the tissue and we refer to this as “local in-phase”.

To summarise, inside a HES5 expressing microcluster, cells predominantly show synchronised ultradian oscillations (or fluctuations) of 3–4 h; on top of that, each microcluster has a persistence time in a high or low state of about 6–8 h, a timescale coincident with the slower varying fluctuations observed in single-cell traces. Each HES5 expressing microcluster is a composite of these two dynamic activities observed at different timescales (diagram in Fig 3K).

Notch inhibition extinguishes dynamic changes in Venus::HES5 microclusters between high and low states

We hypothesised that the periodic microclusters of HES5 are generated through Notch–Delta interactions that locally synchronise dynamic HES5 expression between neighbouring cells. To test this, we treated spinal cord slice cultures with the Notch inhibitor DBZ and performed kymograph analysis in the apical region of DMSO and DBZ treated slices. In Notch inhibitor conditions, the HES5 levels reduce continuously over time (Fig 4A) indicating that the DBZ is effective. The most noticeable difference in the spatiotemporal HES pattern was that the temporal transitions of microclusters from high to low Venus::HES5 were impaired by DBZ. We observed this at a temporal resolution at which single cells are unlikely to leave the region of interest (Appendix Table S3). We saw fewer changes in the phase of the spatial periodic Venus::HES5 pattern indicating the spatial pattern remained stable (Figs 4B–D and EV3A and B). This was quantified with a phase synchronisation index (see Materials and Methods), where low values indicate the presence of

phase changes at the same D–V locations. The phase synchronisation index was significantly higher in DBZ-treated tissue (Fig 4E) indicating that in the absence of Notch signalling, HES5 microclusters were more persistent in the same region and that the dynamic changes in Venus::HES5 microclusters between high and low levels are mediated by Notch signalling. The phase detection method (Hilbert transform) is not dependent on the level of expression and so the reduction in HES5 levels in DBZ does not affect the analysis of microcluster high-to-low and low-to-high phase switches. However, we did account for loss of periodicity in DBZ (discussed below) by comparing phase only over time intervals when spatial periodicity was still detected (see Materials and Methods).

We analysed the spatial periodicity of HES5 and found that the amplitude between high and low microclusters appears diminished compared with control DMSO treated conditions (Fig 4F). Spatial periodicity could be detected at the start of the movie, immediately after DBZ addition; however, the spatial periodicity was gradually extinguished through loss of Venus::HES5 levels and spatial amplitude death (Fig EV3C). Approximately 45% of the DBZ-treated slices did not show significant peaks in the auto-correlation of detrended spatial Venus::HES5 profile by 10–12 h of treatment (Fig 4G) whereas periodicity was maintained in all DMSO conditions. Spatial periodicity in detrended Venus::HES5 levels that could be detected in DBZ treatment at early time points frequently appeared higher in Notch inhibitor treated *ex vivo* slices than in DMSO control (Figs 4H and EV3D). Cell density also decreased in Notch inhibitor conditions suggesting this increase in spatial period was partially due to changes in the spatial arrangement of cells (Fig EV3E).

We also investigated how Notch inhibition may affect ultradian dynamics at single-cell level. We had previously reported that under DBZ conditions, single neural progenitors continue to show oscillations and fluctuations in HES5 before undergoing amplitude death (Manning *et al*, 2019). However, here we wanted to interrogate how DBZ affects the way cells coordinate their activity in the tissue. To do this, we used the Kuramoto Order Parameter (KOP, also known

Figure 4. Notch inhibition increases HES5 pattern persistence.

- A Start-Finish Venus::HES5 intensity ratio in E10.5 Venus::HES5 heterozygous spinal cord slices treated with control (DMSO) and Notch inhibitor DBZ (2 μ M) observed over 16 h; bars indicate mean and standard deviation of DMSO ($n = 3$ experiments) and DBZ ($n = 4$ experiments); 2-tailed t-test **** $P = 0.0001$.
- B Representative spatiotemporal plots of the detrended Venus::HES5 pattern along ventral–dorsal direction in DMSO control (left panel) and DBZ conditions (right panel) obtained by averaging kymographs data in the same region over 2-h time intervals.
- C Schematic indicating the correspondence between Venus::HES5 spatial oscillator represented as detrended level and phase angle characteristics; the spatial oscillator traverses repeated cycles including start (HES5 low-orange arrowhead), middle (HES5-teal arrowhead) and end (HES5 low-red arrowhead) which in phase space corresponds to phase angles 0 , π and 2π , respectively.
- D Phase maps corresponding to DMSO (left panel) and DBZ (right panel) detrended Venus::HES5 data shown in (B).
- E Phase synchronisation measure (see Materials and Methods) of the detrended Venus::HES5 spatial oscillator measured over time in E10.5 Venus::HES5 spinal cord periodic slices treated in DMSO vs DBZ conditions up to 10 h; dots indicate DMSO (21 kymographs, $n = 3$ experiments) and DBZ (19 kymographs, $n = 4$ experiments); bars indicate mean and SD; 2-tailed Mann–Whitney test with significance **** $P < 0.0001$.
- F Spatial peak: trough fold change in Venus::HES5 intensity profile in the D–V axis measured at 2 h and 10 h in DMSO and DBZ-treated E10.5 Venus::HES5 spinal cord slices; dots indicate average over three z-slices from DMSO ($n = 3$) and DBZ ($n = 4$) experiments; lines indicate median per condition; 1-tailed unpaired t-test with significance * $P < 0.05$.
- G Percentage of *ex vivo* slices with significant spatial period detected after 10–12 h of DMSO and DBZ conditions; significant spatial period defined as multiple significant peaks in auto-correlation detected above the 95% confidence bounds; dots indicate % per experiment; bars denote median and inter-quartile range of DMSO ($n = 3$) and DBZ ($n = 4$) experiments; 1-tailed t-test with significance ** $P = 0.0062$.
- H Peak to peak distance in auto-correlation plots of detrended Venus::HES5 spatial profile in DMSO and DBZ-treated E10.5 Venus::HES5 spinal cord slices; grey dots represent significant mean peak to peak distance of DMSO (100) and DBZ (105) auto-correlation functions collected from three z-stacks per slice and two repeats (left and right of ventricle) with multiple timepoints; bars indicate median per experiments from DMSO ($n = 3$) and DBZ ($n = 4$) experiments; error bars indicate SD; 2-tailed Mann–Whitney test **** $P < 0.0001$.

Source data are available online for this figure.

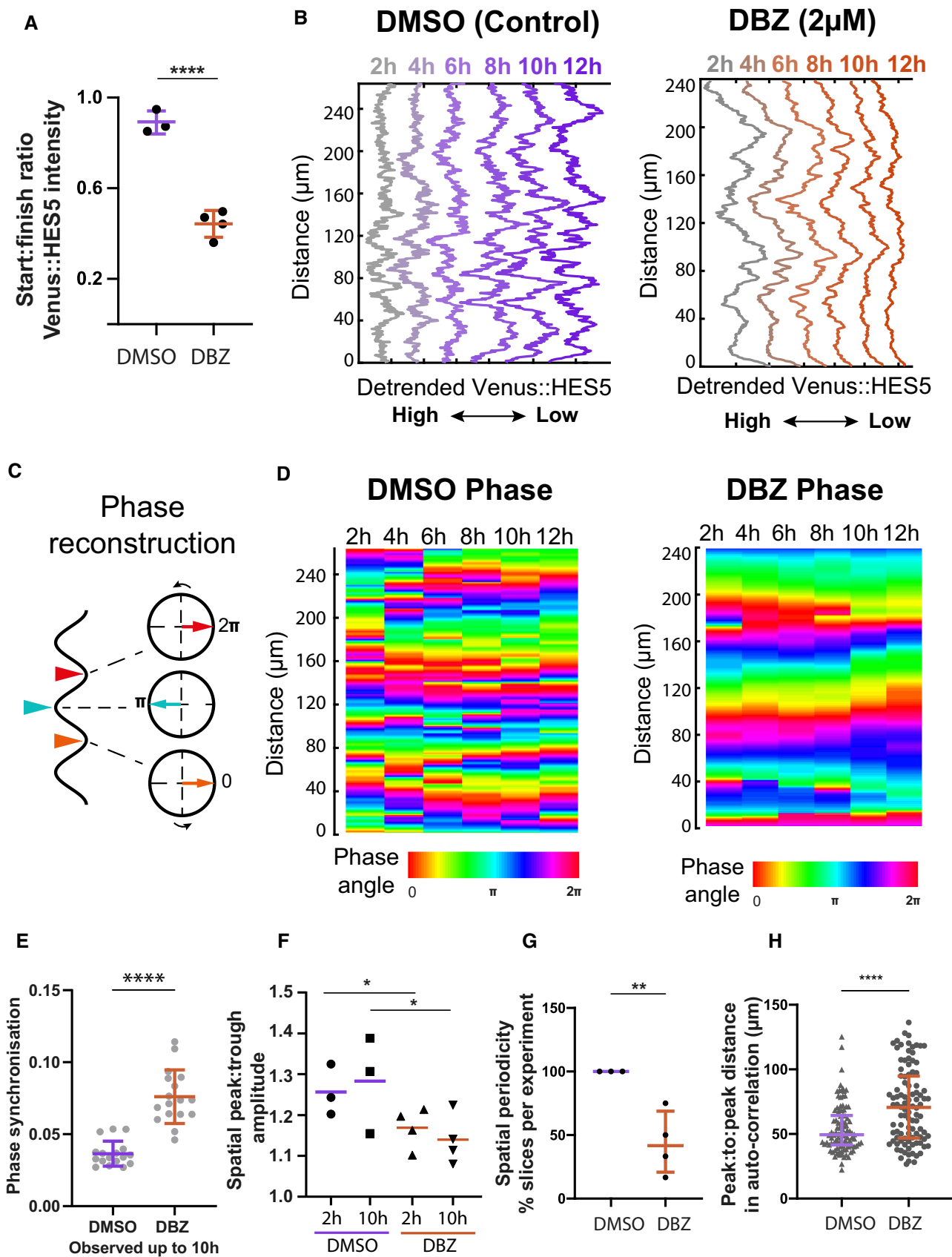


Figure 4.

as mean-field value) a population measure of synchrony (Choi *et al*, 2000). High KOP levels close to 1 are indicative of global in-phase activity whereas low KOP values close to 0 are indicative of no in-phase synchrony (see Materials and Methods). We found that KOP of single progenitors showed weak levels of synchrony under DMSO conditions (Appendix Fig S4H, mean 0.36) consistent with our findings of local in-phase activity but not indicative of global synchrony. Furthermore, we observed a significant reduction in KOP values in DBZ conditions (Appendix Fig S4H, mean 0.15).

Taken together, these findings show that Notch signalling is responsible for certain aspects of the pattern, such as the dynamic switching between high/low HES5 microcluster states over time. However, inhibition of Notch does not seem to abolish the existence of microclusters or their spatial periodicity, as they can still be detected until amplitude death occurs and the HES5 levels are depleted. At single-cell level, we observe that Notch signalling is likely to promote local in-phase ultradian coordination between cells within a microcluster.

A model of Notch–Delta with HES5 auto-repression containing stochasticity and delays recapitulates the existence of local in-phase HES5 dynamics

We used computational modelling to help us understand how positively correlated, spatially periodic, and dynamic microclusters of cells may emerge in the spinal cord. At single-cell level, HES5 protein expression oscillations are due to HES5 self-repression, an intra-cellular transcriptional time delay (τ_H) and short protein and mRNA half-lives (Jensen *et al*, 2003; Monk, 2003; Momiji & Monk, 2008). We represented the auto-repressive interactions between HES5 mRNA and protein using stochastic differential equations with time delay, as previously described in (Galla, 2009; Phillips *et al*, 2016; Manning *et al*, 2019). This single-cell model has been shown to faithfully recapitulate statistics of single-cell HES5 expression dynamics collected from spinal cord tissue (Manning *et al*, 2019). We extended the single-cell mathematical description of HES5 to a coupled dynamical model by incorporating a repressive interaction

in the form of a Hill function, that describes how HES5 protein in one cell represses Hes5 transcription in a neighbouring cell via Delta-Notch signalling (Figs 5A and EV4A). We introduce the following set of inter-cellular parameters (Fig 5B and Materials and Methods): (i) *inter-cellular time delay*, representing the time required to transfer the signal from one cell to another, that is, the time required for a change in HES5 protein in one cell to affect Hes5 transcription in a neighbouring cell through Notch–Delta; (ii) *the inter-cellular repression threshold*, representing the amount of HES5 protein required to reduce Hes5 transcription in a neighbouring cell by half; the inter-cellular repression threshold is inversely proportional to coupling strength where higher coupling strength (or low inter-cellular repression threshold) indicates that less protein is needed to repress the neighbour's Hes5 transcription by 50%; and (iii) *inter-cellular Hill coefficient* indicating how steep the response curve of Hes5 transcription is in response to a change in HES5 protein in the neighbouring cell, with higher values corresponding to increased nonlinearity. Interactions between cells are considered in a hexagonal grid whereby each cell can interact with its immediate six neighbours and repression between cells is calculated through the inter-cellular Hill function by averaging HES5 protein abundance over six neighbours (Fig 5B and C and Materials and Methods). Thus, we generated a comprehensive, multiscale and stochastic model with time delays, representative of the Delta–Notch–Hes interactions in the multicellular tissue environment.

We parameterised this multiscale HES5 model with previously determined experimental measures of HES5 protein and mRNA stability and with parameter values of the single-cell HES5 self-repression loop that can reproduce single neural progenitor HES5 dynamics (see Materials and Methods and Appendix Table S4 Main), as identified through Bayesian inference in our previous work (Manning *et al*, 2019). We then investigated the parameter space of unknown model parameters that are characteristic of cell-to-cell interactions, namely the repression threshold (inverse of coupling strength) and time delay, to identify values that are compatible with the temporal period and phase synchronisation level of single-cell Venus::HES5 expression dynamics (Fig 5D and E). The mean temporal period of Venus::

Figure 5. Multicellular cell–cell coupling model explains the emergence of microclusters.

- Schematic of repressive interactions via Notch–Delta between neighbouring cells whereby the effects of HES5 protein in Cell 1 (marked as P_1) on transcription in Cell 2 and vice versa are represented using an inter-cellular Hill function $J(P_{1,2}(t - \tau_{ND}))$ where t denotes time and τ_{ND} represents the inter-cellular time delay, the time interval required to synthesise the intermediate molecular species (detailed in Fig EV4A); HES5 auto-repression is represented using an intra-cellular Hill function $G(P_{1,2}(t - \tau_H))$ where τ_H represents the inter-cellular time delay, the time interval required for protein to be produced and repress its own transcription.
- Mathematical description of the inter-cellular Hill function and its parameters: time delay (τ_{ND}), repression threshold (P_0) and Hill coefficient (n); (bottom left panel) higher P_0 corresponds to reduced inter-cellular repression (i.e. decreased coupling strength) and conversely lower P_0 corresponds to higher coupling strength; (bottom right panel) increasing values of n correspond to increased steepness of the inter-cellular response.
- Multiscale coupled mathematical model of the tissue environment consisting of a 2D hexagonal grid of cells expressing HES5 protein with corresponding auto-repression (described in (A)) coupled together by repressive interactions between its six immediate neighbours (see Materials and Methods); single-cell inter-cellular repression is a Hill function (with parameters described in (B)) dependent on mean protein abundance in the neighbouring cells.
- Parameter exploration of single-cell temporal period emerging from the model at different repression threshold and time delay values.
- Parameter exploration of phase synchronisation quantified using the Kuramoto Order Parameter (see Materials and Methods) where 1 indicates global in-phase activity and 0 indicates no coordination of phase between cells.
- Parameter selection strategy combining experimentally determined temporal phase (insert left panel) and KOP (insert right panel) values in spinal cord tissue (see (Manning *et al*, 2019) and Materials and Methods) to indicate areas where model statistics (i.e. mean temporal period and KOP of synthetic data) resemble real tissue; values within ± 1 SD and $2\pm$ SD from the mean of the tissue are identified and values found outside of ± 2.4 SD from the mean of tissue are excluded.
- Representative examples of synthetic kymograph data obtained at specific levels of repression threshold: *Alternating high–low* ($P_0 = 400$), *Global in phase* ($P_0 = 15,000$) and *Local in phase* ($P_0 = 21,000$) and corresponding KOP values; the presence of microclusters at weak coupling is indicated with red arrowheads; time delay 150 min, $n = 4$.
- Kymograph data obtained in the absence of coupling between cells; phase relationships are un-coordinated resulting in a $KOP \approx 0$.
- J Synthetic data timeseries corresponding to simulations in (G).

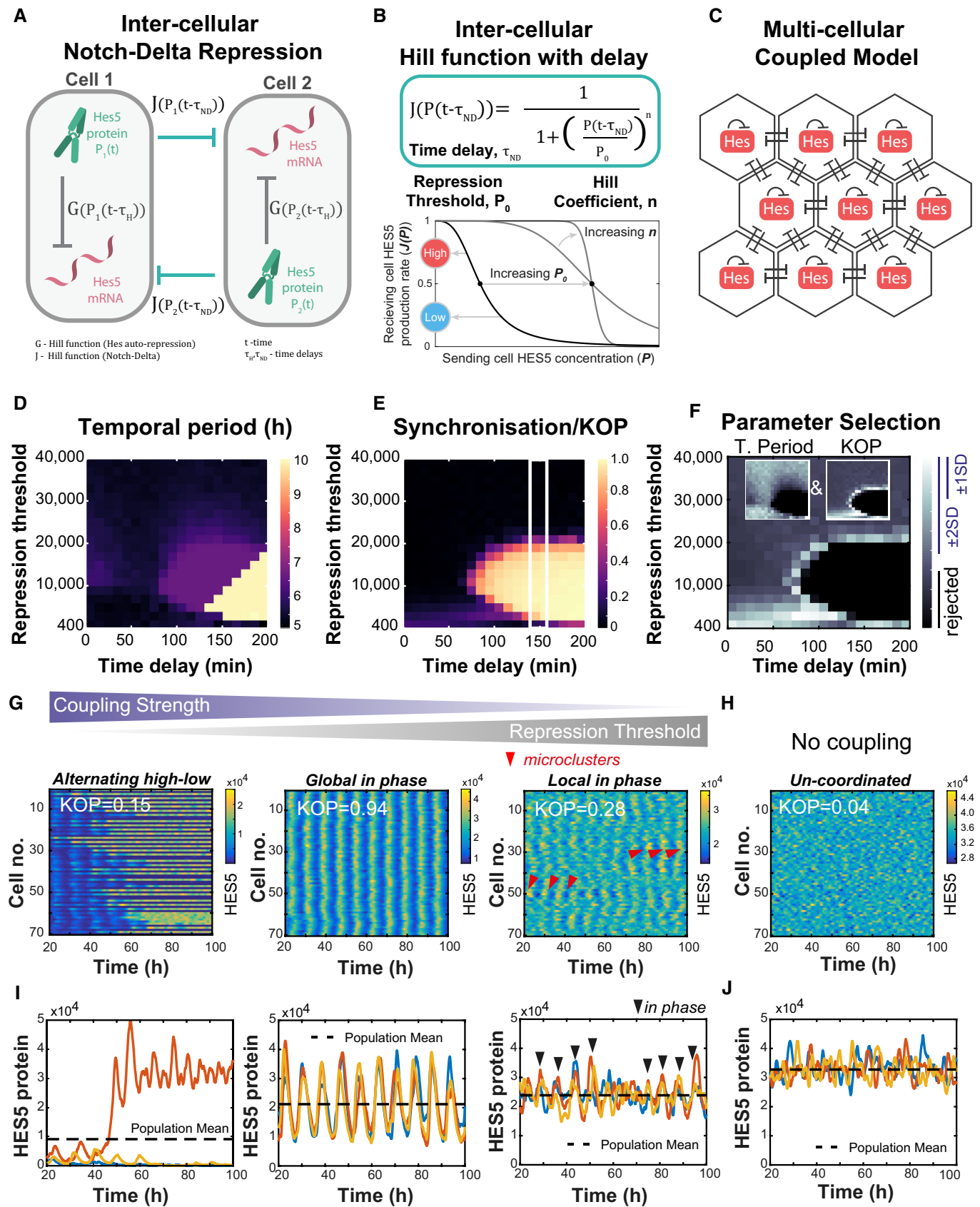


Figure 5.

HES5 in *ex vivo* spinal cord tissue is approx. 2–6 h (mean 3.3 h) (Manning *et al*, 2019), which could be reproduced by the model in a wide range of coupling strength and inter-cellular time delay values (Fig 5D and F). We measured the temporal phase synchronisation (KOP) between single Venus::HES5 expressing cells in the apical region and we found that the KOP was between 0.15 and 0.4 (Appendix Fig S4I, mean 0.3) consistent with KOP in the DMSO data (Appendix Fig S4H). This measure aided us in further reducing the parameter space of repression threshold and inter-cellular time delay that could fit the observed data (Fig 5E and F). The accepted parameter values for inter-cellular time delay were consistent with a Delta to Hes transmission time of 128 min measured experimentally (Isomura *et al*, 2017). A Hill coefficient value larger than 2 was required for notable synchrony (KOP>0), and only minor differences in terms of parameter selection were observed for values between 3 and 6 (Appendix Fig S5A).

This parameter exploration allowed us to optimise the search for spatial patterns that emerge at different coupling strengths using kymograph analysis (Fig 5G and H). We set the inter-cellular time delay to 150 min and Hill Coefficient to 4 (Materials and Methods) and then compared the synthetic HES5 spatiotemporal characteristics at specific coupling strength levels (parameter space indicated by the white box in Fig 5E). Our comparison showed that strong coupling (i.e. high coupling strength or low inter-cellular repression threshold) induces *Alternating high–low* dynamics whereby single neighbouring cells adopt either high oscillatory HES5 or stable low HES5 in an alternating spatial pattern that does not evolve over time (Fig 5G, *Alternating high–low*, Movie EV2 first panel). Meanwhile at mid-level coupling, the multiscale model induces globally synchronised oscillations in all cells (Fig 5G, *Global in phase* and Movie EV2 second panel). At weak coupling strength, the spatial patterns show areas of local synchronisation emerging between neighbouring cells (Fig 5G, *Local in phase* and Movie EV2 third panel) resembling activity observed in tracked single-cell pairs in experimental data (Fig 3 K). Under no coupling conditions, we observed autonomous non-synchronised stochastic oscillations and fluctuations across the tissue (Fig 5H and Movie EV2 fourth panel). These observed changes in synchronisation are indicated by population KOP values (Fig 5G), and we further confirmed that the KOPs correspond to changes in synchrony in terms of single-cell expression dynamics between neighbouring cells (Fig 5I). As expected, in the uncoupled cells we observed no synchrony (KOP≈0) and activity in neighbouring cells was un-coordinated over time (Fig 5H and J). Therefore, the model can recapitulate the local in-phase behaviour in Venus::HES5 observed between single-cell pairs in a microcluster.

Our explorations of synthetic data show that at weak coupling strength microclusters consisting of in-phase cells can be generated in the model with a diameter of 2–6 cells (Appendix Fig S5B and Materials and Methods), consistent with cluster size in spinal cord tissue. However, the occurrence rate of microclusters was low, as these were observed around 20–30% of the time, although still higher than in the uncoupled situation (Appendix Figs S5C and S6A). Thus, weak coupling conditions generate microclusters by promoting in-phase activity between neighbouring cells; however, these appear transiently and with low probability. In addition, the microclusters of locally synchronised cells were not spatially periodic (Appendix Figs S5D and S6B). As expected, at high coupling (low repression threshold) we detected an alternating pattern of

HES5 with a spatial periodicity of two cells, which is a characteristic of the classic lateral inhibition alternating high–low pattern (Appendix Figs S5D and S6B).

In conclusion, our multicellular coupled model shows that spinal cord progenitors can locally synchronise at weak coupling strength to generate microclusters of 2–6 cells in diameter, a similar size to those seen in tissue, (Figs 1D and EV1D) with single-cell Venus::HES5 expression dynamics consistent with previous reports (Manning *et al*, 2019). However, the model cannot recapitulate the repeated spatial coordination and continuous presence of dynamic microclusters, suggesting that additional mechanisms may act in the tissue environment to stabilise their presence and promote spatially periodic emergence.

The model predicts that probability of differentiation is regulated by the coupling strength between cells

To understand how the spatial pattern of HES5 and dynamic micro-patterns in particular may affect properties of neurogenesis, we made the assumption that when HES5 is low, there is increased probability that the cell would differentiate consistent with findings that differentiation is accompanied by switching off of HES5, a repressor of neurogenesis (Bansod *et al*, 2017; Sagner *et al*, 2018; Manning *et al*, 2019). We introduced a “differentiation threshold”, which was set at the level of the HES5 population mean for each simulation (Fig 5I, *Population Mean*) and we reasoned that if expression level in a cell dropped below this threshold there was an increasing probability to switch off HES5 and differentiate (Fig 6A). We found that at high coupling strength (*Alternating high–low* conditions) the probability to differentiate is the highest, whereas medium and weak coupling strength (corresponding to *Global* and *Local in phase* synchronisation, respectively) had progressively lower probability of differentiation (Fig 6B).

To understand why this is happening, we looked at the Coefficient of Variation (CoV, Fig 6C), a measure of variability denoting standard deviation over the mean. We investigated both the temporal (Temporal CoV) and spatial variation (Spatial CoV) in simulated HES5 expression. Indeed, both temporal (indicative of single-cell amplitude) and spatial CoV (indicative of variation between HES5 high and low regions in space) appear highest in *Alternating high–low* conditions and lowest for *Local in phase* micro-patterns (Fig 6 C). However, we found that changes in spatial CoV correlated better with changes in rate of differentiation, especially at low repression threshold/high coupling strength (Fig 6C vs B *Alternating high–low*). Thus, our model predicts that the strength of cell:cell coupling may increase the probability of differentiation through amplifying cell:cell differences in abundance which in turn affects how far the cells dip below the threshold of differentiation.

In tissue, HES5 spatial pattern varies predictably with the rate of differentiation

To test the computational prediction that the spatial pattern of HES5 (determined by the coupling strength) regulates the probability of differentiation, we compared the pattern in motorneuron and interneuron progenitor domains. We chose this comparison because at E10.5 the motorneuron domain is known to have a higher differentiation rate than the interneuron domain (Kicheva *et al*, 2014);

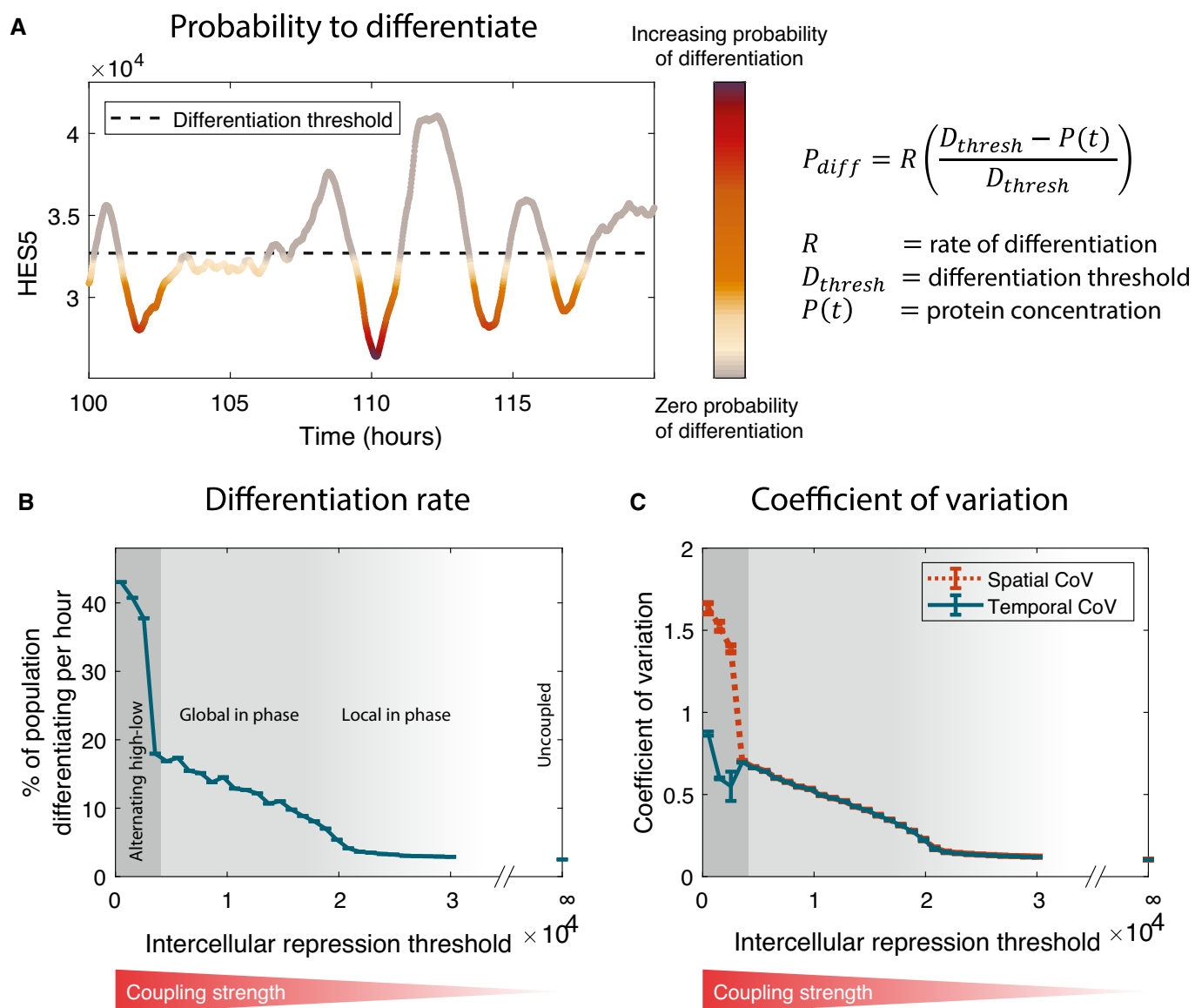


Figure 6. Cell-cell coupling strength can regulate probability of differentiation in a multicellular environment.

A Representative synthetic timeseries example and mathematical description of probability of differentiation (P_{diff}) in relation to population mean HES5 protein levels (referred to as “differentiation threshold”, D_{thresh}) whereby HES5 protein abundance ($P(t)$) dropping below the threshold increases the rate at which cells differentiate.

B Differentiation rates estimated from the multicellular coupled model (detailed in Fig 5) over a wide range of repression threshold values corresponding to decreasing coupling strength; three dynamic regimes are labelled as *Alternating high-low*, *Global in phase* and *Local in phase* mirroring examples shown in Fig 5G and I.

C Analysis of temporal CoV and spatial CoV from synthetic data corresponding to differentiation rates shown in (B); these statistics indicate that spatial variability correlates better with differentiation rates meanwhile temporal variability shows only a moderate quasi-linear increase in *Alternating high-low* conditions compared with the rest.

Data information: Single-cell parameters used to generate (B) and (C) are shown in Appendix Table S4 Main, and the multicellular parameters used in (B) and (C) were $n_{ND} = 4$, $\tau_{ND} = 150$ min. Each value plotted in (B) and (C) shows the mean and SD from 10 simulations at each repression threshold value. Source data are available online for this figure.

therefore, one would expect a different HES5 spatial pattern. We stained for the motorneuron progenitor marker OLIG2 (Figs 7A and EV4B and C) and analysed expression levels of Venus::HES5 and Neurogenin 2 (NGN2) in the two domains. The motorneuron domain had lower HES5 levels and higher NGN2 levels than the interneuron domain (Fig 7B) consistent with the opposing activity of these genes on cell differentiation (Imayoshi & Kageyama, 2014).

We then used nuclear segmentation and pseudo-color analysis of mean Venus::HES5 intensity per nucleus (Fig 7C) and found that the interneuron domain shows the presence of microclusters mainly consisting of 2–3 cells wide in the dorsal to ventral axis whereas in the motoneuron domain high Venus::HES5 cells were mainly found as single cells, alternating with cells expressing lower Venus::HES5 (Fig 7D). We validated this finding further by investigating spatial

periodicity by domain in live tissue slices. The domain border between motorneuron and interneuron progenitors was 35 μm ventral to the peak of HES5 expression (Fig EV4D) allowing us to correctly identify the two domains without the need for an OLIG2 reporter in the same tissue. We found that spatial periodicity was reduced in the motorneuron compared with the interneuron domain when analysed using both peak to peak distance in auto-correlation (Fig 7E, MN mean 31 μm vs IN mean 41 μm and Fig EV4E and F) and dominant spatial period by Lomb-Scargle periodogram (Fig EV4G, MN mean 25 μm vs IN mean 40 μm). Thus, both nuclear segmentation analysis and spatial periodicity indicated that, in the interneuron domain, microclusters of cells are found in a spatially periodic pattern repeated every four cells. Meanwhile, the motorneuron domain shows alternating high and low HES5 levels between neighbouring cells and a significant reduction in spatial periodicity, both of which are pointing to the motorneuron domain more closely resembling *Alternating high–low* conditions.

The model predicts that the coupling strength regulates the type of spatial micro-patterning hence, we hypothesised that the interneuron and motorneuron domains have different coupling strength. The model indicates that weak coupling, likely to be characteristic of the interneuron domain, would generate smaller cell–cell concentration differences compared with strong coupling (Appendix Fig S7A). This is because weakly coupled cells have less ability to repress the transcription of their neighbours and so are more similar in levels. This relationship should persist even after correcting for mean level in each condition. We have previously used fluorescence correlation spectroscopy (FCS) to generate a spatial map of nuclear Venus::HES5 concentration in the E10.5 spinal cord (Manning et al, 2019). Using this data, we calculated the difference in Venus::HES5 concentration between neighbouring cell pairs relative to the mean by domain and indeed found that it is lower in the interneuron domain compared with the motorneuron domain (Fig 7F). The correction by mean was important as variability in expression is expected to scale with the mean. This finding was confirmed by measuring the spatial amplitude of Venus::HES5, which was also higher in the motorneuron domain (Fig EV4H). These findings are consistent with the notion that the coupling strength in the IN domain is lower than in MN one. Taken together, these results show that interneuron progenitors are more likely to

be found in a locally synchronised state through weak coupling which correlates with a lower rate of differentiation. By comparison, progenitors in the motorneuron domain are mostly found in alternating high–low pattern and show a higher rate of differentiation, as predicted computationally by a higher coupling strength.

NGN2 expression is spatially periodic and coordinates with the HES5 pattern

Given that the spatial pattern of HES5 is relevant to the rate of neurogenesis, we investigated the wider applicability of our findings by characterising the spatial patterns of other genes in the Notch–Delta gene network. Chromogenic *in situ* hybridisation of *Dll1* and *Jag1* mRNA shows that *Dll1* has a broad expression domain that covers the motor neuron domain and the ventral-most part of the interneuron domain (Fig EV5A) (Marklund et al, 2010). Alternate stripes of *Jag1* and *Dll1* are observed in the intermediate spinal cord, which covers the remaining part of the interneuron domain (Fig EV5A) (Marklund et al, 2010). We performed smiFISH for *Dll1* to get a high-resolution understanding of *Dll1* expression pattern in the interneuron domain where HES5 is expressed in microclusters. We found that *Dll1* expression is non-uniform and appeared in micro-stripes of a few cells (Fig EV5B and C, Materials and Methods, Appendix Table S5), suggesting that other genes show similarities in local spatial patterning.

We next analysed the spatial expression pattern of the proneural factor NGN2. Using both NGN2 antibody staining and a NGN2::mScarlet fusion reporter mouse (Appendix Fig S8A–C and Materials and Methods), we found that NGN2 also has a spatially periodic expression pattern, with around half the spatial period of Venus::HES5 (Fig 8A–C). The spatial period of NGN2 is smaller in the motorneuron domain with a mean period of 21 μm supporting the conclusion that NGN2 spatial expression patterns are different between motorneuron and interneuron domains (Fig 8D). To understand how the NGN2 and Venus::HES5 periodic patterns map on to each other, we used the cross-correlation function of the NGN2 and Venus::HES5 spatial profile from the same tissue (Fig 8E and F). The cross-correlation analysis showed the presence of multiple peaks indicating coordination between the two signals that was not reflected in the brightfield control (Fig 8F). As expected for signals

Figure 7. Type of HES5 spatial pattern and coupling strength correlates with rate of differentiation in motorneuron and ventral interneuron domains.

- A Transverse cryosection of E10.5 Venus::HES5 spinal cord. Venus::HES5 endogenous signal, OLIG2—motorneuron progenitor marker, NGN2—early marker of neuronal commitment; scale bar 20 μm .
- B Relative nuclear intensities of Venus::HES5 and NGN2 in motorneuron and interneuron progenitors; bars show mean and SD of at least 494 cells per domain from five slices in two experiments; Kruskal–Wallis with Dunn's multiple comparison test adjusted *P*-values ***P* = 0.0032, ****P* < 0.001.
- C Pseudo-color look-up table applied to mean nuclear Venus::HES5 intensity within motorneuron (MN) and interneuron (IN) domains, corresponding to segmented image in (A).
- D Dimension of microclusters in DV axis for MN and IN domains; microclusters counted contained cells with high and similar levels of HES5 (Materials and Methods); bars show mean \pm SD; data consists of 34 microclusters measured from five sections and three independent experiments; 2-tailed Mann–Whitney test. *****P* < 0.0001.
- E Peak to peak distance in auto-correlation plots of detrended Venus::HES5 spatial profile in MN and IN domains; this is a measure of spatial period in Venus::HES5 profile along dorsal–ventral axis of spinal cord; grey data points represent mean peak to peak distance of at least three slices with left and right ventricle analysed separately in six experiments; black dots show median per experiment and line shows overall median; 2-tailed Mann–Whitney test *P*-values *****P* < 0.00001.
- F Cell–cell concentration differences in HES5 between neighbours, normalised to mean concentration of HES5 in that domain; grey data points represent normalised concentration difference between a pair of neighbours, bars shows mean and SD; two independent experiments; 2-tailed Mann–Whitney test with *P*-values ****P* = 0.003, *****P* < 0.00001.

Source data are available online for this figure.

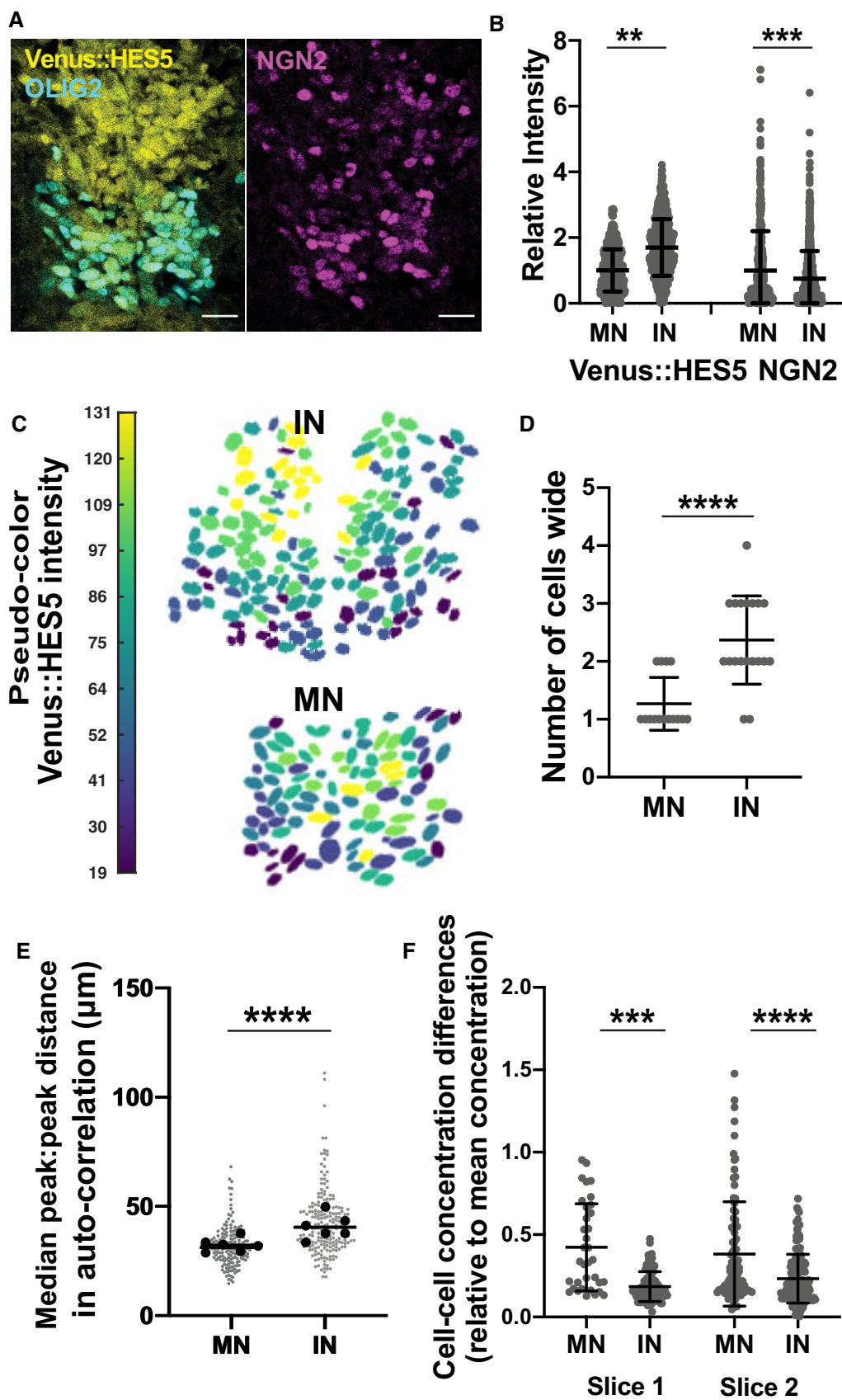


Figure 7.

of different periodicities, we observed primary peaks indicative of positively correlated activity (Fig 8F, red arrowheads) as well as secondary peaks indicative of negatively correlated activity (Fig 8F, black arrowheads). The cross-correlation is also indicative of whether peaks of activity are present in the same area. To ascertain this, we measured phase shift as the absolute lag corresponding to the primary cross-correlation peak closest to lag 0. In Fig 8F, such a peak falls close to lag 0 thus indicating that NGN2 and Venus::HES5 patterns coordinate in the same region. Thus, we concluded that NGN2 shows a spatial periodic pattern of half the period of Venus::HES5 resulting in half of the NGN2 high cells occurring in HES5 high microclusters and half in HES5 low.

Furthermore when we performed phase shift analysis in multiple cross-correlation examples (Materials and Methods), the shift was minimal and consistently less than a single-cell width (Fig 8G). This strongly pointed to coordination not only in the same region but also in the same cells. We subsequently investigated this by using single nuclear segmentation of high-resolution images to visualise the NGN2-HES5 spatial relationship. Indeed, we found that within a HES5 microcluster in the interneuron domain, only 1–2 cells (and in the MN domain only one cell per cluster) show high NGN2 expression levels (Fig 8H). As high NGN2 is an early marker of differentiation, this suggests that similar to the mathematical model (Appendix Fig S7B and C) cells in a cluster do not differentiate in unison; instead, microclusters may act to select a cell for differentiation, hence regulating spatial and temporal aspects of neurogenesis.

Discussion

In this paper, we have addressed how cells coordinate their decisions with that of their neighbours so that neurogenesis takes place at a pace appropriate for the anatomical location. We have investigated the fine-grained pattern of neurogenesis in the spinal cord by

monitoring the spatiotemporal patterning of key progenitor TF HES5 using live imaging analysis that is optimised towards revealing coordinated tissue-level behaviour that would not otherwise be evident. In combination with computational modelling it enabled a multi-scale synthesis of the data with predictive power. We have uncovered an unexpected 3-tiered spatial and temporal organisation, which we discuss below in an ascending order of complexity.

First, within the ventral HES5 expression domain, which encompasses distinct MN and IN domains, we have discovered clusters of cells with positively correlated HES5 expression levels. These clusters, described for the first time here, are 2–3 cells wide in D-V and 3–4 cells wide in A-B axes, hence termed microclusters. To detect microclusters, we removed longer-range spatial trends such as overall gradients of intensity in HES5 expression (which have not been dealt with further here) allowing us to concentrate on local correlations of expression. By following Venus::HES5 in pairs of single cells in proximity, we find that microclusters are a composite of positive correlations in slow-varying mean levels of Venus::HES5 and locally synchronised (in-phase) ultradian HES5 dynamics. This type of composite spectral activity or nested oscillations have been previously described in circadian rhythms containing an ultradian periodicity as well as neuronal firing patterns (Lopes-Dos-Santos *et al*, 2018; Wu *et al*, 2018). We propose that the local synchronisation in ultradian HES5 dynamics comes from coupling through Notch–Delta, although we cannot rule out the possibility that sister cells have synchronous HES5 expression after division. In the latter case, Notch–Delta coupling may act to re-inforce or help maintain local coordination over time. We also found that the microcluster organisation extends to DLL1 although we have not been able to study it with live imaging in this work. The clustering organisation was surprising because previous studies have suggested that in neurogenesis oscillators are in anti-phase in neighbouring cells (Kageyama *et al*, 2008; Shimojo & Kageyama, 2016; Shimojo *et al*, 2016). DLL1 oscillations were observed with live imaging in tissue but only a

Figure 8. NGN2 expression is spatially periodic and positively correlates with the HES5 pattern.

- A Detrended spatial profile of NGN2::mScarlet-I intensity from transverse slice of E10.5 spinal cord from heterozygous knock-in mouse in ventral–dorsal direction; red indicates motorneuron (MN) domain, blue interneuron domain (IN).
- B Auto-correlation analysis of detrended NGN2::mScarlet-I intensity spatial profiles from motorneuron and interneuron domains; multiple peaks indicating spatial periodicity; significant peaks (red triangle) lie outside black dotted lines indicating 95% significance based on bootstrap approach (see Materials and Methods) and non-significant peaks (black triangle).
- C Ratio of NGN2:HES5 spatial period in the same tissue; grey dots show ratio for single image from four experiments; line shows overall median and error bars 95% confidence limits.
- D Peak to peak distance in auto-correlation plots of detrended NGN2::mScarlet-I spatial profile in motorneuron (MN) and interneuron (IN) domains as a measure of spatial period in NGN2 expression along dorsal-ventral axis of spinal cord; Grey data points represent mean peak to peak distance in a single slice, $n = 33$, left and right ventricle analysed separately in four experiments; black line shows overall mean, error bars show SD; 2-tailed Mann–Whitney test with exact P -value *** $P = 0.0003$.
- E Detrended spatial profile of Venus::HES5 (black) and NGN2::mScarlet-I (red) intensity from the same transverse slice of E10.5 spinal cord in ventral–dorsal direction.
- F Example cross-correlation function of Venus::HES5 with NGN2::mScarlet-I (thick black), Venus::HES5 with brightfield signal (black), and NGN2::mScarlet-I with brightfield signal (red) from the same transverse slice of E10.5 spinal cord; markers indicate the presence of two types of coordination namely in-phase (red arrowhead) and out-of-phase (black arrowhead).
- G Phase shift showing absolute lag distance corresponding to in-phase peak in Venus::HES5 vs NGN2::mScarlet-I cross-correlation function of spatial intensity profiles from the same slice. 34 individual data points from six slices, two experiments; red line indicates average inter-nuclear distance in D-V; bars show mean \pm SD; 2-tailed Mann–Whitney test not significant, $P = 0.32$.
- H Pseudo-color look-up tables applied to mean nuclear Venus::HES5 and NGN2 staining intensity in motorneuron (MN) and interneuron (IN) domains. Venus::HES5 microcluster and single NGN2 high cell (red arrow) in IN domain; Alternating high–low expression of Venus::HES5 in MN, red arrows show high cells.
- I Graphical summary: Through a combination of experimental and computational work we characterised the HES5 dynamic expression in the mouse E10.5 ventral spinal cord. We found evidence that progenitors located in two domains (motorneuron, MN and interneuron, IN) give rise to distinct spatiotemporal characteristics that are indicative of differences in coupling strength and can explain increased differentiation rates observed in MN.

Source data are available online for this figure.

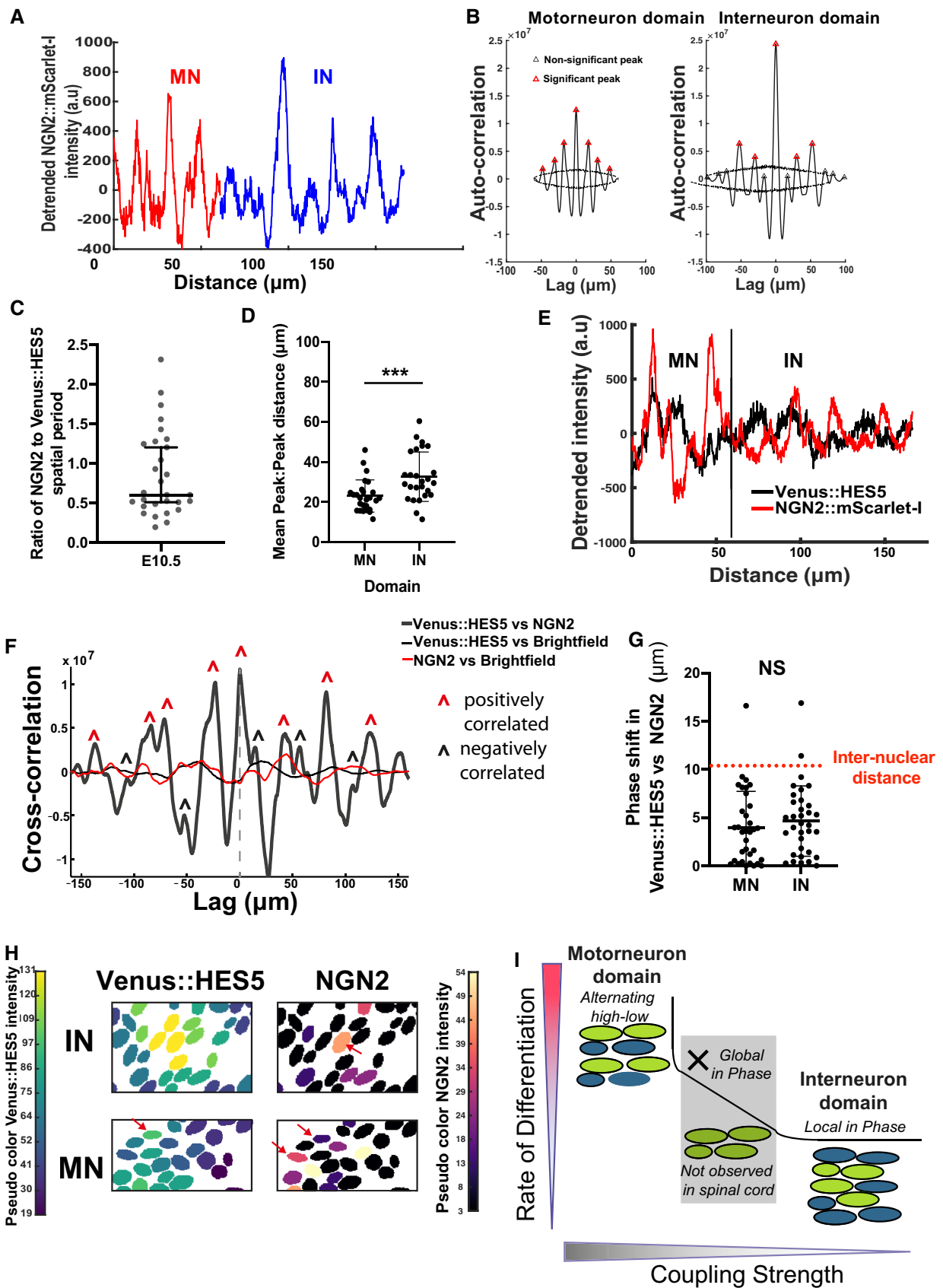


Figure 8.

single example shown for anti-phase oscillations. Thus, the discrepancy could be down to a difference in scale of analysis or perhaps to the different molecules studied. Interestingly single-cell resolution snapshot data from chick embryos appears to be consistent with the presence of microclusters (Baek *et al*, 2018).

Second, we have found that HES5 microclusters are arrayed in a spatially periodic pattern along the D-V axis of the ventral HES5 domain, meaning that high and low HES5 expression clusters alternate regularly in space. We also found that NGN2 is expressed periodically along the D-V axis with half the periodicity of HES5 such that NGN2 high cells are found both within HES5 high and low microclusters. SmiFISH showed *Dll1* expressed in microstripes but the images of single *Dll1* mRNA molecules were not amenable to auto-correlation; thus, it is not known whether they occur on the same spatial scale as HES5. Multiple stripes of *Dll1* and *Jag1* and *Lfng* have been observed, but at the larger progenitor domain scale (Marklund *et al*, 2010; Ramos *et al*, 2010). Such spatial periodicity at a fine level within the ventral HES5 domain contrasts with the large-scale organisation of HES5 in 2 separate broad domains along the D-V axis (Sagner *et al*, 2018).

Thirdly, the HES5 spatial pattern of microclusters was not static but appeared dynamic over time; High HES5 expressing microclusters persisted for 6–8 h and then switched to low expression, while low expressing microclusters showed the opposite behaviour. In other words, high and low expressing microclusters alternated and sometimes created phase waves that travelled through the tissue over time. These waves are somewhat reminiscent of phase waves of LFNG and AXIN2 expression that are observed in somitogenesis (Tsiairis & Aulehla, 2016; Sonnen *et al*, 2018; Baron & Galla, 2019); however, in the spinal cord such phase waves were incoherent. This analysis was performed with a static ROI and it is possible that random movement of nuclei out of the ROI somewhat complicates the analysis of dynamic switching between high and low microcluster states. However, it is unlikely that such random behaviour could generate any of the reproducible phenomena we report in the paper. This complex spatial and temporal dynamic pattern of HES5 in spinal cord generated two important questions: how might it be generated and what might it mean for neurogenesis? Knowing that Hes genes and HES5 in particular, are activated by Notch signalling, we treated *ex vivo* spinal cord tissue with DBZ to disrupt Notch signalling (Falo-Sanjuan & Bray, 2020). We observed that the Notch inhibitor treatment extinguished spatial periodicity gradually and slowly, over a period of 10–12 h, concurrent with HES5 level down-regulation. This is consistent with the amplitude death that we observed in single-cell data under the same treatment (Manning *et al*, 2019). The effect of Notch inhibition was far more pronounced in the temporal nature of the pattern; in the absence of Notch signalling, the HES5 spatially periodic pattern of low and high expressing microclusters became “frozen” in time. These findings suggest that Notch signalling plays a part in making the pattern dynamic over time but cannot account for the entire spatiotemporal complexity of HES5 expression that we see *ex vivo*.

Computational modelling helped us to explore further the role of Notch in generating the spatiotemporal pattern of HES5 expression. We have used a simplified multiscale stochastic model of HES5 self-repression and inter-cellular coupling with delay, parameterised on our own experimental data, namely the single-cell HES5 temporal period and extent of HES5 expression synchronicity between cells

using the KOP. With this model, we were able to explore the influence of the coupling strength between cells in producing spatiotemporal HES5 expression patterns. We found multiple spatiotemporal patterns, namely; an alternating high and low pattern (at high coupling strength), global tissue synchronisation (at mid coupling strength) and un-coordinated pattern (at no coupling), see Movie EV2. Importantly, at weak coupling strength and inter-cellular time delay that is consistent with previous reports, we observed the emergence of dynamic microclusters that matched our experimental observations. The emergence of dynamic patterns that do not resolve into steady HES “on” or “off” static patterns has been previously observed in a stochastic multicellular tissue model combining Notch–Delta and Hes auto-repression but not confirmed in tissue (Tiedemann *et al*, 2017). However, the dynamic microclusters in our model occurred infrequently (with a probability of 20–30%) even though the model takes into consideration stochasticity and time delays; two features that represent the tissue context well. The low frequency of clusters did not improve after detailed optimised exploration of parameter space, which led us to conclude that a Notch-based cell-to-cell signalling with the assumptions we have made, recapitulates only part of the observed pattern *in vivo*. Extension of the model to include (i) longer-range cell–cell interaction via cytonemes, or due to the elongated shape of the progenitor cells, and (ii) increased complexity of the gene network such as cis inhibition between Delta–Notch or differences in signalling between different Notch ligands, may be able to increase the fidelity of microcluster emergence. Indeed, it has been shown that such modifications increase the range of spatial patterns that can be obtained (De Jossineau *et al*, 2003; Cohen *et al*, 2010; Sprinzak *et al*, 2010; Petrovic *et al*, 2014; Boaretto *et al*, 2015; Hadjivasiliou *et al*, 2019). Other ways in which the model can be extended is to incorporate the influence of morphogen signalling gradients along the D-V axis or differentiation gradients along the A-B axis, as these are known to exist in the tissue.

Nevertheless, the computational model we developed, allowed us to explore the advantages that organisation in dynamic microclusters may offer as a developmental strategy for neurogenesis in the embryonic spinal cord. Overall, we found that the spatiotemporal HES5 pattern was affected by the coupling strength between cells and in turn, affected the rate of differentiation. Based on our findings, we propose that a classic lateral inhibition alternating high–low HES5 pattern (achieved at high coupling strength) shows the highest rate of differentiation because it generates two HES5 states (“on” and “off”) in a spatially alternating pattern and this is likely to result in tipping of more cells towards differentiation. Global synchronisation (medium coupling strength) shows a medium rate of differentiation; however, this regime is not observed in spinal cord data perhaps because the synchronous differentiation in “blocks” of cells found close by in tissue, although an appropriate developmental strategy for somitogenesis, may be incompatible with the structural integrity of the neural tissue or the finer diversification of neuronal fates within each domain. The un-coordinated pattern (no coupling between cells) has similar rates of differentiation as weak coupling; however, weak coupling strength is advantageous because it allows local in phase synchronisation, which by analogy to global synchronisation (Fig 6C, *Global vs Local in phase*), appears to transiently increase the amplitude of temporal oscillations in HES5 expression (Fig 5I, *panel 3-Local in phase*). This is

important because a transient amplitude increase (due to the presence of microclusters at *Local in phase* conditions) could facilitate the progression to differentiation. Indeed, we have previously shown that HES5 oscillations in proliferating spinal cord progenitors have low amplitude and show mainly aperiodic fluctuations (noisy dynamics) but the propensity to oscillate as well as the peak-to-trough amplitude increases as cells enter the differentiation pathway (Manning *et al.*, 2019). We have also shown that when the transition from noisy dynamic expression to oscillatory expression does not take place, progenitor cells are unable to downregulate HES levels and differentiate (Soto *et al.*, 2020). We speculate that microclusters may act to reliably select one or two cells that go on to express NGN2 and differentiate and that the spatial periodicity of microclusters may space out differentiating cells to maintain tissue organisation.

We tested the model hypothesis that by changing the HES5 spatiotemporal pattern through tuning the coupling strength, the tissue is able to fine tune the rate of neurogenesis. We compared the motorneuron and interneuron progenitor domains as these two neighbouring domains in the D-V axis are known to have different rates of differentiation (Kicheva *et al.*, 2014; Kuzmicz-Kowalska & Kicheva, 2020). Indeed, we find that that in the MN domain where the rate of differentiation is highest at E10.5, the HES5 and NGN2 pattern most closely matches the alternating high–low pattern (Fig 8 I, MN). In the ventral interneuron domain, we propose that the local in phase synchronisation pattern (predicted to occur at weak coupling strength) is the closest match to the *ex vivo* situation (Fig 8 I, IN). We propose it represents a strategy to balance prolonged neurogenesis, with a reasonable rate of differentiation and a transient increase in oscillation amplitude that is suitable for decoding by downstream genes. There may be additional molecular differences between the motorneuron and interneuron domains that regulate the rate of differentiation. Indeed, the transcription factor OLIG2 is expressed in the motorneuron domain and has been shown to promote differentiation by directly inhibiting HES5 (Sagner *et al.*, 2018). We speculate that this mechanism could interplay or directly affect the cell–cell coupling strength by changing HES5 levels or binding partners.

In conclusion, our findings show HES5 spatially periodic micro-patterns exist in the developing spinal cord, they underlie the rate of neurogenesis and are an emergent property of the multiscale synthesis of dynamical gene expression and Notch coupling. The characterisation of this temporally dynamic expression is a testament to the power of live tissue imaging in providing mechanistic insights of complex phenomena as they unfold in real time.

Materials and Methods

Animals

Animal experiments were performed by personal licence holders under UK Home Office project licence PPL70/8858 and within the conditions of the Animal (Scientific Procedures) Act 1986. Venus::HES5 knock-in mice (ICR. Cg-Hes5<tml(venus)Imayo>) were obtained from Riken Biological Resource Centre, Japan and maintained as a homozygous line. In these mice, the mVenus fluorescent protein is fused to the N terminus of endogenous HES5. Sox1Cre:

ERT2 mice (Sox1tm3(cre/ERT2)Vep) were obtained from James Briscoe with the permission of Robin Lovell-Badge. R26R-H2B::mCherry mice were obtained as frozen embryos from Riken Centre for Life Science Technologies, Japan and C57Bl6 mice were used as surrogates. NGN2::mScarlet-I mouse was generated by the University of Manchester Genome Editing Unit (see Appendix Supplementary Methods 1 and Appendix Fig S8). The mScarlet-I fluorescent protein is fused to the C terminus of endogenous NGN2.

Embryo slicing and live imaging

E0.5 was considered as midday on the day a plug was detected. For matings with R26R-H2B::mCherry Sox1Cre:ERT2, intra-peritoneal injection of pregnant females with 2.5 mg Tamoxifen (Sigma) was performed 18 h prior to embryo dissection. This enables single-cell tracking through mosaic labelling of nuclei with H2B::mCherry. Whole embryos were screened for H2B::mCherry expression using Fluor 10×/0.5 objective on a Zeiss LSM880 confocal microscope. After decapitation, embryo bodies were embedded in 4% low-gelling temperature agarose (Sigma) containing 5 mg/ml glucose (Sigma). 200 µm transverse slices of the trunk containing the spinal cord around the forelimb region were obtained with the Leica VT1000S vibratome and released from the agarose. Embryo and slice manipulation were performed in phenol-red free L-15 media (Thermo Fisher Scientific) on ice and the vibratome slicing was performed in chilled 1×PBS (Thermo Fisher Scientific).

For snapshot imaging of live E10.5 spinal cord, slices were stained with 50 µM Draq5 (Abcam—ab108410) in 1×PBS (Thermo Fisher Scientific) for 1.5 h on ice if required and then placed directly on to a 35 mm glass-bottomed dish (Greiner BioOne). Images were acquired with a Zeiss LSM880 microscope and C-Apochromat 40× 1.2 NA water objective. E10.5 spinal cord slices for live timelapse microscopy were placed on a 12 mm Millicell cell culture insert (MerckMillipore) in a 35 mm glass-bottomed dish (Greiner BioOne) incubated at 37°C and 5% CO₂. The legs of the cell culture insert were sanded down to decrease the distance from the glass to the tissue. 1.5 ml of DMEM F-12 (Thermo Fisher Scientific) media containing 4.5 mg/ml glucose, 1× MEM non-essential amino acids (Thermo Fisher Scientific), 120 µg/ml Bovine Album Fraction V (Thermo Fisher Scientific), 55 µM 2-mercaptoethanol, 1× GlutaMAX (Thermo Fisher Scientific), 0.5× B27 and 0.5× N2 was added. Movies were acquired using Zeiss LSM880 microscope and GaAsP detectors. A Plan-Apochromat 20× 0.8 NA objective with a pinhole of 5AU was used. 10 z-sections with 7.5 µm interval were acquired every 15 min for 18–24 h. DMSO (Sigma) or 2 µM DBZ (Tocris) was added to media immediately before imaging.

Single-cell tracking over time

Single neural progenitor cells in E10.5 spinal cord slices were tracked in Imaris on the H2B::mCherry channel using the “Spots” function with background subtraction and the Brownian motion algorithm. Tracking on the H2B::mCherry signal ensured no bias in the levels of Venus::HES5 in tracked cells. All tracks were manually curated to ensure accurate single-cell tracking. Background fluorescence was measured via an ROI drawn on a non-Venus::HES5 expressing region on the tissue and subtracted from spot intensity. To account for any photobleaching and allow comparison of

intensities between movies, the mean intensity of mCherry and Venus in each spot was normalised to the mean intensity of mCherry or Venus in the whole tissue. The whole tissue volume was tracked using the “Surfaces” and “Track over time” function.

Immunofluorescent staining

Trunks of E10.5 embryos for cryosectioning were fixed in 4% PFA for 1 h at 4°C, followed by three quick washes with 1×PBS and 1 longer wash for 1 h at 4°C. Embryos were equilibrated overnight in 30% sucrose (Sigma) at 4°C before mounting in Tissue-Tek OCT (Sakura) in cryomoulds and freezing at −80°C. 12 µm sections were cut on Leica CM3050S cryostat. E10.5 spinal cord slices cultured on Millicell inserts were fixed in 4% PFA for 4 h. For staining, tissue and sections were washed in PBS followed by permeabilisation in PBS 0.2% Triton X-100 (Sigma) and blocking with PBS 0.05% Tween20 (Sigma) + 5% BSA (Sigma). Primary and secondary antibodies were diluted in PBS 0.05% Tween20 + 5% BSA. Tissue was incubated with primary antibodies overnight at 4°C, then washed three times for 5–10 min in PBS 0.05% Tween20, incubated with secondary antibodies and DAPI (Sigma) for 6 h at room temperature, and washed again three times in PBS-T. Sections were mounted using mowiol 4–88 (Sigma). Primary antibodies used were rabbit anti-SOX2 (ab97959, 1:200), rabbit anti-OLIG2 (EMD Millipore AB9610, 1:200) and goat anti-NGN2 (Santa Cruz Biotechnology sc-19233, 1:200).

smiFISH probe design and synthesis

The smiFISH probes were designed using the probe design tool at <http://www.biosearchtech.com/stellarisdesigner/>. Depending on the GC content of the input sequence, the software can return varied size of probes, 18 and 22 nt, hence giving the largest number of probes at the maximum masking level. It also uses genome information for the given organism to avoid probes with potential off-target binding sites. Using the respective gene mature mRNA sequence, we designed 36 probes for Hes5 and 48 probes for Dll1 (Appendix Table S5) and added a FLAP sequence (5'-CCTCCTAAGTTTCGAGCTGGACTCAGTG-3') to the 5' of each gene-specific sequence (IDT). The designed set of probes were labelled with Quasar 670 (Biosearch Technologies) for Hes5 and CalFluor 610 (Biosearch Technologies) for Dll1 following the protocol from Marra *et al.*, 2019.

smiFISH on mouse sections

smiFISH protocol for mouse section embryos was developed by adapting smiFISH protocol from (Marra *et al.*, 2019) and (Lyubimova *et al.*, 2013). 50-µm-thick sections of E10.5 spinal cord were collected and transferred onto superfrost glass slides (VWR 631-0448) and kept at −80°C. Sections were left at room temperature to dry for 5–10 min and then fixed in 4% formaldehyde in 1× PBS followed by two quick washes in 1×PBS. 1:2,000 dilution of proteinase K (20 mg/ml stock) in 1× PBS was pipetted onto each slide and left for 5–10 min followed by two washes in 2× SSC. Sections were then incubated at 37°C twice in wash buffer (5 ml of 20× SSC, 5 ml of formamide and 45 ml of deionised, nuclease-free water). 250 µl of hybridisation buffer (1 g dextran sulphate, 1 ml 20× SSC, 1 ml deionised formamide, 7.5 ml nuclease-free water) with 100–240 nM the

fluorescent smiFISH probes was pipetted onto each slide and incubated overnight at 37°C in a humid container shielded from light. Samples were then washed as follows: twice in wash buffer at 37°C for 3 min, twice in wash buffer at 37°C for 30 min and one wash in 1× PBS at room temperature for 5 min. After smiFISH staining, sections were washed for 2 min in PBS and mounted using Prolong Diamond Antifade Mountant with DAPI (Thermo Fisher P36962).

smiFISH microscopy and deconvolution

smiFISH images were collected with Leica TCS SP8-inverted confocal microscope using objective HC PL APO CS2 40×/1.30 oil. We acquired three-dimensional stacks 2,048 × 1,024 pixels and z size 0.4 µm. The voxel size was 0.19 × 0.19 × 0.4 µm. Quasar 670 and CalFluor 610 were imaged with pinhole 1 Airy Unit. Channels were sequentially imaged. Deconvolution of confocal images was performed using Huygens Professional Software. As pre-processing steps, the images were adjusted for the “microscopic parameters” and for additional restoration such as “object stabiliser”; the latter was used to adjust for any drift during imaging. Following, we used the deconvolution Wizard tool, the two main factors to adjust during deconvolution were the background values and the signal-to-noise ratio. Background was manually measured for every image and channel, while the optimal signal-to-noise ratio identified for the images was value 3. After deconvolution, the images were generated with Imaris 9.3

Microcluster quantification

The number of cells in HES5 microclusters were automatically determined from images of Venus::HES5 spinal cord tissue stained with the live nuclear marker Draq5. First individual Draq5⁺ nuclei were manually segmented as ellipses using ImageJ, converted to a mask and subsequently eroded using the ImageJ function “erode” to ensure no overlap between nuclei. The mask was applied to the Venus::HES5 channel generating images of nuclei with the raw Venus::HES5 intensities. Next, these segmented images were imported into MATLAB and analysed using custom scripts (available on GitHub see “Data availability”) with the following steps. (i) Dead cells were excluded by removing nuclei with outlying high Draq5 intensity (>top 4% of intensity per slice) indicative of increased membrane permeability and condensed chromatin. (ii) Mean Venus::HES5 intensity was calculated per segmented nuclei. (iii) Intensity distributions of mean Venus::HES5 nuclei intensity were quantile normalised between experiments using the “quantilenorm” function in MATLAB. This ensured that the intensity in each experiment was adjusted to the same range and thus allowing consistent colormapping. (iv) Normalised mean Venus::HES5 intensities were displayed using the “viridis” (Venus::HES5) or “magma” (NGN2) colormap. The colormap was split in to six colour levels, such that nuclei within 80–120% intensity range of each other were given the same colour. This range was chosen because it matches the amplitude of Venus::HES5 ultradian oscillations (see Manning *et al.*, 2019). (v) Microclusters were segmented separately for the top two intensity bins. The automated clustering approach emulated manual clustering by grouping together cells with similar intensity into a microcluster. We defined a microcluster as a minimum of two cells with the binned intensity for which there is a direct path

between the centre of the nucleus that does not intersect cells of different binned intensities (interceding cells). In the automated approach, for a specific binned intensity level, the nuclei found within less than 2.5 of average inter-nuclear distance (d_{\max}) of each other were assigned to a microcluster. To achieve this, nuclear regions were dilated using the MATLAB routine `imdilate.m` with a disc structural element (generated using `strel.m`) of radius d_{\max} in every direction until they merged with neighbouring nuclei forming a microcluster region. Separation between microcluster regions bounded by interceding cells of different intensity values was maintained by subtracting top 1 and top 2 nuclear regions, respectively, using the `imsubtract.m` routine followed by detection of connected regions using `bwlabeln.m`. (vi) The number of cells within a cluster was counted by testing overlap between the microcluster mask and the nuclear regions corresponding to individual nuclei to produce a nucleus-to-microcluster labelling and this is reported in Fig EV1D. (vii) Diameters in DV and AB were computed as the maximum number of nuclei observed in the x- and y-axis per microcluster. 8. Inter-cluster distances between microclusters of the same intensity level were computed in the y-axis between two or more microclusters observed along the DV axis in the same image section; specifically, we used the microcluster regions detected in step 5 and computed the centre of mass per microcluster using the routine `regionprops.m` with option “Centroid”; we then sorted the centroids per slice based on distance in DV and computed the distance between successive centroids; in Fig EV2F, we report the centroid to centroid distance in DV divided by inter-nuclear distance per slice.

Microcluster detection in randomised segmented images

Using the automated microcluster detection method, we performed tests in control synthetic data (Fig EV1D). In Randomisation 1 (Rnd1), we randomly shuffled the existing intensities assigned to each nucleus, and in Randomisation 2 (Rnd2), we randomly sampled from a distribution of intensities with the same mean and standard deviation as the data. For each segmented image, we generated 20 Rnd1 and 20 Rnd2 synthetic images and performed automated counting as described in Microcluster quantification. As expected, randomised images showed doublets with only rare instances of values of three cells or above.

Correlation of nuclear Venus::HES5 intensity with distance and neighbours

The centroids of the manually segmented nuclei were used to measure distance, and hence, rank between neighbours and a correlation of the distance and mean nuclear Venus::HES5 intensity was calculated using the “corr” function in MATLAB. Mean nuclear Venus::HES5 intensity was also randomised between nuclei before undergoing the same distance vs mean intensity correlation; randomisations were repeated five times per image.

Centre of intensity detection and radial gradient removal

The centre of intensity (COI) was calculated using a centre of mass approach. The intensity of each nuclei was multiplied by their position. These were then summed and divided by the sum of all nuclear intensities. The COI was used to sort cells in to five equally

spaced radial zones with increasing distance from the COI. The mean Venus::HES5 intensity of nuclei in these zones was calculated and plotted against distance from the COI. For radial gradient removal, a polynomial of degree 3 was fitted to the mean zone intensity vs distance plot and the intensity subtracted from each nucleus in that zone to remove the radial gradient.

A simulated radial gradient from a single focal point in the image was generated using

$$I_r = Z + \alpha x_r,$$

where I_r is the new intensity of the cells, Z is simulated intensities with the mean and variance similar to that of real data, α is the gradient strength parameter and x_r is a function of the distance from the centre of intensity. As α increases, the radial gradient is less affected by random deviation in HES5 expression.

Quality controls and movie pre-processing

To remove the possibility that changes in cell positions lead to shifts in the kymograph stripes and artefacts in the dynamic analysis, movies underwent image registration to account for global tissue drift and were subject to strict quality controls for local tissue deformation. Image registration was performed in Imaris by tracking a static landmark of the tissue. Furthermore, to avoid artefacts due to local tissue deformation the average motility of tracked single cells over time in the D-V axis was compared with patterns/waves of Venus::HES5 intensity in the kymograph. A maximum threshold of 20 μm for the averaged single nuclear displacement was applied. 1 movie failed this threshold and was not used for analysis of microcluster persistence (see Appendix Table S2). Finally, bleach correction was performed using a ratiometric method in ImageJ.

Generation of spatial expression profiles and kymographs

Spatial expression profiles and kymographs were generated in Zen Blue (Carl Zeiss Microscopy) by drawing a spline 15 μm wide starting ventrally and extending parallel to the ventricle in the dorsal direction, then using the “Line profile” or “Kymograph” function. To understand how much movement individual nuclei undergo during imaging and to help choose the width (apico-basal) of kymographs, single nuclear displacements were measured. A total of 188 individually tracked cells were obtained from three experiments (Exp1 56 cells, Exp2 54 cells, Exp3 78 cells). Tracks were 12 h long with a sampling time of 15 min (total of 49 time points). A subset of these cells were selected such that only apically located cells were included (Exp1 16 cells, Exp2 22 cells, and Exp3 27 cells). For each cell track, positional data values that were 2.5 h apart were used to determine how far a cell moves in this time window. This resulted in 39 displacement values per track, all of which the absolute value was taken and averaged across all cell tracks to give an effective root mean square (RMS) value of 7.9 μm (inter-quartile range 10.9) in apical-basal direction (summarised by experiment in Appendix Table S3).

A 15 μm width was chosen as this was larger than both a cell width and the effective root mean square displacement in 2.5 h. 0 distance corresponded to the ventral-most end of the spline. Apical, medium and basal expression profiles and kymographs were

generated from splines around 10, 30 and 60 μm from the ventricle, respectively, and analysing each side of the ventricle separately. 2–3 non-overlapping z-sections were used to generate kymographs per movie. Expression profile data for Draq5 and NGN2 from single snapshot images of live slices were generated in ImageJ using a rectangular ROI of width 15 μm and the “Plot profile” function.

Detection and periodicity analysis of spatial expression patterns

Kymographs were analysed using custom scripts in MATLAB and averaged along the time axis in 2 h windows. Spatial Venus::HES5 intensity in the ventral–dorsal direction was detrended by fitting a polynomial (order 4–6) and subtracting this from the raw data. This removed the larger trend due to the profile of the HES5 expression domain.

Auto-correlation and Lomb-Scargle periodograms were used to analyse periodicity of the detrended spatial intensity plots. Lomb-Scargle periodograms were generated with the MATLAB “plomb” function and plotting power level thresholds as specified in figure legends. Auto-correlation was performed with the MATLAB “xcorr” function. Auto-correlation functions were smoothed using Savitzky–Golay filter and then peaks identified using the “find peaks” function. Significant peaks were identified using a bootstrap method with 100 randomisations. Auto-correlations were randomised and then re-subjected to auto-correlation. 2 standard deviations of the auto-correlations of randomised data were used as a threshold and peaks were designated as significant if they exceeded this threshold. The mean distance between significant peaks was calculated per kymograph timepoint. Fold changes of spatial intensities were calculated between significant peaks and troughs in the signal identified using “find peaks” on the negative signal.

Splitting Venus::HES5 kymographs in to motoneuron and interneuron domains was based on staining of cryosectioned E10.5 spinal cord with motoneuron progenitor domain marker OLIG2. The peak of the trend in Venus::HES5 was found to occur on average at 35 μm dorsally from the edge of the OLIG2⁺ domain. This criterion was used to split kymographs from movies of Venus::HES5 spinal cords that had not been immuno-stained.

Correlation coefficient analysis in the anterior to posterior (A-P) axis

We produced kymographs from multiple non-overlapping stacks extending in the AP direction using the same region of interest (ROI) which meant that Venus:HES5 intensity was comparable at the same position in DV. We used detrended Venus::HES5 averaged over 2 h per z and compared the detrended coefficients pairwise across subsequent z-stacks. Using the confocal magnification in the AP axis per experiment, we reconstructed the absolute distance between subsequent z-stacks. Data from untreated and tissue treated with DMSO were analysed in the same way.

Hierarchical clustering of local HES5 expression and microcluster persistence time

Kymographs of HES5 expression were split into adjacent 20 μm regions along the D-V axis and the HES5 intensity averaged in these regions to give a timeseries per region. To account for any single-

cell movement in DV, we applied a 2 μm Gaussian blur filter onto the kymograph data using the MATLAB routine *imgaussfilt.m* prior to extracting timeseries per region. These timeseries were normalised to the mean and standard deviation of each region over time (z-scoring) and subject to hierarchical clustering using the *clustergram.m* routine in MATLAB with Euclidean distance and average linkage. The persistence time was calculated as continuous time when the signal in the region was above (high) or below (low) its mean level. The persistence ratio was calculated as the time interval spent in a high state divided by the time interval spent in a low state within the same 20 μm region. Where only high or low persistence time intervals were detected in a region, these observations were excluded from the ratio. We also used an alternative method to compute persistence time relying on zero-crossing of the detrended Venus::HES5 signal averaged over 0 to 2 h timepoints; in this approach, we identified specific areas containing a microcluster with high expression (above the mean) and low expression (below the mean) and repeated the persistence time calculation as described above.

Phase mapping of kymograph Data

We used kymograph data (see Generation of spatial expression profiles and kymographs) to produce spatiotemporal phase mapping from Untreated tissue (Fig EV2L and Appendix Fig S3) as well as DMSO vs DBZ (Figs 4 and EV3). Firstly, kymograph data were averaged over 2 h to produce low temporal resolution information in the dorsal–ventral direction. The resulting spatial signal was detrended in the DV direction using a polynomial order 4 and smoothed using a Savitzky–Golay filter. Phase reconstructions were obtained from DV signal for every 2 h timeblock using the Hilbert transform, and these were presented as a colormap indicating time on the x-axis and space on the y-axis. We refer to this as phase mapping and it enables detection of phase resets (indicative of changes from high to low) in the same region over time.

Phase–phase mapping and phase shift analysis in cell pairs

We analysed Venus::HES5 ultradian dynamics using the approach in Manning et al, 2019, Phillips et al. 2017. Specifically, we used a Gaussian Processes pipeline to fit the single-cell trend of Venus::HES5 expression (examples shown in Appendix Fig S4C). We performed detrending of Venus::HES5, followed by z-scoring and estimated a periodic Ornstein–Uhlenbeck covariance model. This procedure produces a smooth detrended curve (examples shown in Appendix Fig S4C). Using the detrended smoothed curves, we extracted the phase shift using cross-correlation analysis of pairs of timeseries using the *xcorr.m* MATLAB routine. The phase shift corresponded to the lag time interval closest to 0 at which the cross-correlation function shows a peak. From detrended smooth curves, we then performed Hilbert reconstruction of instantaneous phase using the *hilbert.m* MATLAB routine. We used the phase angles corresponding to neighbouring cell pairs at multiple timepoints to produce a phase–phase mapping. We plotted the density of the phase map using the *dscatter.m* routine with 24 × 24 binning of phase values (Eilers & Goeman, 2004). This approach (Hilbert and dscatter) has been previously described in Sonnen et al, 2018. Cells pairs were identified based on the median 3-dimensional Euclidean

distance <20 μm across the whole timeseries. Hence, we also performed a phase–phase analysis using cross-pairing whereby cells in the same experiment were paired with cells found further than 20 μm away (cell1:pair1 versus cell1:pair 2; cell2:pair1 versus cell 2:pair 2 etc.). Phase distributions of proximal pairs (Fig 3J) and those obtained by cross-pairing (Appendix Fig S4F) were compared in likelihood of observations in-phase versus observations out-of-phase at all phase angles. Regions of phase–phase mapping corresponding to in-phase and out-of-phase are outlined in Appendix Fig S4F. Likelihood of cross-paired tests showed values close to 1 indicating no predominant in-phase activity whereas values for paired data were significantly higher.

Stochastic multicellular HES5 model with time delay

The core unit of the multicellular model is a single-cell unit that explicitly models Hes5 protein and mRNA abundance and is adapted from the work done in Manning *et al.*, 2019. The single-cell model makes use of a Langevin approach to include stochastic fluctuations in both protein and mRNA as well as the inclusion of a time delay associated with the inhibitory Hill function used to describe the repressive action of Hes protein on its own mRNA production. This implementation, along with the parameter inference (Manning *et al.*, 2019), results in a single-cell model capable of reproducing stochastic oscillations closely matched with the single-cell dynamics observed in the developing neural tube. The multicellular approach extends the single-cell model by introducing an inhibitory Hill function to couple nearest-neighbour cells (in a fixed, no cell movement, hexagonal geometry) whereby high Hes5 protein in one cell is able to repress Hes5 mRNA production in a neighbouring cell (see Appendix Supplementary Methods 2). This inhibitory Hill function (the coupling function) is representative of the overall behaviour of the Notch Delta pathway and its interaction with Hes5, allowing for the bidirectional interaction of Hes5 dynamics between neighbouring cells. Three parameters are associated with this Hill function that make it flexible enough to explore different possible coupling realisations of the Notch–Delta pathway, the effects of which are illustrated in Fig 5B. The main parameter modulated for the analysis in this paper is the repression threshold which defines the number of protein molecules that is required to repress mRNA in a neighbouring cell.

Cell-to-cell HES5 differences by domain and by coupling strength

We used raw Venus::HES5 data, absolute HES5 quantitation by Fluorescence Correlation Spectroscopy (FCS) and manually segmented nuclear maps made available in (Manning *et al.*, 2019). We obtained average HES5 concentration per nuclei by quantile–quantile matching the Venus distribution to the reference FCS distribution of HES5 levels across the tissue. Using nuclear centroid location, we produced absolute cell-to-cell concentration differences between every cell and its closest neighbour. We performed a by domain analysis by dividing the cell-to-cell concentration differences by the average HES5 concentration by domain. In the synthetic examples, HES5 molecular abundance data obtained from the multicellular model were used to produce absolute cell-to-cell abundance differences over a range of coupling strength values. We also produced synthetic cell-to-cell abundance differences relative to the mean HES5 abundance per simulation over a range of coupling strength values.

Phase reconstruction and Kuramoto order value as a measure of synchrony

To determine the synchronisation of real signals both in the model and experimental data, the phase of each oscillator was first reconstructed in complex space. This reconstruction was achieved by using the Hilbert transform, which shifts the phase of each frequency component in a signal by 90 degrees (Benedetto, 1996). The Hilbert transform of a function $u(t)$ is defined as

$$H(u)(t) = \frac{1}{\pi} \int_{-\infty}^{\infty} \frac{u(\tau)}{t - \tau} d\tau. \quad (1)$$

To obtain a rotating vector that contains both the amplitude and phase information of the signal at a given time t , the original signal and the 90 degrees shifted Hilbert transform can be combined in complex space to give

$$u_a(t) = u(t) + i \cdot H(u)(t). \quad (2)$$

By comparing $u_a(t)$ of two or more cells, a measure of how synchronised a population of cells is can be determined by first calculating what is known as the complex order parameter

$$\psi = \frac{1}{N} \sum_{j=1}^N e^{i\phi_j}, \quad (3)$$

where N is the number of oscillators and ϕ_j is the phase of oscillator j . From this, the Kuramoto order parameter is defined as the absolute value of the complex order parameter ψ , which is the magnitude of the vector and has a value between 0 and 1 (Choi *et al.*, 2000). A value of 1 indicates perfect synchrony and matching phase, meaning that in complex space the phases of each oscillator would be at the same angle and would rotate at the same frequency. A value of 0 indicates no synchronisation, and in complex space would appear as a distribution of phases that average to a point at the origin.

Phase synchronisation index

In addition to calculating KOPs, we also used the Hilbert transform to extract phase from spatial data to determine how dynamic the positions of peak and trough were over time. This involved extracting and plotting the phase from time-averaged spatial signals. The phase synchronisation index for DMSO and DBZ conditions (Fig 4E) was obtained by calculating KOP per position in D-V axis and averaging per z-slice (with left and right of the ventricle analysed separately). To account for the loss of spatial periodicity in DBZ at later timepoints, only data passing significance for an auto-correlation test has been included resulting in an analysis restricted to periodic spatial expression observed in both DMSO and DBZ up to 10 h.

Detrending methods

Multiple detrending methods are used depending on the type of data. Detrending and removal of the radial gradient in images of segmented Venus::HES5 nuclei (as in Fig 1) are covered in Materials and Methods section entitled “Centre of intensity detection and radial gradient

removal". The images are 2-dimensional data and so require removing trends in both the apical–basal and dorsoventral direction. Detrending of spatial profiles of Venus::HES5 and NGN2::mScarlet-I is covered in Materials and Methods "Detection and periodicity analysis of spatial expression patterns". Spatial profiles are generated from a ROI 15 μm wide in apicobasal axis and extending up to 250 μm + in dorsoventral direction. The Venus::HES5 intensity is averaged in the apicobasal axis by the image analysis software (either Zen Blue or ImageJ). This generates the 1-dimensional spatial profile and detrending is applied along the dorsoventral axis. Detrending of single-cell timeseries of Venus::HES5 expression is outlined in "Phase-phase Mapping and Phase Shift Analysis in Cell Pairs".

Statistical testing

Statistical tests were performed in GraphPad Prism 8. Data were tested for normality with D'Agostino–Pearson test. The relevant parametric or non-parametric test was then performed. Bar plots and discrete scatter plots show mean \pm SD where multiple independent experiments are analysed. Statistical significance between 2 datasets was tested with either *t*-test (parametric) or Mann–Whitney test (non-parametric). Statistical significance ($P < 0.05$) for 2+ datasets was tested by Kruskal–Wallis with Dunn's multiple comparison correction. All tests were 2-sided. Multiple comparison testing involved comparing all pairs of data columns. Correlations were analysed using Pearson correlation coefficient. Sample sizes, experiment numbers, *P* values < 0.05 and correlation coefficients are reported in each figure legend.

Data availability

All code is written in MATLAB and is available on GitHub: <https://github.com/Papalopulu-Lab/Biga2020>

Expanded View for this article is available online.

Acknowledgements

We are grateful to members of the Papalopulu lab, Andrew Hazel, James Briscoe and Andy Oates for advice and discussions. The authors would also like to thank Robert Lea, the Biological Services Facility and the Bioimaging Facilities of the University of Manchester for technical support. CM was supported by a Sir Henry Wellcome Fellowship (103986/Z/14/Z) and University of Manchester Presidential Fellowship. VB was supported by a Wellcome Trust Senior Research Fellowship to NP (106185/Z/14/Z). JH (220001/Z/19/Z), EJ (204057/Z/16/Z) and DH (Wellcome Trust Grant No. 215189/Z/19/Z) were supported by Wellcome Trust PhD studentships. JK was supported by Wellcome Trust Senior Research Fellowship to NP and a University of St Andrews Lectureship. The funders had no role in study design, data collection and analysis, decision to publish, or preparation of the manuscript.

Author contributions

Study conception and experiment design: CM and NP. Wet lab experiments, supervision, data analysis, data interpretation and manuscript writing: CM. Supervision and development of method to analyse spatial micro-patterns of HES5 expression both in data and from the model, method for Hilbert phase persistence analysis, data analysis, data interpretation and manuscript writing: VB. Design and implementation of stochastic coupled HES5 model,

parameterisation, analysis and model interpretation: JH. smiFISH and imaging: XS. Data collection and development of method to analyse correlations of HES5 nuclear intensity: EJ. Method to analyse periodic spatial micro-patterns of HES5 expression: DH. Design and generation of Neurog2::mScarlet-I knock-in mouse: HB. Design and generation of Neurog2::mScarlet-I knock-in mouse: ADA. Supervision and assistance in design, analysis and interpretation of the mathematical model: JK. Supervision and assistance in analysis and interpretation of the mathematical model: PG. Supervision and work, data interpretation, and manuscript writing: CM, VB, NP, JH, JK, EJ, DH and PG.

Conflict of interest

The authors declare that they have no conflict of interest.

References

- Baek C, Freem L, Gojame R, Sang H, Morin X, Tozer S (2018) Mib1 prevents Notch Cis-inhibition to defer differentiation and preserve neuroepithelial integrity during neural delamination. *PLoS Biol* 16: e2004162
- Bansod S, Kageyama R, Ohtsuka T (2017) Hes5 regulates the transition timing of neurogenesis and gliogenesis in mammalian neocortical development. *Development* 144: 3156–3167
- Baron JW, Galla T (2019) Intrinsic noise, Delta-Notch signalling and delayed reactions promote sustained, coherent, synchronized oscillations in the presomitic mesoderm. *J R Soc Interface* 16: 20190436
- Benedetto JJ (1996) *Harmonic analysis and applications*. Boca Raton, FL: CRC Press
- Boareto M, Jolly MK, Lu M, Onuchic JN, Clementi C, Ben-Jacob E (2015) Jagged-delta asymmetry in Notch signaling can give rise to a sender/receiver hybrid phenotype. *Proc Natl Acad Sci USA* 112: E402–E409
- Bonev B, Stanley P, Papalopulu N (2012) MicroRNA-9 Modulates Hes1 ultradian oscillations by forming a double-negative feedback loop. *Cell Rep* 2: 10–18
- Briscoe J, Small S (2015) Morphogen rules: design principles of gradient-mediated embryo patterning. *Development* 142: 3996–4009
- Choi MY, Kim HJ, Kim D, Hong H (2000) Synchronization in a system of globally coupled oscillators with time delay. *Phys Rev E Stat Phys Plasmas Fluids Relat Interdiscip Topics* 61: 371–381
- Cohen M, Georgiou M, Stevenson NL, Miodownik M, Baum B (2010) Dynamic filopodia transmit intermittent Delta-Notch signaling to drive pattern refinement during lateral inhibition. *Dev Cell* 19: 78–89
- Corson F, Couturier L, Rouault H, Mazouni K, Schweisguth F (2017) Self-organized Notch dynamics generate stereotyped sensory organ patterns in *Drosophila*. *Science* 356: eaai7407
- Das RM, Storey KG (2012) Mitotic spindle orientation can direct cell fate and bias Notch activity in chick neural tube. *EMBO Rep* 13: 448–454
- Das RM, Storey KG (2014) Apical abscission alters cell polarity and dismantles the primary cilium during neurogenesis. *Science* 343: 200–204
- De Jossineau C, Soulé J, Martin M, Anguille C, Montcourrier P, Alexandre D (2003) Delta-promoted filopodia mediate long-range lateral inhibition in *Drosophila*. *Nature* 426: 555–559
- Delile J, Rayon T, Melchionda M, Edwards A, Briscoe J, Sagner A (2019) Single cell transcriptomics reveals spatial and temporal dynamics of gene expression in the developing mouse spinal cord. *Development* 146: dev.173807
- Eilers PH, Goeman JJ (2004) Enhancing scatterplots with smoothed densities. *Bioinformatics* 20: 623–628
- Falo-Sanjuan J, Bray SJ (2020) Decoding the Notch signal. *Dev Growth Differ* 62: 4–14

- Galla T (2009) Intrinsic fluctuations in stochastic delay systems: theoretical description and application to a simple model of gene regulation. *Phys Rev E* 80: 021909
- Goodfellow M, Phillips NE, Manning C, Galla T, Papalopulu N (2014) microRNA input into a neural ultradian oscillator controls emergence and timing of alternative cell states. *Nat Commun* 5: 3399
- Hadjivasilou Z, Moore RE, McIntosh R, Galea GL, Clarke JDW, Alexandre P (2019) Basal protrusions mediate spatiotemporal patterns of spinal neuron differentiation. *Dev Cell* 49: 907–919
- Henrique D, Schweisguth F (2019) Mechanisms of Notch signaling: a simple logic deployed in time and space. *Development* 146: dev172148
- Herrgen L, Ares S, Morelli LG, Schröter C, Jülicher F, Oates AC (2010) Intercellular coupling regulates the period of the segmentation clock. *Curr Biol* 20: 1244–1253
- Hunter GL, Hadjivasilou Z, Bonin H, He L, Perrimon N, Charras G, Baum B (2016) Coordinated control of Notch/Delta signalling and cell cycle progression drives lateral inhibition-mediated tissue patterning. *Development* 143: 2305–2310
- Imayoshi I, Isomura A, Harima Y, Kawaguchi K, Kori H, Miyachi H, Fujiwara T, Ishidate F, Kageyama R (2013) Oscillatory control of factors determining multipotency and fate in mouse neural progenitors. *Science* 342: 1203–1208
- Imayoshi I, Kageyama R (2014) bHLH factors in self-renewal, multipotency, and fate choice of neural progenitor cells. *Neuron* 82: 9–23
- Isomura A, Ogushi F, Kori H, Kageyama R (2017) Optogenetic perturbation and bioluminescence imaging to analyze cell-to-cell transfer of oscillatory information. *Genes Dev* 31: 524–535
- Jensen MH, Sneppen K, Tiana G (2003) Sustained oscillations and time delays in gene expression of protein Hes1. *FEBS Lett* 541: 176–177
- Kageyama R, Ohtsuka T, Shimojo H, Imayoshi I (2008) Dynamic Notch signaling in neural progenitor cells and a revised view of lateral inhibition. *Nat Neurosci* 11: 1247–1251
- Kicheva A, Bollenbach T, Ribeiro A, Valle HP, Lovell-Badge R, Episkopou V, Briscoe J (2014) Coordination of progenitor specification and growth in mouse and chick spinal cord. *Science* 345: 1254927
- Kobayashi T, Mizuno H, Imayoshi I, Furusawa C, Shirahige K, Kageyama R (2009) The cyclic gene Hes1 contributes to diverse differentiation responses of embryonic stem cells. *Genes Dev* 23: 1870–1875
- Kuzmicz-Kowalska K, Kicheva A (2020) Regulation of size and scale in vertebrate spinal cord development. *Wiley Interdiscip Rev Dev Biol* 10: e383
- Lewis J (2003) Autoinhibition with transcriptional delay. *Curr Biol* 13: 1398–1408
- de Lichtenberg KH, Funa N, Nakic N, Ferrer J, Zhu Z, Huangfu D, Serup P (2018) Genome-wide identification of HES1 target genes uncover novel roles for HES1 in pancreatic development. *bioRxiv* <https://doi.org/10.1101/335869> [PREPRINT]
- Lopes-Dos-Santos V, van de Ven GM, Morley A, Trouche S, Campo-Urriza N, Dupret D (2018) Parsing hippocampal theta oscillations by nested spectral components during spatial exploration and memory-guided behavior. *Neuron* 100: 940–952
- Lyubimova A, Itzkovitz S, Junker JP, Fan ZP, Wu X, van Oudenaarden A (2013) Single-molecule mRNA detection and counting in mammalian tissue. *Nat Protoc* 8: 1743–1758
- Ma Q, Chen Z, del Barco BI, de la Pompa JL, Anderson DJ (1998) neurogenin1 is essential for the determination of neuronal precursors for proximal cranial sensory ganglia. *Neuron* 20: 469–482
- Manning CS, Biga V, Boyd J, Kursawe J, Ymisson B, Spiller DG, Sanderson CM, Galla T, Rattray M, Papalopulu N (2019) Quantitative single-cell live imaging links HES dynamics with cell-state and fate in murine neurogenesis. *Nat Commun* 10: 2835
- Marklund U, Hansson EM, Sundström E, de Angelis MH, Przemeczek GK, Lendahl U, Muhr J, Ericson J (2010) Domain-specific control of neurogenesis achieved through patterned regulation of Notch ligand expression. *Development* 137: 437–445
- Marra AN, Adeeb BD, Chambers BE, Drummond BE, Ulrich M, Addiego A, Springer M, Poureteezadi SJ, Chambers JM, Ronshaugen M et al (2019) Prostaglandin signaling regulates renal multiciliated cell specification and maturation. *Proc Natl Acad Sci USA* 116: 8409–8418
- Momiji H, Monk NAM (2008) Dissecting the dynamics of the Hes1 genetic oscillator. *J Theor Biol* 254: 784–798
- Monk NAM (2003) Oscillatory expression of Hes1, p53, and NF- κ B driven by transcriptional time delays. *Curr Biol* 13: 1409–1413
- Morelli LG, Ares S, Herrgen L, Schröter C, Jülicher F, Oates AC (2009) Delayed coupling theory of vertebrate segmentation. *HFSP J* 3: 55–66
- Nelson BR, Hodge RD, Daza RA, Tripathi PP, Arnold SJ, Millen KJ, Hevner RF (2020) Intermediate progenitors support migration of neural stem cells into dentate gyrus outer neurogenic niches. *eLife* 9: e53777
- Oates AC (2020) Waiting on the Fringe: cell autonomy and signaling delays in segmentation clocks. *Curr Opin Genet Dev* 63: 61–70
- Ohtsuka T, Ishibashi M, Gradwohl G, Nakanishi S, Guillemot F, Kageyama R (1999) Hes1 and Hes5 as notch effectors in mammalian neuronal differentiation. *EMBO J* 18: 2196–2207
- Özbudak EM, Lewis J (2008) Notch signalling synchronizes the zebrafish segmentation clock but is not needed to create somite boundaries. *PLoS Genet* 4: e15
- Paridaen JT, Huttner WB (2014) Neurogenesis during development of the vertebrate central nervous system. *EMBO Rep* 15: 351–364
- Petrovic J, Formosa-Jordan P, Luna-Escalante JC, Abello G, Iban M, Es NJ, Giraldez F, Abelló G, Ibañez M et al (2014) Ligand-dependent Notch signaling strength orchestrates lateral induction and lateral inhibition in the developing inner ear. *Development* 141: 2313–2324
- Phillips NE, Manning CS, Pettini T, Biga V, Marinopoulou E, Stanley P, Boyd J, Bagnall J, Paszek P, Spiller DG et al (2016) Stochasticity in the miR-9/Hes1 oscillatory network can account for clonal heterogeneity in the timing of differentiation. *eLife* 5: e16118
- Ramos C, Rocha S, Gaspar C, Henrique D (2010) Two Notch ligands, Dll1 and Jag1, are differently restricted in their range of action to control neurogenesis in the mammalian spinal cord. *PLoS One* 5: e15515
- Sagner A, Briscoe J (2019) Establishing neuronal diversity in the spinal cord: a time and a place. *Development* 146: dev182154
- Sagner A, Gaber ZB, Delile J, Kong JH, Rousso DL, Pearson CA, Weicksel SE, Melchionda M, Mousavy Gharavy SN, Briscoe J et al (2018) Olig2 and Hes regulatory dynamics during motor neuron differentiation revealed by single cell transcriptomics. *PLoS Biol* 16: e2003127
- Shaya O, Sprinzak D (2011) From Notch signaling to fine-grained patterning: modeling meets experiments. *Curr Opin Genet Dev* 21: 732–739
- Shimojo H, Isomura A, Ohtsuka T, Kori H, Miyachi H, Kageyama R (2016) Oscillatory control of Delta-like1 in cell interactions regulates dynamic gene expression and tissue morphogenesis. *Genes Dev* 30: 102–116
- Shimojo H, Kageyama R (2016) Oscillatory control of Delta-like1 in somitogenesis and neurogenesis: a unified model for different oscillatory dynamics. *Semin Cell Dev Biol* 49: 76–82
- Sonnen KF, Lauschke VM, Uraji J, Falk HJ, Petersen Y, Funk MC, Beaupeux M, François P, Merten CA, Aulehla A (2018) Modulation of phase shift

- between Wnt and Notch signaling oscillations controls mesoderm segmentation. *Cell* 172: 1079–1090
- Soto X, Biga V, Kursawe J, Lea R, Doostdar P, Thomas R, Papalopulu N (2020) Dynamic properties of noise and Her6 levels are optimized by miR-9, allowing the decoding of the Her6 oscillator. *EMBO J* 39: e103558
- Sprinzak D, Lakhapal A, Lebon L, Santat LA, Fontes ME, Anderson GA, Garcia-Ojalvo J, Elowitz MB (2010) Cis-interactions between Notch and Delta generate mutually exclusive signalling states. *Nature* 465: 86–90
- Tiedemann HB, Schneltzer E, Beckers J, Przemeczek GKH, Hrabě de Angelis M (2017) Modeling coexistence of oscillation and Delta/Notch-mediated lateral inhibition in pancreas development and neurogenesis. *J Theor Biol* 430: 32–44
- Tsiarris CD, Aulehla A (2016) Self-organization of embryonic genetic oscillators into spatiotemporal wave patterns. *Cell* 164: 656–667
- Vilas-Boas F, Fior R, Swedlow JR, Storey KG, Henrique D (2011) A novel reporter of notch signalling indicates regulated and random Notch activation during vertebrate neurogenesis. *BMC Biol* 9: 58
- Webb AB, Lengyel IM, Jörg DJ, Valentin G, Jülicher F, Morelli LG, Oates AC (2016) Persistence, period and precision of autonomous cellular oscillators from the zebrafish segmentation clock. *eLife* 5: e08438
- Wu YE, Enoki R, Oda Y, Huang ZL, Honma KI, Honma S (2018) Ultradian calcium rhythms in the paraventricular nucleus and subparaventricular zone in the hypothalamus. *Proc Natl Acad Sci USA* 115: E9469–E9478



License: This is an open access article under the terms of the Creative Commons Attribution License, which permits use, distribution and reproduction in any medium, provided the original work is properly cited.

Expanded View Figures

Figure EV1. Venus::HES5 expression in single progenitor cells located in the ventral domain of spinal cord. Related to Fig 1.

- A Transverse slice of live Venus::HES5 homozygous knock-in mouse spinal cord E10.5 *ex vivo*, Draq5 live nuclear stain and brightfield image. Scale bar 50 μm .
- B Immunofluorescence of E10.5 Venus::HES5 transverse slice of spinal cord *ex vivo*. SOX2+ progenitors and endogenous Venus::HES5 signal. Scale bar 40 μm .
- C Viridis look-up table applied to mean nuclear Draq5 intensity corresponding to transverse slice in Fig 1C.
- D Total number of cells per microcluster detected in Venus::HES5 segmented images versus synthetically generated randomised images (see Materials and Methods); dots indicate individual clusters detected in 14 segmented images with 20x repeats per slice of Rnd1 (random permutation of real intensity observations) and Rnd2 (randomised intensities with same mean and SD); bars indicate mean and SD; Kruskal–Wallis *t*-test with Dunn's multiple comparison, significance **** $p < 0.0001$.
- E Pearson correlation coefficient of mean nuclear Venus::HES5 intensity in relationship to distance for (left panel) E9.5 and (right panel) E11.5 Venus::HES5 spinal cord *ex vivo* slices; red dots indicate average Venus::HES5 correlation per slice of three slices from three experiments with corresponding red line indicating one phase decay fit. Black line denotes 95% confidence levels. Grey dots indicate correlations from randomisations of intensities analysed in the same way.
- F Transverse slice of live (left panel) Venus::HES5 homozygous knock-in mouse spinal cord E10.5 *ex vivo* showing (middle panel) segmentation of Draq5 and (right panel) mask applied to Venus::HES5 channel. Images correspond to slice shown in Fig 1G. Scale bar 30 μm , D—dorsal, V—ventral.
- G, H Left panels—Viridis look-up table applied to mean nuclear Venus::HES5 intensity in E9.5 and E11.5 slices, respectively, after radial gradient removal. Right panels—Pearson correlation coefficient of mean nuclear Venus::HES5 intensity in relationship to distance for E9.5 and E11.5 Venus::HES5 spinal cord *ex vivo* slices, respectively. Red dots indicate average Venus::HES5 correlation per slice of three slices from three experiments with corresponding red line indicating one phase decay fit. Black line denotes 95% confidence levels.

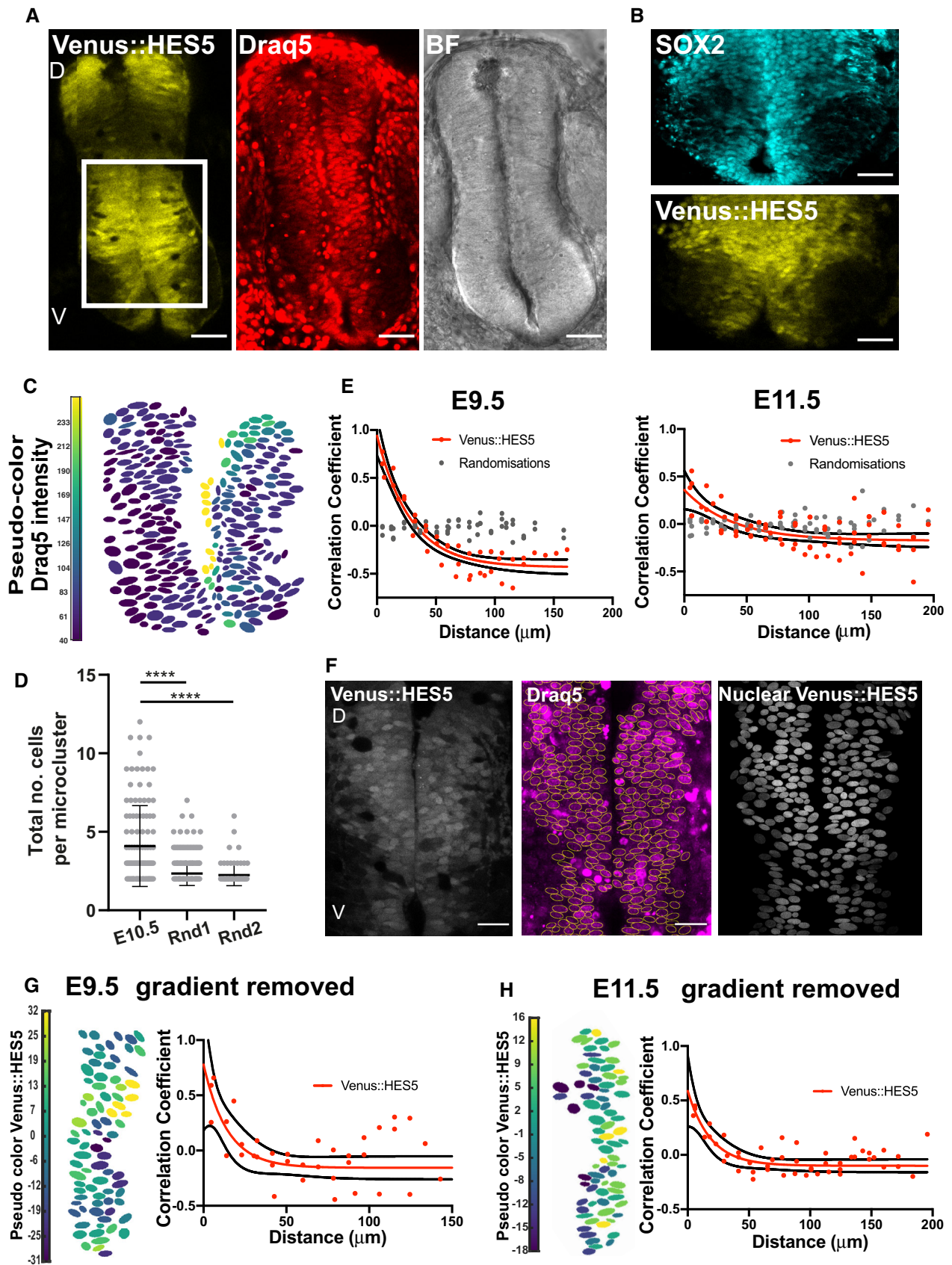


Figure EV1.

Figure EV2. Draq5 and Venus::HES5 spatial periodicity in live spinal cord tissue slices. Related to Fig 2.

- A Transverse slice of live Venus::HES5 (left panel) homozygous knock-in mouse spinal cord E10.5 *ex vivo*, Draq5 live nuclear stain (right panel); rectangle shows region for spatial profile.
- B Viridis look-up table applied to mean nuclear Venus::HES5 intensity in the same slice shown in (A), rectangle shows the same region of interest for spatial profile.
- C Venus::HES5 intensity spatial profile (black) from the yellow box in (a—non-segmented data), and trend line in blue (fitted polynomial order 6).
- D Detrended spatial profile of Venus::HES5 (grey) and Draq5 (red) nuclear stain from region delineated in (A); arrows show regions of Venus::HES5 low and Draq5 high indicating low Venus::HES5 areas are not nuclei free.
- E Distribution of peak to peak distance in auto-correlation plots of Draq5 spatial profile; this is a measure of inter-nuclear distance in Draq5 profile along dorsal–ventral axis of spinal cord; data points represent all peak to peak distances from nine slices, six experiments; mean $9.3 \pm 0.42 \mu\text{m}$ (95% confidence limits).
- F Inter-cluster distance in the dorsoventral (DV) axis computed from multiple microclusters detected in E10.5 spinal cord segmented images using an automated approach (see Materials and Methods); dots indicate individual observations collected from 14 images; bars indicate mean and SD.
- G Spatial periodicity detected by Lomb–Scargle periodogram in apical, medium and basal regions (10, 30 and 60 μm from ventricle, respectively); dots indicate mean periodicity from at least three z-sections and both left and right sides of ventricle analysed in six experiments; lines indicate mean and SD per experiment; Kruskal–Wallis test not significant, $P = 0.3137$.
- H Longitudinal cryosection of neural tube in E10.5 Venus::HES5 embryos. A—anterior, P—posterior. Scale bar 60 μm .
- I Representative detrended spatial profile of Venus::HES5 from neural tube in anterior–posterior (A-P) direction.
- J Representative auto-correlation of Venus::HES5 spatial profile in A-P direction. Multiple significant peaks indicate spatial periodicity in A-P direction. Significant peaks (red triangle) lie outside black dotted lines indicating 95% significance based on bootstrap approach (see Materials and Methods) and non-significant peaks (black triangles).
- K Pearson correlation coefficient of detrended Venus::HES5 spatial profile between subsequent z-sections of transverse E10.5 spinal cord tissue slices at known distances (i.e. correlations in A-P direction); untreated slices—dots show 18 pairs of z-sections from six experiments; DMSO-treated slices—dots show nine pairs from three experiments.
- L (Left panel) Representative spatiotemporal plot of the detrended Venus::HES5 pattern along ventral–dorsal direction (0 to 200 μm) obtained by averaging kymograph data in the same region over 2-h time intervals; (Right panel) Representative phase map of spatially periodic Venus::HES5 intensity obtained using the Hilbert transform (see Materials and Methods) from data shown in the left panel; markers indicate areas underdoing a high-to-low* and low-to-high** transition.

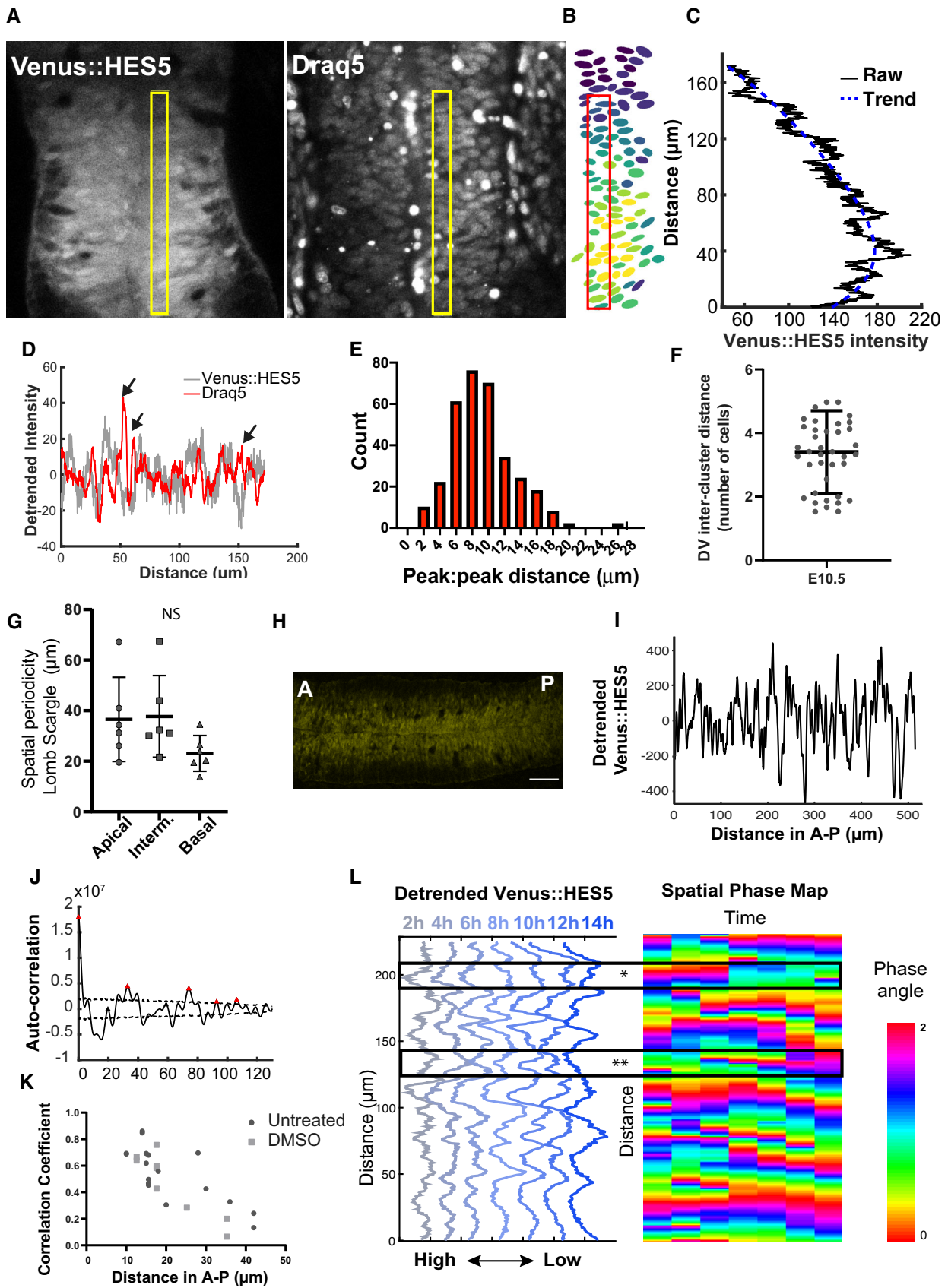


Figure EV2.

Figure EV3. Changes in Venus::HES5 spatiotemporal expression pattern in live slice cultures treated with Notch inhibitor DBZ. Related to Fig 4.

- A Representative examples of the detrended Venus::HES5 signal observed along ventral–dorsal direction in DMSO and DBZ conditions; Venus::HES5 intensity data obtained by averaging kymographs over 2-h intervals; panels represent individual slice cultures (2 per condition) in addition to examples in Fig 4B.
- B Spatial phase maps obtained from detrended Venus::HES5 signal in DMSO and DBZ conditions; panels correspond to Venus::HES5 intensity traces shown in (A).
- C Auto-correlation analysis of detrended apical Venus::HES5 spatial profile in DMSO (control) and DBZ (2 μ M) treated E10.5 Venus::HES5 spinal cord slices; panels show auto-correlation of detrended Venus::HES5 signal averaged from 0–2 h of timelapse video (top panels) and corresponding auto-correlation functions in the same slices averaged in 2 h windows for 10 h; we observed a decrease in amplitude of auto-correlation peaks over time in DBZ-treated slices.
- D Peak to peak distance in auto-correlation from spatial data shown in Fig 4H. Lines show median per experiment from DMSO ($n = 3$ experiments) and DBZ ($n = 4$ experiments); 1-tailed t -test not significant $P = 0.0526$.
- E Nuclear density represented by the % area covered by nuclei in DMSO and DBZ treated *ex vivo* E10.5 spinal cord slice cultures dots indicate multiple z-stacks from DBZ (5 slices) and DMSO (4 slices); bars indicate mean and SD per condition; 2-tailed t -test *** $P = 0.0004$.

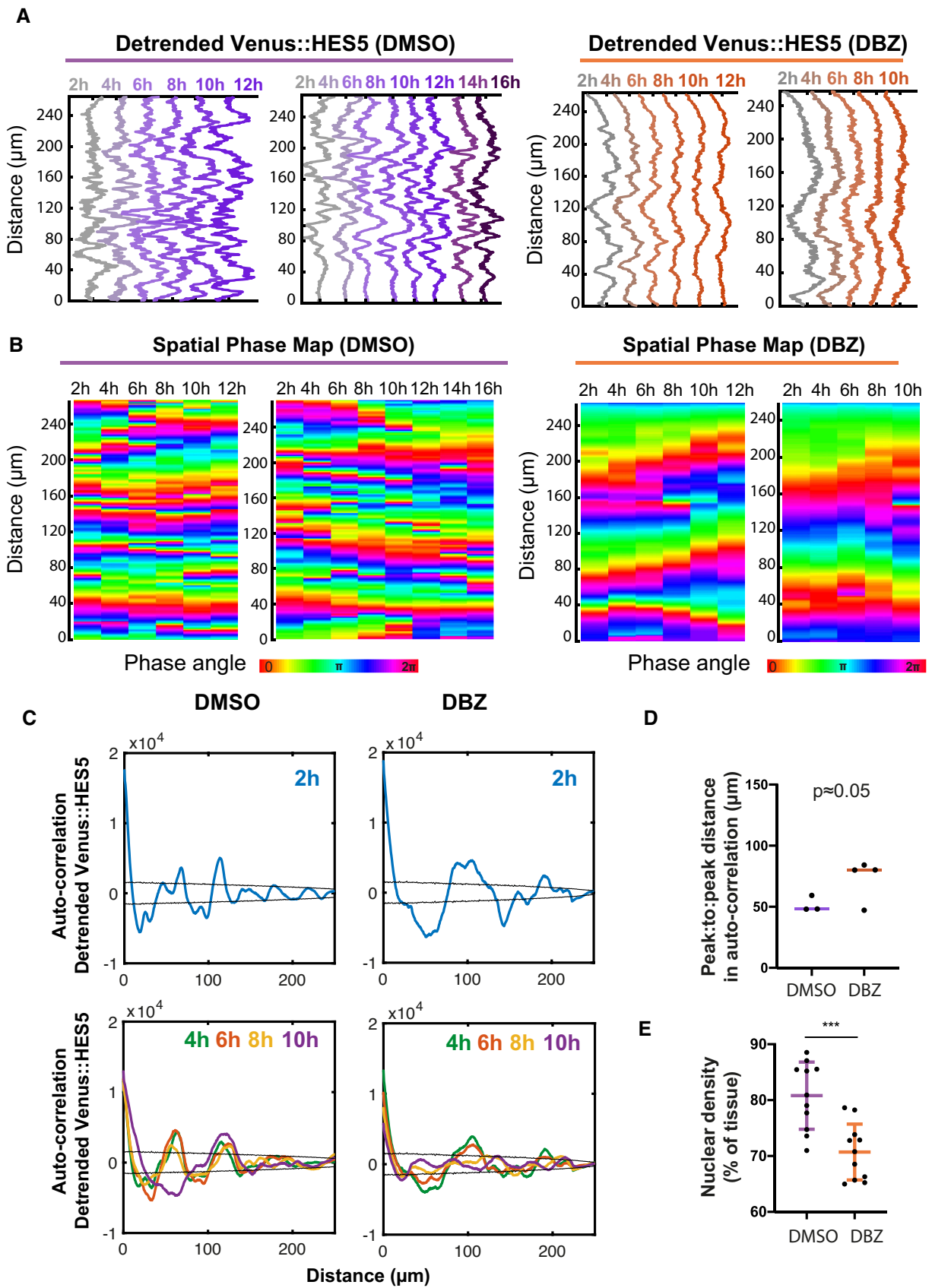


Figure EV3.

Figure EV4. HES5 spatiotemporal dynamics correlate with rate of differentiation.

- A Diagram of Notch–Delta inter-cellular communication and HES5 interactions. Our model takes into account that HES5 negatively regulates its own mRNA production (grey highlighted area), downstream proneural genes and Delta; the direct and/or indirect (via proneural genes) repression of Delta by HES5 is expressed mathematically through the means of an inter-cellular Hill function (see Materials and Methods).
- B Transverse cryosection of E10.5 Venus::HES5 spinal cord. Venus::HES5 endogenous signal, OLIG2: motorneuron progenitor marker, NGN2: early marker of neuronal commitment, DAPI; scale bar 25 μm .
- C Spatial expression profile of Venus::HES5, NGN2 and OLIG2 from the same tissue to help delineate motorneuron (OLIG2+) vs interneuron (OLIG2-) domains.
- D Spatial profile of Venus::HES5 intensity (black) generated by averaging 2.5 h of kymograph data; 0 distance represents ventral end of kymograph; blue dotted line is trend in Venus::HES5 data across the domain determined by polynomial fit order 6; domain boundary between motorneuron progenitors (MN) and interneuron progenitors (IN) marked with red dashed line.
- E Detrended spatial profile of Venus::HES5 corresponding to (C) in motorneuron progenitors (red:MN) and interneuron progenitors (blue:IN).
- F Auto-correlation plot of detrended Venus::HES5 spatial profile in MN and IN progenitors; black lines show confidence limits for peak significance based on bootstrap approach on detrended Venus::HES5 intensity profile (see Materials and Methods); red triangle—significant peak, black triangle—non-significant peak; multiple significant peaks in auto-correlation shows periodicity in spatial profile of Venus::HES5 intensity.
- G Spatial periodicity of Venus::HES5 in motorneuron vs interneuron domain measured with the Lomb–Scargle periodogram; top 2 significant peaks were used to calculate spatial period from 2 to 3 z-sections per experiment, left and right side of ventricle analysed separately and six experiments; bars indicate mean with SD; Mann–Whitney test with two-tail significance for **** $P < 0.0001$.
- H Fold-change in Venus::HES5 spatial pattern between hi-low regions in IN domain relative to MN domain. Data points represent mean per experiment. Lines shows mean and SD of six experiments. 2-tailed Mann–Whitney test ** $P = 0.0022$.

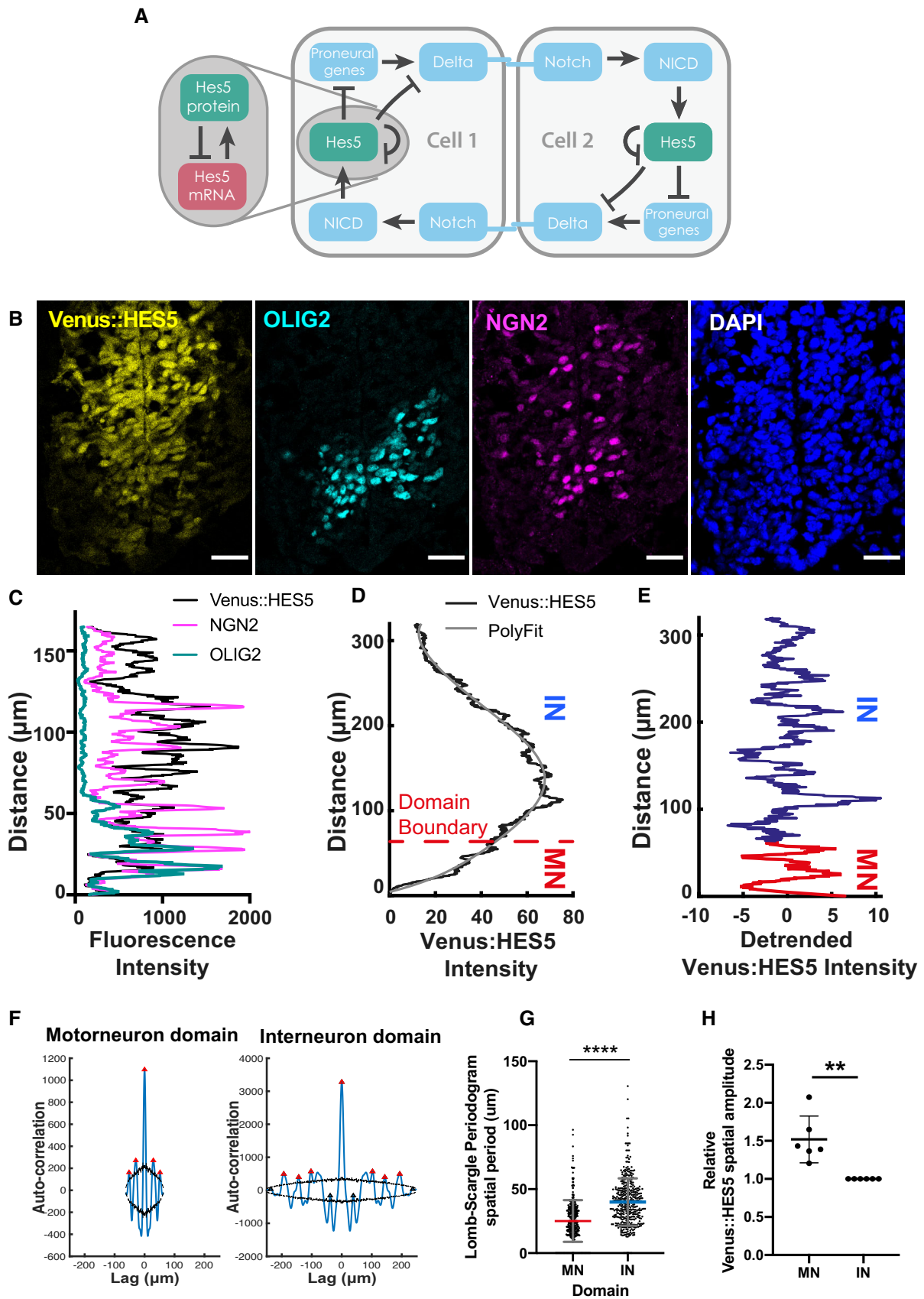


Figure EV4.

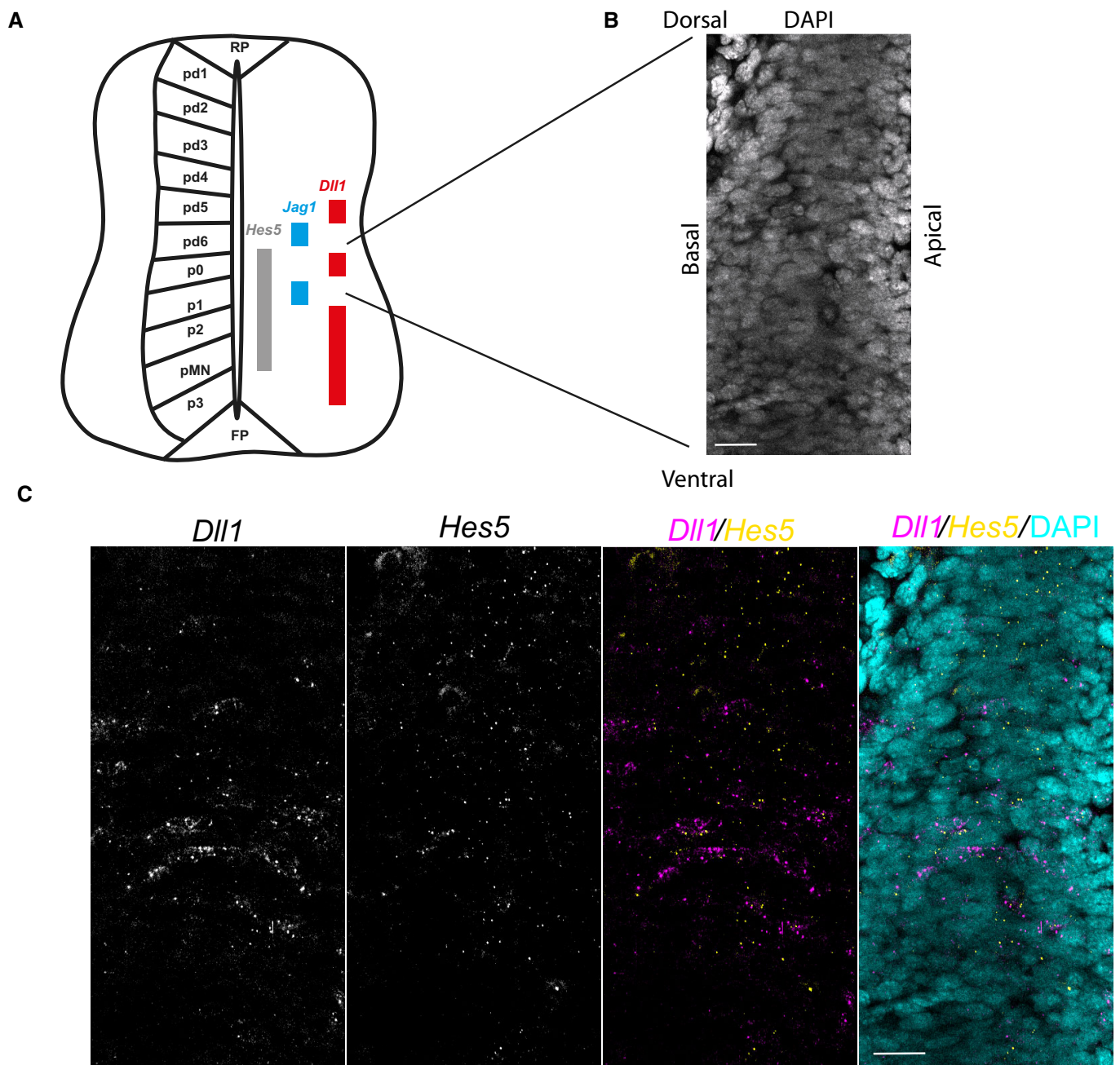


Figure EV5. Exploration of HES spatiotemporal dynamics in a multicellular environment.

A Schematic of *Hes5*, *Dll1* and *Jag1* expression in progenitor domains along D-V axis of E10.5 mouse spinal cord compiled based on data from Manning *et al* (2019) and Marklund *et al* (2010).

B DAPI nuclear stain of interneuron region in E10.5 mouse; lines indicate spatial localisation in tissue. Scale bar 20 μ m.

C Single-molecule FISH of *Dll1* and *Hes5* expression in spinal cord region corresponding to (B) (Materials and Methods); panels 1 and 2 indicate *Dll1* and *Hes5*, respectively; panels 3 and 4 show false-color merged *Dll1/Hes5* and *Dll1/Hes5/DAPI*, respectively; scale bar 20 μ m.

2.4 Modelling Appendix

2.4.1 Stochastic model of auto-repression coupled between cells

We adapted a HES5-parameterised single-cell model from previous work into a Notch-Delta-coupled multicellular model (Figure 5A) (Manning et al., 2019). The single-cell network is the basic unit of the model and consists of a negative feedback loop of HES5 protein onto its own mRNA expression described by stochastic delay differential equations (SDDEs) capable of producing stochastic autonomous oscillations.

The SDDEs implement a Langevin approach over a Gillespie algorithm in favour of reduced computational cost and fixed time steps which enable easier addition of time delays (Gillespie, 2000). For solving stochastic delay differential equations in biochemical systems, two main approaches are commonly used: the Gillespie algorithm and the Chemical Langevin equation (Gillespie, 1977, 2000). The Gillespie algorithm is a discrete-event simulation method that provides exact solutions by simulating every reaction event (every integer increase or decrease in molecule count) according to a defined probability and so it is suitable for simulating low molecule counts.

The Chemical Langevin Equation is a continuous-time approximation of the Gillespie algorithm and so is suitable for efficiently simulating systems with large molecule counts (Yan et al., 2017) such as HES5 dynamics in neural progenitors where the mean abundance of HES5 protein has been measured at around 40,000 molecules (Manning et al., 2019). Another difference between the two methods is that the Gillespie algorithm results in variable time steps, whereas the Langevin approach would typically be solved with a fixed time step.

Therefore a Langevin approach was used preferentially over the Gillespie algorithm for efficiency and ease of implementation with time delays. The Euler-Maruyama method was used to solve the Langevin equations and the noise distribution was chosen to be Gaussian as this was found to describe HES5 dynamics well in the previous implementation of the single-cell HES5 model (Manning et al., 2019).

To extend the single-cell model to a multicellular one, the cells were coupled together with an interaction representative of the Notch-Delta pathway and its interaction with HES5. Instead of modelling every reaction in the chain of events that constitute the Notch-Delta pathway, we used a highly adjustable coupling function – an inhibitory Hill function – that requires only two parameters to specify its shape. This drastically reduced the potential number of parameters required to describe the Notch-Delta pathway that couples HES5 dynamics between cells while maintaining the abil-

ity to describe a wide variety of possible coupling function shapes that may represent the biological system. The Hill function in this model, therefore, describes how the production rate of HES5 in one cell is inhibited by high levels of HES5 expression in a neighbouring cell and has the form of

$$J(\overline{P}_i) = \frac{1}{1 + \left(\frac{\overline{P}_i}{P_0}\right)^n} \quad (2.1)$$

where $J(\overline{P}_i)$ is the mRNA production rate in cell i in response to the average protein abundance in neighbouring cells \overline{P}_i . P_0 is the repression threshold (also known as the effective concentration EC50) and n is the Hill coefficient. P_0 and n define the shape of the Hill function (illustrated in Figure 5B) and thus how a cell will respond to the levels of HES5 in its neighbouring cells. Specifically, the repression threshold is inversely related to the coupling strength as this parameter defines the concentration of HES5 in neighbouring cells that will begin to repress HES5 production in a receiving cell. The Hill coefficient is also capable of changing the coupling strength but to a lesser extent as it affects the slope of the curve around the value of the repression threshold, creating a more step-like response at higher Hill coefficient values and reproducing a Michaelis-Menten curve at a value of 1.

For the analysis in this paper, we chose neighbours to be taken as the closest or first-rank neighbours, which in the case of hexagonal geometry implies a cell can be coupled to a maximum of 6 immediate neighbours (illustrated in Figure 5C). A static hexagonal lattice geometry is used for defining the spatial relationship between cells, as this approximates the average number of neighbours a nucleus would have in densely packed tissue-like pseudostratified epithelia (Gomez et al., 2021), and is sufficient to explore which spatial patterns can emerge through nearest neighbour interactions. The incoming protein concentration that a cell experiences is defined as the average of its neighbours

$$\overline{P}_i = \frac{1}{|\mathcal{N}(i)|} \sum_{k \in \mathcal{N}(i)} P_k, \quad (2.2)$$

where $\mathcal{N}(i)$ is the set of neighbours to cell i , $|\mathcal{N}(i)|$ is the number of neighbours, and P_k is the protein concentration in a neighbouring cell k . Equation (2.2) assumes that a cell receives an equal contribution from each of its neighbouring cells, and there is no efficiency of signalling or scaling parameter in (2.2) as this would be redundant in addition to the intercellular repression threshold. Taking into account the number of neighbours ($1/|\mathcal{N}(i)|$ in (2.2)) rather than a static multiplication term reduces

the effects of different patterning at the boundaries of the simulated tissue and was found to result in similar dynamics as when periodic boundaries were used. Finally, to capture the dynamics of the Notch-Delta pathway more accurately, a time delay was added to the Hill function. The use of a nonlinear function to describe the multiple steps neglects the time delays associated with the reaction, transport/diffusion, and synthesis, so an explicit time delay parameter was added. The full form of the coupling function taking into account the neighbours and time delay is given by

$$J(\bar{P}_i(t - \tau)) = \frac{1}{1 + (\bar{P}_i(t - \tau_{ND})/P_{ND0})^{n_{ND}}}. \quad (2.3)$$

where the subscript ND indicates intercellular parameters associated with Notch-Delta signalling and τ_{ND} is the intercellular time delay. The full set of equations that describe the dynamics in an individual cell within the multicellular model is the single-cell model from previous work (Manning et al., 2019) but with the introduction of (2.3) as a multiplicative term that affects the production rate of mRNA

$$\frac{dM_i(t)}{dt} = -\mu_m M_i(t) + \alpha_m G(P_i(t - \tau)) J(\bar{P}_i(t - \tau)) + \sqrt{\mu_m M_i(t) + \alpha_m G(P_i(t - \tau)) J(\bar{P}_i(t - \tau))} \xi_m(t), \quad (2.4)$$

$$\frac{dP_i(t)}{dt} = -\mu_p P_i(t) + \alpha_p M_i(t) + \sqrt{\mu_p P_i(t) + \alpha_p M_i(t)} \xi_p(t). \quad (2.5)$$

Where $M_i(t)$ is HES5 mRNA concentration, $\mu_{m,p}$ are the degradation rate of HES5 mRNA and protein respectively, $\alpha_{m,p}$ are the transcription and translation rates of HES5, $\xi_{m,p}(t)$ are Gaussian white noise, and $G(P_i(t - \tau))$ is an inhibitory Hill function that describes HES5 autorepression

$$G(P_i(t - \tau)) = \frac{1}{1 + (P_i(t - \tau_H)/P_{H0})^{n_H}}, \quad (2.6)$$

where P_{H0} is the repression threshold for HES5 acting on its own promoter and n_H is the corresponding Hill coefficient. The multiplicative nature of the two Hill functions in (2.4) is based on previous literature (Chikayama & Everroad, 2014; Lewis, 2003). In (2.4) and (2.5), there is a deterministic part which represents the overall increase or decrease in protein or mRNA to be expected at given concentrations and then a stochastic part that accounts for random binding or non-binding of transcription and translation machinery in the cell. The stochastic part is scaled by the square root of the number of events that can happen in a given time and so the stochastic part becomes increasingly significant at low protein/mRNA numbers. The Eu-

ler-Maruyama method was used to numerically calculate solutions to the SDDEs in (2.4) and (2.5) using a time step size of 1 minute.

Parameter values for simulations of the model included in Figure 5 and Appendix Figures S5 are given in Appendix Table S3 marked as Main. We also investigated several other parameter combinations (Appendix Table S3 C15/10/5-1 to 3 and Appendix Figure S6) previously identified to reproduce HES5 tissue data by Bayesian inference (Manning et al., 2019).

Time delay (τ) at the start of simulations was dealt with by setting the protein or mRNA at τ units in the past to just be the initial protein or mRNA levels if $t < \tau$. A condition was also set so that if the protein or mRNA abundance dipped below 0 on any given time step, then the abundance was replaced with 0. A time step of $\Delta t = 1min$ was found to be sufficiently small to produce stable solutions to the SDDEs. A typical single run of the model (200 cells run to 100h of simulation time (6000 time steps)) takes around 1.3 seconds.

2.4.2 Numerical implementation of neighbouring cells

The stored protein expression for each cell was mapped to each cell in the hexagonal lattice and from this a neighbour matrix could be defined which compares cell i to every other cell j . Each element ij of the neighbour matrix is equal to 0 if they are not neighbours and 1 if they are neighbours, as shown below

$$\mathbf{N} = \begin{matrix} & \text{cell}_1 & \text{cell}_2 & \dots & \text{cell}_j \\ \text{cell}_1 & \left[\begin{array}{cccc} 0 & 1 & \dots & 0 \end{array} \right. \\ \text{cell}_2 & \left. \begin{array}{cccc} 1 & 0 & \dots & 1 \end{array} \right. \\ \vdots & \left. \begin{array}{cccc} \vdots & \vdots & \ddots & \vdots \end{array} \right. \\ \text{cell}_i & \left. \begin{array}{cccc} 0 & 1 & \dots & 0 \end{array} \right] \end{matrix} \quad (2.7)$$

The neighbour matrix is used to extract the sum of the neighbouring cells' expression, and the protein expression is stored as

$$\mathbf{P} = \begin{matrix} & t_1 & \dots & t_n \\ \text{cell}_1 & \left[\begin{array}{ccc} P_{11} & \dots & P_{1n} \end{array} \right. \\ \vdots & \left. \begin{array}{ccc} \vdots & \ddots & \vdots \end{array} \right. \\ \text{cell}_m & \left. \begin{array}{ccc} P_{m1} & \dots & P_{mn} \end{array} \right] \end{matrix} \quad (2.8)$$

where P_{mn} is the protein abundance in cell m at time-step n . The protein abundance in every cell at a given time point would then just be a column vector taken from the above matrix

$$\mathbf{P}(\mathbf{t} = \mathbf{n}) = \begin{matrix} & t_n \\ cell_1 & \left(P_{1n} \right) \\ \vdots & \left(\vdots \right) \\ cell_m & \left(P_{mn} \right) \end{matrix} \quad (2.9)$$

Therefore to get the summed expression of the neighbouring cells for each cell in Matlab, the neighbour matrix is multiplied with the protein expression vector at each time point

$$\begin{aligned} NP(t = n) &= \begin{bmatrix} 0 & \dots & 1 \\ \vdots & \ddots & \vdots \\ 1 & \dots & 0 \end{bmatrix} \begin{pmatrix} P_{1n} \\ \vdots \\ P_{mn} \end{pmatrix} \\ &= \begin{pmatrix} \sum_{k \in \mathcal{N}(1)} p_{kn} \\ \vdots \\ \sum_{k \in \mathcal{N}(m)} p_{kn} \end{pmatrix} \end{aligned} \quad (2.10)$$

where $\mathcal{N}(m)$ denotes the set of neighbouring cells that correspond to cell m . To improve performance, \mathbf{N} is stored as a sparse matrix in Matlab, which significantly reduces computational cost at larger numbers of cells.

2.4.3 Parameter space explorations and parameter selection

Parameter space 2D maps were used to visualise regions of different model behaviour (Figure 5, Appendix Figure S54 and Appendix Figure S6). These parameter spaces have intercellular time delay plotted along the x-axis and repression threshold value along the y-axis and at each point, an output value of the model is plotted (e.g. temporal period). For each grid point in parameter space, the average output from 5 simulations with random initial conditions is shown. Parameter selection (Figure 5F) was used to identify suitable ranges for intercellular time delay and repression threshold by comparing statistics from synthetic data against experimental statistics obtained from tissue data whereby synthetic data values found within 2.4 standard deviations away from the experimental mean were accepted. Parameter selection was

performed separately for the temporal period and Kuramoto order parameter (see Phase reconstruction). The temporal period was computed from the synthetic time series of HES5 as the inverse of the dominant frequency peak from power spectrum reconstruction by Fast Fourier Transform. The temporal period used for parameter selection was the average period per simulation where single cell period estimates above 10h were excluded as non-oscillatory.

In addition to exploring grids of parameter space, an optimiser approach was also used to ensure a thorough exploration of possible spatial patterns. To search parameter space for a particular spatial period, the in-built Matlab pattern search optimiser approach was used as this does not rely on defining a gradient and works to globally optimise and works well on non-smooth functions. The error was defined as the absolute difference between the model output spatial period and desired period. Parallelisation was used on the inner for-loops to vastly reduce the optimisation time.

2.4.4 Rate of differentiation from synthetic data

We explored how absolute sensing of HES5 by downstream targets might affect the rate of differentiation at different intercellular repression thresholds (coupling strengths) by assuming a simple linear differentiation condition where lower HES5 levels increase the probability of a cell committing to eventual differentiation (Figure 6A). This assumption is based on the fact that HES5 represses downstream pro-neural targets which promote a cell to head towards a differentiated state. Because the level of expression changes as the coupling strength is varied, no set absolute threshold is assumed, instead a differentiation threshold is determined from the mean population expression in each simulation. Above this threshold, a cell has a zero chance of differentiation, whereas below the threshold has a linearly increasing probability of differentiation the further it drops below the threshold. A probability is calculated at each time point with no memory of past HES5 dynamics and is calculated as

$$P(diff | P_i(t)) = \begin{cases} 0, & P_i(t) > D_{thresh} \\ R \left(\frac{D_{thresh} - P_i(t)}{D_{thresh}} \right), & P_i(t) < D_{thresh} \end{cases} \quad (2.11)$$

where R is the differentiation rate (with units of Δt^{-1} as the probability of differentiation is calculated on every time step), and D_{thresh} is the differentiation threshold.

Cells are simply marked as having differentiated in this setup, and the dynamics of

an individual cell remain the same after a differentiation event, which can be thought of as an asymmetric division, where the differentiating cell leaves the population and its space in the grid is filled with a non-differentiating cell. The differentiation rate is calculated by taking the total number of differentiation events in a simulation and dividing it by the total time. Single-cell parameters used are shown in Appendix Table S3, and the multicellular parameters used were $n_{ND} = 4$, $\tau_N D = 150min$, and the range of repression thresholds explored was $500 < P_{ND0} < 30000$.

Chapter 3

A travelling wave model of dynamic periodic expression

3.1 Introduction

The last chapter explored which aspects of the dynamic spatial pattern a model of multicellular Notch-Hes5 could reproduce. These simulations modelled protein and mRNA expression in single cells which were previously parameterised to single-cell HES5 time traces. The single-cell Hes5 dynamics were then coupled via decreasing Hill functions that approximated the effects of Notch-Delta lateral inhibition. When a time delay between cells in this model was set to the expected Notch signalling time delay, clusters of locally synchronised ultradian oscillations formed which are observed in the data. However, these clusters were infrequent and unable to regularly organise into a spatially periodic pattern.

Other regions of parameter space were found to produce periodic spatial patterns but these were smaller than the observed 3-4 cell periodicity, and consistently produced 2-cell periodicity. While the cells in this 2-cell pattern were able to oscillate and stochastically fluctuate, the pattern was not dynamic in the sense that once cells reached the high or low expression states determined by lateral inhibition, they would remain stuck and unable to switch to the opposite state. Through thorough exploration of the parameter space using an optimisation approach, no parameter sets could be identified that satisfy the 3-4 cell periodicity seen in the data. This implies that either the Notch-Hes5 interactions are not part of the underlying pattern-generating mechanism or there are missing assumptions in the Notch-Hes5 model.

Given that Hes5 expression largely depends on Notch activity, the following two chapters continue with the assumption that Notch signalling underlies the pattern, and two additional models that extend the Notch-Hes5 model presented in Chapter 2 are explored. The first is a travelling wave model, chosen because this type of wave be-

behaviour would create dynamic high and low states as the wave moves through the tissue, and could potentially generate the correct spatial period if the wavelength can be sufficiently tuned. The second model includes extending the signalling distance between cells to produce the 3-4 cell periodicity seen in the data, as well as enabling differentiating cells to perturb the pattern by altering their Notch interactions with neighbouring cells, so as to enable dynamic patterning.

This chapter explores the first hypothesis of travelling waves as an underlying mechanism, which is motivated by the fact that transient travelling wave-type behaviour is occasionally seen in the kymographs produced from the HES5 fluorescence data of the neural tube as shown in Figure 3.1D. Travelling waves also occur during the developmental process of somitogenesis, which is another example of a Notch-Hes system of interacting cells. In somitogenesis these travelling waves occur in the developing presomitic mesoderm as a region of high Hes expression (amongst other genes) which sweeps along the anterior-posterior axis of the tissue repeatedly, always beginning at the tail end and progressing towards the head (Figure 3.1A). Once the travelling wave reaches a certain distance from the tail end, it slows and stops, subsequently defining the location of the next somite (Figure 3.1B&C). Over the course of somitogenesis, this repeating temporal process leads to the repeating spatial distribution of somites which eventually form ribs and skeletal muscle (Maroto et al., 2012).

The synchronisation of the Hes oscillations is maintained via Notch signalling (Özbudak & Lewis, 2008) and so the network of interaction between the cells in the presomitic mesoderm is similar to the multicellular lateral inhibition model presented in the previous chapter. Therefore this model should be able to produce similar travelling waves under the right conditions and because the wave of travelling expression covers multiple cell widths, it could potentially account for the clustering in addition to the dynamic switching that occurs in the developing neural tube. Important to note however is that the travelling waves seen in the kymographs in Figure 3.1D are much less coherent than the waves seen in somitogenesis which are highly regular. Therefore in this chapter, specific attention will be given to how coherent the travelling waves are in a Hes5-specific model when compared to the kymographs in Figure 3.1D.

This chapter is presented in a traditional thesis format and is included at this point to follow the chronological order of research and gives an expanded view into how different models were tested and selected based on their explanatory power. The following section explores how travelling waves can be induced in a lateral inhibition model when spatial parameter gradients are imposed. The spatial period is found

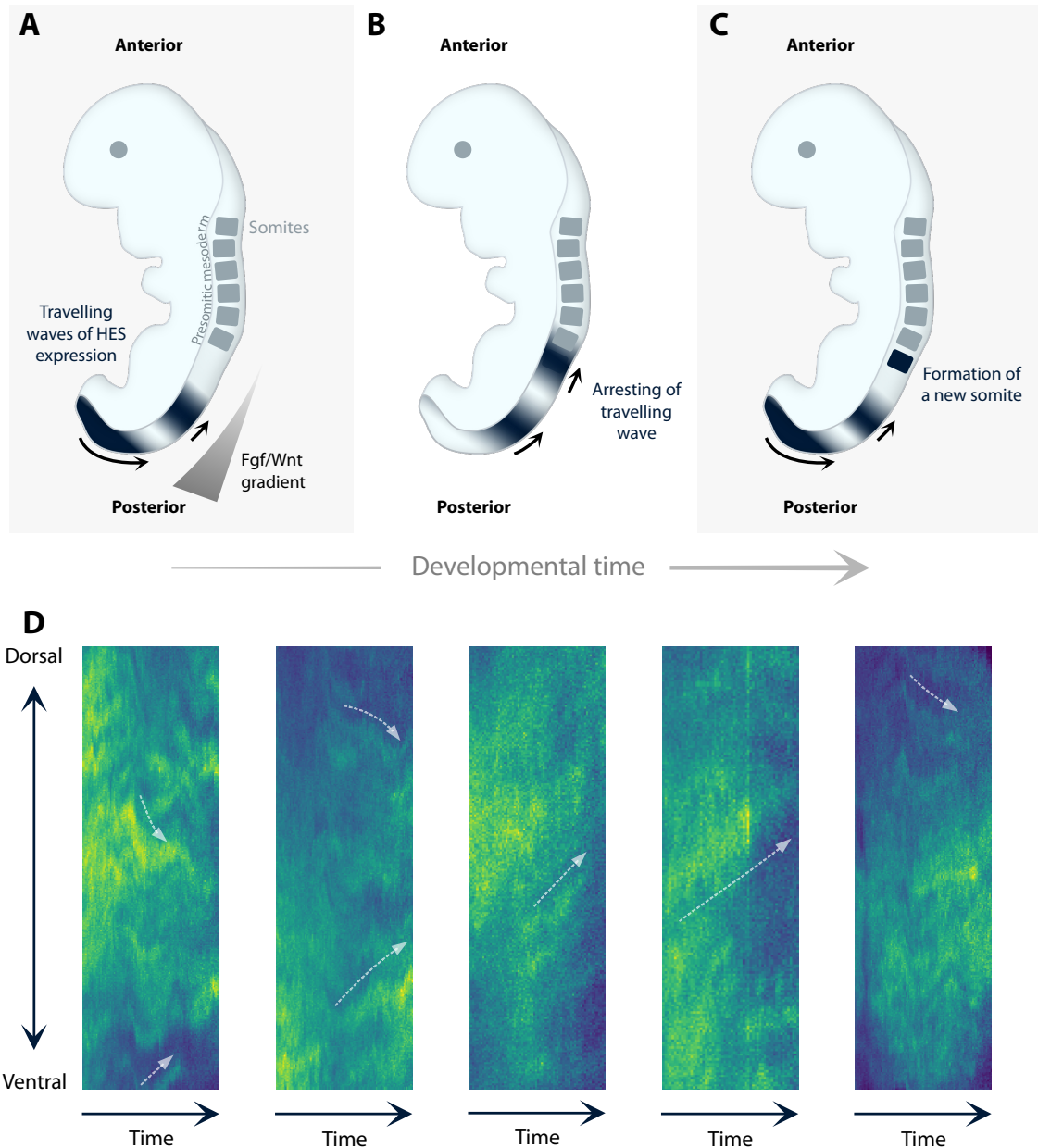


Figure 3.1: How travelling waves progress during somitogenesis and examples of travelling wave behaviour in neural tube HES5 expression. **A** At the posterior end of the presomitic mesoderm a synchronised region of HES expression continuously oscillates, and on each oscillation travels along the Fgf/Wnt gradient towards the anterior end of the tissue. During this time the tail is continuously growing. **B** Once the wave of expression reaches a certain distance from the posterior end, the wave arrests and dictates the position for the next somite to form as shown in **C**. **D** Example kymographs of Venus::HES5 fluorescence in E10.5 embryos taken from data generated for (Biga et al., 2021), with dashed arrows highlighting travelling wave type behaviour. Kymographs were constructed in the same way as described in the methods of (Biga et al., 2021). 5 kymographs generated from 3 embryos are shown.

to be modulated by varying the steepness of the gradient, and the travelling waves make the pattern dynamic, as the peaks and troughs of the spatial pattern change over time. However, the constant travelling of the waves is too coherent when com-

pared to the data and so the introduction of noise is also explored in an attempt to break up the travelling while maintaining the pattern. While the travelling wave mechanism produced interesting dynamic patterning, it ultimately could not account for several key observations in the neural tube HES5 pattern.

3.1.1 The multicellular lateral inhibition HES5 model

The same base model is used as in the published work in Chapter 2 and 4, however, Chapter 4 uses an updated notation which is also used here in this chapter. The methods section from the manuscript in Chapter 4 is copied here and adjusted in relevant places for ease of readability to ensure the modelling approach is clearly outlined (taken from (Hawley et al., 2022)).

The core model is based on previously implemented modelling work, consisting of autoinhibition interactions of HES5 protein back on to expression of its own mRNA, and with HES5 dynamics being coupled between cells in a hexagonal geometry using an inhibitory Hill function representative of Notch lateral inhibition (Collier et al., 1996; Monk, 2003). The single-cell parameters used in the model were previously parameterised to neural tube HES5 data using Bayesian inference (Manning et al., 2019), and a range of multicellular parameters were explored in (Biga et al., 2021). The various interactions and the interactions each parameter of the model maps onto is illustrated in a two-cell model in Figure 3.2A. To simulate the model, a Chemical Langevin equation approach is used (Gillespie, 2000), and the stochastic delay differential equations that govern the dynamics of a cell at row i and column j (see Figure 3.2B) in the multicellular model is given by

$$\frac{dm_{ij}(t)}{dt} = -\mu_m m_{ij}(t) + \alpha_m H_{auto}(p_{ij}(t - \tau_{auto})) H_{LI}(\bar{p}_{ij}(t - \tau_{LI})) + \eta_m, \quad (3.1)$$

$$\frac{dp_{ij}(t)}{dt} = -\mu_p p_{ij}(t) + \alpha_p m_{ij}(t) + \eta_p, \quad (3.2)$$

where $m_{ij}(t)$ is HES5 mRNA concentration in the cell on the i^{th} row and j^{th} column at time t and $p_{ij}(t)$ is HES5 protein concentration. μ_m and μ_p are the degradation rates of mRNA and protein respectively, α_m and α_p are the transcription and translation rates respectively, τ_{auto} is the time delay associated with HES5 autorepression and τ_{LI} is the time delay associated with the lateral inhibition interaction between cells.

The functions H_{auto} and H_{LI} are both inhibitory functions that regulate mRNA pro-

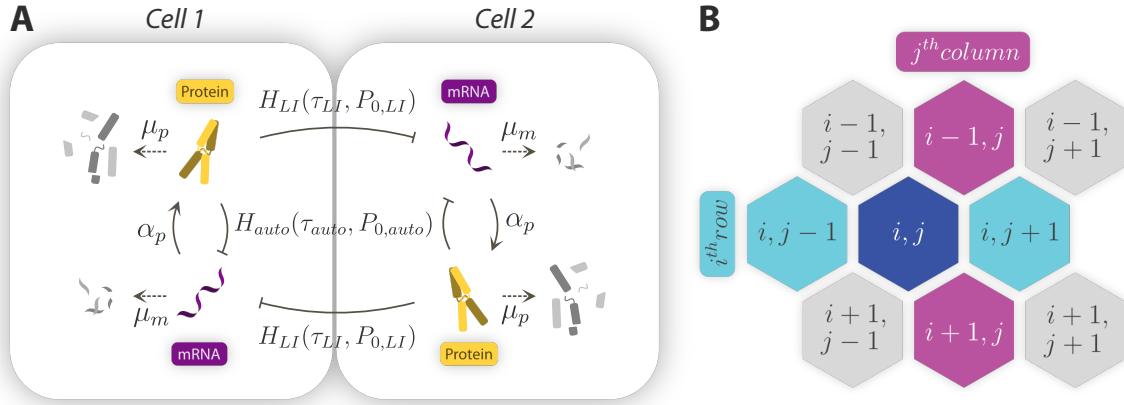


Figure 3.2: Schematic of the model and indices used in Chapter 3. **A** Summary of the updated notation for the model parameters detailed in §3.1.1 and summarised in Table 3.2, and which processes they map to in the multicellular model. **B** Indices in the model equations relate to the hexagonal geometry as shown.

duction rate in response to protein abundance either within a cell (H_{auto}) or between cells (H_{LI}). H_{LI} therefore is the coupling function that enables HES5 dynamics to influence neighbouring HES5 dynamics. For the signalling contribution from each cell in contact with a receiving cell, the approach used by (Collier et al., 1996; Tiedemann et al., 2017) is taken where the amount of HES5 a cell receives is the averaged abundance from all signalling neighbours

$$\bar{p}_{ij} = \frac{1}{|\mathcal{N}(i, j)|} \sum_{(i, j) \in \mathcal{N}(i, j)} p_{ij}, \quad (3.3)$$

where $\mathcal{N}(i, j)$ is the set of neighbours a cell is in signalling contact with and $|\mathcal{N}(i, j)|$ is the total number of neighbours in the set.

The Hill functions are both decreasing functions where $H_{auto}(0) = H_{LI}(0) = 1$ and $H_{auto}(\infty) = H_{LI}(\infty) = 0$ and have the form

$$H_{auto}(p_{ij}(t - \tau_{auto})) = \frac{1}{1 + (p_{ij}(t - \tau_{auto})/P_{0,auto})^{n_{auto}}}, \quad (3.4)$$

$$H_{LI}(\bar{p}_{ij}(t - \tau_{LI})) = \frac{1}{1 + (\bar{p}_{ij}(t - \tau_{LI})/P_{0,LI})^{n_{LI}}}. \quad (3.5)$$

$P_{0,auto}$ and $P_{0,LI}$ are the repression thresholds of each Hill function. The repression threshold defines the amount of protein that results in a 50% reduction in mRNA

production rate. For example, within an individual cell, the value of $P_{0,auto}$ defines the abundance of HES5 protein, p_{ij} , at which mRNA production rate will be 50% within that same cell. In the case of $P_{0,LI}$, this defines when mRNA production in a receiving cell will be 50% in response to the averaged incoming abundance of HES5 protein in the neighbouring cells \bar{p}_{ij} . n_{auto} and n_{LI} are the Hill coefficients which define how steep the gradient of the Hill function is at P_0 (higher values give a sharper transition between no repression and repression).

The terms η_m and η_p in equations 3.1 and 3.2 are the stochastic noise terms for mRNA and protein which are Gaussian white noise scaled by the square root of the number of events that occur in each process:

$$\eta_m = \sqrt{\mu_m m_{ij}(t) + \alpha_m H_{auto}(p_{ij}(t - \tau_{auto})) H_{LI}(\bar{p}_{ij}(t - \tau_{LI}))} \xi_m(t), \quad (3.6)$$

$$\eta_p = \sqrt{\mu_p p_{ij}(t) + \alpha_p m_{ij}(t)} \xi_p(t), \quad (3.7)$$

where $\xi_m(t)$ and $\xi_p(t)$ are Gaussian white noise with mean of 0 and variance of 1. Equations are solved using the Euler-Maruyama method, implemented in MATLAB.

3.2 Results

3.2.1 Perturbations do not result in travelling waves in the base lateral inhibition model

In systems that exhibit travelling wave behaviour, some sort of perturbation is required to initiate the wave. For example, a rock hitting the surface of a body of water perturbs the otherwise flat surface, causing ripples to travel outward and eventually return to a non-moving surface. If this perturbation were made regular then it can be seen how a dynamic spatially periodic pattern would form. This section aims to characterise how the multicellular model responds to perturbation and whether it naturally exhibits a travelling wave behaviour.

This involved simulating a grid of cells (Figure 3.3A&C) and solving deterministically using a set of parameters that resulted in a uniform steady state across the tissue (Table 3.1). The coupling strength ($P_{0,LI}$) was chosen to be weak enough so that lateral inhibition didn't result in alternating high and low expression between neighbouring cells, but still strong enough to cause a change in neighbouring cell expression when perturbed as can be seen in Figure 3.3A&B. The perturbations are applied

by clamping or forcing the expression in a small region of the grid to zero expression. After a short period of time, unclamping allows the region to resume normal kinetics according to the model equations.

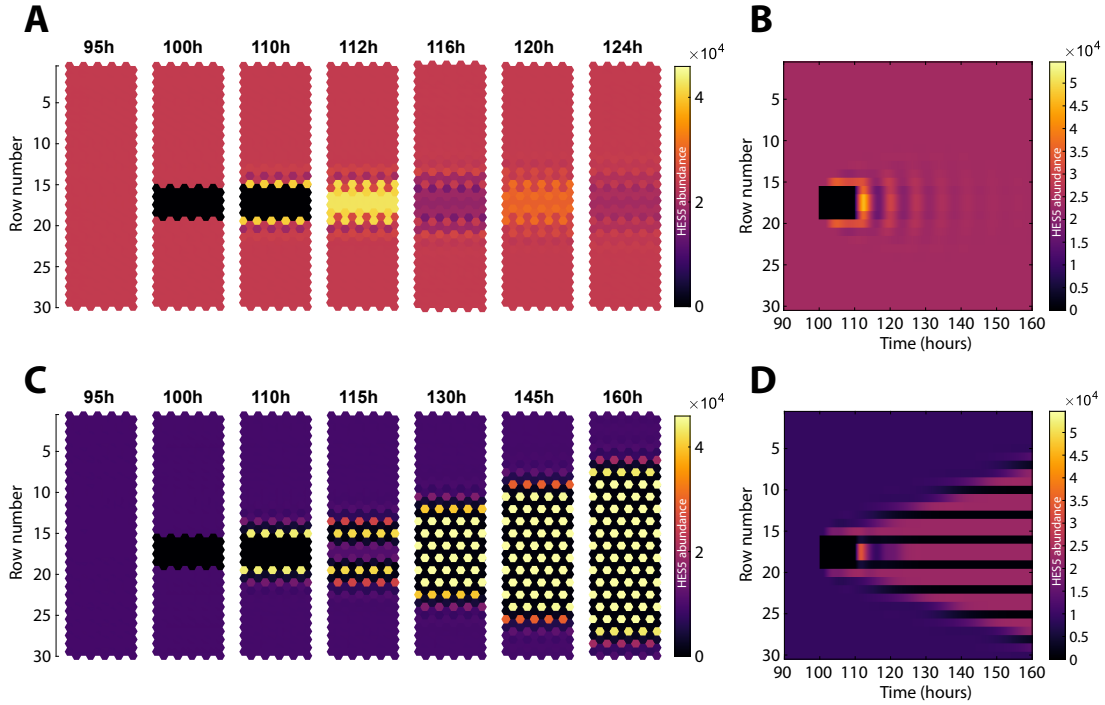


Figure 3.3: *In-silico* clamping experiment shows that travelling waves do not naturally occur in a grid of cells coupled by lateral inhibition. The grid size used is 10 columns by 30 rows, all cells begin with the same initial conditions and simulations are deterministic. **A** Several snapshots from different time points in the simulation where coupling strength is relatively weak (parameters given in Table 3.1). **B** The same simulation as in **A** is plotted as a kymograph which shows the averaged expression from all columns over time. **C** Several snapshots from a simulation using a relatively strong coupling strength (parameters given in Table 3.1). **D** Kymograph of the simulation shown in **C**.

Table 3.1: Model parameters used in Figure 3.3.

Symbol	Panels A&B	Panels C&D	Biological definition
a_m	0.70 min^{-1}	0.70 min^{-1}	Transcription rate
a_p	18.5 min^{-1}	18.5 min^{-1}	Translation rate
u_m	$\ln(2)/30 \text{ min}^{-1}$	$\ln(2)/30 \text{ min}^{-1}$	mRNA degradation rate
u_p	$\ln(2)/90 \text{ min}^{-1}$	$\ln(2)/90 \text{ min}^{-1}$	Protein degradation rate
$P_{0,auto}$	54,656 proteins	54,656 proteins	HES5 autoinhibition repression threshold
$P_{0,LI}$	20,000 proteins	5,000 proteins	Lateral inhibition coupling repression threshold
n_{auto}	2.6	2.6	HES5 autoinhibition Hill coefficient
n_{LI}	3	3	Lateral inhibition Hill coefficient
τ_{auto}	38 mins	38 mins	HES5 autoinhibition time delay
τ_{LI}	100 mins	50 mins	Lateral inhibition time delay

Figure 3.3A shows several snapshots from a simulation where zero-expression clamp-

ing is applied at 100h to rows 16-19 and is released at 110h. The same simulation is also seen in Figure 3.3B as a kymograph and the clamping can be seen as a black square starting at 100h. If the system were to exhibit travelling wave behaviour in response to this perturbation, the expected outcome would be diagonal lines in the kymograph. However, when clamping is applied the perturbation doesn't travel far, affecting only 2-3 cells away and inducing a localised lateral inhibition high-low stationary pattern (Figure 3.3A&B). After the clamping is released at 110h, expression quickly recovers, overshoots, and subsequently undergoes damped temporal oscillations. Importantly these oscillations do not spread across the tissue, remaining confined to the previously clamped region, before eventually returning to a uniform steady state.

This result indicates that in the current model, information does not spread far through the tissue from individual cells, meaning that, unlike ripples on the surface of a body of water, perturbations remain relatively confined in space due to the lateral inhibition interaction. However, if coupling strength is increased, the perturbation results in the system collapsing into a high-low salt and pepper pattern and this does indeed spread as a wavefront throughout the whole tissue (Figure 3.3C&D). While this indicates that information can spread further with increased coupling strength, the travelling wavefront is not of the type seen in ripples of water or somitogenesis. The salt and pepper pattern left behind prevents any further wavefronts from following after it. Therefore an additional change in the model is required to induce travelling waves.

3.2.2 A spatial gradient in any model parameter results in travelling waves

Somitogenesis modelling studies have found that applying a spatial gradient to the reaction kinetics of cells such as mRNA/protein half-life, degradation and even coupling strength results in travelling waves (Ishimatsu et al., 2018; Uriu et al., 2009). To determine if gradients result in travelling waves in the Notch-Hes5 model, spatial gradients were applied in one direction to a given model parameter. This was implemented by defining a minimum and maximum gradient value g_{min} and g_{max} and then for a simulated grid size of I -rows by J -columns, the gradient value in each cell was defined as

$$G_{ij} = g_{min} + \left(\frac{i-1}{I-1} \right) (g_{max} - g_{min}), \quad (3.8)$$

where G_{ij} is the value of the parameter in cell i, j as defined in Figure 3.2B. In this way, cells in the same row will all have the same parameter value and the gradient is linearly interpolated along the vertical axis of the grid.

As travelling waves in somitogenesis are a wave of synchronised oscillations, a parameter set (Table 3.2) that results in global synchronisation was chosen to ensure cells synchronise with each other, as shown by the kymograph in Figure 3.4A (kymographs were constructed as outlined in Methods 3.4.2). A grid size of 26 rows by 6 columns was used as these are the approximate dimensions of the p0-p2 & pMN neuron domains which express HES5.

In Figure 3.4Bi, a gradient is applied to the lateral inhibition repression threshold parameter ($P_{0,LI}$) which runs from $P_{0,LI} = g_{min} = 8000$ proteins at the top of the grid up to $P_{0,LI} = g_{max} = 16000$ proteins at the bottom. The subsequent dynamics that arise can be seen as diagonal lines travelling upwards in the kymograph, indicating the presence of travelling waves. Previous somitogenesis modelling studies suggest that a number of different parameters should be able to generate travelling waves, not just $P_{0,LI}$ (Ishimatsu et al., 2018; Uriu et al., 2009). Indeed it was found that any parameter in this model can result in travelling waves when a gradient is applied, as is shown in the rest of the kymographs in Figure 3.4Ci&D. These kymographs display a mix of travelling wave speeds and direction of travel. Wave speed can be seen by the angle of the lines in the kymographs, with slower travelling waves stretching further along the time axis before reaching the other end of the tissue.

Table 3.2: Nominal model parameters used in Figure 3.4, 3.5, 3.6, 3.7. If a gradient is used instead of the nominal parameters here, then this is made explicit in the figure. This parameter set results in global synchrony in the absence of gradients and was identified using the work in Chapter 2.

Parameter	Value
a_m	0.77 min^{-1}
a_p	26 min^{-1}
u_m	$\ln(2)/30 \text{ min}^{-1}$
u_p	$\ln(2)/90 \text{ min}^{-1}$
$P_{0,auto}$	25,000 proteins
$P_{0,LI}$	12,000 proteins
n_{auto}	3.5
n_{LI}	4
τ_{auto}	30 min
τ_{LI}	140 min

The reason why parameter gradients induce travelling waves at all seems to be because the kinetics of the reactions either slow or accelerate depending on the value of

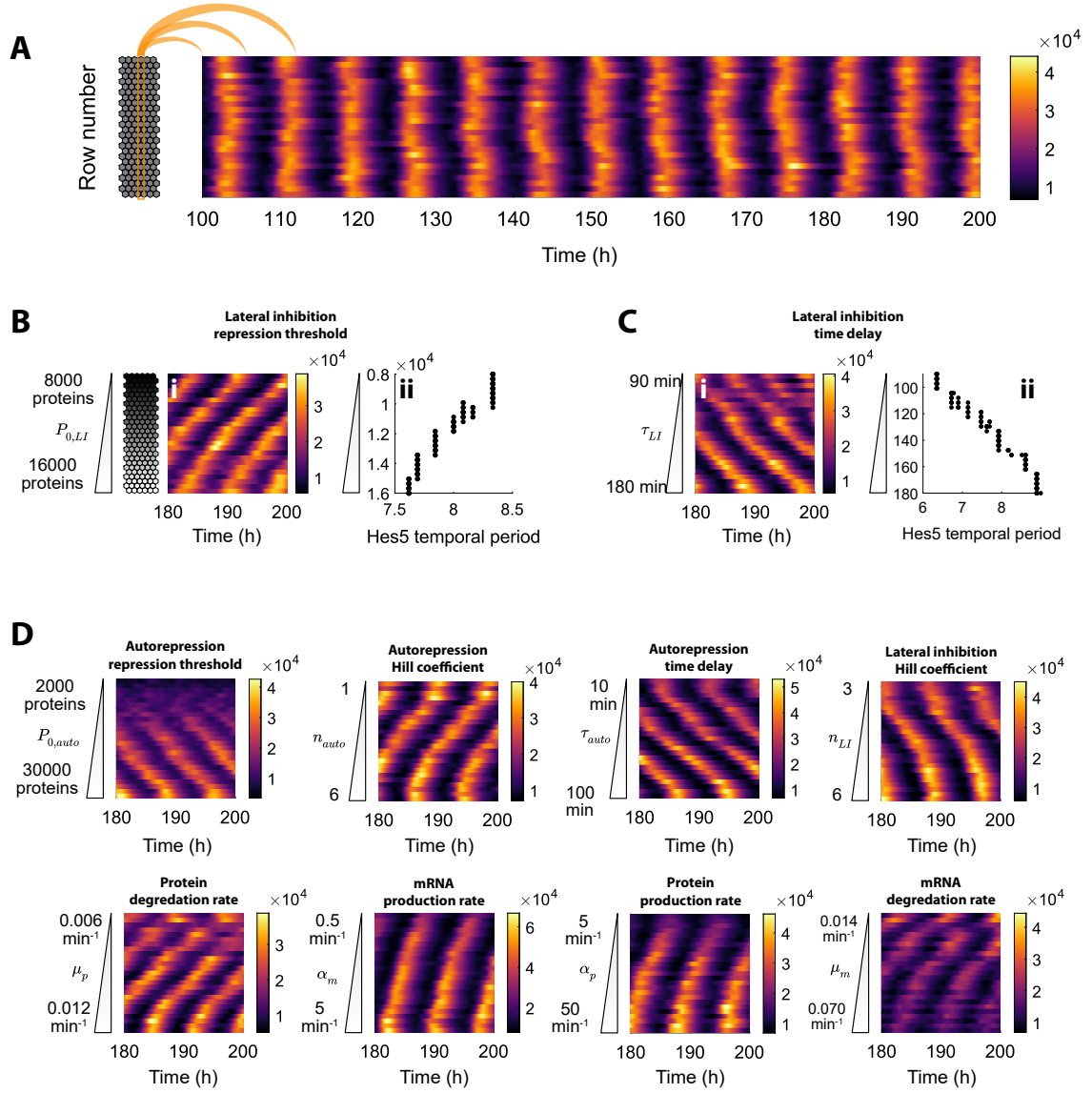


Figure 3.4: Applying a spatial gradient to any parameter results in travelling waves. **A** Kymograph of the model run with the parameters in Table 3.2, with no gradient applied spatially to any of the parameters, which results in global synchronisation. A grid size of 6 columns by 26 rows was used in the simulations and the kymographs are constructed as outlined in Methods §3.4.2. **Bi** The same simulation as in **A** but with a gradient applied to the lateral inhibition repression threshold, $P_{0,LI}$ (which determines coupling strength). **Bi** Plot of individual cell oscillation periods against the parameter value in that cell (temporal period calculated as described in Methods §3.4.1). **Ci** & **ii** are the same as **B** but the gradient is in the lateral inhibition time delay, τ_{LI} . **D** Kymographs of all remaining model parameter gradients.

the parameter being changed. This means that along the axis of the gradient, there will always be a neighbour on one side of an oscillating cell that will respond more slowly than the other side, resulting in a progressive phase shift in what would otherwise be a globally synchronised tissue if the parameter gradient were absent.

This gradient in reaction speed can be quantified by looking at the distribution of temporal period versus parameter value in each cell. In Figure 3.4Bii where a gra-

gradient is applied to $P_{0,LI}$, higher $P_{0,LI}$ values result in shorter temporal periods (i.e. faster reaction kinetics), with temporal periods of around 7.5h at the bottom of the grid and 8.5h at the top. Furthermore, upon inspection of the direction of the travelling waves for each parameter gradient, it is found that waves always travel from the end with faster kinetics towards the end that has slower kinetics (from shorter temporal periods towards longer periods shown in Figure 3.4B&Cii). This supports the idea that cells try to synchronise phase but the slower kinetics in the neighbour leads to a progressive phase shift along the gradient.

3.2.3 Steeper gradients result in slower travelling waves and shorter spatial periods

In Figure 3.4, τ_{auto} produced one of the slowest travelling waves, and so the difference between when a gradient is present versus absent is one of the most extreme out of all the parameters. Therefore it is used in this section to visualise how gradient steepness affects the wave speed and importantly how this affects the spatial period.

Starting with the absence of a gradient in τ_{auto} ($\tau_{auto} = 60\text{min}$ across the whole grid), oscillations globally synchronise as expected (Figure 3.5Ai). Upon visual inspection of Figure 3.5Aii which shows the final time point from the same simulation, no clear spatial period can be seen. To quantify the spatial period at each time point, a Fourier transform method is combined with a Fisher-G test to identify statistically significant periods (Methods §3.4.3). The distribution of significant spatial periods is shown in Figure 3.5Aiii, and while an average period of 8.4 cells is detected, it is important to note that these spatial periods were detected at a very low rate of about 2-5% of all time points tested in each simulation, which is generated by chance due to stochasticity and imperfect synchrony in the model.

Figure 3.5Bi through to Di show that as the τ_{auto} gradient steepness increases, the slower the travelling waves become, appearing more diagonal in the kymographs. Additionally Figure 3.5Biii through to Diii indicates that slower travelling waves result in smaller spatial periods. Important to note is that wavelengths (spatial periods) equal to the length of the simulated grid (in this case 26 cells) were excluded as valid detected periods and so the largest detected period via this method is half the grid size (13 cells). Therefore in Figure 3.5, detected periods become more frequently detected once the travelling waves are slanted enough to form two peaks of expression within the tissue.

The maximum range tested for τ_{auto} was 10min-110min, which is a rather large fold-change biologically. Previous modelling studies have estimated the nominal value of

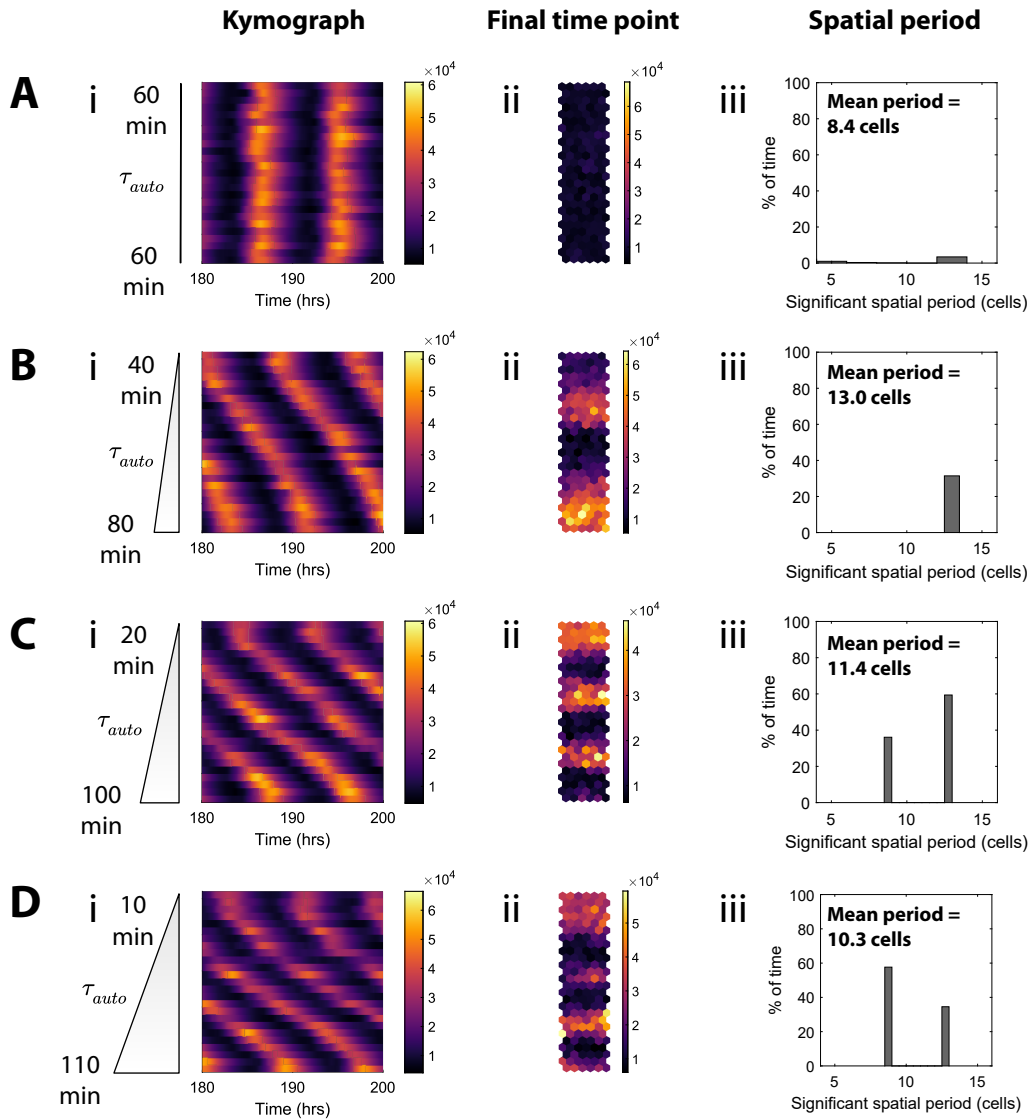


Figure 3.5: Steeper parameter gradients result in slower travelling waves and shorter spatial periods. Panels **A-D i** show kymographs with increasing τ_{auto} gradient steepness. **A-D ii** Show the final time point for the same simulations in **i** (grid size 6 columns by 26 rows). **A-D iii** Histograms of spatial period detected and the percent of time point where a spatial period is detected using the significance testing outlines in Methods §3.4.3.

τ_{auto} is around 15-30min (Lewis, 2003; Manning et al., 2019; Phillips et al., 2016), and further estimates of how much τ_{auto} varies along the length of the developing presomitic mesoderm during somitogenesis is around 4.4 fold, ranging from around 10 minutes to 40 minutes (Ay et al., 2014). Assuming a range of 10-110min is possible, this only produces a mean spatial period of around 10 cells (Figure 3.5Diii), whereas the neural tube pattern has a spatial period of 3-4 cells.

Another mismatch between the travelling wave model and the neural tube data is

how coherent the waves are. While the fact the waves mean the pattern is dynamic like in the neural tube, the neural tube only occasionally exhibits coherent travelling waves and they do not last for long, with the pattern being much noisier than in the simulations presented thus far (see Figure 3.1D for the type of travelling wave seen in the data). The next section attempts to break up these coherent travelling waves by using noisy parameter gradients to see if the output is more similar to the data.

3.2.4 Noise in the parameter gradient does not bring the model output closer to the travelling wave behaviour of the neural tube

The neural tube HES5 pattern exhibits more incoherent dynamics than that seen in the continuous travelling waves produced by the simulations. Therefore to see if the travelling waves in the model could be made more incoherent, noise was added to the pre-defined gradient values by modifying (3.8) to

$$G_{ij} = g_{min} + \left(\frac{i-1}{I-1} \right) (g_{max} - g_{min}) + \xi_{ij}(\sigma), \quad (3.9)$$

where ξ_{ij} is Gaussian noise with a mean of zero and a standard deviation σ . The gradient range for this section was set to $10\text{min} \leq \tau_{auto} \leq 110\text{min}$. Figure 3.6A-Ci show increasing standard deviation (σ) values applied to noise in the parameter gradients, where cells are coloured by τ_{auto} values.

The noise was either stationary throughout the whole simulation, i.e. $\xi_{ij}(\sigma)$ in (3.9) is only calculated once for each cell, or the noise was dynamic and allowed to refresh at set time intervals. That is, every N -time steps, a different random seed was used to recalculate the noise term $\xi_{ij}(\sigma)$ in every cell.

In the stationary case (Figure 3.6A-Cii), the gradual increases in σ leads to a gradual disruption of the travelling waves with some disruption at $\sigma = 30\text{min}$, and substantial disruption when $\sigma = 100\text{min}$. The addition of noise effectively brings the system closer to global synchronisation, as can be seen by the increased travel speed of the waves and thus longer periodicity. This is because the noise disrupts the directionality of the gradient as σ increases, and introduces small regions of the tissue where neighbouring cells oppose the global gradient direction. This if anything makes the model output less similar to the neural tube HES5 data because the spatial period is moving further away from the desired 3-4 cell periodicity.

A potentially more realistic type of noise in the gradient could be one where the pa-

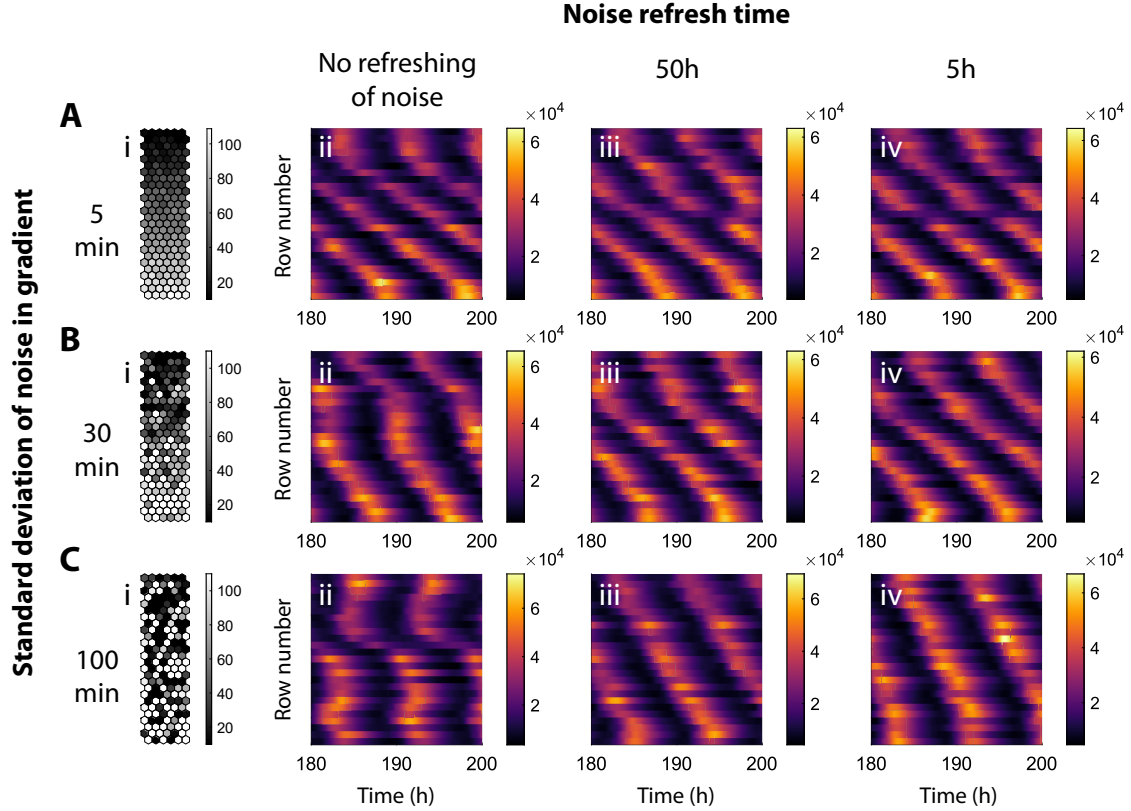


Figure 3.6: The effect of stationary noise and dynamic noise on travelling waves. Panels **A-C i** show the noise in the parameter gradient used in the stationary case in **ii** (no refreshing of noise). **A-C ii** Kymographs of the simulations that use only one noisy gradient over the whole simulation. **A-C iii** Simulations results when the noise in the parameter gradient is refreshed every 50h of simulation time, and **iv** when noise is refreshed every 5h.

parameter in each cell fluctuates around a mean value over time rather than being stationary. To do this in the simulation, the Gaussian noise was recalculated with a new random seed at set time intervals. One set of results refreshed the noise every 50h (Figure 3.6A-C iii) and a second set of results refreshed the noise every 5h (Figure 3.6A-C iv). This tended to result in a recovery from any disruption seen in the stationary noise cases and the coherent travelling waves returned. Therefore the constant refreshing of the noise appears to have an averaging effect rather than fragmenting the waves to something more like the transient and infrequent travelling waves observed in the neural tube HES5 expression (Figure 3.1D).

In sum, while the addition of noise to the parameter gradients does disrupt the travelling waves, it does so in a manner that takes the model's output further away from the desired output. The spatial period is lengthened and the system approaches a more globally synchronised behaviour when large amplitude stationary noise is applied. When dynamic noise is applied, the system simply recovers to a coherent travelling wave behaviour, as the continuously fluctuating noise acts the average out any

irregularities in the gradient.

3.2.5 HES5 oscillations are not nested within the longer period, larger amplitude oscillations

An additional aspect of the data that should be produced by the model is the nested autonomous HES5 oscillations within the longer period switching of the spatial pattern that occurs. Simulations of the uncoupled model show what the autonomous HES5 oscillations look like (Figure 3.7Ai), and averaged power spectra (Methods §3.4.1) of all the individual cell time-traces indicate that the autonomous oscillations have an average period of 5.9h. From the power spectra, a coherence measure as described in Methods §3.4.4 indicates that the autonomous oscillators across the population have a low coherence indicating that they are noisy and have variation in their temporal period as can be seen in the histogram of temporal periods within Figure 3.7Aii.

Cells were then coupled together, (using the nominal parameters in Table 3.2), which resulted in global synchrony (Figure 3.7Bi). In comparison with the autonomous oscillations, the coupled dynamics exhibit larger amplitude (larger peak to trough fold difference) as well as a longer temporal period of 8h (Figure 3.7Bii). Upon inspection of the traces in Figure 3.7Bi, there are no obvious smaller amplitude autonomous HES5 oscillations nested within the coupled dynamics, and the power spectrum (Figure 3.7Bii) is highly coherent with no substantial second peak around the expected autonomous period of 5.9h.

This indicates that global synchrony, which turns into travelling waves when a gradient is applied, does not exhibit nested oscillations like that observed in the neural tube HES5 data, and so this is an additional aspect of the data that is not reproduced by this model.

3.3 Discussion

Through exploring the travelling wave model as a mechanism to describe the neural tube HES5 pattern, it has been found that it shares similar qualitative features with the data. The first is that travelling waves result in a dynamic expression that switches between high and low states over time within the same spatial location. The second is that a travelling wave is itself a cluster of similar expression, and when multiple travelling waves are present across the tissue this results in a spatial pattern.

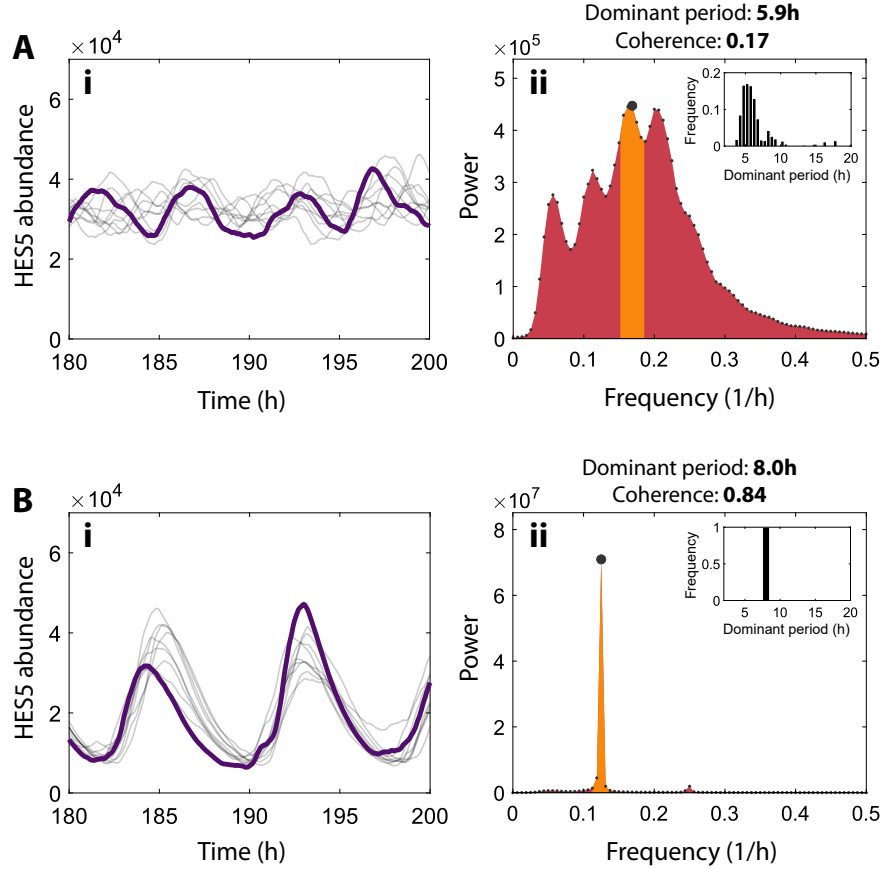


Figure 3.7: Autonomous HES5 oscillations are not nested within the coupling-induced globally synchronised oscillations. Example traces were generated using the nominal parameters in Table 3.2 for uncoupled (A) and coupled (B) cells. A total of 5000 cells were simulated in a grid of 100 by 50 cells to generate the data shown. **Ai & Bi** Traces from 10 randomly selected cells are shown as grey lines with one trace highlighted in dark purple. **Aii & Bii** Power spectra with coherence measurement band highlighted in orange. Histograms of the periods from the same power spectrums are shown within the top right corner of the plots.

Under normal conditions the lateral inhibition system was found not to exhibit travelling waves, instead requiring the presence of a gradient in one of the model parameters to be induced, and this is consistent with previous studies of somitogenesis. Additionally, it was determined that the reason parameter gradients induce travelling waves in an otherwise globally synchronous tissue is that it establishes a gradient of reaction kinetic speeds. One oscillating cell that would otherwise attract a neighbouring oscillator to the same phase can no longer do so because the neighbour is slower to respond and so a phase lag is introduced. Scaled along the whole length of the simulated tissue, the ever-slowng kinetics in the next neighbouring cell leads to a progressive phase shift and thus the travelling wave behaviour emerges.

While this mechanism produces somewhat similar patterns to the data, there has been no experimental exploration of graded parameters in the HES5 domain of the neural tube. Therefore to assess how likely a parameter gradient might be, the origin

and values of parameters in somitogenesis can be considered as a ballpark estimate. During somitogenesis, it is the gradient of FGF that enables travelling waves to form (Ishimatsu et al., 2010), though the exact cellular parameter FGF affects has had many proposed candidates. One study managed to predict that the transcriptional and translational time delays were the most likely graded parameters and then went on to measure translational delays along the anterior-posterior axis, finding a 4.4-fold difference in protein translation rate occurs across the length of the presomitic mesoderm (Ay et al., 2014). The lateral inhibition model in this chapter used parameter gradients with fold changes ranging between 2-fold in the protein degradation rate up to 10-fold in the autorepression time delay. Given that these lie within the same order of magnitude as the experimentally measured fold change in somitogenesis, the parameter gradients tested seem to be within a reasonable range.

However, if it is assumed that it is the morphogen gradients present in the neural tube are what set up any potential parameter gradient, the existence of a parameter gradient seems less feasible. Shh, Wnt, and BMP are the known morphogens present in the neural tube and determine the location of distinct progenitor domains, and are produced at either the dorsal or ventral extremes of the neural tube (Zagorski et al., 2017). Therefore the HES5 domain which is being modelled here represents only a small region within the entire length of these morphogen gradients, meaning that the cells in the HES5 domain would need to be very sensitive to a specific range of morphogen concentration in order to have such a high fold-change in parameters. While unlikely, there is no existing literature on kinetic parameters and how they vary along the length of neural tube domains, which would be a key point of exploration if this model were to be considered further.

The simulations presented here also suggest a limit to how much the travelling wave can be slowed down and therefore a limit to how small the spatial period can be made. Increasing the steepness of the gradient beyond that presented in this chapter tended to result in the collapse or fragmentation of the travelling wave (data not shown) rather than making it any smaller, and so a period of about 10 cells appears to be the smallest possible period in this model, whereas the data shows an average period of 3-4 cells. One way to shorten the spatial periodicity other than slowing down the travelling waves could be to shorten the temporal period of oscillation so that travelling waves are produced more regularly, however, this would then reduce the switching time of individual clusters and stray further from matching with the data.

Two final discrepancies were found between the model output and the data. Firstly, that the travelling waves are too persistent and not as incoherent as the transitions seen in the data. Disruption to the gradient was tested in the form of adding noise

to the gradients to see if this would break up the smooth travel of the waves. However, it was found that stationary noise made the output of the model less similar to the data and that travelling waves are robust in the presence of dynamic noise that refreshes over time. Secondly, this model did not recapitulate the autonomous HES5 oscillations being nested within the longer period, larger amplitude switching behaviour induced by synchronising cells. Instead, the longer period switching behaviour seemed to dominate over the autonomous oscillations that can be seen when the cells are uncoupled.

Therefore, while the model reproduced an interesting pattern that is both dynamic and spatially periodic, the finer details of the neural tube HES5 pattern are not captured by the model. Therefore it seems unlikely that this is the underlying mechanism considering all the points discussed above. The following chapter explores the final model presented in this thesis and includes two additional mechanisms that result is able to reproduce the missing key features of the data that the travelling wave model did not.

3.4 Methods

All code for this chapter was written in Matlab and is available [here](#).

3.4.1 Measuring temporal periods of single cells

To detect temporal periods in the data, the in-built Fast Fourier Transform (FFT) Matlab function was used on detrended single-cell time traces over the last 80% of the time traces. This was to avoid any spurious dynamics induced by initial conditions affecting the measured period. The detrending method used was a Savitsky-Golay method with a polynomial order of 2 and a frame length equivalent to 40h of simulation time. This produced a detrending line that did not remove short-term variation such as autonomous oscillations but did remove long-term mean expression and thus was able to remove sustained mean expression changes such as when lateral inhibition forces cells to adopt high or low expression.

3.4.2 Extracting spatial signals from the model

The same method as in the published paper in Chapter 4 was used for this Chapter and is copied here for ease of reading (taken from (Hawley et al., 2022)):

To understand what sort of spatial patterns are being produced by the model, spatial signals are extracted using a similar approach to that used for the *ex vivo* analysis in Biga et al., 2021. In the hexagonal grid of cells, $p(x_{i,j}, t_k) = p_{ij}(t_k)$, denotes the protein expression at the i^{th} row, j^{th} column, and k^{th} time-step, and I, J, K are the total number of rows, columns, and time-steps in a given simulation. In the case of simulating a single column of cells ($J = 1$) such as in Figure M3.1A, a spatial signal can be generated for each time point by taking the protein expression along the entire column such that the spatial signal at time-step k and $j = 1$ is

$$S_k(x) = p(x_{1:I,1}, t_k). \quad (3.10)$$

Each spatial signal is therefore a vector of length I where each entry is the expression from an individual cell, and the total number of spatial signals that can be generated from a single simulation is $N_s = K$ (Figure M3.1B). To visualise both spatial and temporal aspects of the data in one plot, the spatial signal can be plotted over a range of time points $S_{k_1:k_2}(x)$ as a kymograph, shown in Figure M3.1A&C.

In the case of simulating multiple columns (i.e. a 2D grid of cells), spatial signals are extracted using a selection region with a width of 1 cell and length I cells (see grey dashed boxes in Figure M3.1C). Due to the hexagonal geometry, on the even rows, two cells fall within this selection region and so the spatial signal is constructed as

$$S_{jk}(x_i) = \begin{cases} p(x_{i,j}, t_k), & \text{if } i \text{ odd} \\ \frac{p(x_{i,j}, t_k) + p(x_{i,j-1}, t_k)}{2}, & \text{if } i \text{ even} \end{cases} \quad (3.11)$$

where even rows use the average of the two cells that fall within the selection region. As there are multiple columns the number of spatial signals generated from a single simulation is $N_s = K(J - 1)$ (Figure M3.1D).

3.4.3 Detecting statistically significant spatial periods

The same method as in the published paper in Chapter 4 was used for this Chapter and is copied here for ease of reading (taken from (Hawley et al., 2022)):

From the extracted spatial signals, a method is needed to detect the presence of statistically significant spatial periodicity in the inherently noisy model outputs. Using

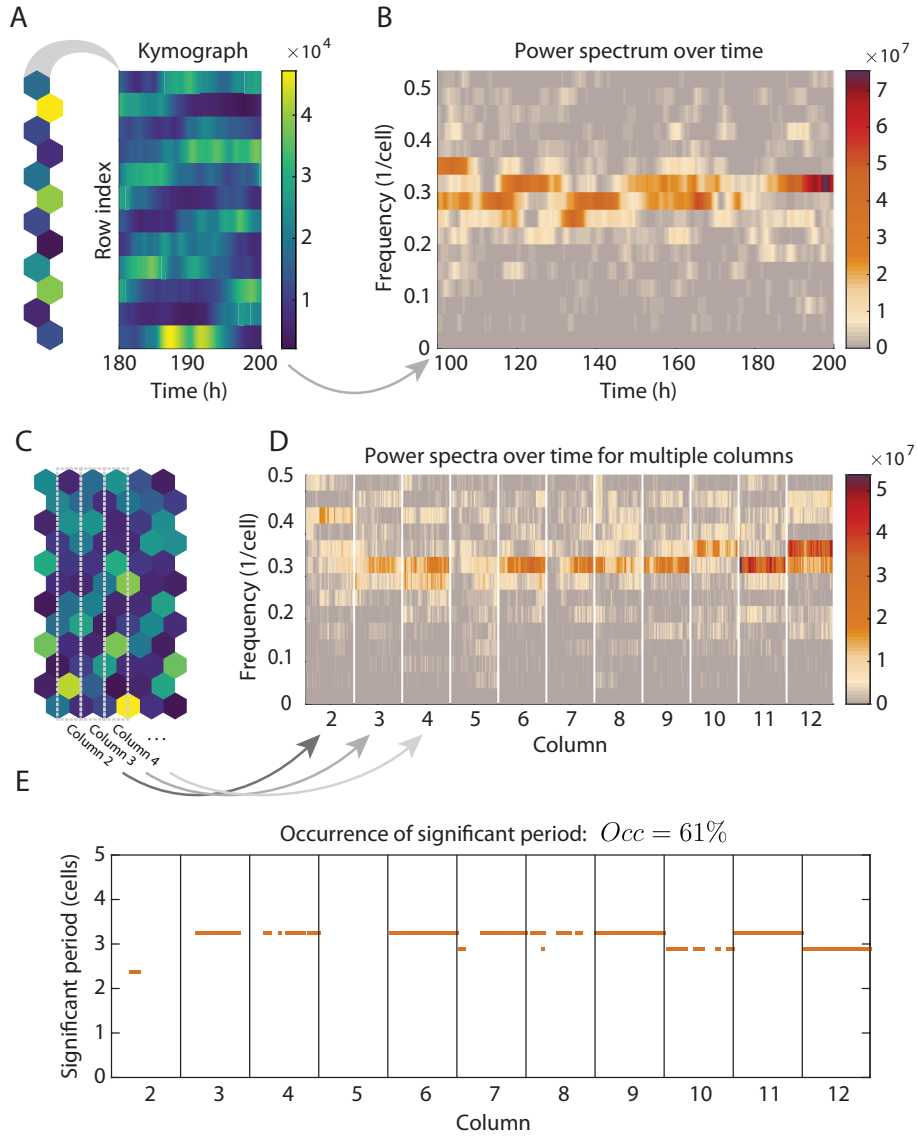


Figure M3.1: Outline of the process used for detecting the presence of significant periodic spatial patterns. **A** In the case of 1D simulations, kymographs are generated from the expression on each row (y-axis) and over time (x-axis). **B** A Fourier transform of the spatial signal in **A** is shown as a power spectrum over time, where colour indicates the power contribution of each frequency at each time point. **C** For 2D simulations, spatial signals are generated from the cells that fall within selection regions (grey dashed boxes). **D** A power spectrum is generated for the spatial signal in each column (within each division the power spectrum over time is given, like in **B**). **E** The peaks of each individual power spectra are tested for significance using the Fisher g -test (Methods §3.4.3) and the significant spatial periods are plotted with orange dots and the occurrence measure is shown above the plot (Occ is defined in Methods §3.4.3).

a fast Fourier transform method (MATLAB), a power spectrum can be obtained for each spatial signal

$$\mathcal{P}(S_{jk}(x)) = |\mathcal{F}(S_{jk}(x))|^2, \quad (3.12)$$

where $\mathcal{F}(S_{jk}(x))$ is the Fourier transform of the spatial signal. The highest power

frequency in the power spectrum indicates the dominant periodicity in the spatial signal (Figure M3.1B&D). To distinguish if the detected peak is due to noise or genuine periodicity, a Fisher's g -test is implemented which compares the peak value in the power spectrum with the sum of the whole power spectrum and is defined as

$$g = \frac{\mathcal{P}(\omega_{peak})}{\sum_{n=1}^{N/2} \mathcal{P}(\omega_n)}, \quad (3.13)$$

where $\mathcal{P}(\omega_n)$ is the power/contribution from the n^{th} frequency ω analysed in the Fourier transform. The g -value tends to 1 in the case of genuine periodic signals, and 0 for noisy/apperiodic signals. To determine significance, a p-value can be calculated by comparing the likelihood of obtaining a higher g -value than the observed g if the power spectrum was generated from a purely noisy signal $S_\xi(x)$. This formally would be

$$p_{val} = P(g_\xi > g \mid H_0), \quad (3.14)$$

where g_ξ is the expected g -value obtained from $S_\xi(x)$, and H_0 is the null hypothesis. In this case, the null hypothesis is that the power spectrum is generated by Gaussian white noise, for which an analytical calculation of $P(g_\xi > g \mid H_0)$ is given in (Liew et al., 2009; Wichert et al., 2004). Spatial signals with $p_{val} < 0.05$ are accepted as having significant periodicity present. Additionally, we define occurrence to be the fraction of all the spatial signals analysed (over all columns over all time points) that are found to have significant periodicity

$$Occ = \frac{N_s^{p_{val} < 0.05}}{N_s}. \quad (3.15)$$

Figure M3.1E shows an example of the significant periods detected in a 2D simulation, with the Occ value given.

3.4.4 Coherence

Coherence is a measure of how pure an oscillator is and the measurement of coherence can be affected by noise or multiple frequencies contributing to a signal. It can be applied to single-cell power spectra or averaged spectra from a population of cells and so has to be interpreted in context. Coherence values range between 0 and 1, where 1 implies an oscillator (or population of oscillators) is a perfect single-frequency

oscillator with no noise. Low coherence values imply there may be noise in the signal, that the signal changes frequency over time, the population of signals have a spread of frequencies, or that the oscillator switches between periodic and aperiodic over time.

Here the definition of coherence from (Phillips et al., 2016) is used, which takes the area 20% around the highest power frequency in a power spectrum (10% in either direction, as shown in Figure M3.2A) and then divides this area by the area under the whole power spectra (Figure M3.2B), giving an indication of how concentrated the power spectra is around its peak value. Because the Fast Fourier Transform is discrete, linear interpolation is used between frequency values to estimate the area when the 20% regions don't coincide with the frequency values in the power spectrum.

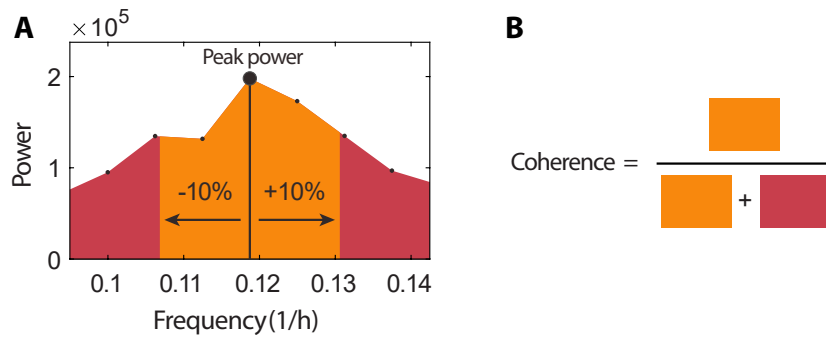


Figure M3.2: How coherence is calculated from power spectra. **A** Example power spectra with the 20% area around the peak frequency highlighted in orange and the rest of the power spectra in magenta. **B** Visual of how the areas in **A** are used to calculate coherence.

Chapter 4

Manuscript 2: Dynamic switching of lateral inhibition spatial patterns

4.1 Guide to the manuscript and supplementary files

Here the manuscript in its published format is included. Supplementary figures are included after the manuscript and can be found on page 129. Supplementary movie legends and links can be found on page 132.

4.2 Author contributions

Joshua Hawley: conceptualization, formal analysis, investigation, methodology, software, visualization, writing—original draft, writing—review and editing. Contributions to specific figures are given below in Table 4.1.

Table 4.1: Specific figure contributions from Joshua Hawley in Manuscript 2.

Figure	Contribution
1	Design of the outlined multicellular model and conceptualisation of the hypothesis that differentiating cells increasing their Notch signalling could make the pattern dynamic.
2	Implementation of the multicellular model.
3	Implementation of statistical spatial period testing. Veronica Biga helped with the implementation of the Fisher g -test.
4	Development of a method to detect dynamic switching in temporal signals.
5	Design and implementation of the differentiation-based perturbation algorithm.
6	Exploration of proximal and distal signalling distances.
7	Parameter exploration of the 1D model.
8	Parameter exploration of the 2D model.
9 A-C	Plotting of persistence times from the model. Cerys Manning provided the Venus::HES5 single-cell fluorescence time traces in panel D.
10	Plotting of the spatial distributions of differentiating cells and differentiation rates.

Paul Glendinning: conceptualization, formal analysis, investigation, methodology, supervision, writing—original draft, writing—review and editing.

Nancy Paplopulu: conceptualization, investigation, supervision, writing—original draft, writing—review and editing.

Cerys Manning: data curation, writing—review and editing. **Veronica Biga:** methodology, writing—review and editing.

Research



Cite this article: Hawley J, Manning C, Biga V, Glendinning P, Papalopulu N. 2022 Dynamic switching of lateral inhibition spatial patterns. *J. R. Soc. Interface* **19**: 20220339. <https://doi.org/10.1098/rsif.2022.0339>

Received: 4 May 2022

Accepted: 2 August 2022

Subject Category:

Life Sciences—Mathematics interface

Subject Areas:

computational biology, biomathematics, biophysics

Keywords:

lateral inhibition, dynamic switching, spatial pattern, Notch signalling, HES5, neural tube

Authors for correspondence:

Paul Glendinning

e-mail: paul.glendinning@manchester.ac.uk

Nancy Papalopulu

e-mail: nancy.papalopulu@manchester.ac.uk

Electronic supplementary material is available online at <https://doi.org/10.6084/m9.figshare.c.6135944>.

Dynamic switching of lateral inhibition spatial patterns

Joshua Hawley¹, Cerys Manning¹, Veronica Biga¹, Paul Glendinning² and Nancy Papalopulu¹

¹Faculty of Biology Medicine and Health, and ²Department of Mathematics, The University of Manchester, Manchester, UK

JH, 0000-0003-2122-7530; CM, 0000-0001-8656-5878; VB, 0000-0001-9592-385X; PG, 0000-0003-1544-9161; NP, 0000-0001-6992-6870

Hes genes are transcriptional repressors activated by Notch. In the developing mouse neural tissue, HES5 expression oscillates in neural progenitors (Manning *et al.* 2019 *Nat. Commun.* **10**, 1–19 (doi:10.1038/s41467-019-10734-8)) and is spatially organized in small clusters of cells with synchronized expression (microclusters). Furthermore, these microclusters are arranged with a spatial periodicity of three–four cells in the dorso-ventral axis and show regular switching between HES5 high/low expression on a longer time scale and larger amplitude than individual temporal oscillators (Biga *et al.* 2021 *Mol. Syst. Biol.* **17**, e9902 (doi:10.15252/msb.20209902)). However, our initial computational modelling of coupled HES5 could not explain these features of the experimental data. In this study, we provide theoretical results that address these issues with biologically pertinent additions. Here, we report that extending Notch signalling to non-neighbouring progenitor cells is sufficient to generate spatial periodicity of the correct size. In addition, introducing a regular perturbation of Notch signalling by the emerging differentiating cells induces a temporal switching in the spatial pattern, which is longer than an individual cell's periodicity. Thus, with these two new mechanisms, a computational model delivers outputs that closely resemble the complex tissue-level HES5 dynamics. Finally, we predict that such dynamic patterning spreads out differentiation events in space, complementing our previous findings whereby the local synchronization controls the rate of differentiation.

1. Introduction

The developing neural tube is a densely packed pseudostratified neuroepithelium, and starting from E10 in mouse, apically located progenitors called radial glial (RG) cells asymmetrically divide, detach from the apical wall and migrate basally to generate differentiating neuronal cells (figure 1a) [1,2]. In specific dorsal–ventral regions of the neural tube, RG cells express the transcriptional repressor HES5 (figure 1a,b), which maintains cells in a progenitor state by repressing proneural gene expression [3–8]. HES5 expression is dependent on active Notch signalling, which is a pathway that enables contacting cells to signal to each other. Notch signalling can either act to laterally induce expression between cells or laterally inhibit, and this is dependent on the ligand that is interacting with the Notch receptor. If Notch interacting cells express Jagged (1 or 2), then active Notch signalling in one cell will induce active Notch in neighbouring cells. On the other hand, if cells express Delta (1 or 4), then active Notch signalling in one cell will lead to inhibition of active Notch signalling in neighbouring cells. There are further considerations to bear in mind such as *cis*-inhibition where Delta on the same cell binds to and blocks Notch from becoming activated, as is the case with the ligand Delta-3 or high levels of Delta-1/4 [9,10]. In the ventral HES5 domain, the

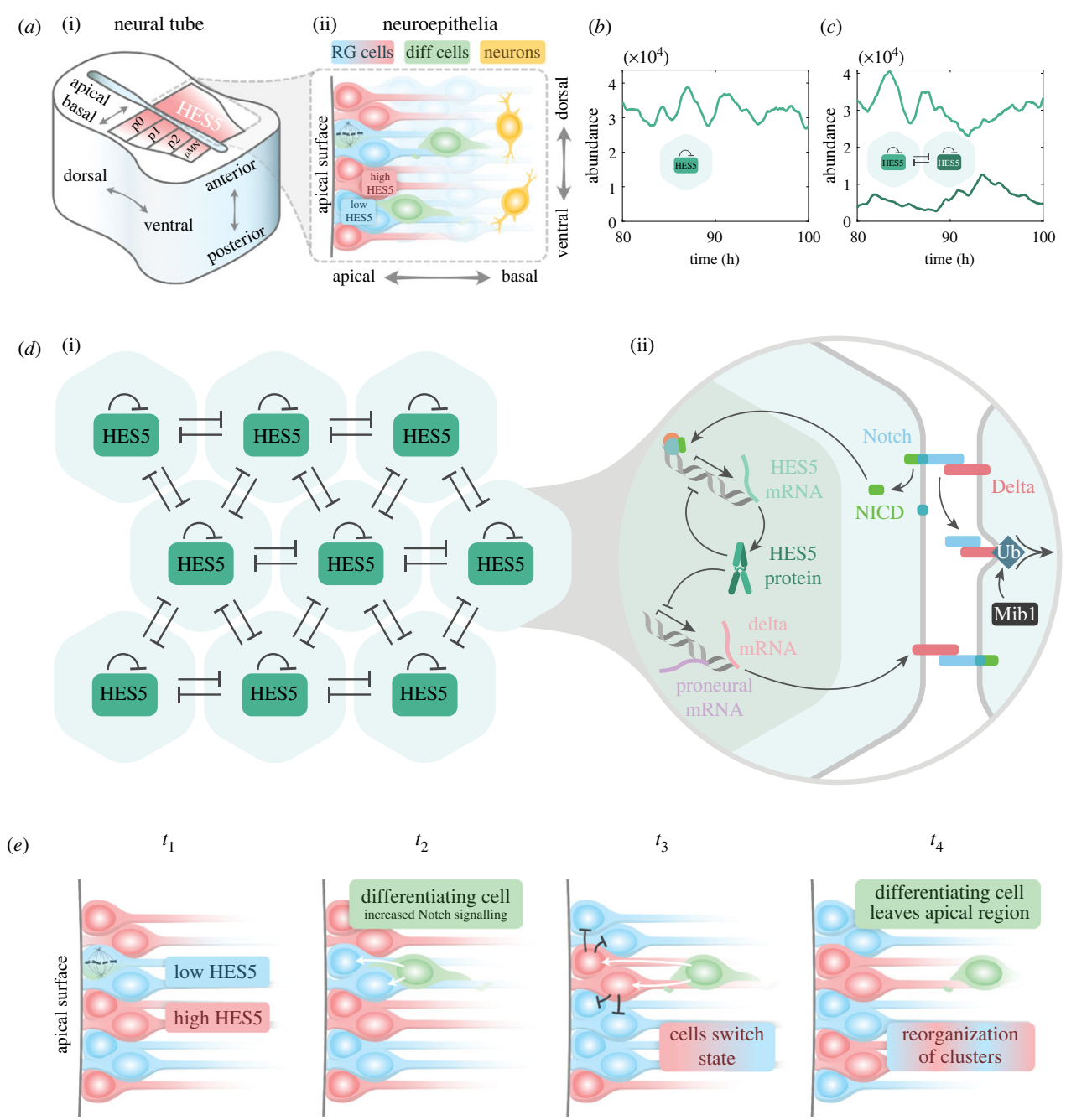


Figure 1. (a) (i) Diagram of a neural tube cross section with domains p0–p2 and pMN highlighted, which correspond to where HES5 is expressed. (ii) Structure of the neuroepithelium that makes up the neural tube, with various cell types highlighted. (b) Single-cell simulation time trace showing an example of HES5 auto-inhibition producing noisy ultradian oscillations (single-cell parameters in table 1 were used to generate the time trace). (c) Time traces for a two-cell simulation with LI coupling (parameters in table 1 used, $\tau_{LI} = 0$ and $P_{0,LI} = 4500$). (d) (i) Hexagonal lattice summarizing the interactions in the model, which include nearest-neighbour lateral inhibition and HES5 auto-inhibition. (ii) Detailed interactions of the Notch-HES pathway, which the modelling is based on. Abbreviations: Ub, ubiquitination; Mib1, mindbomb1. (e) The proposed mechanism by which differentiating cells could cause a reorganization of the LI spatial pattern by increasing Notch activation in neighbouring cells. At time point t_1 , a spatial period is already present as a result of Notch signalling, and an individual cell is shown undergoing mitosis that will give rise to a differentiating cell in t_2 . At t_2 , a cell with low HES5 commits to differentiation and starts increasing both Delta and Mib1 expression. At t_3 , the increased signalling from the differentiating cell causes an increase in the amount of HES5 in the receiving cell, and the differentiating cell starts migrating basally. At t_4 , the differentiating cell eventually loses signalling contact with the RG cells at the apical surface, and a reorganized spatial pattern remains.

main Notch ligand expressed is Delta-1 [11], and so from here onwards, Notch signalling will refer to Notch/Delta-1 lateral inhibition (LI) (figure 1c).

This study investigates HES5 expressed in the p0–p2 and pMN domains of the neural tube, which are distinct progenitor domains that give rise to different neuronal subtypes (figure 1a) [12]. It was previously known that individual cells are capable of oscillatory HES5 dynamics due to transcriptional auto-inhibition [13] with a temporal period of

around 3.3 h [3], which we will refer to as ultradian oscillations. Around 50% of cells in the HES5 domain are found to exhibit oscillatory behaviour and otherwise have aperiodic noisy expression [3]. Two recently uncovered key aspects of HES5 expression observed in *ex vivo* slices of neural tube are first, that within the p0–p2 domains, HES5 is expressed in clusters of similar expression (groups of 3–7 cells), and these are arranged regularly to form an average spatial period of three to four cells measured along the dorsal–ventral axis [14].

Table 1. Model parameter values used [14].

symbol	value	biological definition
a_m	0.77 min^{-1}	transcription rate
a_p	26 min^{-1}	translation rate
u_m	$\ln(2)/30 \text{ min}^{-1}$	mRNA degradation rate
u_p	$\ln(2)/90 \text{ min}^{-1}$	protein degradation rate
$P_{0,\text{auto}}$	25 000 proteins	HES5 auto-inhibition repression threshold
$P_{0,\text{LI}}$	0–10 000 proteins	LI coupling repression threshold
n_{auto}	3.5	HES5 auto-inhibition Hill coefficient
n_{LI}	3	lateral inhibition Hill coefficient
τ_{auto}	30 min	HES5 self-repression time delay
τ_{LI}	0–100 min	lateral inhibition time delay

Second, the location of high and low expression is not fixed over time, with clusters of similarly expressing cells spending an average of around 8 h in a high or low state before switching to the opposite state. The ultradian oscillations have a mean temporal period of 3.3 h as well as a smaller amplitude than the observed 8 h switching behaviour, indicating that ultradian oscillations alone are not responsible for the longer switching behaviour. Indeed, both noisy and oscillatory single-cell HES5 dynamics are found to be nested within the larger amplitude switching behaviour of the cells when looking at individual cell traces [14]. Specifically, the amplitude of the longer switching dynamics is approximately twice that of the ultradian amplitude as determined previously [3].

Most theoretical models of Notch LI produce stationary patterns where cells do not switch between high and low states once the spatial pattern has formed [15–21]. Some literature explores anti-phase oscillations of downstream Notch genes between coupled cells, but this concerns ultradian oscillations only, rather than ultradian oscillations nested within a distinct larger amplitude, longer time scale switching behaviour [22,23]. Therefore, the dynamic switching behaviour of the HES5 spatial pattern, as far as we are aware, is not accounted for in the literature. To simulate neural tube HES5 dynamics, Biga *et al.* [14] used a multi-cellular Notch-HES5 model composed of parametrized single-cell dynamics that were coupled together via LI interactions, signalling only between closest neighbours (figure 1*d*). This work considered that ultradian HES5 oscillations may interact via LI to generate an emergent behaviour similar to that observed in the neural tube. Aspects such as local synchronization of HES5 dynamics could be reproduced; however, other aspects of the data such as three- to four-cell spatial periodicity and larger amplitude temporal switching could not be reproduced, indicating that additional mechanisms are required to explain the observed patterns of dynamic behaviour.

To understand the complexity and generation of the *ex vivo* neural tube pattern, we consider two new additions to the multi-cellular Notch-HES5 model presented in the study by Biga *et al.* [14]. The first addition is extending the LI signalling distance between cells, inspired by the modelling work that shows how protrusions can extend Notch signalling distance, which leads to longer period spatial patterns [18]. This is in line with experimental observations of

filopodia in *Drosophila*, which have been shown to carry Notch ligands and induce Notch signalling several cell diameters away [17,24], and various literature points to the existence of protrusions in the neuroepithelia that are probably capable of Notch signalling [25–28]. The second addition to the model is the introduction of a differentiation process that alters the amount of Notch signalling that neighbouring cells receive from a differentiating cell. This process in the model is based on the fact that early differentiating cells migrating out of the RG population increase their expression of Delta [29] as well as Mindbomb1 (Mib1), which greatly increases the efficiency of Delta trans-activation of Notch [30–32]. Via ubiquitination, Mib1 marks Delta for endocytosis, which subsequently provides the mechanical force required for successful Notch receptor activation on neighbouring cells [30,33] (figure 1*e*).

To identify outputs similar to *ex vivo* dynamics in the new model, we use significance testing on power spectra to identify spatial periodicity and define a new measure, the dynamicity coefficient, to indicate the proportion of time cells spend in high and low states. By plotting these measured outputs in parameter space, we identified that extended signalling distance generates spatial periods of three to four cells, and the inclusion of a differentiation process that dynamically alters signalling between cells produced switching behaviour between high and low HES5 expression over time. In addition, the model output showed cases of ultradian oscillations nested within the larger amplitude, longer time-scale switching behaviour, as observed in single-cell data [14]. This is a unique exploration of how Notch LI signalling can be prevented from permanently settling into fixed peak and trough locations while maintaining the spatial pattern forming ability of LI. The reorganization of peak and trough locations of HES5 is found to enable differentiation events to be spread out spatially over time and prevents hotspots where differentiating cells are repeatedly produced, potentially important in ensuring an even production of neurons across the dorsal–ventral axis.

2. Methods

2.1. Multi-cellular lateral inhibition HES5 model

Our core model is based on previously implemented modelling work, consisting of auto-inhibition interactions of HES5 protein back on to expression of its own mRNA, and with HES5 dynamics being coupled between cells in a hexagonal geometry using an inhibitory Hill function representative of Notch LI [16,34]. The single-cell parameters used in the model were previously parametrized to neural tube HES5 data using Bayesian inference [3], and a range of multi-cellular parameters were explored in [14]. Figure 1*d* outlines the biological interactions considered and the core interactions that are described mathematically in the model. A chemical Langevin equation approach is used [35], and the stochastic delay differential equations that govern the dynamics of a cell at row i and column j (see figure 2) in the multi-cellular model are given by

$$\frac{dm_{ij}(t)}{dt} = -\mu_m m_{ij}(t) + \alpha_m H_{\text{auto}}(p_{ij}(t - \tau_{\text{auto}})) H_{\text{LI}}(\bar{p}_{ij}(t - \tau_{\text{LI}})) + \eta_m \quad (2.1)$$

and

$$\frac{dp_{ij}(t)}{dt} = -\mu_p p_{ij}(t) + \alpha_p m_{ij}(t) + \eta_p, \quad (2.2)$$

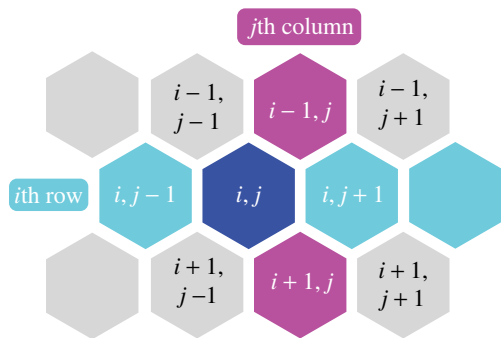


Figure 2. Hexagonal geometry of the model and how the i and j indices in the model equations map onto this grid.

where $m_{ij}(t)$ is HES5 mRNA concentration in the cell on the i th row and j th column at time t and $p_{ij}(t)$ is HES5 protein concentration. μ_m and μ_p are the degradation rates of HES5 mRNA and protein, respectively; α_m and α_p are the transcription and translation rates; τ_{auto} is the time delay associated with HES5 autorepression; and τ_{LI} is the time delay associated with the lateral inhibition interaction between cells. In Results §3.2, we find that over a range of τ_{LI} values (0–100 min), the model exhibited a similar behaviour. The somitogenesis literature points to a range of possible τ_{LI} values (20–120 min), and so to reduce the complexity of the model, we set $\tau_{LI}=0$ for the main results and give an exploration of non-zero time delays in electronic supplementary material, figures S2 and S3 [36–40].

Both the functions H_{auto} and H_{LI} are inhibitory functions that regulate mRNA production rate in response to protein abundance either within a cell (H_{auto}), or between cells (H_{LI}). H_{LI} therefore is the coupling function that enables HES5 dynamics to influence neighbouring HES5 dynamics. For the signalling contribution from each cell in contact with a receiving cell, we take the approach used in [16,23], and the amount of HES5 a cell receives is the averaged abundance from all signalling neighbours

$$\bar{p}_{ij} = \frac{1}{|\mathcal{N}(i, j)|} \sum_{(i', j') \in \mathcal{N}(i, j)} \varepsilon_{i', j'} p_{i', j'} \quad (2.3)$$

where $\mathcal{N}(i, j)$ is the set of neighbours a cell is in signalling contact with and $|\mathcal{N}(i, j)|$ is the total number of neighbours in the set. Neighbouring cells are defined in §3.1, and this introduces proximal and distal cells. Proximal cells are adjacent cells, i.e. any neighbours within a one-cell distance, and distal cells are signalling neighbours that lie further than one-cell distance away (see figure 6). Coupling strength of distal and proximal cells, ε_d and ε_p respectively, can be varied independently in the model, and so $\varepsilon_{i, j}$ in equation (2.3) defines a coupling weighting depending on whether the signalling neighbour is proximal or distal and can have one of two values

$$\varepsilon_{i, j} = \begin{cases} 1, & \text{if } \mathcal{N}(i, j) \text{ is a proximal neighbour} \\ \frac{\varepsilon_d}{\varepsilon_p}, & \text{if } \mathcal{N}(i, j) \text{ is a distal neighbour.} \end{cases} \quad (2.4)$$

The Hill functions are both decreasing functions, where $H_{\text{auto}}(0) = H_{LI}(0) = 1$ and $H_{\text{auto}}(\infty) = H_{LI}(\infty) = 0$ and have the form

$$H_{\text{auto}}(p_{ij}(t - \tau_{\text{auto}})) = \frac{1}{1 + (p_{ij}(t - \tau_{\text{auto}})/P_{0, \text{auto}})^{n_{\text{auto}}}} \quad (2.5)$$

and

$$H_{LI}(\bar{p}_{ij}(t - \tau_{LI})) = \frac{1}{1 + (\bar{p}_{ij}(t - \tau_{LI})/P_{0, LI})^{n_{LI}}}. \quad (2.6)$$

$P_{0, \text{auto}}$ and $P_{0, LI}$ are the repression thresholds of each Hill function. The repression threshold defines the amount of protein

that results in a 50% reduction in mRNA production rate. For example, within an individual cell, the value of $P_{0, \text{auto}}$ defines the abundance of HES5 protein, p_{ij} , at which mRNA production rate will be 50% within that same cell. In the case of $P_{0, LI}$, this defines when mRNA production in a receiving cell will be 50% in response to the averaged incoming abundance of HES5 protein in the neighbouring cells \bar{p}_{ij} . n_{auto} and n_{LI} are the Hill coefficients that define how steep the gradient of the Hill function is at P_0 (higher values give a sharper transition between no repression and repression).

The terms η_m and η_p in equations (2.1) and (2.2) are the stochastic noise terms for mRNA and protein, which are Gaussian white noise scaled by the square root of the number of events that occur in each process

$$\eta_m = \sqrt{\mu_m m_{ij}(t) + \alpha_m H_{\text{auto}}(p_{ij}(t - \tau_{\text{auto}})) H_{LI}(\bar{p}_{ij}(t - \tau_{LI}))} \xi_m(t) \quad (2.7)$$

and

$$\eta_p = \sqrt{\mu_p p_{ij}(t) + \alpha_p m_{ij}(t)} \xi_p(t), \quad (2.8)$$

where $\xi_m(t)$ and $\xi_p(t)$ are Gaussian white noise with mean of 0 and variance of 1, respectively. Equations are solved using the Euler–Maruyama method, implemented in Matlab. Model parameters are summarized in table 1.

2.2. Extracting spatial signals from the model

To understand what sort of spatial patterns are being produced by the model, we extract spatial signals using a similar approach to that used for the *ex vivo* analysis in [14]. In the hexagonal grid of cells, $p(x_{ij}, t_k) = p_{ij}(t_k)$ denotes that the protein expression at the i th row, j th column and k th time-step, and I, J, K are the total number of rows, columns and time-steps. In the case of simulating a single column of cells ($J=1$) such as in figure 3*a*, a spatial signal can be generated for each time point by taking the protein expression along the entire column such that the spatial signal at time-step k and $j=1$ is expressed as follows:

$$S_k(x) = p(x_{1: I, 1}, t_k). \quad (2.9)$$

Each spatial signal is therefore a vector of length I , where each entry is the expression from an individual cell, and the total number of spatial signals that can be generated from a single simulation is $N_s = K$ (figure 3*b*). To visualize both spatial and temporal aspects of the data in one plot, the spatial signal can be plotted over a range of time points $S_{k_1: k_2}(x)$ as a kymograph, shown in figure 3*a, c*.

In the case of simulating multiple columns (i.e. a two-dimensional grid of cells), we extract the spatial signal by using a selection region with a width of one cell and length I cells (see grey dashed boxes in figure 3*c*). Due to the hexagonal geometry, on the even rows, two cells fall within this selection region, and so the spatial signal is constructed as follows:

$$S_{jk}(x_i) = \begin{cases} p(x_{ij}, t_k), & \text{if } i \text{ odd} \\ \frac{p(x_{ij}, t_k) + p(x_{i-1, j}, t_k)}{2}, & \text{if } i \text{ even} \end{cases} \quad (2.10)$$

where even rows use the average of the two cells that fall within the selection region. As there are multiple columns, the number of spatial signals generated from a single simulation is $N_s = K(J-1)$ (figure 3*d*).

2.3. Detecting spatial periodicity

From the extracted spatial signals, a method is needed to detect the presence of statistically significant spatial periodicity in the inherently noisy model outputs. By using a fast Fourier transform method (Matlab), a power spectrum can be obtained for

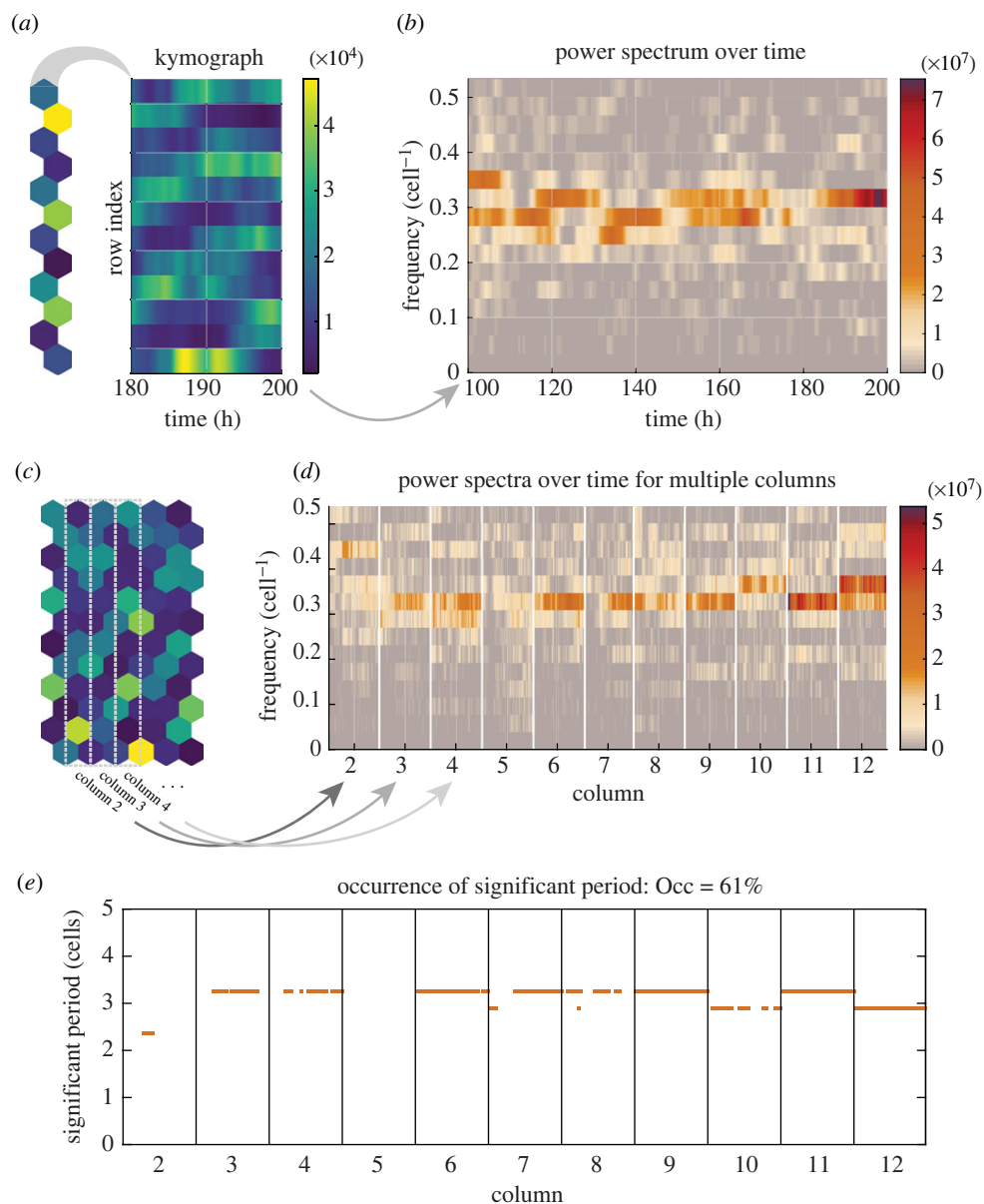


Figure 3. Outline of the process used for detecting the presence of significant periodic spatial patterns. (a) In the case of one-dimensional simulations, kymographs are generated from the expression on each row (y -axis) and over time (x -axis). (b) A Fourier transform of the spatial signal in *a* is shown as a power spectrum over time, where colour indicates the power contribution of each frequency at each time point. (c) For two-dimensional simulations, spatial signals are generated from the cells that fall within selection regions (grey dashed boxes). (d) A power spectrum is generated for the spatial signal in each column (within each division the power spectrum over time is given, like in *b*). (e) The peaks of each individual power spectra are tested for significance using the Fisher g -test (S2.3) and the significant spatial periods are plotted with orange dots and the occurrence measure is shown above the plot (Occ is defined in S2.3).

each spatial signal

$$\mathcal{P}(S_{jk}(x)) = |\mathcal{F}(S_{jk}(x))|^2, \quad (2.11)$$

where $\mathcal{F}(S_{jk}(x))$ is the Fourier transform of the spatial signal. The highest power frequency in the power spectrum indicates the dominant periodicity in the spatial signal (figure 3*b,d*). To distinguish if the detected peak is due to noise or genuine periodicity, a Fisher's g -test is implemented that compares the peak value in the power spectrum with the sum of the whole power spectrum and is defined as follows:

$$g = \frac{\mathcal{P}(\omega_{\text{peak}})}{\sum_{n=1}^{N/2} \mathcal{P}(\omega_n)}, \quad (2.12)$$

where $\mathcal{P}(\omega_n)$ is the power/contribution from the n th frequency ω analysed in the Fourier transform. The g -value tends to 1 in the case of genuine periodic signals and 0 for noisy/apertic signals. To determine significance, a p -value can be calculated by comparing the likelihood of obtaining a higher g -value than

the observed g if the power spectrum was generated from a purely noisy signal $S_{\xi}(x)$. This formally would be

$$p_{\text{val}} = P(g_{\xi} > g \mid H_0), \quad (2.13)$$

where g_{ξ} is the expected g -value obtained from $S_{\xi}(x)$, and H_0 is the null hypothesis. In this case, the null hypothesis is that the power spectrum is generated by Gaussian white noise, for which an analytical calculation of $P(g_{\xi} > g \mid H_0)$ is given in [41,42]. Spatial signals with $p_{\text{val}} < 0.05$ are accepted as having significant periodicity present. In addition, we define occurrence to be the fraction of all the spatial signals analysed (over all columns over all time points) that are found to have significant periodicity

$$\text{Occ} = \frac{N_s^{p_{\text{val}} < 0.05}}{N_s}. \quad (2.14)$$

Figure 3*e* shows an example of the significant periods detected in a two-dimensional simulation, with the Occ value given.

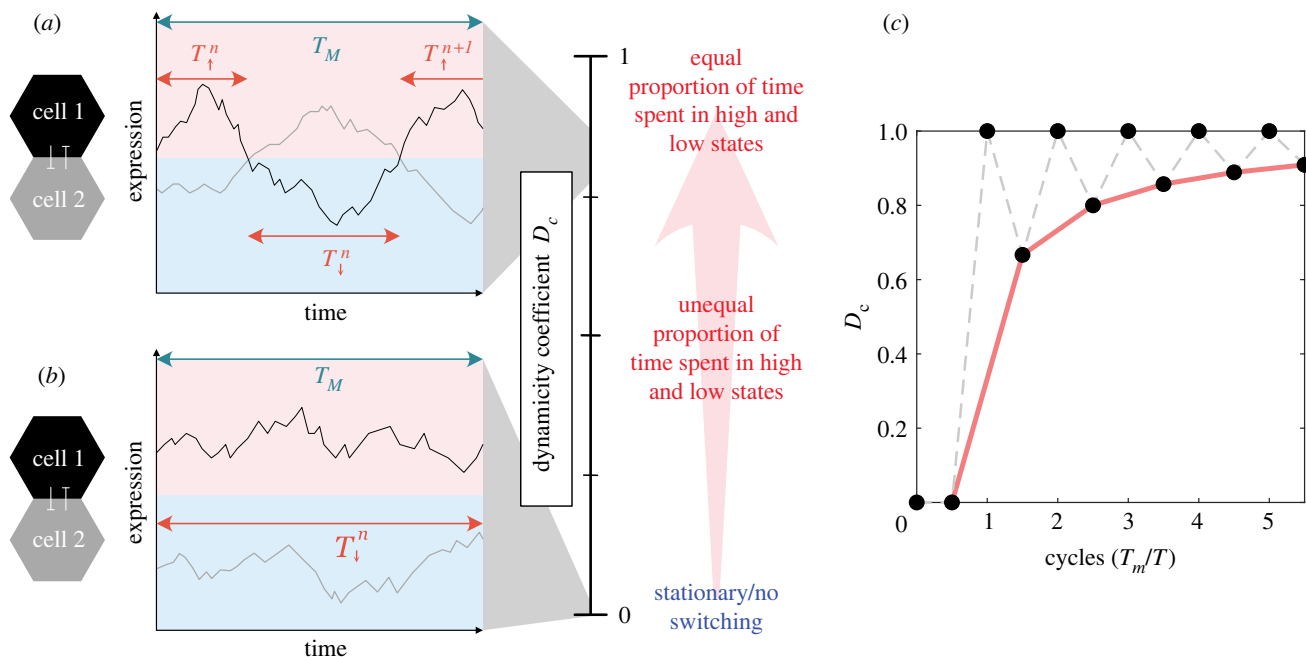


Figure 4. Illustrative examples and plot of the dynamicity coefficient. T_M is defined as the total measurement time/the length of the signal analysed and $T_{\uparrow, \downarrow}^n$ denotes the time spent above or below the mean population expression. (a) Plot of expression in two individual cells (black and grey) that exhibit dynamic LI, where each cell can switch between a high state (pink upper half of the graph) and low state (lower pale blue half). (a) Corresponds to a high D_c value. (b) Two cells exhibiting a stationary LI interaction where one cell remains high (black) and one cell remains low (grey) over the whole measurement time. (b) corresponds to $D_c = 0$. (c) D_c values that would be obtained for a perfectly switching (regular period) signal at integer and half cycles (black dots). Half cycle measurements are joined with a red line.

2.4. Distinguishing dynamic and stationary spatial patterns

To develop a mathematical measure of how stationary or dynamic a pattern is over time, the dynamicity coefficient is defined here, which measures the proportion of time the expression in an individual cell spends in a high versus low state.

The choice of threshold that defines high and low states for the dynamicity measure is driven by our desire to analyse the dynamics at all levels of expression. As coupling strength is increased, the mean population expression reduces, but the signal is still dynamic. Therefore, an absolute threshold cannot be used to measure dynamicity across a range of parameters. Instead, we define a relative threshold for each simulation by using the mean population expression level to ensure the threshold lies between the high and low states generated by lateral inhibition. While this ensures a high and low state is always defined, it comes with the caveat that when LI is too weak to produce distinct high and low states, the dynamicity coefficient is reflecting switches due to the noisy fluctuations and ultradian oscillations of HES5.

The amount of time spent in an individual high or low state, which we call persistence time, is denoted by $T_{\uparrow, n}$ and $T_{\downarrow, n}$ respectively, where n is the n th occurrence of a high or low state (see figure 4a). Therefore, the proportion of time a cell spends in a high state in a signal of length T_M (the measurement time) is expressed as follows:

$$\alpha_{\uparrow} = \frac{1}{T_M} \sum_{n=1}^N T_{\uparrow, n}, \quad (2.15)$$

where N is the total number of occurrences of the cell being in a high state. Similarly, the proportion of the measurement time that a cell spends in a low state is expressed as follows:

$$\alpha_{\downarrow} = \frac{1}{T_M} \sum_{n=1}^N T_{\downarrow, n}. \quad (2.16)$$

As α_{\uparrow} and α_{\downarrow} are proportions of the total measurement time, their values lie between 0 and 1, and $\alpha_{\uparrow} = 1 - \alpha_{\downarrow}$. If $\alpha_{\uparrow} = \alpha_{\downarrow} = 0.5$, then this implies that an individual cell spends equal amounts of time in high and low states. In the opposite case where either $\alpha_{\uparrow} = 1$ and $\alpha_{\downarrow} = 0$, or $\alpha_{\uparrow} = 0$ and $\alpha_{\downarrow} = 1$, this implies that the cell spends the entire measurement time in one state and therefore is classed as a stationary signal (figure 4b). By using these proportions of time spent in high and low states, we define here the dynamicity coefficient as follows:

$$D_c = 2 \times \min(\alpha_{\uparrow}, \alpha_{\downarrow}), \quad (2.17)$$

which rescales the proportions to give a value between 0 and 1: 0 if the signal/patterning is stationary and 1 if the signal spends equal amounts of time in the high and low state ($\alpha_{\uparrow} = \alpha_{\downarrow} = 0.5$). To prevent transient fluctuations above or below the population mean contributing to the $\alpha_{\uparrow}, \alpha_{\downarrow}$ values, a Savitzky–Golay filter (inbuilt Matlab function) was used to smooth the signal first, using polynomial order of 1 and frame length of 165 minutes [43].

Another property that is useful to extract from the data is how frequently cells switch between high and low states. Here, we define the persistence time as how long the signal persists in a high or low state, which is just the mean time spent high or low

$$\bar{T}_{\uparrow} = \frac{1}{N} \sum_{n=1}^N T_{\uparrow, n} \quad (2.18)$$

and

$$\bar{T}_{\downarrow} = \frac{1}{N} \sum_{n=1}^N T_{\downarrow, n}. \quad (2.19)$$

In the case of regular temporal switching between states, i.e. an oscillator with a well-defined, non-varying period, then the period of the oscillator is given by $T = \bar{T}_{\uparrow} + \bar{T}_{\downarrow}$.

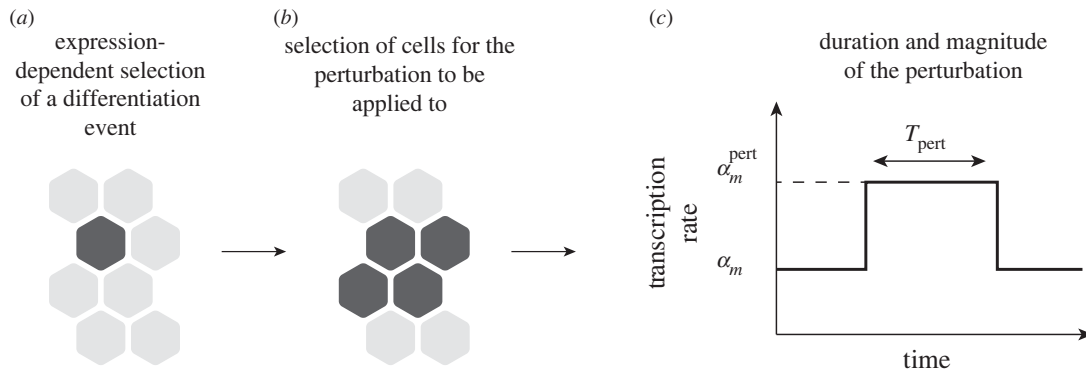


Figure 5. Outline of the differentiation-based perturbation (DBP) algorithm. (a) The probability-dependent differentiation algorithm is used to first identify a region where a cell is most likely to differentiate (single dark grey hexagon) based on HES5 expression levels (equation (2.21)). (b) An area around the selected cell in a is then selected (four dark grey hexagons), and these cells will have the perturbation applied to the HES5 transcription rate with magnitude $F_{\text{pert}} = \alpha_m^{\text{pert}} / \alpha_m$ for a period T_{pert} shown in c.

Note that the measurement time, T_M , will affect the D_c value to some extent, depending on how comparable T_M is to the expected period of switching T . Take for example a perfectly switching signal where $\alpha_{\uparrow} = \alpha_{\downarrow} = 0.5$, if we define the number of measured cycles $n_c = T_M/T$, then when n_c is integer, $D_c = 1$. However, when the measurement time does not coincide with a full cycle, i.e. n_c is non-integer, then $D_c < 1$, because $\alpha_{\uparrow} \neq \alpha_{\downarrow}$. α_{\uparrow} and α_{\downarrow} will be most different and therefore D_c values will reach a minimum at half cycles, and for a perfectly switching signal, the D_c value at half cycles ($n_c = 0.5, 1.5, 2.5, \dots$) is

$$D_c = \frac{2(n_c - \frac{1}{2})}{2(n_c - \frac{1}{2}) + 1}. \quad (2.20)$$

This effect of measurement time cutting off at non-integer cycles only becomes a significant issue when n_c is on the order of a few cycles, and so the longer the measurement time relative to the switching period, the more accurate the D_c value becomes (see figure 4c).

2.5. Implementation of the differentiation-based perturbation algorithm

To implement a process in the model that represents the signalling strength changes due to cell differentiation, we first require a process to determine the locations of differentiating cells and then a process to apply a changed signalling strength to the area around the differentiating cell. For differentiation, we make use of our previously developed differentiation algorithm [14]. This decision process is based on the assumption that lower levels of HES5 are more likely to enable the upregulation of proneural genes, and therefore, cells are marked for differentiation in a probabilistic manner based on expression (figure 5a). The probability of a given cell to be marked for differentiation is given by

$$P(\text{diff} | p_{ij}(t)) = \begin{cases} 0, & p_{ij}(t) > D_{\text{thresh}} \\ R \left(\frac{D_{\text{thresh}} - p_{ij}(t)}{D_{\text{thresh}}} \right), & p_{ij}(t) < D_{\text{thresh}}, \end{cases} \quad (2.21)$$

where D_{thresh} is the differentiation threshold (set as the population mean expression), and R is the rate of differentiation. For further details on the differentiation algorithm, see [14].

In the neural tube, differentiating cells delaminate from the apical side in a process called apical abscission [2], and migrate outward towards the basal side [44]. However, cell movement is not modelled here, and so differentiation events have to represent something less than the full picture of cell differentiation. Here, we model the effects of a changed signalling strength coming from a differentiating cell in a given area, rather than simulating the differentiating cell explicitly as a separate cell. This involves choosing a number of cells around the

area of the already-selected differentiation location that are defined to be in contact with a differentiating cell in that area (figure 5b). A perturbation is then applied to the HES5 transcription rate, α_m , in these cells to reflect increased Notch activation in these cells (figure 5c). The magnitude of the perturbation applied to α_m is determined by a perturbation factor F_{pert} , so the perturbed HES5 transcription rate is α_m^{pert} , where

$$\alpha_m^{\text{pert}} = F_{\text{pert}} \alpha_m. \quad (2.22)$$

Finally, a period of time for the perturbation to be applied is denoted by T_{pert} (figure 5c). Values for T_{pert} and F_{pert} are discussed in §3.2.

In the single-column simulation, if cell i is the location where a differentiation event is chosen, then the perturbation is applied to both cell i and with equal probability either cell $i - 1$ or $i + 1$. If it is a grid simulation, then the perturbation is applied to a group of four cells: always i, j and $i, j + 1$ and then either the two cells above ($i - 1, j$ and $i - 1, j + 1$) or below ($i + 1, j$ and $i + 1, j + 1$). The entire process described in this section is referred to as the differentiation-based perturbation (DBP) algorithm.

Differentiation rates in the simulations are characterized in two different ways. First, the average rate of differentiation over the whole population is calculated as the number of differentiation events that occur per hour as a percentage of the total number of cells in the simulation. Second, to look at how differentiation rates vary in individual cells, the frequency of differentiation per cell is calculated as the number of differentiation events per hour for every cell and then the distribution can be visualized in a histogram (figure 10d–f).

3. Results

3.1. Extended signalling distance generates the correct spatial periodicity

Previous work found that the largest spatial period that can be generated from a HES5-Notch model with nearest-neighbour coupling is a two-cell period of alternating high and low expression shown in figure 6a–c [14]. However, HES5 expression in the neural tube exhibits clusters of similarly expressing cells that are arranged to generate a higher spatial periodicity of three to four cells; therefore, an additional mechanism is required. Given that extending Notch signalling distance has been shown to enable longer spatial periodicity [18,45,46], and protrusions have been observed in many neuroepithelial tissues [17,25–28], we add *distal*

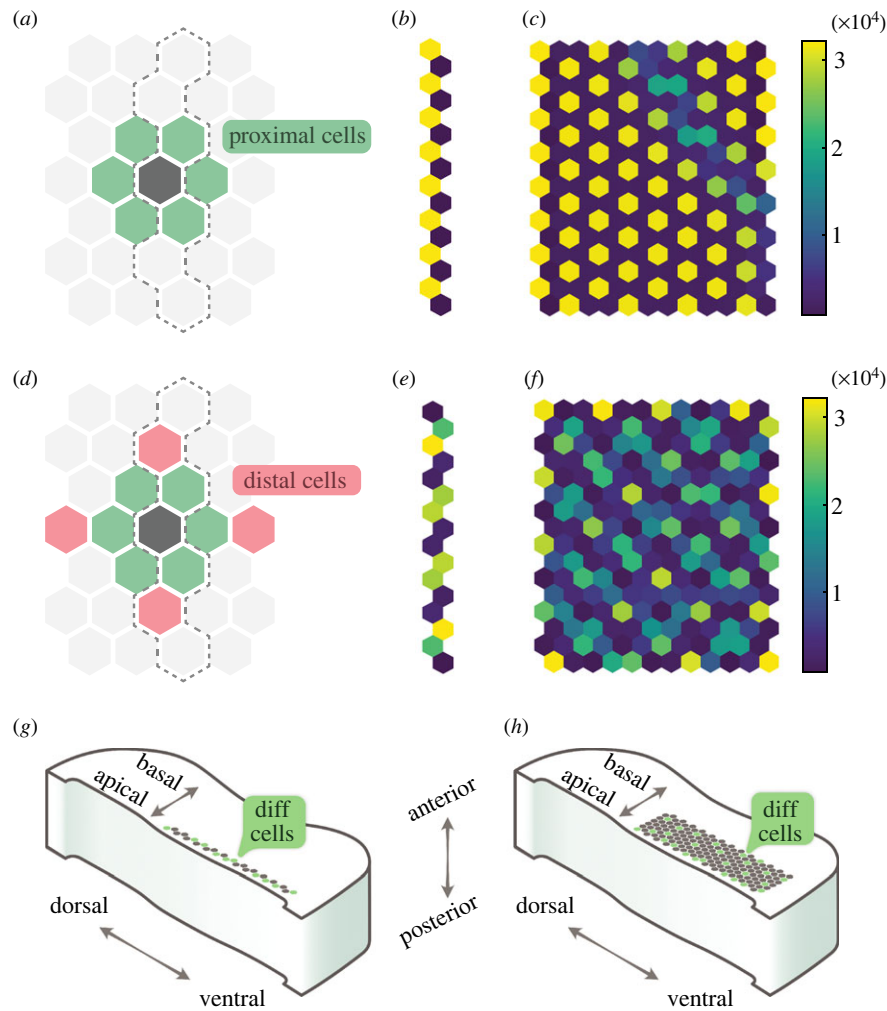


Figure 6. Comparison of deterministic model outputs with and without distal cells (*a–f*), and the mapping of the model lattice to the neural tube (*g,h*). (*a*) A cell (dark grey) and the cells it is coupled to in a hexagonal grid in the case when only proximal cells (green) are considered, and the dashed outline indicates the interactions included for one-dimensional simulations. (*b,c*) The final time point (200 h simulation) of a one- and two-dimensional simulation, respectively, using the interactions shown in (*a*). (*d*) The extended interactions used for all subsequent simulations, which includes the distal cells (red) in addition to the proximal cells (green). (*e,f*) The final time point (200 h simulation) of a one- and two-dimensional simulation, using $\varepsilon_d/\varepsilon_p = 1.5$. All simulations shown used $P_{0,U} = 4000$. (*g*) The one-dimensional lattice represents a line of cells in the dorsal–ventral direction towards the apical side of the tissue. Green cells indicate differentiating cells. (*h*) The two-dimensional model lattice maps to the dorsal–ventral, apical–basal plane of the tissue.

cell interactions to represent the longer range protrusion-based signalling (figure 6*d–f*).

The distal geometry shown in 6*d* was found to generate sufficiently clustered patterns of the correct spatial period of three to four cells (figure 6*e,f*), whereby groups of neighbouring cells form areas of high or low expression. In the one-dimensional case (figure 6*e*), distal cell interactions enable a clear alternating pattern of two cells high and two cells low. In the two-dimensional case (figure 6*f*), the periodic repeating also extends in the second dimension, and a mixture of cluster sizes is shown in figure 6*f*.

HES5 clusters *ex vivo* are composed of three to seven cells on average and are elongated in the apical–basal direction [14]. Although no quantification is done on cluster size in this model, the high expressing clusters can be seen to be more of the order of two to four cells in size in 6*f*. The cluster sizes being lower than *ex vivo* measurement is probably due to there being no elongation of clusters in the model, and it is not known what causes the elongation *ex vivo*. Despite the apical–basal elongation not being reproduced, the dorsal–ventral spatial period of three to four cells is reproduced in the model, which is shown in the spatial period

analysis in figures 7 and 8. Other distal geometries were explored and simulations with higher numbers of neighbours produced less clustered or less robust patterns (electronic supplementary material, figure S1). For all subsequent simulations, the distal geometry shown in figure 6*d* is used.

Inspired by modelling work done by [18], proximal and distal signalling strength can be varied relative to each other and distal signalling efficiency here is given by $\varepsilon_d/\varepsilon_p$, where ε_d is the distal coupling strength (LI repression threshold) and ε_p is the proximal coupling strength. The effect of distal signalling efficiency is explored in the next section.

The one-dimensional simulations represent a strip of cells in the dorso-ventral direction in the neural tube, towards the apical side where progenitor cells are located and differentiating cells are born (figure 6*g*). The two-dimensional simulations map on to a dorsal–ventral, apical–basal plane (figure 6*h*). In both cases, this is to match the location of the HES5 domain and the axes that have been studied experimentally. In §3.3, differentiating cells are allowed to appear anywhere in the two-dimensional lattice, and so for the dorsal–ventral, anterior–posterior plane assumption to make sense, differentiating cells would need to be distributed

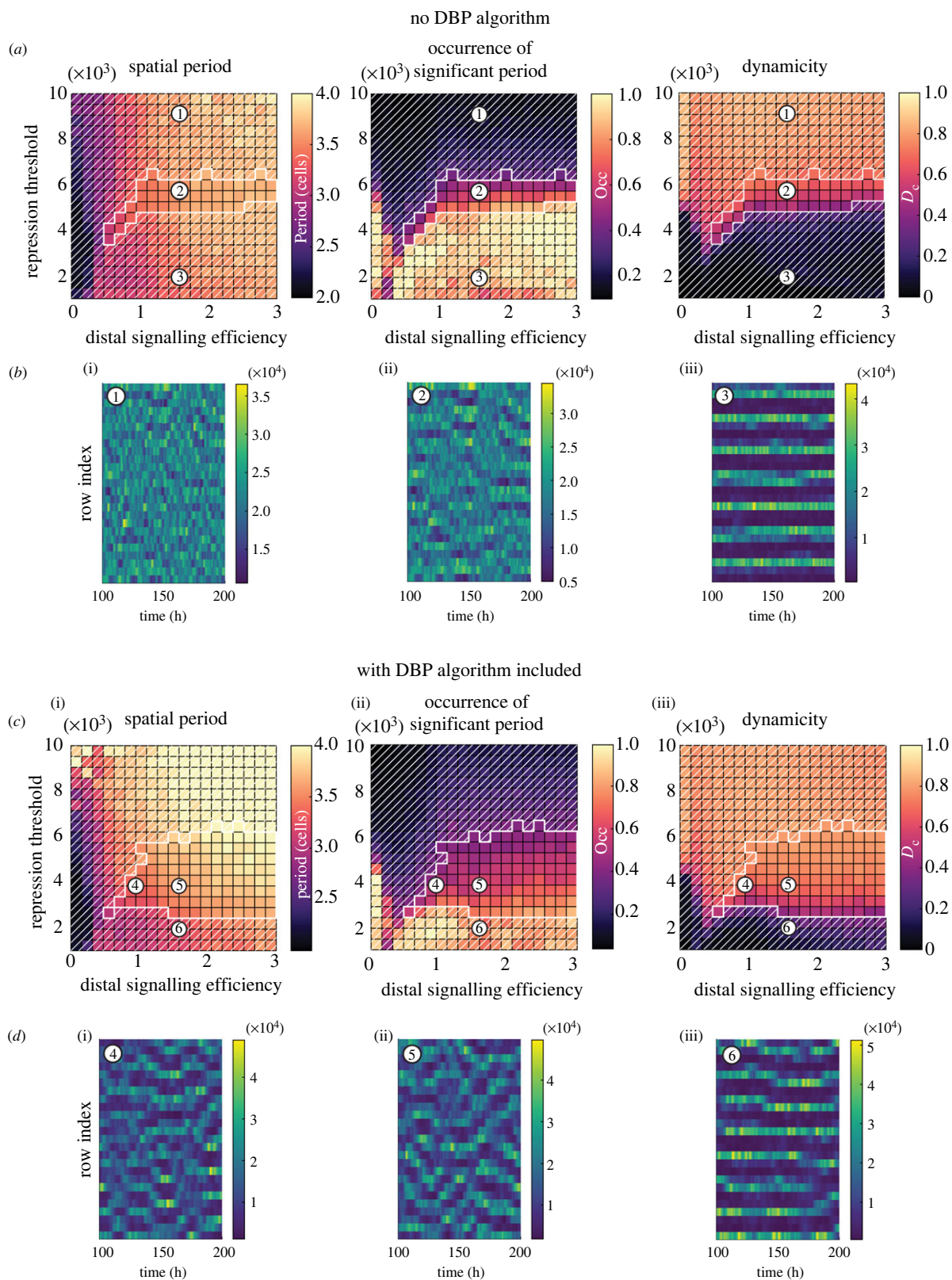


Figure 7. Simulations of a single column of cells (26 rows, 1 column). Parameter space values were generated by taking the mean value from 20 simulations with random initial conditions. The top two rows show model output without the DBP algorithm, and the bottom two rows show the output with DBP included. (a) and (c) Parameter spaces show distal signalling efficiency, $\varepsilon_d/\varepsilon_p$, versus lateral inhibition repression threshold, $P_{0,U}$, and three different measured model outputs are indicated by the colour scale. Areas without white diagonal lines overlaid indicate regions that satisfy equation (3.1) ($T_{\text{spatial}} > 3$, $\text{Occ} > 0.4$, $D_c > 0.4$), which is where dynamic spatial patterns occur. (i) Spatial period where only statistically significant periods are plotted (see §2.3). (ii) Occurrence of significant spatial period (see §2.3). (iii) The dynamicity measure (see §2.4). (b) and (d) Example kymograph plots from corresponding numbered regions in parameter space. Kymographs used the following parameters: (1) $P_{0,U} = 9053$, $\varepsilon_d/\varepsilon_p = 1.58$, (2) $P_{0,U} = 5737$, $\varepsilon_d/\varepsilon_p = 1.58$, (3) $P_{0,U} = 1947$, $\varepsilon_d/\varepsilon_p = 1.58$, (4) $P_{0,U} = 3842$, $\varepsilon_d/\varepsilon_p = 0.95$, (5) $P_{0,U} = 3842$, $\varepsilon_d/\varepsilon_p = 1.58$, and (6) $P_{0,U} = 1947$, $\varepsilon_d/\varepsilon_p = 1.58$.

across the apical–basal direction of the HES5 domain *ex vivo*. This is probably the case, as differentiating cells are born in the apical domain and subsequently migrate basally (as

illustrated in figure 1e) and so will probably contact a number of different cells throughout the apical–basal axis. If this is not the case and differentiating cells have a spatial

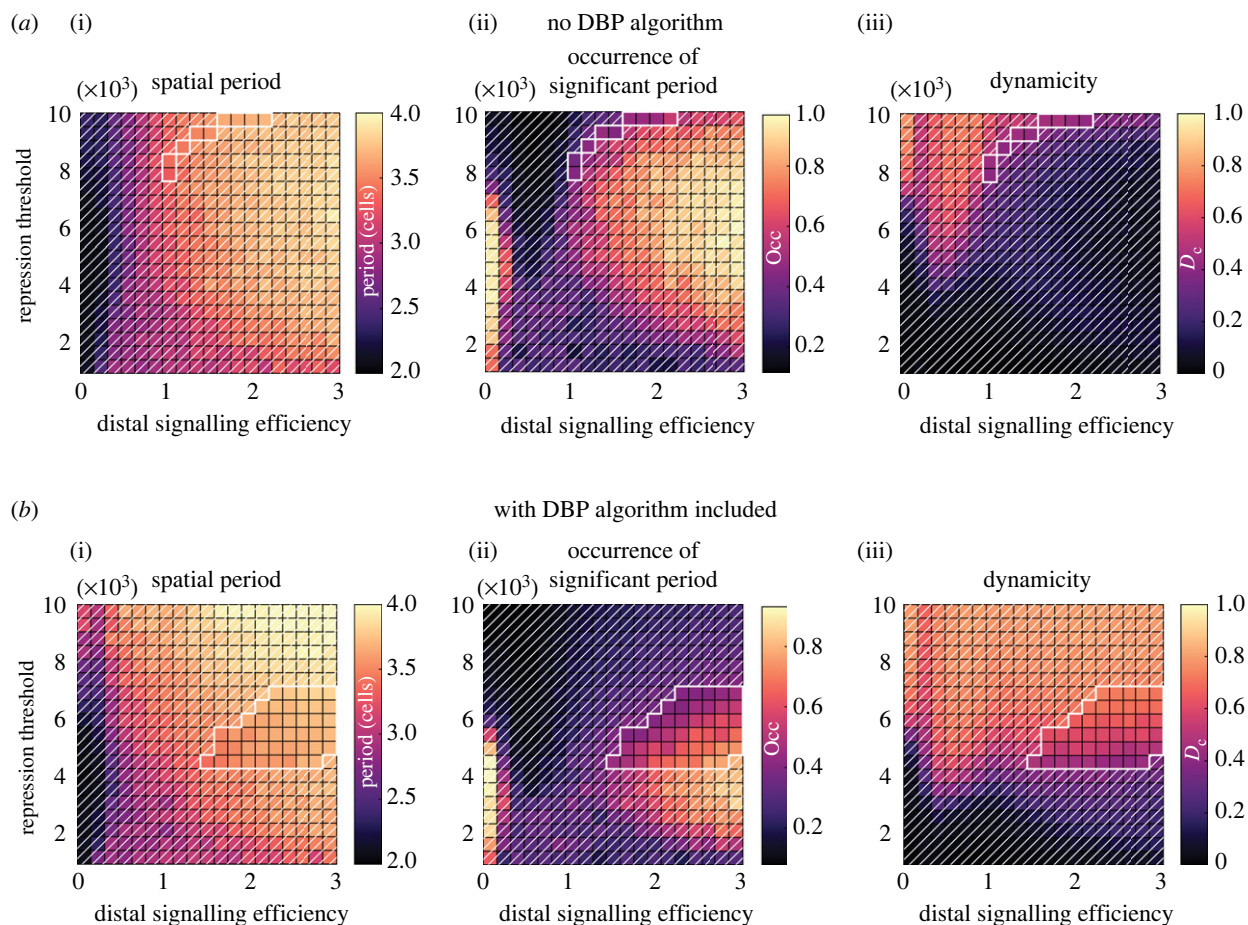


Figure 8. The same parameter spaces as in figure 7 are plotted here but for two-dimensional simulations (26 rows, 6 columns). Parameter space values were generated by taking the mean value from 20 simulations with random initial conditions. (a) Model output when the DBP algorithm is not included, and (b) is with the DBP algorithm included. Areas without white diagonal lines overlaid indicate regions that satisfy equation (3.1) (spatial period > 3 , occurrence of spatial period > 0.4 and a dynamicity coefficient > 0.4), and where dynamic spatial patterns are expected to occur.

distribution in a particular apical–basal area, then future work could look at the effects of restricting where these differentiating cells appear in the model.

3.2. Differentiation expands the dynamic patterning regime in one-dimensional simulations

In addition to the periodic expression of three to four cells, the clusters of similar expression exhibit dynamic switching between high and low expression *ex vivo*. The DBP algorithm described in §2.5 outlined the process through which differentiating cells perturb neighbouring progenitor cells through altered signalling strength. We present the model both with and without the DBP algorithm included to compare which model is more consistent with the dynamic switching observed *ex vivo*. This first set of results uses one-dimensional simulations of 26 rows by 1 column, as this roughly matches the number of nuclei within the dorsal–ventral HES5 expression domain (figure 6g) as seen in [14].

To analyse the output of the model, three measurements were plotted in parameter space of distal signalling efficiency (ϵ_d/ϵ_p), versus the LI repression threshold (the coupling strength between cells) (figure 7). Without DBP (figure 7a), the spatial period tends towards two cells at zero/low distal signalling efficiency and towards higher periodicity as distal signalling increases. Occurrence of a significant spatial period (§2.3) becomes more likely at lower repression threshold values (stronger coupling strength). However, as occurrence

increases, the D_c value decreases, indicating that the spatial patterns forming are largely stationary ones.

Regions of the parameter space are defined to be a good match to the experimental observations and exhibit dynamic spatial patterns if the spatial period T_{spatial} , occurrence Occ and dynamicity coefficient D_c satisfy

$$T_{\text{spatial}} > 3, \text{ Occ} > 0.4, \text{ and } D_c > 0.4. \quad (3.1)$$

Despite the DBP algorithm not being present, there are perturbations due to expression noise and ultradian oscillations. It is these inherent variations in expression that cause the thin dynamic pattern region of parameter space in figure 7b (region without white diagonal lines overlaid), when the coupling strength is sufficiently strong to induce a weak spatial pattern, but weak enough for the inherent perturbations to enable dynamic switching between high and low states. See electronic supplementary material, movie S1 for an animated one-dimensional simulation without DBP included.

For simulations that include the DBP algorithm, we estimated values for T_{pert} and F_{pert} from the literature. Experimental work in the chick neural tube found that Tis21, a marker for neurogenically dividing neural progenitors, was upregulated around 8 h after Delta-1 was expressed in the same cell, followed by the generation of neurons around 16 h [47]. Assuming that within this time, signalling from the Delta-1 expressing cell upregulates Notch signalling in neighbouring cells, then at least 8h perturbation seems reasonable,

and we choose a value of $T_{\text{pert}} = 7$ h. In electronic supplementary material, figures S2 and S3, an exploration of other T_{pert} values found that longer perturbation enhanced the range of parameters in which dynamic patterning occurred. To estimate a value for F_{pert} we searched for literature that explores upregulation of Mib1 and its effect on neighbouring cell's Notch response, as Mib1 determines the efficiency of transactivation of Notch signalling. One study looked at the effect of coculturing mouse neocortex Mib1-positive intermediate progenitors and Mib1-negative RG cells with Notch1 expressing cells and compared the resulting levels of Hes1 expression within these Notch1 cells [31]. Two methods were used to isolate populations of Mib1-positive cells, and it was found that compared with RG cells, Mib1-positive cells caused between a 1.8- to 3.7-fold increase in Hes1 expression. In an *in vivo* study of chick neural tube, upregulation of both Delta-1 and membrane-localized Mib1 caused a 1.8-fold increase in HES5 intensity in RG cells [32]. We chose a value from the higher range of these Mib1-induced increases in HES and set $F_{\text{pert}} = 3$.

With the DBP algorithm included in the simulation (figure 7c,d), the parameter space for spatial period and occurrence remains broadly similar. However, high D_c values extend further into lower repression thresholds (high coupling strength) when compared with the simulations without DBP (figure 7a,b). This generates an expanded region of parameter space that satisfies equation (3.1) (region without white diagonal lines overlaid in figure 7c). The kymographs *d*(4) and (5) further confirm and visualize how the dynamic pattern evolves, showing a more definite and higher amplitude spatial pattern forming (compared with *b*(2)) but still with switching of peaks and troughs, and even some transient travelling wave type behaviour. At very low repression threshold *d*(6), stationary patterns still emerge when the perturbation strength cannot overcome the effects of strong coupling. See electronic supplementary material, movie S2 for an animated one-dimensional simulation with DBP included.

We explored the effect of varying the LI time delay between cells. The literature indicates a wide range of possible values this could take, from 20 to 120 min [36–40], and in the electronic supplementary material, figures S2 and S3, τ_{LI} values between 0 and 100 min are tested, along with T_{pert} values between 0 and 14 h. The results show that as τ_{LI} increases, the dynamic patterning region decreases, but crucially the region still expands when DBP is included, indicating robustness of the proposed mechanism. This reduced dynamic patterning region at longer LI time delays can be expanded by increasing the duration of T_{pert} , which is the time that a differentiating cell exerts higher signalling on its neighbours. As the expanding effect of DBP inclusion was found to occur across all LI time delays, and due to uncertainty in the actual value of the time delay, we chose to reduce the complexity of the model for the main results and use a value of $\tau_{\text{LI}} = 0$ min.

Taken together this set of results indicates that from the underlying stationary pattern formed by LI, the pattern can be made dynamic by the introduction of perturbations to HES5 levels. The perturbations drive individual cells away from the two attractor states generated by LI (higher/lower phenotype between signalling neighbours) and thus enable opportunities for the reorganization of peak and trough locations. The ability to switch states is a balance between coupling strength and perturbation size; at higher coupling strengths, perturbations cannot change the abundance of HES5 enough to enable a switch between low/high abundance

in their neighbours. Conversely, at weak coupling strength, the system has no spatial pattern forming ability. Between these extremes lies a region where lateral inhibition is strong enough to form spatial patterns if unperturbed but capable of switching states given sufficient perturbation.

3.3. Dynamic spatial patterning occurs in two-dimensional simulations

To explore how introducing more signalling neighbours affects the dynamic pattern forming ability of the model, we simulate a two-dimensional hexagonal grid and show that the one-dimensional results of the previous section extend to the two-dimensional case. A grid size of 26 rows by 6 columns is chosen as this corresponds approximately to the number of nuclei within the dorsal–ventral, apical–basal HES5 expression domain (figure 6h) [14]. The two-dimensional arrangement involves an additional four proximal and two distal neighbours compared with the one-dimensional simulations, meaning that each cell receives an average input signal generated from a larger number of neighbours.

Without DBP included (figure 8a), the parameter space outputs were generally similar to the one-dimensional case (figure 7a). However, the dynamicity was found to be largely low in the region where high occurrence of a spatial period was found, indicating that only stationary patterns can be generated. The absence of robust dynamic patterning is confirmed by the thin band where equation (3.1) is met (region without a white diagonal line overlay in figure 8a), much smaller than in the one-dimensional case. This appears to be due to the additional signalling from the higher number of cells (10 signalling neighbours in the two-dimensional case versus four neighbours in the one-dimensional case), which reinforce the strength of lateral inhibition, making switching states due to stochastic noise and HES5 oscillations less likely. In addition, at low repression threshold values/high coupling strength (0–2000 in figure 8a), occurrence was found to be lower than in the one-dimensional case. In this region, LI is found to still drive expression to high and low states as expected; however, due to the higher number of neighbours, the increased signalling strength resulted in irregular patterns, causing a spread of frequency values in the power spectrum, and therefore, no single significant peak detected using the Fisher *g*-test.

When the DBP algorithm is included (figure 8b), dynamic patterning is recovered, and a region of high dynamicity is found to overlap with high occurrence of a spatial period. Comparing the acceptance region that satisfies equation (3.1) in figure 8b with the one-dimensional case in figure 7d, it can be seen that the area is reduced and shifted slightly towards higher distal signalling efficiencies. However, in the one-dimensional case, where distal signalling efficiencies of 1 were found to generate dynamic patterning, the minimum efficiency required in two dimensions is $\varepsilon_d/\varepsilon_p > 1$. This need for higher distal signalling is due to the fact that when there are higher numbers of neighbours, individual cells contribute less of an effect on their neighbours due to the incoming signal being the averaged expression of the neighbours. See electronic supplementary material, movie S3 for an animated two-dimensional simulation with DBP included.

As protrusions have a much smaller contact area than when two-cell bodies contact, one might intuitively expect more Notch signalling to occur at the cell body. However, one study identified that not only is contact area an important

consideration but that also the diffusion rate of Notch and Delta across the cell membrane influences the amount of signalling that occurs. Higher diffusion rates of Notch and Delta, probably enabled by active transport within protrusions, can in fact enable higher rates of Notch signalling in protrusions than in a larger contact area of cell body with lower diffusion rates of Notch/Delta [48]. In other modelling work, Hadjivasilou *et al.* suggested the ability to mechanically pull on Delta and subsequently activate Notch signalling may be different at the cell body versus the protrusions [18]. They hypothesized that this difference could be caused by either a reduced amount of endocytosis at the cell body or that the dynamic extending/retracting nature of protrusions could provide the mechanical force required for Notch activation. A final possibility is that *cis*-inhibition may be more common in the cell body than in protrusions, and this would occur if high amounts of both Notch and Delta are present on the cell body, but only one of Notch or Delta is found in the protrusions.

As discussed in the previous section, when DBP is not present in the one-dimensional simulations, the noisy fluctuations and ultradian oscillations are capable of producing a thin region of parameter space where weak dynamic patterning can occur (figure 7*a*). This prompts the question: to what extent do these smaller amplitude fluctuations affect switching when DBP is included? Without DBP, dynamic patterning occurs at weaker LI coupling strengths, where the two high and low attractor states are not sufficiently attracting to prevent noise/ultradian oscillations from inducing switches between the two states. However, at stronger coupling strengths, the LI states attract more strongly, and make smaller amplitude fluctuations increasingly unlikely to induce switching between states when compared with the larger amplitude perturbations provided by DBP (figures 7*c* and 8*b*). This does not rule out that noise/ultradian oscillations play some role in enhancing switching, but it is clear from this analysis these smaller amplitude fluctuations are not sufficient to induce switching at stronger coupling strengths.

3.4. Ultradian oscillations are nested within the larger amplitude DBP switching behaviour

Ex vivo observations from the study by Biga *et al.* [14] indicate that the temporal dynamics of single cells consist of both noisy and ultradian oscillations (average temporal period of 3.3 h) nested within larger amplitude, longer time scale switching behaviour (average time spent high or low was 8 h). Through measuring persistence times and plotting single-cell time traces, DBP is found to produce similar nested dynamics to that in the neural tube.

In addition to D_c values, persistence time gives useful information about which mechanisms are contributing to any switching behaviour that is occurring. As defined in §2.4, persistence time refers to the amount of time a cell spends in a high or low state before switching to the opposite fate, and the distribution of low and high persistence times is plotted in figure 9*a–c* (ii). Noisy/ultradian dynamics are characterized by mean persistence times of around 3.6–3.9 h, as revealed by running the model without LI and without DBP (figure 9*a* (ii)). These noisy/ultradian persistence times that make up the left-most parts of the distributions are found to be present in all model conditions (figure 9*a–c* (ii)).

When LI coupling is included in the simulations, but DBP is not (figure 9*b* (ii)), the distribution is shifted to longer

persistence times than in the uncoupled case. The LI induces two larger amplitude high and low states (figure 9*b* (i)), while maintaining smaller amplitude noisy/ultradian oscillations at the mean levels dictated by the LI. This results in noisy/ultradian dynamics not being able to contribute to the switching as much, and the mean persistence times are longer at 27.3–30.9 h. In addition, a peak at 150 h is found (figure 9*b* (ii)), which means that a fraction of the cells spend the entire measurement time stuck in one state, indicating more stationary patterning.

Crucially, the inclusion of DBP into the LI model (figure 9*c*) removes the peak at 150 h, while still maintaining longer mean persistence times (10.8–12.9 h) than the uncoupled model. The single-cell time trace in figure 9*c* (i) shows a more regular switching than in figure 9*b* (i), while still being distinct from the shorter timescale ultradian oscillations in figure 9*a* (i). Relating this back to the observation of nested dynamics in [14], it can be seen that a similar nested oscillation behaviour occurs in the model with DBP included (figure 9*c* (i)), with a mixture of smaller amplitude noisy dynamics and ultradian oscillations (red arrows in 9*c* (i)) being nested within the larger amplitude switching dynamics generated by the LI and DBP algorithm.

While there is more regularity in the switching in figure 9*c* than in figure 9*a* or *b*, the distribution still has a wide spread of possible persistence times in figure 9*c* (ii). The *ex vivo* observations are limited to measurement times of at most 16 h, and the mean experimental persistence times indicated a tighter distribution with a mean value of around 8 h. While inclusion of DBP in the model fits the data closest, further exploration is needed to understand how the persistence time distributions can be made tighter in line with the *ex vivo* observations.

For a visual comparison between the model with DBP (figure 9*c* (i)) and the experimental data, single-cell time traces are plotted in figure 9*d* (i–vi), which show Venus::HES5 fluorescent intensities tracked over 12 h (replotted from source data in [3]). These traces are limited to 12 h due to experimental constraints, much shorter than the plotted simulation outputs, and so at most show two switches between high and low states (figure 9*d* (i) and (vi)). Both high-to-low and low-to-high switches are observed in the experimental data, with a mix of aperiodic and period dynamics observed. Figure 9*d* (ii) and (iii) show more pronounced transient ultradian oscillations which then become aperiodic noisy expression at later time points (red arrows indicate peaks of ultradian dynamics). Importantly, the amplitude (peak to trough difference in fluorescence) is smaller in the ultradian oscillations than in the long-term switching behaviour of the single cells, and previous analysis found that the long-term trend has an amplitude (standard deviation of normalized HES5 expression levels) approximately twice that of the ultradian oscillations [3]. Though not quantified here, it can be seen in figure 9*c* (i) that the ratio of longer switching to ultradian oscillation amplitude is of the same order as the experimental data.

3.5. Dynamic patterning spreads out differentiation events spatially while maintaining a higher differentiation rate than the uncoupled model

To explore the potential functionality of the dynamic patterning, the spatial distribution of differentiation events and the

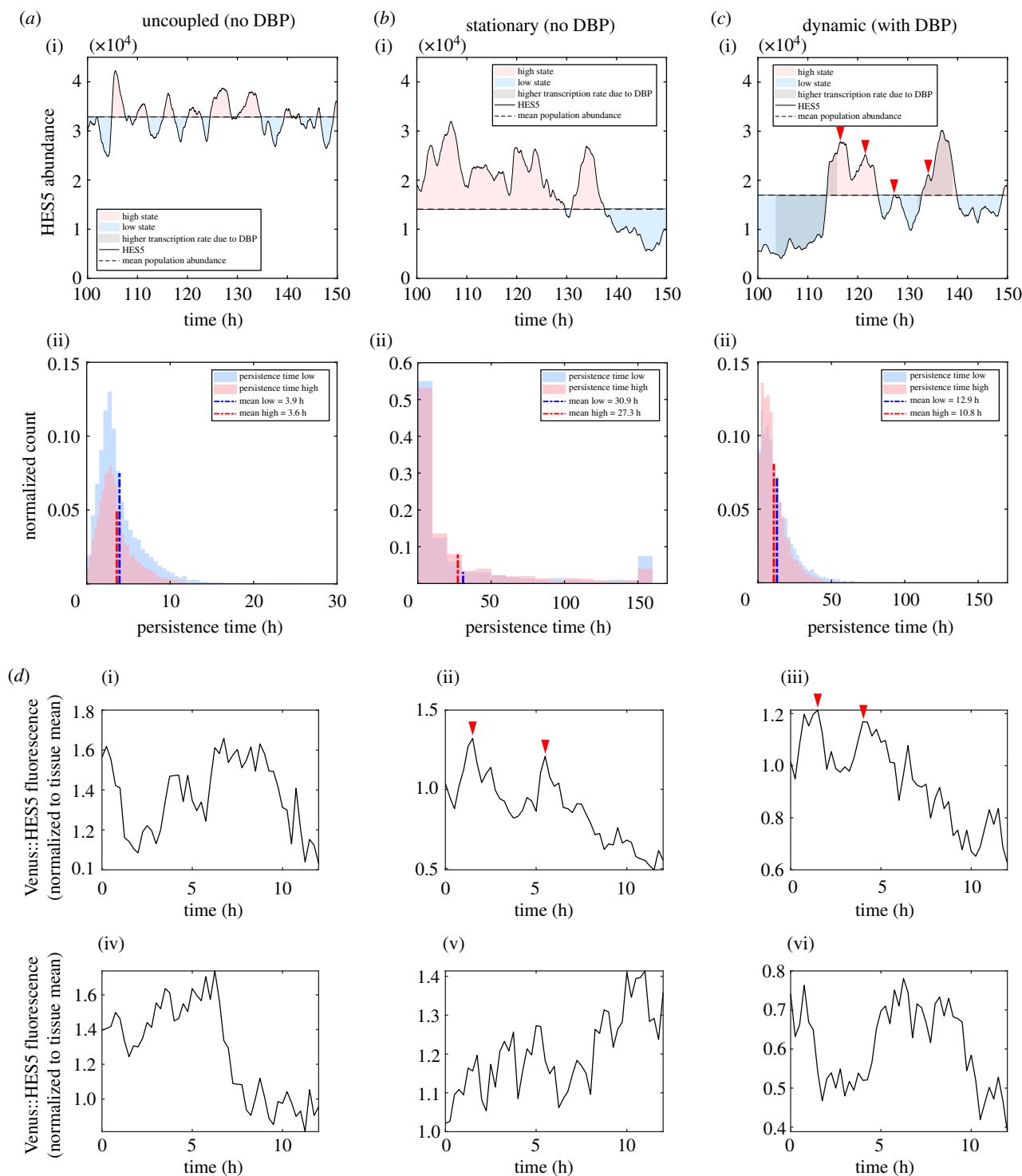


Figure 9. (a–c), (i) Representative single-cell time traces, (ii) histograms of individual persistence times $T_{\uparrow,n}$ (pink), and $T_{\downarrow,n}$ (blue) (see S2.4 for a definition of persistence times). (a) Model output with no DBP algorithm included and no LI coupling between the cells. (b) The model output with no DBP algorithm included and $P_{0,LI} = 4000$. (c) The model output with DBP algorithm included and $P_{0,LI} = 4000$, and red arrows indicate peaks in ultradian oscillations. Simulations in (i) used 1 column, 26 rows, and simulation run time of 200 h. (ii) Data from 30 individual simulations plotted. Each simulation used 26 rows, 1 column, and simulation run time of 300 h, and only the last 150 h of the simulation was used to measure persistence time. (d) (i–vi) Single-cell Venus::HES5 fluorescence time traces taken from experiment source data in [3] and replotted here.

rate of differentiation was explored by comparing three different conditions: a stationary spatial pattern (figure 10a,d), a dynamic spatial pattern (figure 10b,e), and no spatial pattern via uncoupled cells (figure 10c,f).

To visualize how patterning affects the spatial aspect of differentiation, bar graphs showing the total number of differentiation events that occurred over a simulation were plotted to the right of the kymographs in figure 10a–c. In

the stationary patterning case figure 10a, it can be seen that the likelihood of differentiating is spatially inhomogeneous. Because low-expressing areas are more likely to incur a differentiation event and because these low-expression regions are fixed in time, the differentiation distribution reflects the periodicity of the pattern. Conversely, the dynamic spatial pattern and no spatial pattern case (figure 10b and c) have more homogeneous spatial

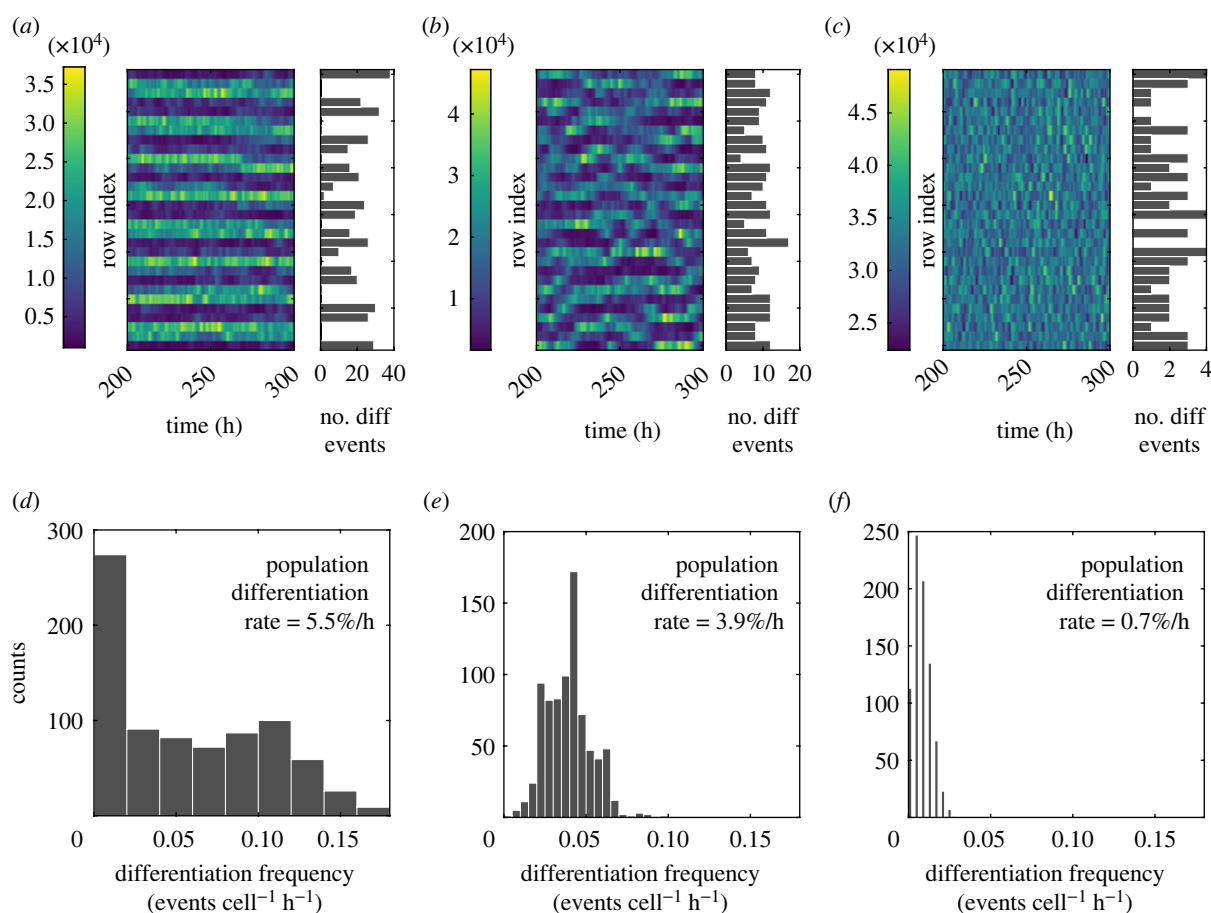


Figure 10. Spatial and temporal measurements of differentiation in three different simulation conditions: (a) and (d) output from a stationary spatial pattern (no DBP algorithm used), (b) and (e) a dynamic spatial pattern (DBP algorithm included) and (c) and (f) show no spatial pattern (uncoupled cells/no lateral inhibition). (a–c) The last 100 h of simulation as kymographs and plotted to the right of each kymograph is a histogram showing the total number of differentiation events that occur in each row over the entire 300 h, though only the last 100 h is plotted in the kymographs. (d–f) Histograms of the differentiation frequency ($\$2.5$) in individual cells (events $\text{cell}^{-1} \text{h}^{-1}$), and also the rate of differentiation of the population is given as the a percentage of the population size per hour (800 h of simulation to produce graphs (d–f)). All simulation conditions use $P_{NDO} = 3500$, $\epsilon_d/\epsilon_p = 1.5$, with a grid size of 26 columns by 1 row.

distributions of differentiation events, since every cell can switch between higher and lower expression.

To explore how differentiation rate is affected, the distribution of differentiation frequency in individual cells was plotted (figure 10d–f), along with the differentiation rate of the population as a percentage. The stationary pattern had the highest rate of differentiation at $5.5\% \text{h}^{-1}$ (D), and the distribution of differentiation frequency in individual cells showed a bimodal distribution, which reflects the two different rates of differentiation occurring in the low and high expressing cells. The dynamic pattern showed a slightly lower rate of differentiation compared with the stationary pattern at $3.9\% \text{h}^{-1}$, and the distribution has a single peak. The uncoupled no pattern case showed a very low rate of differentiation rate at $0.7\% \text{h}^{-1}$, and also with a single peak. See electronic supplementary material, movies S1 and S2 for animated one-dimensional simulations without and with DBP included.

The spatial and temporal measures taken together indicate that for a dynamic pattern, differentiation events are spread out spatially rather than concentrated in one position as is the case in stationary patterns. This spatial spreading of differentiation is also naturally achieved in the case when there is no coupling/no LI; however, in the absence of Notch amplifying the differences between cells, cells do not have such a high amplitude between high and low expression, resulting in a

much lower rate of differentiation. Therefore, dynamic patterning maintains a high differentiation rate like that in stationary patterning, but enables a more homogeneous distribution of differentiating cells in space.

4. Discussion

In this paper, we have investigated the mechanism and function of dynamic spatial patterns in development, motivated by observations of periodic clusters of HES5 expression that change peak and trough location over time [14]. We introduced two methods that can be used to identify dynamic spatial patterns. First, spatial signals at individual time points can be tested for periodicity using a Fisher g -test on the generated power spectra. Second, we proposed the dynamicity coefficient as a measure to test whether peaks and troughs in a spatial signal switch states over time by comparing proportions of time spent in high and low states. Previous models accounted for the observed synchronization of ultradian oscillations between neighbouring cells, but did not capture the generation of three- to four-cell periodicity or the dynamic switching of the spatial pattern.

To address the generation of a three- to four-cell spatial period, we extended the signalling distance in the model by introducing distal cells (figure 6d), which generated three- to four-cell periodicity, compared with the two-cell

periodicity that occurs in nearest-neighbour signalling. We propose that dynamically extending and retracting protrusions carrying Notch ligands probably account for extended signalling in the neural tube tissue [17,25–28]. If protrusions are the underlying mechanism, then distal signalling efficiency is interpreted as the amount of Notch signalling occurring at the cell body versus at the protrusions. The model predicts that the type of dynamic pattern observed in the neural tube is more likely to occur at higher distal strengths ($\epsilon_d/\epsilon_p > 1$). As discussed in §3.3, this could be due to differences in mechanical activation, diffusion rates or *cis*-inhibition between the cell body and the protrusions [18,48]. Future experimental work should focus around characterizing the extent and dynamics of protrusions in the developing mouse neural tube, and where Notch and Delta are localized on cell membranes to get a better picture of where Notch signalling is most active.

To understand how dynamic switching of the spatial pattern arises in the neural tube, we explored the potential role of differentiation and dynamic signalling strength. To translate the differentiation process into the model, we implemented a perturbation process where cells that contact a differentiating cell experience an upregulation in HES5 transcription rate (DBP algorithm, outlined in §2.5). The inclusion of DBP in the model resulted in a region of parameter space being identified where dynamic spatial patterning occurs, indicating that with sufficient and regular perturbation, high and low states generated by the underlying Notch LI circuit can be dynamically switched and reorganized. In addition, nested dynamics of ultradian oscillations on top of the larger amplitude switching dynamics were observed in the model-generated single-cell time traces (figure 9), similar to that observed *ex vivo* [14]. One aspect that remains unclear due to experimental limits of the observation time of the *ex vivo* slices, is the regularity of switching. Future experimental work therefore would be very informative if longer observation times could be obtained, as this would enable more detailed comparison of the model-generated persistence time distributions against the data.

Due to higher numbers of signalling interactions in the two-dimensional simulations, regions of dynamic patterning in parameter space were found to be more restricted than in the one-dimensional simulations. From biological studies, the average number of signalling neighbours per RG cell is not known, so whether the one- or two-dimensional simulations are more representative of the biological system is unclear. Some studies suggest that most of the Notch signalling occurs at the apical side of the neuroepithelium [29,49], in which case the restricted number of spatial interactions might be more akin to the one-dimensional model. Other studies show that Delta-carrying protrusions extend down from the basally located newborn neurons to interact with apically located RG cells, and RG cells extend dynamic protrusions in both apical and non-apical locations, in which case the two-dimensional simulations may be more representative of the number of signalling interactions [25,26,28]. An additional consideration is where and when differentiating cells have an altered signalling effect on their neighbours. It would be interesting to introduce cell movement into future modelling so as to investigate the effect of the apical–basal migration of differentiating cells.

It is important to consider that perturbations could reasonably come from sources other than altered signalling

in differentiating cells. Processes such as the extension and retraction of signalling protrusions, cell cycle variations in HES5/coupling strength, interkinetic nuclear migration and pulsatile Dll1 signalling are all reasonable candidates in contributing to the switching behaviour [25,28,50–52]. The DBP algorithm is general enough that it could reasonably be adapted to any of the listed alternatives, by altering the magnitude and duration of the perturbation, as well as the parameter it is applied to. Furthermore, there are also entirely separate mechanisms that could underlie the observed HES5 pattern that are not perturbation based. For example, we also explored morphogen gradient-induced travelling waves as a potential mechanism (not included in this study), inspired by somitogenesis studies. We found the travelling waves did not as closely match the data and required assumptions that seemed less likely from the literature, but we cannot rule this mechanism out without further exploration. For the mechanism underlying the clustered/extended spatial periodicity, it may be also worth considering modifications of Notch signalling such as *cis*-inhibition or lateral induction from other Notch ligands such as Jagged, as both of these mechanisms show a tendency to form longer range or clustered patterning [53,54].

Regardless of underlying mechanisms, this is a model that produces a dynamic pattern sufficiently similar to that of HES5 in the neural tube and so we tested what functional advantage such a dynamic pattern might provide during development, finding that dynamic patterning spreads out differentiation events spatially, rather than generating hot-spots of differentiation like in the stationary case. Stationary patterning seems most suited to tissues where differentiating cells remain within the progenitor population and need to be regularly spaced apart such as in the formation of sensory hairs in *Drosophila* [19]. In the developing neural tube, differentiating cells do not form a regular pattern of differentiated cells within the progenitor population itself, rather they leave the progenitor population and migrate basally to form neurons and glia at later stages [55]. Although the functional advantage of dynamic patterning is not established, we conjecture that it ensures that the production of neurons is evenly distributed across the dorsal–ventral axis and prevents many differentiating cells from being repeatedly produced in the same locations as in the stationary patterning case.

In sum, we have explored how a stationary pattern generating signalling network, Notch LI, can be made dynamic through the introduction of perturbations that enable cells to switch between high and low expression. We suggest that a combination of protrusions and altered signalling strength coming from differentiating cells are the most likely underlying mechanisms that produce the dynamic HES5 spatial pattern found in the developing neural tube. However, further experiments need to be carried out regarding the presence of Notch carrying protrusions, and whether these protrusions are capable of generating extended spatial periodicity, along with tests of how much perturbation comes from differentiating cells in the developing neural tube.

Data accessibility. All code is written in Matlab and is available at <https://github.com/Papalopulu-Lab/Hawley2022>.

The data are provided in electronic supplementary material [56].

Authors' contributions. J.H.: conceptualization, formal analysis, investigation, methodology, software, visualization, writing—original draft, writing—review and editing; P.G.: conceptualization, formal

analysis, investigation, methodology, supervision, writing—original draft, writing—review and editing; N.P.: conceptualization, investigation, supervision, writing—original draft, writing—review and editing; C.M.: data curation, writing—review and editing; V.B.: methodology, writing—review and editing.

All authors gave final approval for publication and agreed to be held accountable for the work performed therein.

Conflict of interest declaration. We declare we have no competing interest.

Funding. J.H. was supported by a Wellcome Trust PhD studentship (220001/Z/19/Z). The work was supported by a Wellcome Trust Investigator award to N.P. (224394/Z/21/Z). C.M. was funded by an MRC Career Development Award (MR/V032534/1). The funders had no role in study design, data collection and analysis, decision to publish, or preparation of the manuscript.

Acknowledgements. The authors thank members of the Papalopulu Lab for their useful input to this work.

References

- Götz M, Huttner WB. 2005 The cell biology of neurogenesis. *Nat. Rev. Mol. Cell Biol.* **6**, 777–788. (doi:10.1038/nrm1739)
- Das RM, Storey KG. 2014 Apical abscission alters cell polarity and dismantles the primary cilium during neurogenesis. *Science* **343**, 200–204. (doi:10.1126/science.1247521)
- Manning CS *et al.* 2019 Quantitative single-cell live imaging links HES dynamics with cell-state and fate in murine neurogenesis. *Nat. Commun.* **10**, 1–19. (doi:10.1038/s41467-019-10734-8)
- Hatakeyama J, Bessho Y, Katoh K, Ookawara S, Fujioka M, Guillemot F, Kageyama R. 2004 HES genes regulate size, shape and histogenesis of the nervous system by control of the timing of neural stem cell differentiation. *Development* **131**, 5539–5550. (doi:10.1242/dev.01436)
- Shimojo H, Ohtsuka T, Kageyama R. 2008 Oscillations in Notch signaling regulate maintenance of neural progenitors. *Neuron* **58**, 52–64. (doi:10.1016/j.neuron.2008.02.014)
- Martínez-Cerdeño V, Noctor SC. 2018 Neural progenitor cell terminology. *Front. Neuroanatomy* **12**, 104. (doi:10.3389/fnana.2018.00104)
- Sagner A *et al.* 2018 Olig2 and HES regulatory dynamics during motor neuron differentiation revealed by single cell transcriptomics. *PLoS Biol.* **16**, e2003127. (doi:10.1371/journal.pbio.2003127)
- Kageyama R, Shimojo H, Ohtsuka T. 2019 Dynamic control of neural stem cells by bHLH factors. *Neurosci. Res.* **138**, 12–18. (doi:10.1016/j.neures.2018.09.005)
- Andersson ER, Sandberg R, Lendahl U. 2011 Notch signaling: simplicity in design, versatility in function. *Development* **138**, 3593–3612. (doi:10.1242/dev.063610)
- Preuß K *et al.* 2015 Context-dependent functional divergence of the Notch ligands DLL1 and DLL4 in vivo. *PLoS Genet.* **11**, e1005328. (doi:10.1371/journal.pgen.1005328)
- Marklund U, Hansson EM, Sundström E, de Angelis MH, Przemeczek GKH, Lendahl U, Muhr J, Ericson J. 2010 Domain-specific control of neurogenesis achieved through patterned regulation of Notch ligand expression. *Development* **137**, 437–445. (doi:10.1242/dev.036806)
- Kutejova E, Sasai N, Shah A, Gouti M, Briscoe J. 2016 Neural progenitors adopt specific identities by directly repressing all alternative progenitor transcriptional programs. *Dev. Cell* **36**, 639–653. (doi:10.1016/j.devcel.2016.02.013)
- Imayoshi I, Kageyama R. 2014 Oscillatory control of bHLH factors in neural progenitors. *Trends Neurosci.* **37**, 531–538. (doi:10.1016/j.tins.2014.07.006)
- Biga V *et al.* 2021 A dynamic, spatially periodic, micro-pattern of HES5 underlies neurogenesis in the mouse spinal cord. *Mol. Syst. Biol.* **17**, e9902. (doi:10.15252/msb.20209902)
- Muskavitch MAT. 1994 Delta-Notch signaling and *Drosophila* cell fate choice. *Dev. Biol.* **166**, 415–430. (doi:10.1006/dbio.1994.1326)
- Collier JR, Monk NAM, Maini PK, Lewis JH. 1996 Pattern formation by lateral inhibition with feedback: a mathematical model of Delta-Notch intercellular signalling. *J. Theor. Biol.* **183**, 429–446. (doi:10.1006/jtbi.1996.0233)
- Cohen M, Georgiou M, Stevenson NL, Miodownik M, Baum B. 2010 Dynamic filopodia transmit intermittent Delta-Notch signaling to drive pattern refinement during lateral inhibition. *Dev. Cell* **19**, 78–89. (doi:10.1016/j.devcel.2010.06.006)
- Hadjivasiliou Z, Hunter GL, Baum B. 2016 A new mechanism for spatial pattern formation via lateral and protrusion-mediated lateral signalling. *J. R. Soc. Interface* **13**, 20160484. (doi:10.1098/rsif.2016.0484)
- Corson F, Couturier L, Rouault H, Mazouni K, Schweisguth F. 2017 Self-organized Notch dynamics generate stereotyped sensory organ patterns in *Drosophila*. *Science* **356**, eaai7407. (doi:10.1126/science.aai7407)
- Couturier L, Mazouni K, Corson F, Schweisguth F. 2019 Regulation of Notch output dynamics via specific E (spl)-HLH factors during bristle patterning in *Drosophila*. *Nat. Commun.* **10**, 1–13. (doi:10.1038/s41467-019-11477-2)
- Bocci F, Onuchic JN, Jolly MK. 2020 Understanding the principles of pattern formation driven by Notch signaling by integrating experiments and theoretical models. *Front. Physiol.* **11**, 929. (doi:10.3389/fphys.2020.00929)
- Shimojo H, Isomura A, Ohtsuka T, Kori H, Miyachi H, Kageyama R. 2016 Oscillatory control of Delta-like1 in cell interactions regulates dynamic gene expression and tissue morphogenesis. *Genes Dev.* **30**, 102–116. (doi:10.1101/gad.270785.115)
- Tiedemann HB, Schneltzer E, Beckers J, Przemeczek GKH, de Angelis MH. 2017 Modeling coexistence of oscillation and Delta/Notch-mediated lateral inhibition in pancreas development and neurogenesis. *J. Theor. Biol.* **430**, 32–44. (doi:10.1016/j.jtbi.2017.06.006)
- De Jossineau C, Soule J, Martin M, Anguille C, Montcourrier P, Alexandre D. 2003 Delta-promoted filopodia mediate long-range lateral inhibition in *Drosophila*. *Nature* **426**, 555–559. (doi:10.1038/nature02157)
- Nelson BR, Hodge RD, Bedogni F, Hevner RF. 2013 Dynamic interactions between intermediate neurogenic progenitors and radial glia in embryonic mouse neocortex: potential role in DLL1-Notch signaling. *J. Neurosci.* **33**, 9122–9139. (doi:10.1523/JNEUROSCI.0791-13.2013)
- Hadjivasiliou Z, Moore RE, McIntosh R, Galea GL, Clarke JDW, Alexandre P. 2019 Basal protrusions mediate spatiotemporal patterns of spinal neuron differentiation. *Dev. Cell* **49**, 907–919. (doi:10.1016/j.devcel.2019.05.035)
- Moore RE, Clarke J, Alexandre P. 2020 Protrusion-mediated signaling regulates patterning of the developing nervous system. *Front. Cell Dev. Biol.* **8**, 579073. (doi:10.3389/fcell.2020.579073)
- Kasioulis I, Dady A, James J, Prescott A, Halley PA, Storey KG. 2022 A lateral protrusion latticework connects neuroepithelial cells and is regulated during neurogenesis. *J. Cell Sci.* **135**, jcs259897. (doi:10.1242/jcs.259897)
- Hatakeyama J, Wakamatsu Y, Nagafuchi A, Kageyama R, Shigemoto R, Shimamura K. 2014 Cadherin-based adhesions in the apical endfoot are required for active Notch signaling to control neurogenesis in vertebrates. *Development* **141**, 1671–1682. (doi:10.1242/dev.102988)
- Koo B-K *et al.* 2005 Mind bomb 1 is essential for generating functional Notch ligands to activate Notch. *Development* **132**, 3459–3470. (doi:10.1242/dev.01922)
- Yoon K-J, Koo B-K, Im S-K, Jeong H-W, Ghim J, Kwon M-c, Moon J-S, Miyata T, Kong Y-Y. 2008 Mind bomb 1-expressing intermediate progenitors generate Notch signaling to maintain radial glial cells. *Neuron* **58**, 519–531. (doi:10.1016/j.neuron.2008.03.018)
- Baek C, Freem L, Goïame R, Sang H, Morin X, Tozer S. 2018 Mib1 prevents Notch cis-inhibition to defer differentiation and preserve neuroepithelial integrity during neural delamination. *PLoS Biol.* **16**, e2004162. (doi:10.1371/journal.pbio.2004162)
- Meloty-Kapella L, Shergill B, Kuon J, Botvinick E, Weinmaster G. 2012 Notch ligand endocytosis

- generates mechanical pulling force dependent on dynamin, epsins, and actin. *Dev. Cell* **22**, 1299–1312. (doi:10.1016/j.devcel.2012.04.005)
34. Monk NAM. 2003 Oscillatory expression of HES1, p53, and NF- κ B driven by transcriptional time delays. *Curr. Biol.* **13**, 1409–1413. (doi:10.1016/S0960-9822(03)00494-9)
35. Gillespie DT. 2000 The chemical Langevin equation. *J. Chem. Phys.* **113**, 297–306. (doi:10.1063/1.481811)
36. Lewis J. 2003 Autoinhibition with transcriptional delay: a simple mechanism for the zebrafish somitogenesis oscillator. *Curr. Biol.* **13**, 1398–1408. (doi:10.1016/S0960-9822(03)00534-7)
37. Herrgen L, Ares S, Morelli LG, Schröter C, Jülicher F, Oates AC. 2010 Intercellular coupling regulates the period of the segmentation clock. *Curr. Biol.* **20**, 1244–1253. (doi:10.1016/j.cub.2010.06.034)
38. Isomura A, Ogushi F, Kori H, Kageyama R. 2017 Optogenetic perturbation and bioluminescence imaging to analyze cell-to-cell transfer of oscillatory information. *Genes Dev.* **31**, 524–535. (doi:10.1101/gad.294546.116)
39. Baron JW, Galla T. 2019 Intrinsic noise, Delta-Notch signalling and delayed reactions promote sustained, coherent, synchronized oscillations in the presomitic mesoderm. *J. R. Soc. Interface* **16**, 20190436. (doi:10.1098/rsif.2019.0436)
40. Yoshioka-Kobayashi K, Matsumiya M, Niino Y, Isomura A, Kori H, Miyawaki A, Kageyama R. 2020 Coupling delay controls synchronized oscillation in the segmentation clock. *Nature* **580**, 119–123. (doi:10.1038/s41586-019-1882-z)
41. Wichert S, Fokianos K, Strimmer K. 2004 Identifying periodically expressed transcripts in microarray time series data. *Bioinformatics* **20**, 5–20. (doi:10.1093/bioinformatics/btg364)
42. Liew AW-C, Law N-F, Cao X-Q, Yan H. 2009 Statistical power of Fisher test for the detection of short periodic gene expression profiles. *Pattern Recognit.* **42**, 549–556. (doi:10.1016/j.patcog.2008.09.022)
43. Schafer RW. 2011 What is a Savitzky-Golay filter? [Lecture notes]. *IEEE Signal Process Mag.* **28**, 111–117. (doi:10.1109/MSP.2011.941097)
44. Kawaguchi A. 2021 Neuronal delamination and outer radial glia generation in neocortical development. *Front. Cell Dev. Biol.* **8**, 1883. (doi:10.3389/fcell.2020.623573)
45. Vasilopoulos G, Painter KJ. 2016 Pattern formation in discrete cell tissues under long range filopodia-based direct cell to cell contact. *Math. Biosci.* **273**, 1–15. (doi:10.1016/j.mbs.2015.12.008)
46. Bajpai S, Prabhakar R, Chelakkot R, Inamdhar MM. 2021 Role of cell polarity dynamics and motility in pattern formation due to contact-dependent signalling. *J. R. Soc. Interface* **18**, 20200825. (doi:10.1098/rsif.2020.0825)
47. Hämmerle B, Tejedor FJ. 2007 A novel function of Delta-Notch signalling mediates the transition from proliferation to neurogenesis in neural progenitor cells. *PLoS ONE* **2**, e1169. (doi:10.1371/journal.pone.0001169)
48. Khait I, Orsher Y, Golan O, Binshtok U, Gordon-Bar N, Amir-Zilberstein L, Sprinzak D. 2016 Quantitative analysis of Delta-like 1 membrane dynamics elucidates the role of contact geometry on Notch signaling. *Cell Rep.* **14**, 225–233. (doi:10.1016/j.celrep.2015.12.040)
49. Banda E, McKinsey A, Germain N, Carter J, Anderson NC, Gabel L. 2015 Cell polarity and neurogenesis in embryonic stem cell-derived neural rosettes. *Stem Cells Dev.* **24**, 1022–1033. (doi:10.1089/scd.2014.0415)
50. Spear PC, Erickson CA. 2012 Interkinetic nuclear migration: a mysterious process in search of a function. *Dev., Growth Differ.* **54**, 306–316. (doi:10.1111/j.1440-169X.2012.01342.x)
51. Nandagopal N, Santat LA, LeBon L, Sprinzak D, Bronner ME, Elowitz MB. 2018 Dynamic ligand discrimination in the Notch signaling pathway. *Cell* **172**, 869–880. (doi:10.1016/j.cell.2018.01.002)
52. Sabherwal N, Rowntree A, Marinopoulou E, Pettini T, Hourihane S, Thomas R, Soto X, Kursawe J, Papalopulu N. 2021 Differential phase register of HES1 oscillations with mitoses underlies cell-cycle heterogeneity in ER⁺ breast cancer cells. *Proc. Natl Acad. Sci. USA* **118**, e2113527118. (doi:10.1073/pnas.2113527118)
53. Owen MR, Sherratt JA, Wearing HJ. 2000 Lateral induction by juxtacrine signaling is a new mechanism for pattern formation. *Dev. Biol.* **217**, 54–61. (doi:10.1006/dbio.1999.9536)
54. Formosa-Jordan P, Ibañes M. 2014 Competition in Notch signaling with CIS enriches cell fate decisions. *PLoS ONE* **9**, e95744. (doi:10.1371/journal.pone.0095744)
55. Paridaen JTML, Huttner WB. 2014 Neurogenesis during development of the vertebrate central nervous system. *EMBO Rep.* **15**, 351–364. (doi:10.1002/embr.201438447)
56. Hawley J, Glendinning P, Papalopulu N, Manning C, Biga V. 2022 Dynamic switching of lateral inhibition spatial patterns. Figshare. (doi:10.6084/m9.figshare.c.6135944)

4.3 Supplementary figures

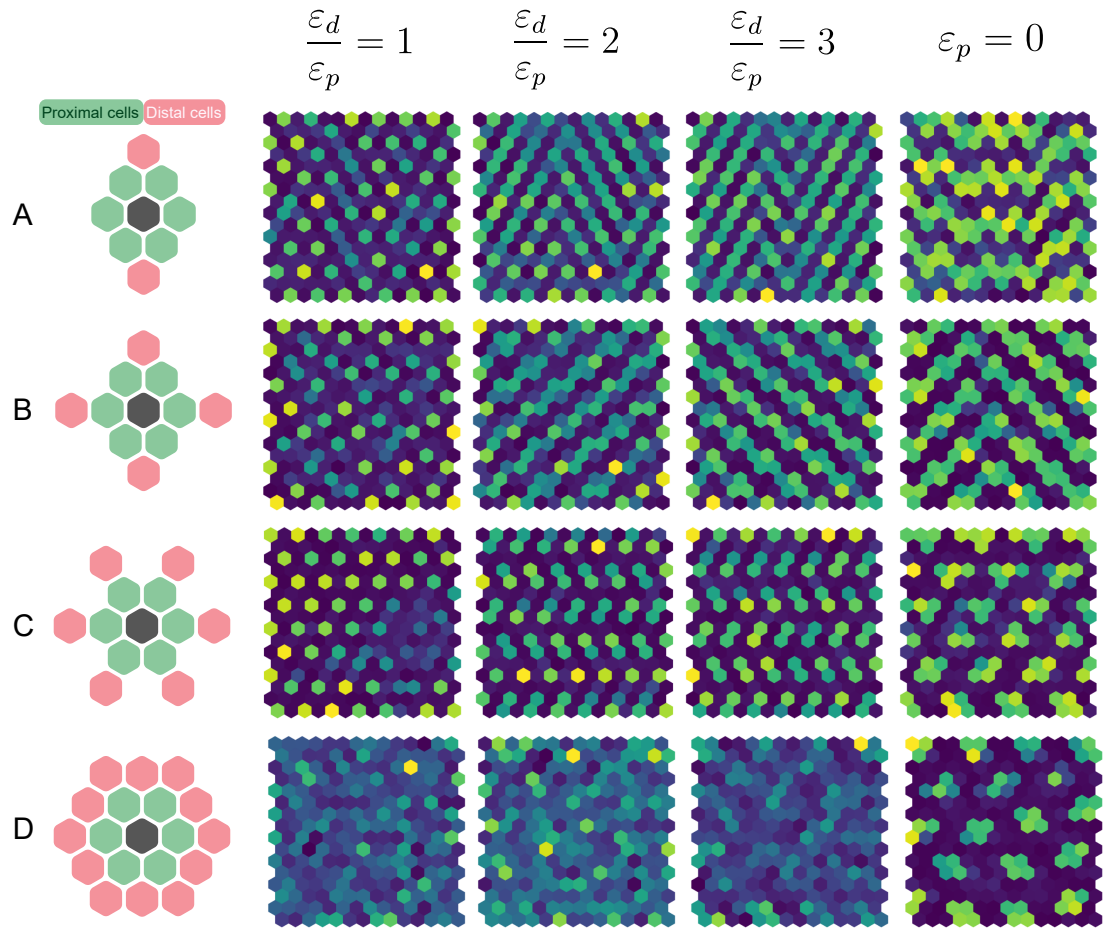


Figure S4.1: Exploration of different distal cell geometries. Each row (**A-D**) corresponds to a different geometry and each column corresponds to a different distal signalling efficiency with the last column showing the model output when no proximal cells are included. Simulations were run stochastically for 300h and the final time point is shown. A repression threshold value of $P_{0,LI} = 4000$ was used for all simulations.

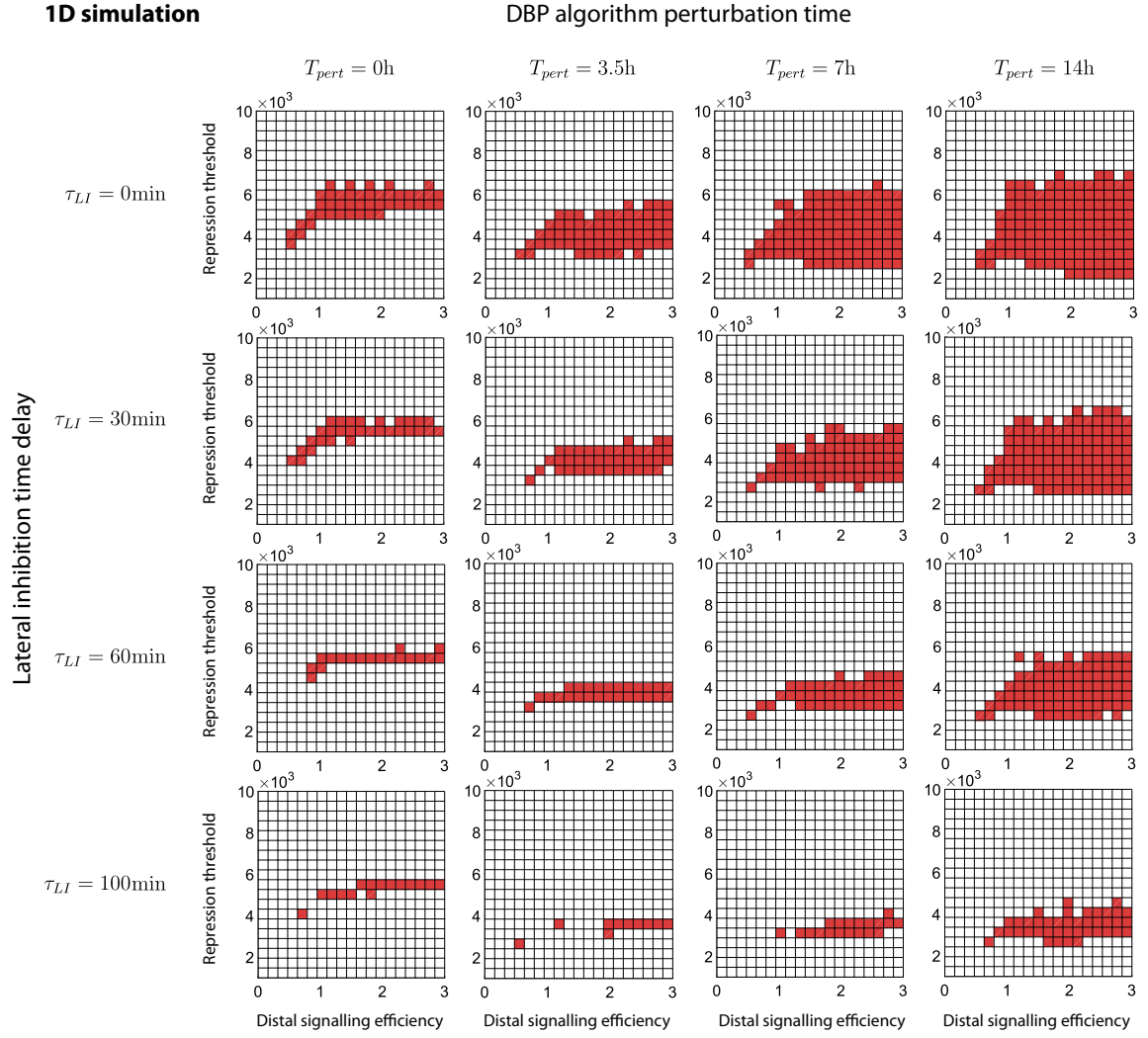


Figure S4.2: Effect of lateral inhibition time delay, T_{LI} , and differentiation time, T_{pert} , on the region of dynamic patterning (red) in 1D simulations (simulation final time 200h, 20 repeats, 26 row, 1 column).

2D simulation

DBP algorithm perturbation time

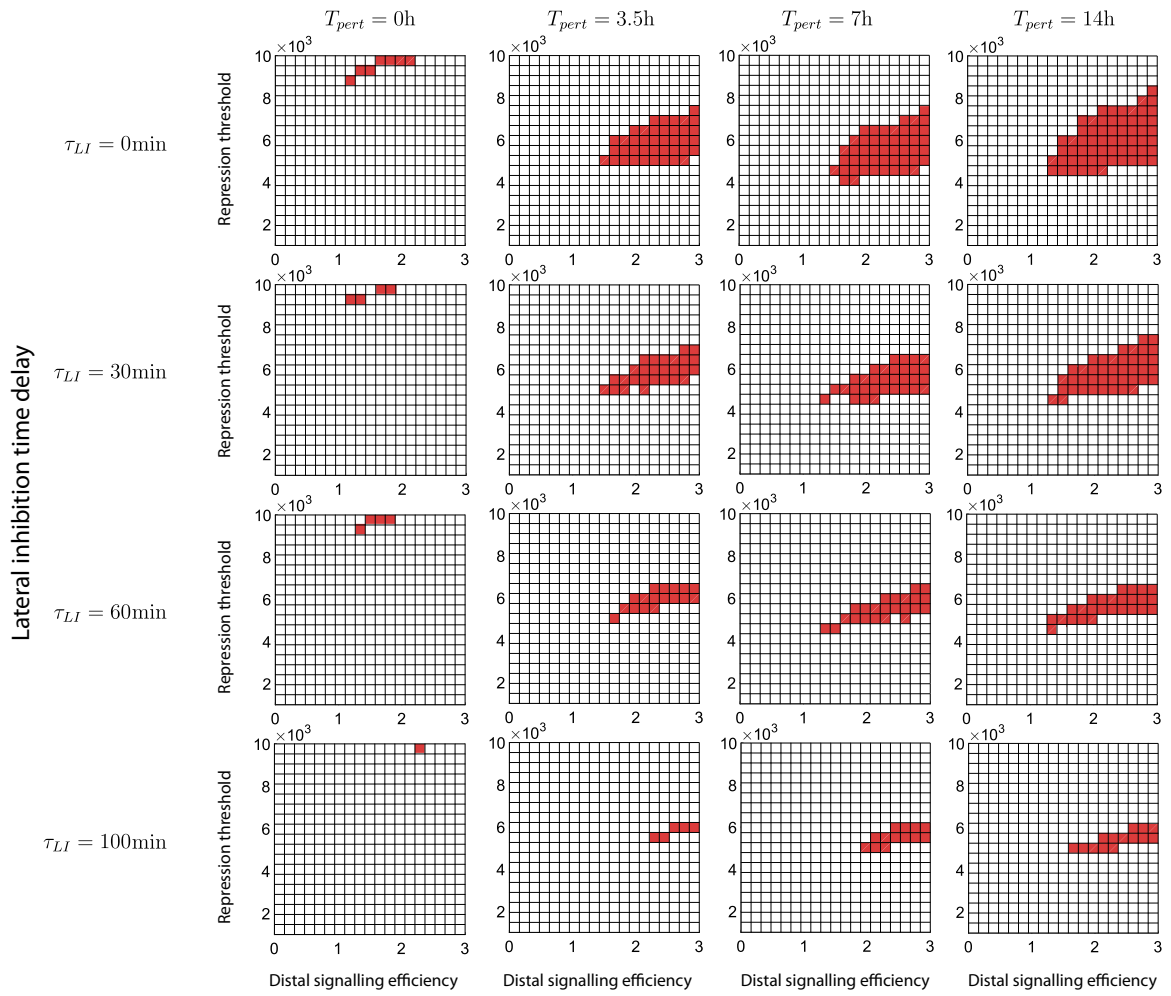


Figure S4.3: Effect of lateral inhibition time delay, T_{LI} , and differentiation time, T_{pert} , on the region of dynamic patterning (red) in 2D simulations (simulation final time 200h, 20 repeats, 26 row, 6 columns).

4.4 Supplementary movies

Supplementary Movie 1: 1D simulation of 26 rows by 1 column with no DBP algorithm included. A rolling kymograph is shown, as is the HES5 expression in the hexagonal lattice. Locations of differentiating cells are recorded but these do not change the signalling in neighbouring cells. The bar chart shows the total number of differentiation events recorded on each row. Simulation used $P_{0,LI} = 3500$, $\frac{\varepsilon_d}{\varepsilon_p} = 1.5$, simulation run time of 500h.

Supplementary Movie 2: 1D simulation of 26 rows by 1 column that does include the DBP algorithm. A rolling kymograph is shown, as is the HES5 expression in the hexagonal lattice. Locations of differentiating cells are recorded which alter the signalling in the neighbouring cells. The bar chart shows the total number of differentiation events recorded on each row. Simulation used $P_{0,LI} = 3500$, $\frac{\varepsilon_d}{\varepsilon_p} = 2$, $F_{pert} = 3$, $T_{pert} = 7h$, simulation run time of 500h.

Supplementary Movie 3: 2D simulation of 26 rows by 6 columns that does include the DBP algorithm. A rolling kymograph is shown which is plotting the expression in the first column of the simulated grid. HES5 expression in the hexagonal lattice is shown also. Locations of differentiating cells are recorded which alter the signalling in the neighbouring cells. Simulation used $P_{0,LI} = 6000$, $\frac{\varepsilon_d}{\varepsilon_p} = 2$, $F_{pert} = 3$, $T_{pert} = 7h$, simulation run time of 500h.

Chapter 5

Characterising protrusions and their role in patterning

The model described in Chapter 4 successfully reproduced many aspects of the neural tube HES5 data, and had higher explanatory power than the travelling wave model in Chapter 3. Therefore this chapter follows on from the work presented in Chapter 4 and aims to experimentally test one of the modelling assumptions to probe whether it is indeed involved in generating the observed HES5 pattern.

In Chapter 4 it was shown that extending cell-to-cell signalling distance beyond immediate neighbours resulted in longer period spatial patterns. As Notch signalling is contact-dependent, immediate neighbours are defined as any cells with direct membrane contact. In a 2D plane, the dense packing of RG cell nuclei in the developing neural tube approximates a hexagonal lattice and thus direct membrane contacts would on average be expected to occur with the 6 nearest neighbouring nuclei. However, RG cells also extend two thin stretches of membrane from the cell body (where the nucleus is located) and are called radial glial processes (RG processes). One RG process extends in the apical direction and the other extends in the basal direction; these attach to other cells at either end.

RG processes occupy the gaps between other cell membranes and so this means RG cells contact many more cells in the apical-basal (AB) axis than when only the nearest 6 nuclei are considered as immediate neighbours. RG cell morphology is therefore an essential consideration in understanding the full extent of Notch signalling in the tissue. However, the focus of this thesis has largely been on the spatial pattern that is measured in the dorsal-ventral (DV) axis, so it seems unlikely that processes would contribute a significant extension to the signalling distance in this orthogonal direction.

Instead in this chapter, the potential role of protrusions extending signalling distance beyond nearest neighbours will be examined, as these structures are expected to ex-

tend in the relevant AB axis. Protrusions are extensions of the cell membrane and can be categorised into specific types based on the shape and underlying molecular dynamics. Lamellopodia, for example, are often associated with cell movement, exhibit a wide fan-like structure, and are composed of a mesh of short actin filaments. Filopodia are long thin protrusions often associated with being involved in environmental sensing and are composed of long unbranched actin filaments.

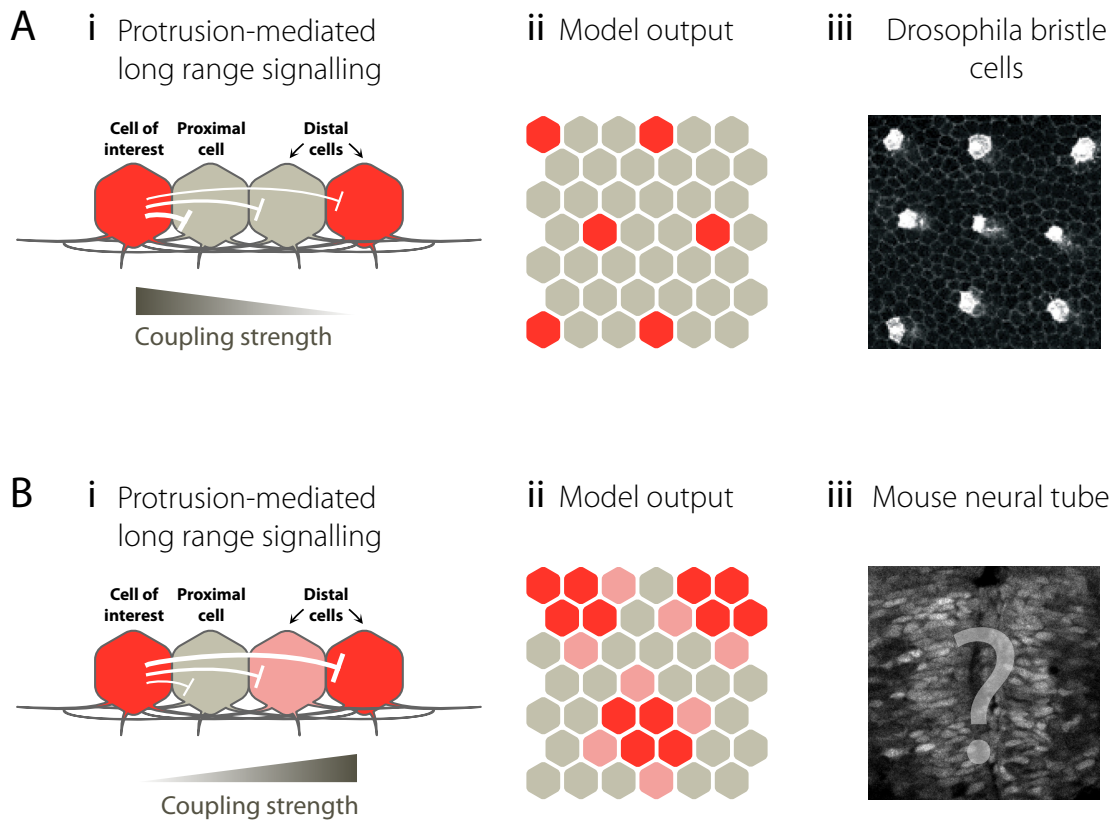


Figure 5.1: Protrusion mediated Notch signalling and the effects of distal and proximal coupling strengths on the resulting pattern. **Ai** Notch signalling over several cell diameters where coupling strength decreases with distance and the resulting model pattern shown in **Aii**. **Aiii** Shows the larger spaces Notch-Delta pattern found to be caused by signalling protrusions (taken from (Cohen et al., 2010)). **Bi** Notch signalling over several cell diameters where coupling strength is higher at longer distances away from the cell with the resulting model pattern shown in **Bii**. **Biii** Protrusion-mediated signalling may underly the clustered expression seen in the neural tube HES5 pattern (taken from (Biga et al., 2021)).

Importantly protrusions have been shown to be involved in Notch-Delta signalling, for example, in *Drosophila*, long-range protrusions carrying Dll1 are found to account for the wider spacing seen in bristle cells as shown in Figure 5.1Aiii (Cohen et al., 2010; De Jussineau et al., 2003). Mathematical modelling was able to reproduce the correct spacing of single isolated Delta-high cells seen in this tissue by simulating dynamic protrusions where the probability of forming contacts was inversely proportional to the distance between cells, as illustrated in Figure 5.1Ai&ii. Models where

protrusion signalling strength can be varied independently at proximal and distal distances (Figure 5.1Bi) have shown that more clustered spatial patterns can form if coupling strength is higher at distal signalling distances (Figure 5.1Bii) (Bajpai et al., 2021; Hadjivasiliou et al., 2016; Vasilopoulos & Painter, 2016). This was also found to be the case in Chapter 4 and was suggested as a potential underlying mechanism in generating the clustered 3-4 cell periodicity in the neural tube HES5 pattern (Figure 5.1Biii).

Protrusions have indeed been observed in similar tissues to mouse neural tube neuroepithelia, with Nelson et al. reporting the presence of protrusions in mouse neocortex RG cells which protrude orthogonally to the AB axis. Additionally, intermediate neurogenic progenitors (not present in the neural tube) extend protrusions along the AB axis to contact RG cells at the apical surface (Nelson et al., 2013). In the basal region of the zebrafish neural tube, Hadjivasiliou et al. showed that differentiating neurons extend long Delta-positive protrusions at the basal side of the tissue in the anterior-posterior direction. And at the apical end of chick neural tube Kasioulis et al. used live imaging to reveal that protrusions are dynamically and frequently extended, likely reaching beyond nearest neighbours.

This Chapter characterises protrusions specifically in the mouse neural tube and examines how likely it is that these confer extended signalling distance to RG cells by enabling Notch signalling between distal cells.

5.1 Results

5.1.1 Sox2CreERT2 mTmG embryos enable visualisation of protrusions in neural progenitors

To enable visualisation of protrusions in RG cells in the neural tube, a double fluorescent membrane reporter mouse system, mTmG, was used (Snyder et al., 2013). These mice normally express membrane-targeted tdTomato (mT) under strong ubiquitous expression of an ACTB promoter (β -actin promoter). Membrane localisation is achieved through N-terminus modifications that enable covalent bonding of fatty acids, and subsequent association with the lipid bilayer of the cell membrane (Ballesteros et al., 2021). This results in the membranes of all cells in the embryo being fluorescently labelled red. Figure 5.2 summarises the mTmG system.

Downstream of the mT sequence is a membrane-eGFP (mG) sequence which is not normally expressed due to the polyA tail at the end of the mT sequence. Cells can

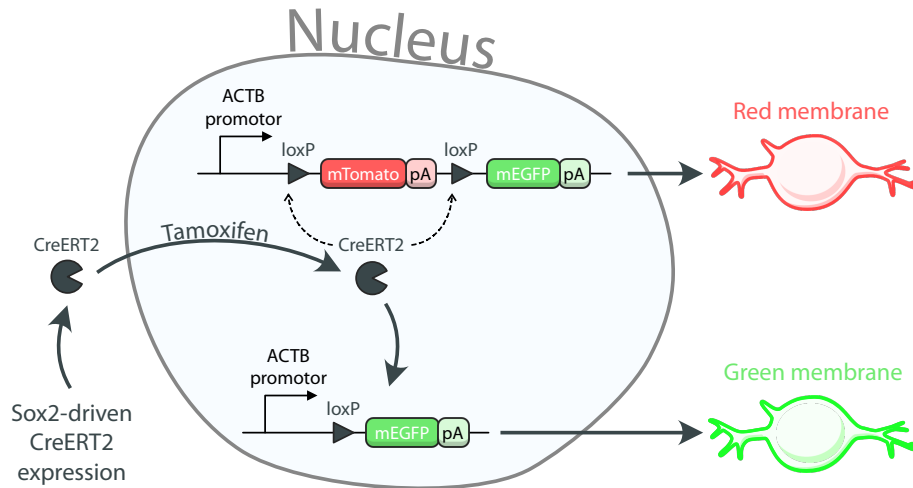


Figure 5.2: Summary of the Sox2CreERT2 mTmG system used to mosaically label the membranes of neural progenitor cells in the neural tube. CreERT2 refers to Cre recombinase which targets and excises genes located between two loxP sites and also has an estrogen ligand-binding domain that requires tamoxifen for it to be localised to the nucleus. The ACTB promoter ubiquitously expresses the downstream genes. pA is the abbreviation for polyA tails. See Methods §5.3.1 for further details.

be made to express mG if the mT sequence is excised, which is achieved by the presence of a loxP sequence on either side of the mT sequence. LoxP sequences specify the region to be excised by the protein Cre-recombinase when it is present in the nucleus. Thus when the mT sequence is excised, a cell begins to express only mG and the cell membrane fluoresces green.

To specify Cre expression to only occur in neural progenitors, Sox2-driven CreERT2 mice were crossed with the mTmG mice. CreERT2 is a fusion of Cre and a mutant estrogen ligand-binding domain that requires tamoxifen to be active and subsequently localises to the nucleus. Therefore to achieve a mosaic expression of mG-expressing cells, a concentration of tamoxifen sufficient to enable a minority of cells to excise the mT sequence was used so that individual GFP cells would be easily visible amongst the mainly mT-positive tissue (see Methods §5.3.1 for further details on the Sox2CreERT2 mTmG system).

Figure 5.3A shows single z-stack images of a Sox2CreERT2^{+/-} mTmG^{+/-} embryo neural tube cryosection. The red mT fluorescence can be expressed across the whole tissue, while the green mG fluorescence is expressed more sparsely and is also found primarily in the progenitor population. Some mG expression will also mark early differentiated cells due to the fact the embryos were incubated with tamoxifen for ~12 hours before cryosectioning and so Sox2-positive progenitor cells marked with mG will have had time to start differentiating and move basally. Upon closer inspection

of the mG fluorescence, various lengths of thin membrane can be seen to protrude from the cells (highlighted with white arrows in Figure 5.3Ai&ii). The protrusions can be seen to emanate both from the cell body (where the nucleus is located) as well as the RG processes (the thinner parts of the cell that attach at the apical and basal ends of the tissue).

The extent of protrusions is better visualised in z-projections and various examples are shown in Figure 5.3B-D. Figure 5.3B shows a zoomed-in view of a group of cells where two cells have adjacent nuclei (purple and green nuclei in Figure 5.3Biii) and their processes are intertwined, likely because they share the same parent cell which divided shortly before fixing. Figure 5.3Bii&iii highlight protrusions emanating from the intertwined cells, traced with white lines with a blue base (see Methods §5.3.3 for how these traces were generated).

Figure 5.3B-D collectively indicate that protrusions are common, can occur in most mG-positive RG cells, and that they can be present anywhere along the length of the AB axis of an RG cell. In Figure 5.3C, the white arrows pointing to red highlighted protrusions indicate the presence of very long protrusions originating from the basal end of the tissue. These are possibly coming from apically detached differentiating cells rather than RG cells, as similar protrusions have been reported to extend back down into the RG population from interneuron progenitors in the mouse neocortex (Nelson et al., 2013). Additionally apically detaching cells are highlighted in red in Figure 5.3Dii. Overall this section highlights the suitability of the Sox2CreERT2 mTmG system for visualising individual cells and their plasma membranes in the densely packed neuroepithelium.

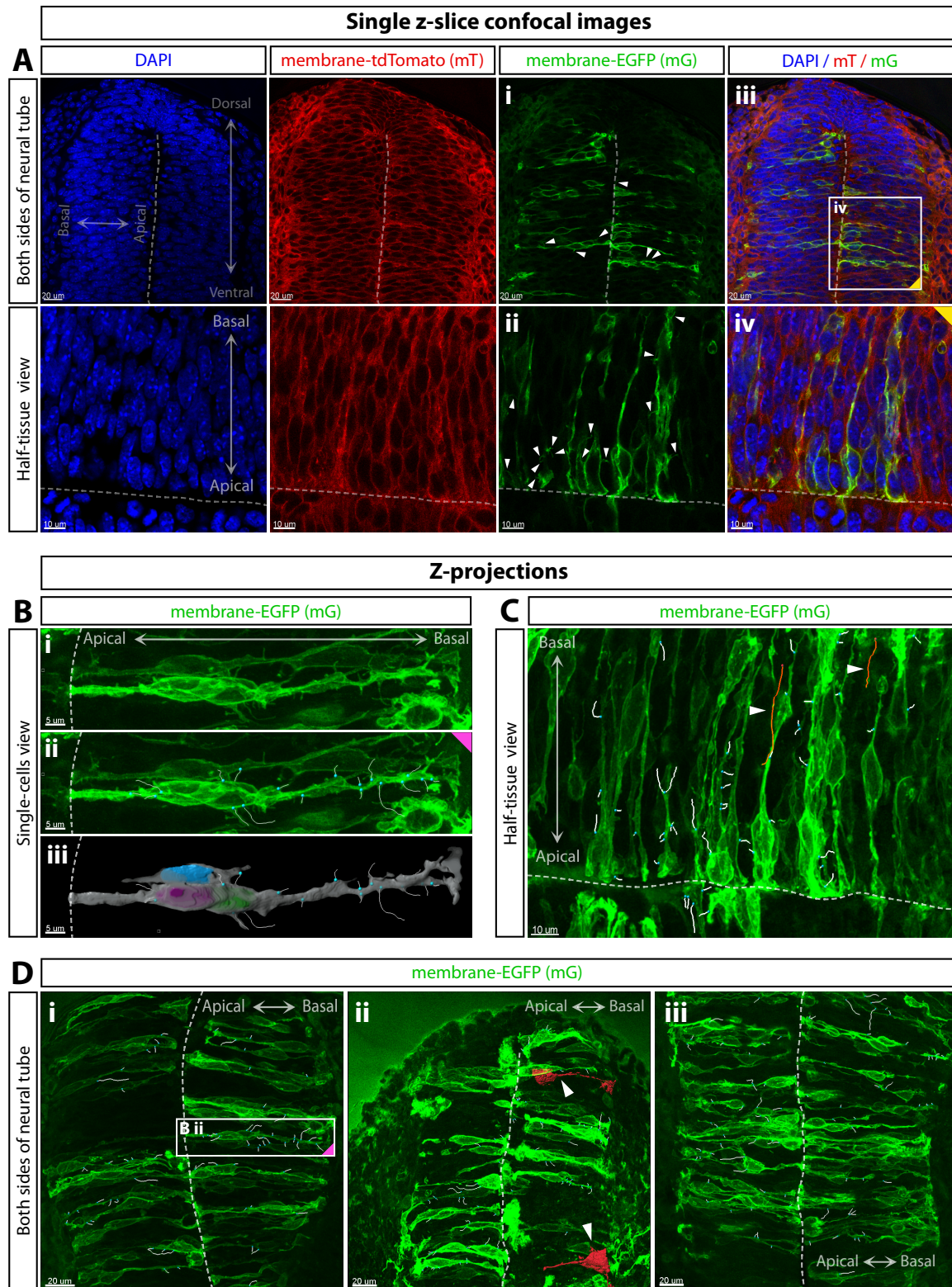


Figure 5.3: Visualising and tracing of protrusions using confocal imaging of E10.5 Sox2CreERT2^{+/-} mTmG^{+/-} mouse neural tube cryosections. **A** Single z-slice images of embryos stained with DAPI and endogenously tagged mT and mG fluorescence. The top panels show a wider view of the neural tube and the bottom panels show a cropped region of the same cryosection rotated by 90°, indicated by the white box with the yellow triangle in the corner in **Aiii**. The dashed lines indicate the apical wall of the neural tube. The arrows in **Ai&ii** highlight various protrusions that can be seen emanating from the processes and cell body of the neuroepithelial cells. *Figure legend continues on next page.*

Figure 5.3: **B** Z-projections (typically around $20\mu\text{m}$ deep) of a cluster of cells with mG fluorescence. **Bi** Shows the raw data, **Bii** shows the data with traced protrusions where the blue sphere highlights the base of the protrusion and the white line is the trace of the whole protrusion (see Methods §5.3.4 for how traces were made). **Bii** is also the same region highlighted in **Di**. **Biii** shows a 3D fill (using Imaris) of the membrane and nucleus of the cells. **C** Z-projections of one side of the neural tube with traced protrusions. The two protrusions traced in red and marked with white arrows are examples of protrusions that originate from basal cells detached from the apical surface. **Di-iii** Three additional embryos with traced protrusions. **Di** Highlights two apically detached cells in red with white arrows. 5 separate embryos were used to generate the embryos in this figure.

5.1.2 Protrusions exhibit a wide range of possible lengths and angles of extension

To get a better idea of how far protrusions can reach and potentially signal in this tissue, lengths and angles were extracted from the traced protrusions across all imaged slices (Methods §5.3.4). The distribution of protrusion lengths in Figure 5.4A reveals that the majority of protrusions are less than $5\mu\text{m}$ in length, with the most common protrusion length being around $2\mu\text{m}$ and the mean length of protrusions being $4.5\mu\text{m}$.

Interestingly the length distribution also shows a long tail with a small second peak at around $10\mu\text{m}$, and some protrusions are recorded as being $\sim 20\mu\text{m}$ long (though these are relatively rare). Considering these measurements are from snapshot data rather than timelapse, the presence of the second peak and long tail could indicate one of two possibilities. Either short protrusions ($<10\mu\text{m}$) are more stable than long protrusions ($>10\mu\text{m}$) and so it is less likely that the transient long protrusions are caught in snapshot data. Or alternatively, short and long protrusions could have similar lifetimes but short protrusions form more frequently.

Work done by (Kasioulis et al., 2022) which analysed live imaging dynamics of subapical protrusions in chick neural tube progenitors indicates that short protrusions ($\sim 2\mu\text{m}$) are more stable than longer protrusions, but that transient long protrusions frequently extend from these short protrusions on average 5 times per hour in the subapical regions imaged. They characterised the more stable short protrusions as having more lamellipodial-type molecular markers, while the longer extensions were characterised as filopodia due to their smaller diameter and longer length. To understand how far protrusions might extend signalling distance, it is important to bear in mind this dynamic aspect of the protrusions, and this will be discussed as the protrusions are characterised.

To gain insight into the possible direction of signalling, protrusion angles were mea-

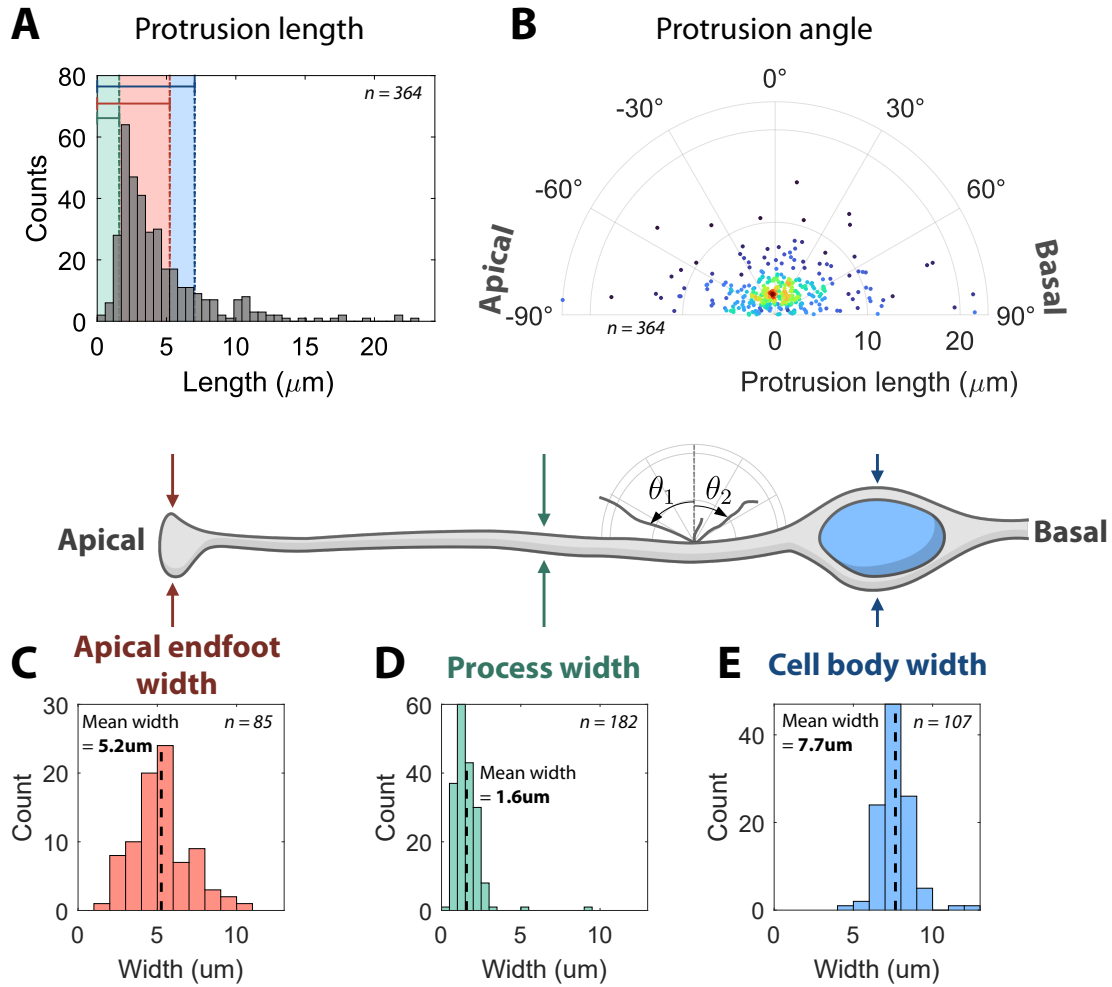


Figure 5.4: Quantitative characterisation of protrusion length and orientation, and RG cell width. **A** Histogram of 364 protrusion lengths measured in 12 slices from 5 different E10.5 Sox2CreERT2^{+/−} mTmG^{+/−} embryos. Green, red, and blue regions indicate the average measured widths of the cells shown in **C-E**. **B** Orientation of the protrusions relative to the AB axis (using the same data set as in **A**). The colouring of the points indicates plot density. 0° indicates a protrusion oriented in the AB direction, -90° is a protrusion oriented towards the apical surface and 90° is a basally directed protrusion. **C** Histogram of apical endfoot widths ($n = 85$, average width $5.2 \pm 1.8 \mu\text{m}$ (mean \pm SD)). **D** Histogram of RG process widths ($n = 182$, average width $1.6 \pm 0.9 \mu\text{m}$). **E** Histogram of cell body widths ($n = 107$, average width $7.7 \pm 1.1 \mu\text{m}$). See Methods §5.3.3 for how protrusions and cell widths were measured.

sured relative to the AB axis with -90° defined as pointing apically, +90° pointing basally, and 0° pointing perpendicular from the AB axis (along the AB axis). Shorter length protrusions were more likely to be perpendicular to the AB axis, which can be seen by the higher density of points around 0° for protrusions less than 5 μm in Figure 5.4B. This tendency is likely due to shorter-length protrusions being less susceptible to buckling, and so they protrude orthogonally to the membrane. In the 5-10 μm range, which is the range in which buckling of actin filaments in filopodia is predicted to occur by theoretical modelling (Mogilner & Rubinstein, 2005), the dis-

tribution of angles becomes more spread out, and protrusions extend with similar probability in all directions. Finally above the $10\mu\text{m}$ range, there seems to be a tendency for protrusions to align more to the AB axis. This may be due to the fact that at these longer length scales, combined with buckling, the protrusions will likely find less resistance following the spaces between RG cells in the AB direction due to the structure of the tissue.

5.1.3 Protrusions can extend contact distance beyond immediate neighbours

Following the definitions in Chapter 4, neighbouring cells in direct contact with a signalling cell are defined as proximal cells whereas cells further away are referred to as distal cells (Figure 5.5A). The modelling work in Chapter 4 found that when cells are able to signal distally, periodic patterns of 3-4 cells can be generated. Here it is examined whether protrusions are likely to contact distal cells using the mean protrusion lengths and cell widths obtained in the previous section.

To define what distance a protrusion would need to traverse in order to contact a distal cell, the width of RG cells needs to be measured. This was done by measuring three distinct parts of an RG cell: the apical endfoot width, the process width, and the cell body width (see Methods §5.3.3). Figure 5.4C-D shows the histograms and mean widths were measured as $1.6 \pm 0.9\mu\text{m}$ (mean \pm SD) for process width, $5.2 \pm 1.8\mu\text{m}$ for apical endfoot width, and $7.7 \pm 1.1\mu\text{m}$ for cell body width.

These measured cell widths were then used to construct a scaled, idealised picture of what a 3D arrangement of RG cells would look like in order to understand how long a protrusion should be so that it makes contact with a distal cell. This arrangement is visualised in Figure 5.5A, and as apical endfeet are tightly connected together at the apical wall by adherens junctions (Veeraval et al., 2020), it is assumed that the apical endfoot width determines the spacing between cells. Another assumption is that the processes of cells run parallel to each other. In reality, there is some bending of the processes as they fill the spaces between nuclei, but for simplicity, this is not considered here. Proximal cells are defined as the 6 cells in black that contact the pink cell, and the distal cells are shown in white.

Within this idealised model, protrusion lengths are set to either the RG process diameter, endfoot diameter or cell-body diameter, and then for each length, it is considered how likely it is for the protrusion to reach a distal cell, given the distribution of measured protrusion lengths. Where protrusions emanate from is also considered; if they start from wider parts of the cell, such as the cell body, they will be able to reach further than if they had started at a thinner part of the cell.

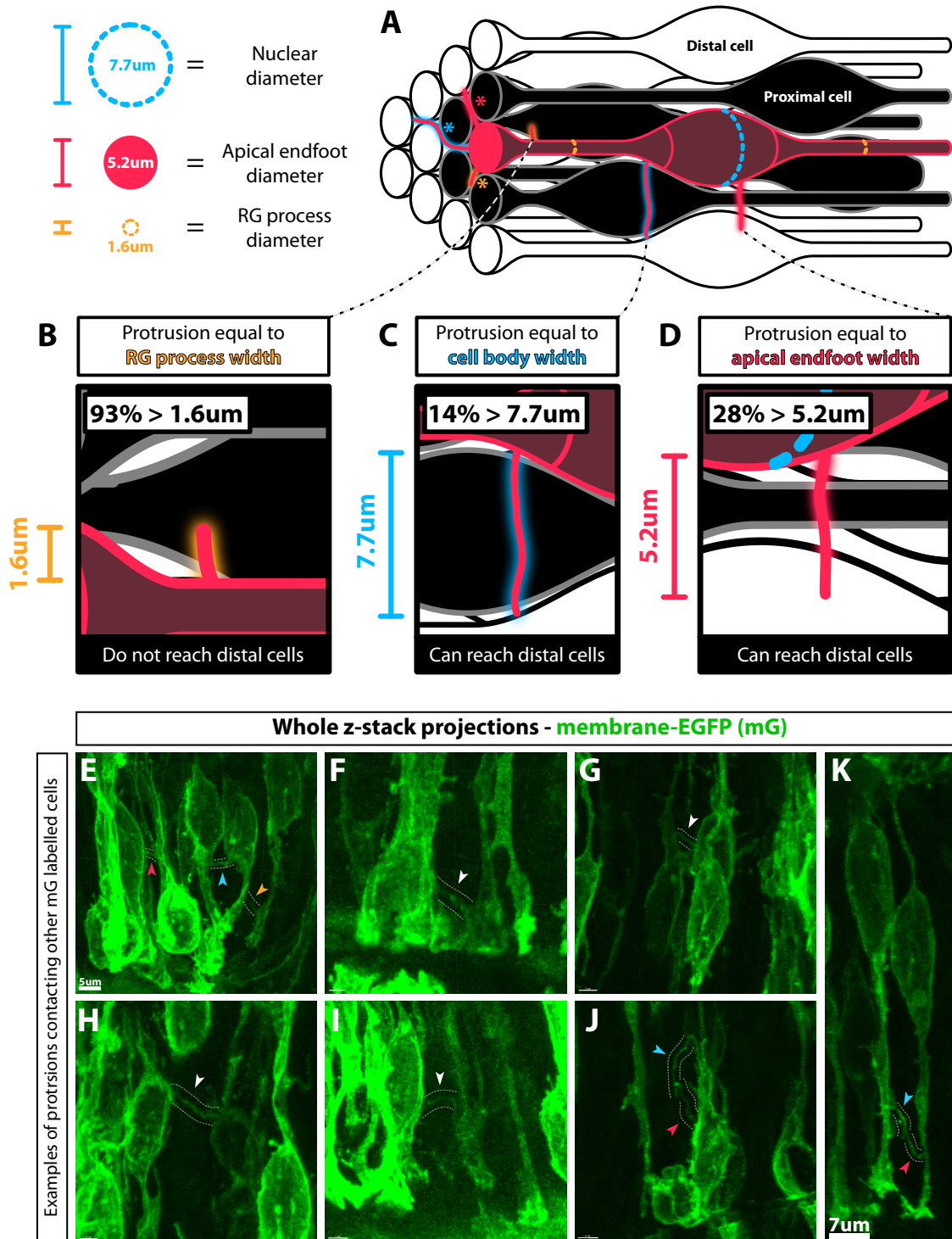


Figure 5.5: Idealised arrangement of RG cells scaled by measured cell widths, and example images of protrusions touching other mG fluorescent cells. **A** Proximal cells (black) are cells in direct contact with the pink cell, and distal cells are ones further away (white). The apical endfeet, RG processes, and cell body widths are scaled to the measured widths of real RG cells in the neural tube. Protrusions are illustrated as thin pink lines emanating from the pink cell, and the colour of the glow around each indicates which length they are set to according to the key to the left of the illustration. Asterisks highlight three different length protrusions emanating from the apical endfoot, with each colour indicating the length of the protrusion (see key). Protrusions emanating from the cell processes/cell body are shown in more detail in **B-D**. *Figure legend continues on next page.*

Figure 5.5: **B** Shows the scaled length of a protrusion (pink) that is equal to the average process width, emanating from a process. **C** Shows the scaled length of a protrusion (pink) that is equal to the average cell body width, emanating from the edge of the cell body. **D** Shows the scaled length of a protrusion (pink) that is equal to the average apical endfoot width, emanating from the cell body. **E** Red and orange arrows indicate protrusions between otherwise non-contacting (distal) cells that are also mG labelled. The blue arrow shows an example of a protrusion occurring between two cells where their cell bodies touch (proximal neighbours). **F-I** Further examples of distal cells contacting via a protrusion (white arrow & dashed lines). **J** Two protrusions emanating from the same cell (red and blue arrows) appear to contact each other. **K** Two cells with touching cell bodies (proximal cells) with a protrusion that emanates from each cell and where the protrusions contact each other.

Protrusions that have a length equal to RG process widths ($1.6\mu\text{m}$) or greater account for 93% of protrusions when using the distribution of protrusion lengths obtained for Figure 5.4A. At a length of $1.6\mu\text{m}$, a protrusion would not extend beyond proximal cells in the idealised model regardless of where it emanates from along the cell membrane, and so protrusions at this length scale would not be able to contact distal cells (Figure 5.5B).

If protrusions have a length of the apical endfoot width ($5.2\mu\text{m}$) or greater (28% of protrusions), then contacting a distal cell becomes a possibility but depends on which part of the cell the protrusion emanates from and also which part of the distal cell is closest to the site of protrusion formation. Three potential scenarios are outlined to illustrate how morphology plays an important role. The first scenario is where a protrusion $5.2\mu\text{m}$ in length emanates from the thinnest part of the cell, the process, and extends towards the process of the nearest distal cell. In this scenario, the protrusion would not be long enough to cross this distance and contact the distal cell (process-to-process distance is $8.8\mu\text{m}$). The second scenario is if the protrusion emanates from the apical endfoot (pink asterisk in Figure 5.5A), where it would almost certainly extend beyond the proximal cell and contact the apical endfoot of a distal cell. Finally, if a protrusion is emanating from the bulge of the cell body, and a distal cell also has the bulge of its cell body in close range, then contact is likely to be made (Figure 5.5D).

Finally, protrusions with a length equal to the cell body width ($7.7\mu\text{m}$) would again be able to contact distal cells if emanating from the endfeet, and in fact, may be able to contact up to two distal cells away (blue asterisk in Figure 5.5A). These protrusions would also easily reach distal cells if they emanate from the cell body (Figure 5.5C). However a $7.7\mu\text{m}$ length is just shy of the $8.8\mu\text{m}$ process-to-process distance, and so to be guaranteed to reach distal cells regardless of where a protrusion emanates from a protrusion would need to be $\geq 8.8\mu\text{m}$, which accounts for 10% of protrusions.

In sum, the idealised model predicts that if protrusions emanate from the apical end-foot (asterisks in Figure 5.5A), then they need to be at least as long as the average endfoot width to guarantee contact with a distal cell, and around 28% of protrusions are longer than this. In the case where protrusions emanate from other parts of the cell, the required length to reach distal cells varies, but to guarantee contact, a length of $8.8\mu\text{m}$ is required which only 10% of protrusions satisfy.

Taken at face value the snapshot data presented here suggest that a subset of protrusions should be capable of making contact with distal cells, and these are indeed observed in some of the Sox2CreERT2 mTmG images where mG-positive cells that would otherwise not be in contact (distal cells), do contact via a protrusion, as highlighted in Figure 5.5E-I). This confirms that while distal contacts may be less frequent than proximal contacts, they can indeed extend contact distance between cells and it is worth coming back to the fact that the dynamic aspect of these protrusions is not accounted for in this analysis. Shorter protrusions likely extend dynamic long filopodia frequently (Kasioulis et al., 2022) and another aspect that may extend signalling distance is when protrusions from two cells meet and an example is given in Figure 5.5K. Another intriguing observation is that protrusions can contact other protrusions on the same cell (Figure 5.5J), potentially acting as a mode of cis-activation if both Notch and Delta are present in the protrusions.

The frequency of these different types of possible contacts is not possible to assess here because of the complexity of the tissue morphology, the data only being snapshot images, and the nature of the mosaic labelling. This would be an interesting aspect to explore going forward, but the main question remains as to how much signalling actually occurs in the protrusions and whether they extend signalling distance beyond proximal cell distance which is addressed in the remaining results sections.

5.1.4 Expression of Dll1 can be found within protrusions

To get an idea of where Dll1 is present in cells and if any Notch signalling is occurring in the protrusions, immunostaining for Dll1 was carried out in Sox2CreERT2^{+/-} mTmG^{+/-} cryosections.

Dll1 immunostaining shows that in line with previous observations (Marklund et al., 2010; Wiszniak & Schwarz, 2019), Dll1 is present across most of the neural tube except in 2 bands where there is reduced Dll1 expression (white arrows in Figure 5.6A) which coincides with a region of Jagged1 expression, another Notch ligand (as was characterised in (Marklund et al., 2010)). Dll1 is also largely found to be expressed

at the membrane as shown by the colocalization with the red mT fluorescence and tendency to outline the nuclei of cells and follow RG processes in Figure 5.6B.

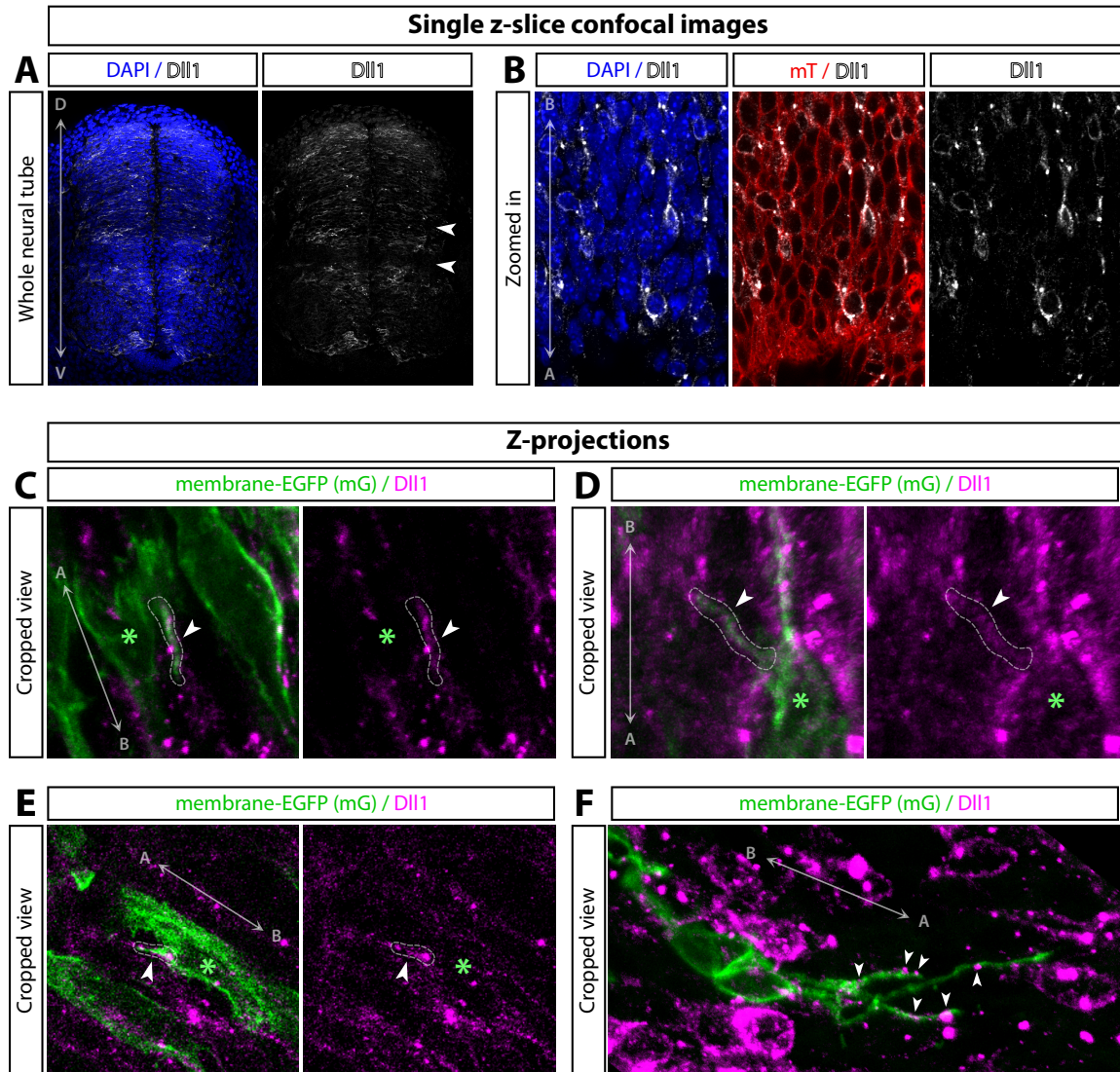


Figure 5.6: Dll1 immunostaining in E10.5 Sox2CreERT2^{+/-} mTmG^{+/-} cryosections. Double-ended arrows indicate DV or AB axis directions. **A** Single z-slice confocal image of a whole neural tube cryosection showing DAPI and Dll1 immunostaining (see Methods §5.3.2). **B** Higher magnification images of DAPI, membrane-tdTomato fluorescence, and Dll1. **C-E** Z-projections of membrane-EGFP and Dll1 where the dashed lines and white arrows highlight protrusions that contain Dll1. Green asterisks indicate the cell body from which the protrusion emanates. **F** Apically detached cell with multiple protrusions/processes. White arrows highlight punctate Dll1 expression.

Interestingly Dll1 largely appears as a punctate expression which has been reported previously (Bardot et al., 2005; Meloty-Kapella et al., 2012; Nandagopal et al., 2018; Nichols et al., 2007). A more recent study which compared Dll1 to Dll4, which has a more dispersed expression compared to Dll1, found that Dll1 operates by exhibiting pulses of Notch activation (Nandagopal et al., 2018). The proposed mechanism is that Dll1 cannot activate Notch receptors until a cluster of Dll1 has formed and

that this clustering is facilitated by the intracellular domain of Dll1. Therefore in the images in Figure 5.6, larger/brighter clusters of Dll1 may indicate areas of higher activation versus regions where Dll1 is more diffuse.

Within regions where Dll1 is expressed, it is not present within every cell, as seen clearly by the DAPI/Dll1 stain in Figure 5.6B and the darker areas in the z-projections in Figure 5.6C-F. This variation in expression is not surprising given that this is a lateral inhibition signalling network shown to dynamically switch between high and low expression. Identifying Dll1 expression in protrusions was done by comparing the green fluorescence in the mG cells with the Dll1 signal. Of the cells that expressed both Dll1 and were fluorescently tagged with mG, some protrusions were found to clearly colocalise Dll1 which followed the general shape of the protrusion as shown in Figure 5.6C-E. These images show cases when the shape of expression in Dll1 closely follows the shape of the protrusion outline, and a mix of punctate and dispersed expression can be seen within the protrusions.

Intensity and distribution of Dll1 in the cells is variable, with Figure 5.6C showing an example where there is clear expression within the protrusion, but no obvious expression in the surrounding main membrane of the cell. Figure 5.6D on the other hand shows clear expression in the cell body and RG process, but weaker Dll1 expression in the protrusion. Figure 5.6F shows strong punctate expression in a cell that has apically detached and is extending multiple protrusions in the apical direction.

Overall this indicates that while only a few easily identifiable Dll1-positive protrusions were found, they are indeed capable of carrying the Notch signalling ligand Dll1, and this suggests that signalling distance may be extended as a result.

5.2 Discussion

This Chapter sought to characterise the presence and function of protrusions in the neuroepithelia of the mouse neural tube in the context of the modelling assumption in Chapter 4 that protrusions may be a means of extending Notch signalling and generating the 3-4 cell periodicity observed in the HES5 pattern.

Visualisation of protrusions was carried out with an inducible membrane fluorescence system, mTmG, which allowed for mosaic labelling of the plasma membrane of neural progenitor cells. This technique enabled the visualisation of fine membrane structures and was able to reveal the presence of thin protrusions emanating from the main membranes of RG cells. In agreement with imaging analysis in other systems

such as mouse neocortex and chick neural tube (Kasioulis et al., 2022; Nelson et al., 2013), protrusions in the mouse neural tube are common and in this chapter it was shown that they are present throughout the tissue, occurring anywhere along the AB axis of a cell with no obvious bias for location along this axis. Through 3D tracing, protrusion lengths were found to show a broad range of possible lengths with short protrusions ($< 10\mu\text{m}$) being much more common than long protrusions in the 10-20 μm range.

It was next considered whether protrusions are capable of contacting distal cells, and examples of non-contacting neighbours contacting through protrusions (distal contacts) were observed in the mG-labelled cells. To get an idea of how often these distal protrusion contacts may form, the distribution of protrusion lengths was compared with measurements of RG cell widths within an idealised model of RG cell arrangement. This analysis concluded that while longer protrusions are capable of contacting distal cells, they represent a minority of protrusions (between 10-28%).

An important point regarding this analysis is that it is based on assumptions from snapshot data and does not take into consideration how the distribution of protrusion lengths is generated dynamically. Live imaging of sub-apical protrusions carried out in a study by Kasioulis et al. showed that short protrusions are relatively stable compared to longer protrusions but that long filopodia frequently extend from these shorter lamellopodia-like protrusions (Kasioulis et al., 2022). Therefore it may be the case that considering the dynamics of these protrusions over time completely changes the interpretation of the snapshot data, as protrusions that transiently but frequently contact distal cells may contribute significantly to Notch signalling.

This also highlights the question of where and when cells transfer most of the signalling, whether it is largely through the main cell membrane or through protrusions. This has implications for the modelling in Chapter 4 which found that in order for clusters of HES5 expression to form, more Notch activation has to occur at distal cells than at proximal neighbours. It was discussed in Chapter 4 that three possible ways in which more Notch activation may occur between distal cells is through higher diffusion rates of Notch/Delta in the protrusions, protrusion movement mechanically stimulating Notch activation (Hunter et al., 2019), or through *cis*-inhibition being higher at the main cell membrane (Hadjivasiliou et al., 2016; Khait et al., 2016). Additionally, Dll1 has been shown to exhibit discrete pulses of activity which is in contrast to other ligands like Dll4 which activate Notch in a sustained manner, and so in this way, transient protrusions contacts may be able to deliver significant amounts of Notch signalling via bursts of activation (Nandagopal et al., 2018).

The punctate expression observed in the Dll1 immunostainings may indicate such sites of high/pulsatile activation, but ultimately the data only indicates the possibility that protrusions can activate Notch in other cells. To clarify further whether Dll1 activates signalling in neighbouring cells, methods such as a proximity ligand assay (Alam, 2018) could be utilised to identify the extent to which Dll1 binds Notch1 in the protrusions versus the main cell membrane. Further, Notch1 immunostaining could be carried out on the Sox2CreERT2^{+/-} mTmG^{+/-} cryosections to identify if Notch1 is also expressed in protrusions and this would indicate whether protrusions are also capable of receiving Notch signals from other cells.

Consideration of where along the AB axis signalling is occurring is important too. The study by Hatakeyama et al. found a bias for Notch1 and Dll1 to be expressed towards the apical region of mouse cortex neuroepithelia, and that NICD is transported from the apical endfeet towards the nucleus of the cell (Hatakeyama et al., 2014). Presenilin 1 and 2, which are catalytic subunits of the γ -secretase enzyme which is required for cleaving and activating Notch are also found to be localised to the apical endfeet (Banda et al., 2015; Hatakeyama et al., 2014). These studies strongly suggest that the majority of Notch signalling in neural progenitor cells occurs at the apical endfeet of RG cells. This potential spatial bias would be an important consideration in any future modelling work as this affects the number of signalling neighbours and the likelihood of protrusional contact.

While the observations as a whole indicate that protrusions may well be capable of extending the signalling distance between cells in the neuroepithelium, the extent to which they are involved in the HES5 pattern remains unclear. The key future experiment here will be to inhibit the formation of these protrusions and observe how the HES5 pattern is affected. If protrusions are responsible for cluster formation, then inhibiting protrusions would be expected to either result in a 2-cell periodic pattern rather than 3-4 cells due to the fact that cells would only be signalling via proximal interactions, or that the pattern would cease entirely if proximal Notch signalling alone is not sufficient to generate a pattern.

5.3 Methods

5.3.1 Mosaic membrane marking of progenitor cells using Sox2CreERT2 mTmG system

To make the tamoxifen-inducible mouse system, the following mice were ordered from The Jackson Laboratory (JAX) and crossed: Strain number – 007676 – (B6.129(Cg)-Gt(ROSA)26Sor^{tm4}(ACTB-tdTomato,-eGFP)^{Luo}/J homozygous. Strain number – 017593 - B6;129S-Sox2^{tm1}(cre/ERT2)^{Hoch}/J heterozygous.

Pregnant mice were injected intra-peritoneally with either 250 μ g or 125 μ g of tamoxifen in 100ul of corn oil 15-20h before harvesting the embryos at E10.5. Screening for the correct phenotype of tdTomato expressing embryos with mosaic eGFP expression in neural progenitors was done by separating heads from trunks, dissociating the neural cells from the head by pipetting up and down in PBS, and then identifying embryos which had both red and green fluorescent cells. Positive phenotype trunks were then fixed and cryosectioned as described in the Methods §5.3.2.

5.3.2 Cryosection preparation and immunostaining

Preparation of the cryosections for imaging was as follows and adapted from the methods in (Wiszniak & Schwarz, 2019): Embryos were fixed in 4% paraformaldehyde for 1h at 4°C, washed 3 times in PBS at 4°C, left at 4°C in 20% sucrose overnight, and then embedded in OCT compound for cryosectioning. Sections between 20-40 μ m were cut and placed on superfrost slides.

Sections were washed twice with PBS. Sections were then blocked in 10% Dako serum-free blocking reagent for 15 minutes followed by incubation in primary antibody for 2h at room temperature or overnight at 4°C (in blocking reagent). Sections were washed 3 \times 10 minute PBS + 0.05% Tween-20 washes. Fluorescent Alexafluor-conjugated secondary antibodies were incubated for 1 h at room temperature. Sections were washed 3 \times 10 minute PBS + 0.05% Tween-20, then incubated with DAPI in PBS 5-15 minutes. Sections were washed twice with PBS and a final wash with H₂O. Movial was added to the sections and a coverslip was placed over them, followed by incubation at 37°C for 1h. Primary antibody: sheep anti-DLL1, 1:100 (RD Systems AF5026). Secondary antibody: Alexafluor 647 anti-sheep, 1:500.

5.3.3 Measurement of cell widths and protrusion lengths

The measurement tool in Imaris was used to determine the width of apical endfeet, processes, and cell bodies. For apical endfeet, the widest part of the endfoot bulge in the AB direction was measured. The width of processes varies along the AB axis, and so multiple measurements were made at intervals of roughly every $10\mu\text{m}$ along the AB axis, meaning each cell contributed multiple process width measurements to the data set. Measurements were only made of processes that were clearly from a single cell. Finally, the cell body width was measured again at the widest point parallel to the AB axis.

5.3.4 Measuring protrusion length

The filament tool was utilised in Imaris in a semi-automatic way whereby automatic filament tracking was skipped and instead the beginning and end point of the protrusion were defined manually and then the software identified the path of brightest pixels between those two points. This method worked well for sufficiently bright protrusions.

Chapter 6

General discussion

6.1 Introduction

The work presented here focussed on the pattern of HES5 expression in the developing mouse neural tube; a system which depends on Notch signalling for controlling differentiation during neurogenesis. Early modelling of Notch-Delta lateral inhibition focussed mainly on what happens in tissues where steady-state spatial patterns form (Collier et al., 1996). Developmental tissues where steady-state Notch patterns emerge include drosophila sensory bristle cells and inner ear basilar papilla where fine-grained, non-clustered, and stationary patterns of differentiating arise (De Jossineau et al., 2003; Goodyear & Richardson, 1997). In contrast, the spatial pattern of HES5 in the developing neural tube presents as clusters of similarly expressing cells which rather than reaching a steady-state pattern, continually switch between higher and lower expression over time. In the context of Notch signalling and neural development, three key questions emerged around the observed HES5 pattern: how are clusters of HES5 formed, what generates the long-term switching dynamic, and what is the functional role of a dynamic spatial pattern? This general discussion section is split into three sections that address each of the three questions above, summarising the findings and how these results can be interpreted in the wider context of the literature, as well as potential areas of focus for future work.

6.2 How are clusters formed?

6.2.1 Summary of findings

In the Notch signalling literature, a plethora of models have been generated since the study by Collier et al. (Collier et al., 1996). Of particular relevance to the HES5 pattern, which exhibits longer spatial periodicity than the Collier et al. model, are models that explore the role of protrusions in extending Notch signalling distance (Bajpai

et al., 2021; Hadjivasiliou et al., 2016; Vasilopoulos & Painter, 2016). These models generally distinguish between immediate cell body contacts and protrusion contacts, and in Chapter 4, a similar approach was implemented in a HES5-specific model. By extending the signalling distance to just beyond immediate neighbours, cell periodicities of 3-4 cells were obtained which match the observed HES5 spatial period. Additionally, clusters of expression only formed when more signalling occurred in protrusion contacts compared to cell-body contacts.

Motivated by these modelling results, Chapter 5 began experimental explorations into whether protrusions exist in the mouse neural tube and whether they can account for extending Notch signalling distance. Through mosaic membrane labelling, protrusions were found to be present throughout the neural tube and various examples of protrusions extending contact distance between cells were found. Additionally, immunostaining for Dll1 indicated that protrusions are likely capable of transducing Notch signals.

6.2.2 Interpretation and future work

An interesting result from the modelling is that if protrusions are to account for a clustered spatial pattern, then protrusions need to transduce Notch signalling more efficiently than cell-body contacts. Given that protrusions have a much smaller surface area than the cell body, it initially seems unlikely that protrusions would transduce more signalling, but there are several conditions under which this would be possible. The first is the case when Notch/Delta is actively transported to or within the protrusions and not in the cell body. One study found that the diffusion rate of Notch/Delta is sufficiently higher in protrusions than in the cell body which has a much larger surface area. As a result, modelling suggested that Notch/Delta is able to replenish more quickly in protrusions and result in higher signalling rates relative to the cell body (Khait et al., 2016). A second possibility is that the dynamic nature of the protrusions actively extending and retracting may enable additional mechanical force that is required for Notch activation and increase the number of Notch activations in protrusions relative to the cell body (Hunter et al., 2019). Third, differences in *cis/trans* signalling in the cell body versus protrusions may enable protrusion signalling to be relatively more efficient, but exactly how such a difference would be set up has not been explored explicitly in the literature.

Outside of HES5 signalling, the general question of where and when Notch signalling occurs in a given system is a deceptively hard question to address. The complexity comes from the bidirectional nature of Notch signalling, the balance of *cis* versus

trans signalling, cell movement, and cell morphology, all of which make it hard to tease apart the influence of one cell on another within a population of cells (Baek et al., 2018). One potential way to explore the extent to which protrusions versus cell body contacts signal Notch could be through methods such as proximity ligand assays which in combination with the mTmG system described in Chapter 5 would fluorescently pinpoint areas of the membrane where Notch and Delta are bound to each other (Alam, 2018). While this would indicate differences in the amount of Notch binding between protrusions and the cell body, this would be restricted to snapshot images and would not indicate the amount of activation (NICD cleavage) that is occurring at each site. Systems like synthetic Notch could be used to gain insight into the extent that protrusion contacts activate Notch signalling as this synthetic approach severs the bidirectional feedback of Notch signalling into two types of cells, senders and receivers, making it easier to determine when cell-cell contact occurs and the extent to which it is activating Notch (Khamaisi et al., 2022; Malaguti et al., 2022; Morsut et al., 2016).

While the current experimental work presented in this thesis indicates that protrusions may indeed be able to extend Notch signalling distance, a functional experiment to show its involvement in generating the HES5 spatial pattern remains to be carried out. To address this, future work should focus on inhibiting the formation of protrusions to see if it results in a significant change to the HES5 spatial pattern. Latrunculin A is one potential way of inhibiting protrusion formation as it sequesters actin monomers and therefore inhibits the formation of actin filaments which are required for filopodia formation (Fujiwara et al., 2018). However, if this is found to not be specific enough to just filopodia at low concentrations, then more specific genetic modifications like the WAVE1 mutant work carried out in (Kasioulis et al., 2022) would need to be done.

6.3 What generates the long-term switching dynamic?

6.3.1 Summary of findings

The second aspect of the data that needed to be accounted for was the long-term switching of clusters between higher and lower HES5 expression. Particularly relevant models in the literature are ones that look at antiphase Hes oscillations (Momiji & Monk, 2009; Pfeuty, 2022; Tiedemann et al., 2017). In these models, Notch patterns are made dynamic by the presence of the autonomous Hes oscillations. However, the observations of the HES5 dynamics presented in Chapter 2 showed that

long-term switching dynamics do not come from antiphase autonomous HES5 oscillations, but rather the autonomous HES5 dynamics are nested within the longer-term, larger-amplitude switching behaviour and so the dynamic switching is a novel observation.

This motivated the exploration of how stationary Notch/Hes patterns can be made to dynamically switch over time. A travelling wave hypothesis was explored in Chapter 3 and while this model could generate dynamic spatial patterns, they were not of the type observed in the data and so this hypothesis was ruled out. Chapter 4 explored an alternative mechanism based on the behaviour of differentiating cells in the neural tube and their altered Notch signalling. Based on evidence from various studies (Baek et al., 2018; Hatakeyama et al., 2014; Yoon et al., 2008), this mechanism put forward the idea that differentiating cells act to perturb cells in low-expression states into high-expressing states; this was implemented in a mathematical model which faithfully reproduced the nested autonomous HES5 dynamics within a larger-amplitude switching behaviour.

6.3.2 Interpretation and future work

The idea that differentiating cells would change their Notch signalling is based on the fact that prospective neurons are expected to increase their ability to *trans*-activate Notch on contacting cells due to increased expression of Mindbomb1 (Baek et al., 2018; Yoon et al., 2008) and they also increase Dll1 expression (Hatakeyama et al., 2014). While this modelling has high explanatory power, the next step is to experimentally test if the modelling assumptions underly the switching behaviour in the tissue. To test whether this altered Notch signalling plays a significant role in neural progenitors, HES5 levels could readily be tested in a system that reports both HES5 expression as well as a marker that indicates the early onset of differentiation, such as Ngn2 or another proneural gene downstream of Hes5.

An ideal system for this would be one where neighbouring/contacting cells are easily identifiable and cell movement is restricted. 2D cell cultures are convenient but neural stem cells tend to migrate quickly in such an environment, and tend to actively change shape and length, making it hard to determine neighbours over a sustained period of time. Either a micropatterned plate that restricts movement or culturing cells as neurospheres, where cells are much more restricted in their movement, would be an ideal setup to observe how differentiating cells affect HES5 expression in neighbouring cells. Within these cultured approaches, either expression of proneural genes could be induced through a differentiation protocol from embryonic stem cells (Gouti

et al., 2014), or proneural gene expression could be induced in a neural stem cell culture with electroporation of a Tet-On system (T Das et al., 2016) that expresses a proneural gene along with a fluorescent tag.

To test the extent that differentiating cells affect neighbouring HES5 levels, functional experiments would require an *in vivo* set-up where the ability of differentiating cells to signal Notch can be altered. This could be achieved, for example, by conditionally inhibiting transcription of Mindbomb1 with small interfering RNA sequences in cells that express early differentiation markers. An absence of Mindbomb1 would inhibit the ability of these cells to *trans*-activate Notch.

As discussed in Chapter 4 the perturbation algorithm is general enough to accommodate other possible biological mechanisms that might perturb the pattern, and so other potential candidates that could reasonably cause perturbations in the neural tube HES5 pattern is the cell cycle (Olivera-Martinez et al., 2014; Sabherwal et al., 2021), interkinetic nuclear migration (Spear & Erickson, 2012), the dynamic extension and retraction of protrusions (Kasioulis et al., 2022), and the pulsatile dynamics of Dll1 (Nandagopal et al., 2018).

6.4 What is the function of the dynamic spatial pattern?

Summary of findings

From the two models in Chapter 2 and 4, two functional roles were associated with different aspects of the pattern. In Chapter 2 the model predicted a lower rate of differentiation when the system locally synchronised compared to when salt and pepper patterns formed at stronger coupling strengths. This change in predicted differentiation rate was due to the fact that as a coupling strength increases, the cell-cell concentration difference increases, and therefore more cells are below the differentiation threshold. Within the HES5 expression domain, the pMN domain exhibits a higher rate of differentiation, and experimental analysis showed that the pMN region follows the predicted increase in cell-cell concentration difference along with a shorter spatial period compared to the p0-p2 domains where clustered expression occurs. Therefore the modelling suggests that variations in coupling strength may account for the variation in differentiation rate across the HES5 expression domain.

What then is the functional advantage of a dynamic spatial pattern over one that is stationary? This was explored with the model in Chapter 4, which recapitulated many aspects of the HES5 pattern. Again, from the angle of differentiation, it was

found that the main difference between stationary and dynamic spatial patterns is in how differentiating cells are distributed spatiotemporally, with the stationary pattern producing hotspots of differentiation, and the dynamic pattern alternating the locations at which differentiation events occurred, leading to a more uniform spatial distribution of differentiating cells over time.

6.4.1 Interpretation and future work

As mentioned, stationary Notch patterns result in hotspots of differentiation, which is appropriate for a system like *Drosophila* sensory bristle cells (De Jossineau et al., 2003) and inner ear basilar papilla (Goodyear & Richardson, 1997) where one round of differentiation across the tissue results in a regularly spaced pattern of specialised cells. In contrast, neurogenesis is a process where many rounds of differentiation take place, which is how a vast number of neuronal cells are generated from a relatively small population of progenitor cells, and the balance of these two populations of cells is maintained by Notch signalling. Given this key homeostatic function of Notch in neurogenesis, does the presence of a dynamically switching spatial pattern add any additional functional role or is it just a byproduct of the fact Notch is being used for homeostatic purposes?

The modelling suggests a potential role could be in ensuring cells are distributed evenly in space. In another study, the production of neurons in the anterior-posterior direction in the neural tube has been found to proceed in a very similar way to the modelling prediction whereby recently differentiated neurons transiently inhibit further differentiation in the area they were produced, and subsequent neurons appear in the gaps between them (Hadjivasiliou et al., 2019). Another potential role of the dynamic spatial pattern is that it may help achieve a steady rate of differentiation by ensuring a fraction of the population is always expressing low HES5 and therefore primed for differentiation. In future work, if differentiating cells are found to be the cause of dynamic switching, then modifying the Notch signalling in differentiating cells would be one way to test the specific function of dynamic versus stationary patterning. Comparing the distribution of Ngn2 in a stationary versus dynamic HES5 patterned tissue would be one way of testing the modelling prediction that dynamic switching spreads out differentiation. Further to that, the distribution of the neurons as they migrate out of the neural tube would be a definitive way to test the developmental importance of dynamic switching.

Finally, given that the longer-term switching in Chapter 4 was found to largely determine where cells differentiate in the model, it leaves an open question as to what

role the smaller-amplitude ultradian oscillations play in the differentiation process. Ultradian oscillations have been shown to control transitions from quiescent to proliferative states (Marinopoulou et al., 2021; Sueda et al., 2019), and are more likely to be oscillating in differentiating cells (Manning et al., 2019). When Hes1 oscillations are dampened, proliferation is reduced and cell death is increased (Ochi et al., 2020). Therefore the oscillations play an important regulatory role in differentiation, but as of now, it is unclear how this fits into the modelling and may indicate a limitation of its descriptive power.

One area of the modelling that could be explored in relation to this is the implementation of the differentiation algorithm. Currently, it is a level-based approach that increases the differentiation probability the further below a threshold a cell's HES5 level drops. This means that in most simulations, it is largely the differentiation-based perturbations that drive the switching above and below this threshold, but it is not known if this is the case in reality. For example, the threshold could be much lower, and switching to a low state may bring cells just within reach of the differentiation threshold, and subsequent ultradian oscillations may enable the cell to dip below the threshold and therefore play an important role in this way. Future work would require monitoring of HES5 and a downstream proneural gene in order to establish an accurate picture of how HES5 dynamics are interpreted by downstream proneural genes.

6.5 Overall conclusion

This work presented a unique dynamic pattern of HES5 expression observed in the developing mouse neural tube, and this brought into question how the observed dynamic pattern forms and what developmental function it plays.

Through computational modelling, it was found that the known Notch-Hes5 interactions are insufficient to explain all aspects of the data. This then led to the incorporation of other biologically pertinent mechanisms to extend the model, which resulted in a novel modelling study whereby cells are able to switch between the two steady-state HES5 expression levels set up by Notch lateral inhibition due to the presence of differentiating cells that perturb Notch signalling in the cells they contact. The functional role of these dynamic transitions was suggested to be a combination of enabling optimal differentiation rates alongside being able to spatially distribute differentiating cells along the dorsal-ventral axis. Experimental work is now needed to test the modelling assumptions and predictions.

Overall this work highlights the importance of considering how cell-cell signalling changes over time, where cells spatially contact and signal to each other, and how both of these feed back into the developmental process of differentiation. While much work has been carried out in the field of Notch signalling in the developing neural tube, there remain many open questions and exciting avenues of exploration in regard to understanding the intricate and robust coordination that takes place in spinal cord development.

References

- Adler, M., & Alon, U. (2018). Fold-change detection in biological systems. *Current Opinion in Systems Biology*, 8, 81–89 (cit. on p. 22).
- Alam, M. S. (2018). Proximity ligation assay (pla). *Current protocols in immunology*, 123(1), e58 (cit. on pp. 148, 153).
- Andersson, E. R., Sandberg, R., & Lendahl, U. (2011). Notch signaling: Simplicity in design, versatility in function. *Development*, 138(17), 3593–3612 (cit. on p. 28).
- Ay, A., Holland, J., Sperlea, A., Devakanmalai, G. S., Knierer, S., Sangervasi, S., Stevenson, A., & Özbudak, E. M. (2014). Spatial gradients of protein-level time delays set the pace of the traveling segmentation clock waves. *Development*, 141(21), 4158–4167 (cit. on pp. 99, 104).
- Baek, C., Freem, L., Goïame, R., Sang, H., Morin, X., & Tozer, S. (2018). Mib1 prevents notch cis-inhibition to defer differentiation and preserve neuroepithelial integrity during neural delamination. *PLoS biology*, 16(4), e2004162 (cit. on pp. 28, 153, 154).
- Bajpai, S., Prabhakar, R., Chelakkot, R., & Inamdar, M. M. (2021). Role of cell polarity dynamics and motility in pattern formation due to contact-dependent signalling. *Journal of the Royal Society Interface*, 18(175), 20200825 (cit. on pp. 135, 151).
- Balaskas, N., Ribeiro, A., Panovska, J., Dessaud, E., Sasai, N., Page, K. M., Briscoe, J., & Ribes, V. (2012). Gene regulatory logic for reading the sonic hedgehog signaling gradient in the vertebrate neural tube. *Cell*, 148(1-2), 273–284 (cit. on p. 23).
- Ballesteros, A., Fitzgerald, T. S., & Swartz, K. J. (2021). Expression of a membrane-targeted fluorescent reporter disrupts auditory hair cell mechano-electrical transduction and causes profound deafness. *Hearing research*, 404, 108212 (cit. on p. 135).

- Banda, E., McKinsey, A., Germain, N., Carter, J., Anderson, N. C., & Grabel, L. (2015). Cell polarity and neurogenesis in embryonic stem cell-derived neural rosettes. *Stem cells and development*, *24*(8), 1022–1033 (cit. on p. 148).
- Bansod, S., Kageyama, R., & Ohtsuka, T. (2017). Hes5 regulates the transition timing of neurogenesis and gliogenesis in mammalian neocortical development. *Development*, *144*(17), 3156–3167 (cit. on p. 20).
- Bardot, B., Mok, L.-P., Thayer, T., Ahimou, F., & Wesley, C. (2005). The notch amino terminus regulates protein levels and delta-induced clustering of drosophila notch receptors. *Experimental cell research*, *304*(1), 202–223 (cit. on p. 145).
- Baron, J. W., & Galla, T. (2019). Intrinsic noise, delta-notch signalling and delayed reactions promote sustained, coherent, synchronized oscillations in the pre-somitic mesoderm. *Journal of the Royal Society Interface*, *16*(160), 20190436 (cit. on pp. 38, 39).
- Biga, V., Hawley, J., Soto, X., Johns, E., Han, D., Bennett, H., Adamson, A. D., Kursawe, J., Glendinning, P., Manning, C. S., et al. (2021). A dynamic, spatially periodic, micro-pattern of hes5 underlies neurogenesis in the mouse spinal cord. *Molecular systems biology*, *17*(5), e9902 (cit. on pp. 16, 29, 30, 90, 91, 106, 134).
- Bridges, C. B., & Morgan, T. H. (1923). *The third-chromosome group of mutant characters of drosophila melanogaster*. Carnegie Institution of Washington. (Cit. on p. 23).
- Briscoe, J., & Small, S. (2015). Morphogen rules: Design principles of gradient-mediated embryo patterning. *Development*, *142*(23), 3996–4009 (cit. on p. 23).
- Chen, V. S., Morrison, J. P., Southwell, M. F., Foley, J. F., Bolon, B., & Elmore, S. A. (2017). Histology atlas of the developing prenatal and postnatal mouse central nervous system, with emphasis on prenatal days e7. 5 to e18. 5. *Toxicologic pathology*, *45*(6), 705–744 (cit. on p. 20).
- Chikayama, E., & Everroad, R. C. (2014). A theory of decomposition of complex chemical networks using the hill functions. *arXiv preprint arXiv:1405.5621* (cit. on p. 83).
- Cohen, M., Georgiou, M., Stevenson, N. L., Miodownik, M., & Baum, B. (2010). Dynamic filopodia transmit intermittent delta-notch signaling to drive pattern

- refinement during lateral inhibition. *Developmental cell*, 19(1), 78–89 (cit. on p. 134).
- Collier, J. R., Monk, N. A., Maini, P. K., & Lewis, J. H. (1996). Pattern formation by lateral inhibition with feedback: A mathematical model of delta-notch intercellular signalling. *Journal of theoretical Biology*, 183(4), 429–446 (cit. on pp. 30, 32–36, 91, 92, 151).
- Conlon, R. A., Reaume, A. G., & Rossant, J. (1995). Notch1 is required for the coordinate segmentation of somites. *Development*, 121(5), 1533–1545 (cit. on p. 38).
- Dawson, S. R., Turner, D. L., Weintraub, H., & Parkhurst, S. M. (1995). Specificity for the hairy/enhancer of split basic helix-loop-helix (bhlh) proteins maps outside the bhlh domain and suggests two separable modes of transcriptional repression. *Molecular and cellular biology*, 15(12), 6923–6931 (cit. on p. 24).
- De Jossineau, C., Soule, J., Martin, M., Anguille, C., Montcourrier, P., & Alexandre, D. (2003). Delta-promoted filopodia mediate long-range lateral inhibition in drosophila. *Nature*, 426(6966), 555–559 (cit. on pp. 134, 151, 156).
- Dessaud, E., Yang, L. L., Hill, K., Cox, B., Ulloa, F., Ribeiro, A., Mynett, A., Novitch, B. G., & Briscoe, J. (2007). Interpretation of the sonic hedgehog morphogen gradient by a temporal adaptation mechanism. *Nature*, 450(7170), 717 (cit. on p. 22).
- Doostdar, P., Hawley, J., Marinopoulou, E., Lea, R., Biga, V., Papalopulu, N., & Soto, X. (2022). Cell coupling compensates for changes in single-cell her6 dynamics and provides phenotypic robustness. *bioRxiv*, 2022–12 (cit. on p. 17).
- Fujiwara, I., Zweifel, M. E., Courtemanche, N., & Pollard, T. D. (2018). Latrunculin a accelerates actin filament depolymerization in addition to sequestering actin monomers. *Current Biology*, 28(19), 3183–3192 (cit. on p. 153).
- Gillespie, D. T. (1977). Exact stochastic simulation of coupled chemical reactions. *The journal of physical chemistry*, 81(25), 2340–2361 (cit. on p. 81).
- Gillespie, D. T. (2000). The chemical langevin equation. *The Journal of Chemical Physics*, 113(1), 297–306 (cit. on pp. 81, 91).
- Goentoro, L., Shoval, O., Kirschner, M. W., & Alon, U. (2009). The incoherent feed-forward loop can provide fold-change detection in gene regulation. *Molecular cell*, 36(5), 894–899 (cit. on p. 22).

- Gomez, H. F., Dumond, M. S., Hodel, L., Vetter, R., & Iber, D. (2021). 3d cell neighbour dynamics in growing pseudostratified epithelia. *Elife*, *10*, e68135 (cit. on p. 82).
- Goodwin, B. C. (1965). Oscillatory behavior in enzymatic control processes. *Advances in enzyme regulation*, *3*, 425–437 (cit. on p. 35).
- Goodyear, R., & Richardson, G. (1997). Pattern formation in the basilar papilla: Evidence for cell rearrangement. *Journal of Neuroscience*, *17*(16), 6289–6301 (cit. on pp. 33, 35, 151, 156).
- Götz, M., & Huttner, W. B. (2005). The cell biology of neurogenesis. *Nature reviews Molecular cell biology*, *6*(10), 777–788 (cit. on p. 21).
- Gouti, M., Tsakiridis, A., Wymeersch, F. J., Huang, Y., Kleinjung, J., Wilson, V., & Briscoe, J. (2014). In vitro generation of neuromesodermal progenitors reveals distinct roles for wnt signalling in the specification of spinal cord and paraxial mesoderm identity. *PLoS biology*, *12*(8), e1001937 (cit. on p. 154).
- Hadjivasiliou, Z., Hunter, G. L., & Baum, B. (2016). A new mechanism for spatial pattern formation via lateral and protrusion-mediated lateral signalling. *Journal of the Royal Society Interface*, *13*(124), 20160484 (cit. on pp. 36, 135, 147, 152).
- Hadjivasiliou, Z., Moore, R. E., McIntosh, R., Galea, G. L., Clarke, J. D., & Alexandre, P. (2019). Basal protrusions mediate spatiotemporal patterns of spinal neuron differentiation. *Developmental cell*, *49*(6), 907–919 (cit. on pp. 135, 156).
- Hatakeyama, J., Bessho, Y., Katoh, K., Ookawara, S., Fujioka, M., Guillemot, F., & Kageyama, R. (2004). Hes genes regulate size, shape and histogenesis of the nervous system by control of the timing of neural stem cell differentiation. *Development*, *131*(22), 5539–5550 (cit. on p. 24).
- Hatakeyama, J., Wakamatsu, Y., Nagafuchi, A., Kageyama, R., Shigemoto, R., & Shimamura, K. (2014). Cadherin-based adhesions in the apical endfoot are required for active notch signaling to control neurogenesis in vertebrates. *Development*, *141*(8), 1671–1682 (cit. on pp. 148, 154).
- Hawley, J., Manning, C., Biga, V., Glendinning, P., & Papalopulu, N. (2022). Dynamic switching of lateral inhibition spatial patterns. *Journal of the Royal Society Interface*, *19*(193), 20220339 (cit. on pp. 17, 91, 105, 106).

- Hicks, C., Johnston, S. H., diSibio, G., Collazo, A., Vogt, T. F., & Weinmaster, G. (2000). Fringe differentially modulates jagged1 and delta1 signalling through notch1 and notch2. *Nature cell biology*, *2*(8), 515–520 (cit. on p. 28).
- Hill, A. V. (1910). The possible effects of the aggregation of the molecules of hemoglobin on its dissociation curves. *j. physiol.*, *40*, iv–vii (cit. on p. 34).
- Hirata, H., Yoshiura, S., Ohtsuka, T., Bessho, Y., Harada, T., Yoshikawa, K., & Kageyama, R. (2002). Oscillatory expression of the bhlh factor hes1 regulated by a negative feedback loop. *Science*, *298*(5594), 840–843 (cit. on p. 26).
- Holley, S. A., Geisler, R., & Nüsslein-Volhard, C. (2000). Control of her1 expression during zebrafish somitogenesis by a delta-dependent oscillator and an independent wave-front activity. *Genes & Development*, *14*(13), 1678–1690 (cit. on p. 38).
- Holmberg, J., Hansson, E., Malewicz, M., Sandberg, M., Perlmann, T., Lendahl, U., & Muhr, J. (2008). Soxb1 transcription factors and notch signaling use distinct mechanisms to regulate proneural gene function and neural progenitor differentiation (cit. on p. 24).
- Hunter, G. L., He, L., Perrimon, N., Charras, G., Giniger, E., & Baum, B. (2019). A role for actomyosin contractility in notch signaling. *BMC biology*, *17*, 1–15 (cit. on pp. 147, 152).
- Imayoshi, I., Sakamoto, M., Yamaguchi, M., Mori, K., & Kageyama, R. (2010). Essential roles of notch signaling in maintenance of neural stem cells in developing and adult brains. *Journal of Neuroscience*, *30*(9), 3489–3498 (cit. on p. 29).
- Imayoshi, I., Shimogori, T., Ohtsuka, T., & Kageyama, R. (2008). Hes genes and neurogenin regulate non-neural versus neural fate specification in the dorsal telencephalic midline. *Development*, *135*(15), 2531–2541 (cit. on p. 24).
- Ishimatsu, K., Hiscock, T. W., Collins, Z. M., Sari, D. W. K., Lischer, K., Richmond, D. L., Bessho, Y., Matsui, T., & Megason, S. G. (2018). Size-reduced embryos reveal a gradient scaling-based mechanism for zebrafish somite formation. *Development*, *145*(11), dev161257 (cit. on pp. 36, 95, 96).
- Ishimatsu, K., Takamatsu, A., & Takeda, H. (2010). Emergence of traveling waves in the zebrafish segmentation clock. *Development*, *137*(10), 1595–1599 (cit. on p. 104).

- Isomura, A., & Kageyama, R. (2014). Ultradian oscillations and pulses: Coordinating cellular responses and cell fate decisions. *Development*, *141*(19), 3627–3636 (cit. on p. 22).
- Kageyama, R., Niwa, Y., Isomura, A., González, A., & Harima, Y. (2012). Oscillatory gene expression and somitogenesis. *Wiley Interdisciplinary Reviews: Developmental Biology*, *1*(5), 629–641 (cit. on p. 38).
- Kasioulis, I., Dady, A., James, J., Prescott, A., Halley, P. A., & Storey, K. G. (2022). A lateral protrusion latticework connects neuroepithelial cells and is regulated during neurogenesis. *Journal of Cell Science*, *135*(6), jcs259897 (cit. on pp. 135, 139, 144, 147, 153, 155).
- Kato, T. M., Kawaguchi, A., Kosodo, Y., Niwa, H., & Matsuzaki, F. (2010). Lunatic fringe potentiates notch signaling in the developing brain. *Molecular and Cellular Neuroscience*, *45*(1), 12–25 (cit. on p. 28).
- Khait, I., Orsher, Y., Golan, O., Binshtok, U., Gordon-Bar, N., Amir-Zilberstein, L., & Sprinzak, D. (2016). Quantitative analysis of delta-like 1 membrane dynamics elucidates the role of contact geometry on notch signaling. *Cell reports*, *14*(2), 225–233 (cit. on pp. 147, 152).
- Khamaisi, B., Luca, V. C., Blacklow, S. C., & Sprinzak, D. (2022). Functional comparison between endogenous and synthetic notch systems. *ACS Synthetic Biology*, *11*(10), 3343–3353 (cit. on p. 153).
- Kicheva, A., Bollenbach, T., Ribeiro, A., Valle, H. P., Lovell-Badge, R., Episkopou, V., & Briscoe, J. (2014). Coordination of progenitor specification and growth in mouse and chick spinal cord. *Science*, *345*(6204), 1254927 (cit. on p. 23).
- Koo, B.-K., Lim, H.-S., Song, R., Yoon, M.-J., Yoon, K.-J., Moon, J.-S., Kim, Y.-W., Kwon, M.-c., Yoo, K.-W., Kong, M.-P., et al. (2005). Mind bomb 1 is essential for generating functional notch ligands to activate notch. *Development*, *132*(15), 3459–3470 (cit. on p. 28).
- Ladi, E., Nichols, J. T., Ge, W., Miyamoto, A., Yao, C., Yang, L.-T., Boulter, J., Sun, Y. E., Kintner, C., & Weinmaster, G. (2005). The divergent dsl ligand dll3 does not activate notch signaling but cell autonomously attenuates signaling induced by other dsl ligands. *The Journal of cell biology*, *170*(6), 983–992 (cit. on p. 28).

- Lanford, P. J., Shailam, R., Norton, C. R., Ridley, T., & Kelley, M. W. (2000). Expression of *math1* and *hes5* in the cochleae of wildtype and *jag2* mutant mice. *Journal of the Association for Research in Otolaryngology*, *1*(2), 161–171 (cit. on p. 24).
- Le Dréau, G., & Martí, E. (2012). Dorsal–ventral patterning of the neural tube: A tale of three signals. *Developmental neurobiology*, *72*(12), 1471–1481 (cit. on p. 23).
- Lewis, J. (2003). Autoinhibition with transcriptional delay: A simple mechanism for the zebrafish somitogenesis oscillator. *Current Biology*, *13*(16), 1398–1408 (cit. on pp. 38, 83, 99).
- Lewis, J., Hanisch, A., & Holder, M. (2009). Notch signaling, the segmentation clock, and the patterning of vertebrate somites. *Journal of biology*, *8*, 1–7 (cit. on p. 40).
- Liew, A. W.-C., Law, N.-F., Cao, X.-Q., & Yan, H. (2009). Statistical power of fisher test for the detection of short periodic gene expression profiles. *Pattern Recognition*, *42*(4), 549–556 (cit. on p. 108).
- Malaguti, M., Portero Migueles, R., Annoh, J., Sadurska, D., Blin, G., & Lowell, S. (2022). Synpl: Synthetic notch pluripotent cell lines to monitor and manipulate cell interactions in vitro and in vivo. *Development*, *149*(12), dev200226 (cit. on p. 153).
- Manning, C. S., Biga, V., Boyd, J., Kursawe, J., Ymisson, B., Spiller, D. G., Sanderson, C. M., Galla, T., Rattray, M., & Papalopulu, N. (2019). Quantitative single-cell live imaging links *hes5* dynamics with cell-state and fate in murine neurogenesis. *Nature Communications*, *10*(1), 2835 (cit. on pp. 26, 29–31, 37, 81, 83, 84, 91, 99, 157).
- Marinopoulou, E., Biga, V., Sabherwal, N., Miller, A., Desai, J., Adamson, A. D., & Papalopulu, N. (2021). *Hes1* protein oscillations are necessary for neural stem cells to exit from quiescence. *iScience*, *24*(10), 103198 (cit. on pp. 26, 157).
- Marklund, U., Hansson, E. M., Sundström, E., de Angelis, M. H., Przemeck, G. K., Lendahl, U., Muhr, J., & Ericson, J. (2010). Domain-specific control of neurogenesis achieved through patterned regulation of notch ligand expression. *Development*, *137*(3), 437–445 (cit. on pp. 29, 144).

- Maroto, M., Bone, R. A., & Dale, J. K. (2012). Somitogenesis. *Development*, *139*(14), 2453–2456 (cit. on pp. 38, 89).
- Meloty-Kapella, L., Shergill, B., Kuon, J., Botvinick, E., & Weinmaster, G. (2012). Notch ligand endocytosis generates mechanical pulling force dependent on dynamin, epsins, and actin. *Developmental cell*, *22*(6), 1299–1312 (cit. on pp. 28, 145).
- Miele, L. (2011). Transcription factor rbpj/csl: A genome-wide look at transcriptional regulation. *Proceedings of the National Academy of Sciences*, *108*(36), 14715–14716 (cit. on p. 26).
- Miyata, T., Kawaguchi, A., Okano, H., & Ogawa, M. (2001). Asymmetric inheritance of radial glial fibers by cortical neurons. *Neuron*, *31*(5), 727–741 (cit. on p. 22).
- Mogilner, A., & Rubinstein, B. (2005). The physics of filopodial protrusion. *Biophysical journal*, *89*(2), 782–795 (cit. on p. 140).
- Momiji, H., & Monk, N. A. (2009). Oscillatory notch-pathway activity in a delay model of neuronal differentiation. *Physical Review E*, *80*(2), 021930 (cit. on pp. 39, 153).
- Monk, N. A. (1997). Cell communities and robustness in development. *Bulletin of mathematical biology*, *59*(6), 1183–1189 (cit. on p. 20).
- Monk, N. A. (2003). Oscillatory expression of *hes1*, *p53*, and *nf- κ b* driven by transcriptional time delays. *Current Biology*, *13*(16), 1409–1413 (cit. on pp. 36, 37, 91).
- Morsut, L., Roybal, K. T., Xiong, X., Gordley, R. M., Coyle, S. M., Thomson, M., & Lim, W. A. (2016). Engineering customized cell sensing and response behaviors using synthetic notch receptors. *Cell*, *164*(4), 780–791 (cit. on p. 153).
- Mussmann, C., Huebner, R., Trilck, M., Rolfs, A., & Frech, M. J. (2014). Hes5 is a key mediator of wnt-3a-induced neuronal differentiation. *Stem cells and development*, *23*(12), 1328–1339 (cit. on p. 24).
- Nandagopal, N., Santat, L. A., & Elowitz, M. B. (2019). Cis-activation in the notch signaling pathway. *Elife*, *8* (cit. on p. 28).
- Nandagopal, N., Santat, L. A., LeBon, L., Sprinzak, D., Bronner, M. E., & Elowitz, M. B. (2018). Dynamic ligand discrimination in the notch signaling pathway. *Cell*, *172*(4), 869–880 (cit. on pp. 23, 145, 147, 155).

- Nelson, B. R., Hodge, R. D., Bedogni, F., & Hevner, R. F. (2013). Dynamic interactions between intermediate neurogenic progenitors and radial glia in embryonic mouse neocortex: Potential role in *dll1*-notch signaling. *Journal of Neuroscience*, *33*(21), 9122–9139 (cit. on pp. 135, 137, 147).
- Nichols, J. T., Miyamoto, A., Olsen, S. L., D’Souza, B., Yao, C., & Weinmaster, G. (2007). *Dsl* ligand endocytosis physically dissociates *notch1* heterodimers before activating proteolysis can occur. *The Journal of cell biology*, *176*(4), 445–458 (cit. on p. 145).
- Nikolaou, N., Watanabe-Asaka, T., Gerety, S., Distel, M., Köster, R. W., & Wilkinson, D. G. (2009). Lunatic fringe promotes the lateral inhibition of neurogenesis (cit. on p. 27).
- Noctor, S. C., Flint, A. C., Weissman, T. A., Dammerman, R. S., & Kriegstein, A. R. (2001). Neurons derived from radial glial cells establish radial units in neocortex. *Nature*, *409*(6821), 714–720 (cit. on p. 22).
- Norden, C., Young, S., Link, B. A., & Harris, W. A. (2009). Actomyosin is the main driver of interkinetic nuclear migration in the retina. *Cell*, *138*(6), 1195–1208 (cit. on p. 22).
- Ochi, S., Imaizumi, Y., Shimojo, H., Miyachi, H., & Kageyama, R. (2020). Oscillatory expression of *hes1* regulates cell proliferation and neuronal differentiation in the embryonic brain. *Development*, *147*(4), dev182204 (cit. on pp. 26, 157).
- Ogawa, Y., Takebayashi, H., Takahashi, M., Osumi, N., Iwasaki, Y., & Ikenaka, K. (2005). Gliogenic radial glial cells show heterogeneity in the developing mouse spinal cord. *Developmental neuroscience*, *27*(6), 364–377 (cit. on p. 21).
- Ohtsuka, T., Ishibashi, M., Gradwohl, G., Nakanishi, S., Guillemot, F., & Kageyama, R. (1999). *Hes1* and *hes5* as notch effectors in mammalian neuronal differentiation. *The EMBO journal*, *18*(8), 2196–2207 (cit. on p. 26).
- Ohtsuka, T., Sakamoto, M., Guillemot, F., & Kageyama, R. (2001). Roles of the basic helix-loop-helix genes *hes1* and *hes5* in expansion of neural stem cells of the developing brain. *Journal of Biological Chemistry*, *276*(32), 30467–30474 (cit. on pp. 24, 26).
- Olivera-Martinez, I., Schurch, N., Li, R. A., Song, J., Halley, P. A., Das, R. M., Burt, D. W., Barton, G. J., & Storey, K. G. (2014). Major transcriptome re-organisation

- and abrupt changes in signalling, cell cycle and chromatin regulation at neural differentiation in vivo. *Development*, *141*(16), 3266–3276 (cit. on p. 155).
- Özbudak, E. M., & Lewis, J. (2008). Notch signalling synchronizes the zebrafish segmentation clock but is not needed to create somite boundaries. *PLoS Genet*, *4*(2), e15 (cit. on pp. 38, 89).
- Pfeuty, B. (2022). Multistability and transitions between spatiotemporal patterns through versatile notch-hes signaling. *Journal of Theoretical Biology*, *539*, 111060 (cit. on pp. 36, 39, 153).
- Phillips, N. E., Manning, C. S., Pettini, T., Biga, V., Marinopoulou, E., Stanley, P., Boyd, J., Bagnall, J., Paszek, P., Spiller, D. G., et al. (2016). Stochasticity in the mir-9/hes1 oscillatory network can account for clonal heterogeneity in the timing of differentiation. *Elife*, *5*, e16118 (cit. on pp. 99, 109).
- Prasad, A., Dana, S. K., Karnatak, R., Kurths, J., Blasius, B., & Ramaswamy, R. (2008). Universal occurrence of the phase-flip bifurcation in time-delay coupled systems. *Chaos: An Interdisciplinary Journal of Nonlinear Science*, *18*(2), 023111 (cit. on p. 39).
- Preuße, K., Tveriakhina, L., Schuster-Gossler, K., Gaspar, C., Rosa, A. I., Henrique, D., Gossler, A., & Stauber, M. (2015). Context-dependent functional divergence of the notch ligands dll1 and dll4 in vivo. *PLoS genetics*, *11*(6), e1005328 (cit. on p. 28).
- Reynolds, C. W. (1987). Flocks, herds and schools: A distributed behavioral model. *Proceedings of the 14th annual conference on Computer graphics and interactive techniques*, 25–34 (cit. on p. 29).
- Ribes, V., Balaskas, N., Sasai, N., Cruz, C., Dessaud, E., Cayuso, J., Tozer, S., Yang, L. L., Novitch, B., Marti, E., et al. (2010). Distinct sonic hedgehog signaling dynamics specify floor plate and ventral neuronal progenitors in the vertebrate neural tube. *Genes & development*, *24*(11), 1186–1200 (cit. on p. 22).
- Riesenberg, A. N., Conley, K. W., Le, T. T., & Brown, N. L. (2018). Separate and coincident expression of hes1 and hes5 in the developing mouse eye. *Developmental Dynamics*, *247*(1), 212–221 (cit. on p. 24).
- Sabherwal, N., Rowntree, A., Marinopoulou, E., Pettini, T., Hourihane, S., Thomas, R., Soto, X., Kursawe, J., & Papalopulu, N. (2021). Differential phase register of hes1 oscillations with mitoses underlies cell-cycle heterogeneity in er+

- breast cancer cells. *Proceedings of the National Academy of Sciences*, *118*(45), e2113527118 (cit. on p. 155).
- Sáez, M., Blassberg, R., Camacho-Aguilar, E., Siggia, E. D., Rand, D. A., & Briscoe, J. (2022). Statistically derived geometrical landscapes capture principles of decision-making dynamics during cell fate transitions. *Cell systems*, *13*(1), 12–28 (cit. on p. 19).
- Sagner, A., Gaber, Z. B., Delile, J., Kong, J. H., Rousso, D. L., Pearson, C. A., Wickse, S. E., Melchionda, M., Gharavy, S. N. M., Briscoe, J., et al. (2018). Olig2 and hes regulatory dynamics during motor neuron differentiation revealed by single cell transcriptomics. *PLoS biology*, *16*(2), e2003127 (cit. on p. 26).
- Sasai, Y., Kageyama, R., Tagawa, Y., Shigemoto, R., & Nakanishi, S. (1992). Two mammalian helix-loop-helix factors structurally related to drosophila hairy and enhancer of split. *Genes & development*, *6*(12b), 2620–2634 (cit. on p. 24).
- Shimojo, H., Isomura, A., Ohtsuka, T., Kori, H., Miyachi, H., & Kageyama, R. (2016). Oscillatory control of delta-like1 in cell interactions regulates dynamic gene expression and tissue morphogenesis. *Genes & development*, *30*(1), 102–116 (cit. on pp. 38, 39).
- Shimojo, H., Ohtsuka, T., & Kageyama, R. (2008). Oscillations in notch signaling regulate maintenance of neural progenitors. *Neuron*, *58*(1), 52–64 (cit. on pp. 26, 39).
- Shimojo, H., Ohtsuka, T., & Kageyama, R. (2011). Dynamic expression of notch signaling genes in neural stem/progenitor cells. *Frontiers in neuroscience*, *5*, 78 (cit. on p. 26).
- Snyder, C. S., Harrington, A. R., Kaushal, S., Mose, E., Lowy, A. M., Hoffman, R. M., & Bouvet, M. (2013). A dual color, genetically engineered mouse model for multi-spectral imaging of the pancreatic microenvironment. *Pancreas*, *42*(6), 952 (cit. on p. 135).
- Sonnen, K. F., & Aulehla, A. (2014). Dynamic signal encoding—from cells to organisms. *Seminars in cell & developmental biology*, *34*, 91–98 (cit. on p. 23).
- Spear, P. C., & Erickson, C. A. (2012). Interkinetic nuclear migration: A mysterious process in search of a function. *Development, growth & differentiation*, *54*(3), 306–316 (cit. on pp. 22, 155).

- Sprinzak, D., Lakhapal, A., LeBon, L., Santat, L. A., Fontes, M. E., Anderson, G. A., Garcia-Ojalvo, J., & Elowitz, M. B. (2010). Cis-interactions between notch and delta generate mutually exclusive signalling states. *Nature*, *465*(7294), 86–90 (cit. on p. 28).
- Sueda, R., Imayoshi, I., Harima, Y., & Kageyama, R. (2019). High hes1 expression and resultant ascl1 suppression regulate quiescent vs. active neural stem cells in the adult mouse brain. *Genes & development*, *33*(9-10), 511–523 (cit. on p. 157).
- T Das, A., Tenenbaum, L., & Berkhout, B. (2016). Tet-on systems for doxycycline-inducible gene expression. *Current gene therapy*, *16*(3), 156–167 (cit. on p. 155).
- Tiedemann, H. B., Schneltzer, E., Beckers, J., Przemeck, G. K., & de Angelis, M. H. (2017). Modeling coexistence of oscillation and delta/notch-mediated lateral inhibition in pancreas development and neurogenesis. *Journal of theoretical biology*, *430*, 32–44 (cit. on pp. 36, 39, 92, 153).
- Turing, A. M. (1990). The chemical basis of morphogenesis. *Bulletin of mathematical biology*, *52*(1-2), 153–197 (cit. on p. 36).
- Ulrich, H. (2010). *Perspectives of stem cells: From tools for studying mechanisms of neuronal differentiation towards therapy*. Springer Netherlands. (Cit. on pp. 20, 24).
- Uriu, K., Morishita, Y., & Iwasa, Y. (2009). Traveling wave formation in vertebrate segmentation. *Journal of theoretical biology*, *257*(3), 385–396 (cit. on pp. 95, 96).
- Vasilopoulos, G., & Painter, K. J. (2016). Pattern formation in discrete cell tissues under long range filopodia-based direct cell to cell contact. *Mathematical Biosciences*, *273*, 1–15 (cit. on pp. 135, 152).
- Veeraval, L., O’Leary, C. J., & Cooper, H. M. (2020). Adherens junctions: Guardians of cortical development. *Frontiers in Cell and Developmental Biology*, *8*, 6 (cit. on p. 141).
- Waddington, C. H. (2014). *The strategy of the genes*. Routledge. (Cit. on pp. 18, 19).
- Weiss, J. N. (1997). The hill equation revisited: Uses and misuses. *The FASEB Journal*, *11*(11), 835–841 (cit. on p. 34).

- Wichert, S., Fokianos, K., & Strimmer, K. (2004). Identifying periodically expressed transcripts in microarray time series data. *Bioinformatics*, *20*(1), 5–20 (cit. on p. 108).
- Wiszniak, S., & Schwarz, Q. (2019). Notch signalling defines dorsal root ganglia neuroglial fate choice during early neural crest cell migration. *BMC neuroscience*, *20*, 1–13 (cit. on pp. 144, 149).
- Wolpert, L. (1969). Positional information and the spatial pattern of cellular differentiation. *Journal of theoretical biology*, *25*(1), 1–47 (cit. on p. 22).
- Yan, C.-C. S., Chepyala, S. R., Yen, C.-M., & Hsu, C.-P. (2017). Efficient and flexible implementation of langevin simulation for gene burst production. *Scientific reports*, *7*(1), 16851 (cit. on p. 81).
- Yoon, K.-J., Koo, B.-K., Im, S.-K., Jeong, H.-W., Ghim, J., Kwon, M.-c., Moon, J.-S., Miyata, T., & Kong, Y.-Y. (2008). Mind bomb 1-expressing intermediate progenitors generate notch signaling to maintain radial glial cells. *Neuron*, *58*(4), 519–531 (cit. on pp. 28, 154).
- Zagorski, M., Tabata, Y., Brandenberg, N., Lutolf, M. P., Tkačik, G., Bollenbach, T., Briscoe, J., & Kicheva, A. (2017). Decoding of position in the developing neural tube from antiparallel morphogen gradients. *Science*, *356*(6345), 1379–1383 (cit. on pp. 22, 104).